



**Max-Planck-Institut für Intelligente Systeme
(ehemals Max-Planck-Institut für Metallforschung)
Stuttgart**

Interaction of carbon and nitrogen in iron

Holger Göhring

Dissertation
an der
Universität Stuttgart

Bericht Nr. 257
September 2016

Interaction of carbon and nitrogen in iron

Von der Fakultät Chemie der Universität Stuttgart zur Erlangung
der Würde eines Doktors der Naturwissenschaften (Dr. rer. nat.)
genehmigte Abhandlung

vorgelegt von

Holger Göhring

aus Waiblingen

Hauptberichter:

Prof. Dr. Ir. E.J. Mittemeijer

Mitberichter:

Prof. Dr. J. Bill

Prüfungsvorsitzender:

Prof. Dr. T. Schleid

Tag der Abgabe:

15. März 2016

Tag der mündlichen Prüfung: 6. September 2016

MAX-PLANCK-INSTITUT FÜR INTELLIGENTE SYSTEME, STUTTGART
(ehemals MAX-PLANCK-INSTITUT FÜR METALLFORSCHUNG)
INSTITUT FÜR MATERIALWISSENSCHAFT DER UNIVERSITÄT STUTTGART

Stuttgart 2016

Contents

1 General introduction	9
1.1 Phases in the binary Fe–C and Fe–N systems and the ternary Fe–N–C system	9
1.2 Thermodynamics of gaseous nitriding and nitrocarburising of iron	10
1.3 Thermodynamic modelling – the CALPHAD approach	14
1.3.1 Software for thermodynamic calculations	18
1.4 Ternary interstitial diffusion	18
1.5 Outlook of the thesis	19
2 N and C interstitial diffusion and thermodynamic interactions in ϵ-iron carbonitride	21
2.1 Introduction	21
2.2 Evaluation method	23
2.3 Modelling of interstitial diffusion	25
2.4 Experimental	28
2.5 Results	33
2.5.1 Microstructure, layer thickness and kinetics	33
2.5.2 Concentration-depth profiles in the ϵ (sub)layers	34
2.5.3 Fluxes at upper and lower boundaries of the ϵ (sub)layers	36
2.5.4 Diffusivity matrix	38
2.6 Discussion	41
2.6.1 Merits and limitations of the model and the evaluation method	41
2.6.2 N and C diffusion in the ϵ phase; comparison with literature data	43
2.6.3 Application to other microstructures	46
2.7 Conclusions	50
3 Microstructural development and crystallographic properties of decomposing Fe–N–C compound layers	51
3.1 Introduction	51
3.1.1 Phases in the Fe–N–C system	52
3.1.2 Phase transformations in Fe–N–C compound layers	53
3.2 Experimental	56
3.2.1 Specimen preparation	56
3.2.2 Nitrocarburising treatment	56
3.2.3 Secondary annealing	58
3.2.4 Microstructure characterisation	58
3.3 Results	59
3.3.1 Quenched high-temperature microstructure	59

3.3.2	Microstructure development upon slow cooling and upon secondary annealing	60
3.3.3	Orientation relationship of ϵ and γ'	66
3.4	Discussion	69
3.4.1	Microstructure after quenching	69
3.4.2	Microstructure after cooling slowly	70
3.4.3	Microstructure after secondary annealing	72
3.5	Conclusions	73
4	The $\alpha+\epsilon$ two-phase equilibrium in the Fe–N–C system – experimental investigations and thermodynamic calculations	75
4.1	Introduction	76
4.1.1	Equilibrium, metastable equilibrium, local equilibrium	76
4.1.2	Constitution and invariant reactions in the Fe–N–C system	77
4.2	Thermodynamic considerations	81
4.2.1	Thermodynamics of interstitial solid solutions	81
4.2.2	Comparison of thermodynamic descriptions – invariant reactions	82
4.3	Experimental	83
4.4	Results of experimental investigation	86
4.4.1	Nitrocarburizing of Fe–C alloys	86
4.4.2	Nitriding of Fe–C alloys	88
4.5	Discussion	90
4.5.1	Development of the compound-layer microstructure between 823 K and 863 K (550 °C and 590 °C)	90
4.5.2	The $\alpha+\epsilon$ two-phase field – nature of the invariant reactions and their temperatures	94
4.5.3	Compatibility of experimental data with the models from the literature .	96
4.6	Conclusions	97
5	A thermodynamic model for non-stoichiometric cementite; the Fe–C phase diagram	99
5.1	Introduction	99
5.2	Thermodynamic models for Fe–C solution phases	101
5.3	The employed experimental data set	103
5.3.1	Gibbs energy of cementite	104
5.3.2	Mono-variant (at 1 atm) equilibria	105
5.3.3	Invariant (at 1 atm) equilibria	105
5.4	Optimisation of the thermodynamic model	105
5.5	Discussion	108
5.5.1	Thermodynamics of cementite	108
5.5.2	The Fe–C phase diagram	111
5.5.3	Comparison to other models for non-stoichiometric cementite	116
5.6	Conclusions	119

6 Thermodynamics of the Fe–N and Fe–N–C systems; the Fe–N and Fe–N–C phase diagrams revisited	121
6.1 Introduction	121
6.2 Thermodynamic model of the Fe–N and Fe–N–C solid solution phases	124
6.3 Employed data for the thermodynamic parameter optimization	125
6.3.1 Binary Fe–N data	125
6.3.2 Ternary Fe–N–C data	126
6.4 Applied models; optimization process	127
6.5 Discussion	128
6.5.1 The binary Fe–N phase diagram	128
6.5.2 The ternary Fe–N–C system	135
6.5.3 The appropriateness of a model for the γ' phase	138
6.5.4 The thermodynamics of the ϵ phase	141
6.6 Conclusions	144
7 Summary	147
7.1 Experimental	147
7.1.1 Specimen preparation	147
7.1.2 Nitriding and nitrocarburising treatments, secondary annealing	148
7.1.3 Specimen characterisation	148
7.2 Results and discussion	148
7.2.1 N and C interstitial diffusion and thermodynamic interactions in ϵ -iron carbonitride	148
7.2.2 Microstructural development and crystallographic properties of decomposing Fe–N–C compound layers	149
7.2.3 The $\alpha+\epsilon$ two-phase equilibrium in the Fe–N–C system – experimental investigations and thermodynamic calculations	150
7.2.4 A thermodynamic model for non-stoichiometric cementite; the Fe–C phase diagram	151
7.2.5 Thermodynamics of the Fe–N and Fe–N–C systems; the Fe–N and Fe–N–C phase diagrams revisited	151
8 Zusammenfassung	153
8.1 Experimentalteil	153
8.1.1 Probenherstellung	153
8.1.2 Nitrier- und Nitrocarburierbehandlungen, Auslagerungsversuche	154
8.1.3 Untersuchungsmethoden	154
8.2 Ergebnisse und Diskussion	155
8.2.1 Interstitielle Diffusion von N und C und thermodynamische Wechselwirkungen in ϵ -Eisencarbonitrid	155
8.2.2 Entwicklung der Mikrostruktur und kristallographische Eigenschaften von sich zersetzen Fe–N–C-Verbindungsschichten	156
8.2.3 Das $\alpha+\epsilon$ -Zweiphasengleichgewicht im Fe–N–C-System – experimentelle Untersuchungen und thermodynamische Berechnungen	157

8.2.4	Ein thermodynamisches Modell für nicht-stöchiometrischen Zementit; das Fe–C-Phasendiagramm	157
8.2.5	Thermodynamik der Systeme Fe–N und Fe–N–C; die Fe–N- und Fe–N–C-Phasendiagramme	158
Bibliography		159

Chapter 1

General introduction

Without doubt, C is the most important interstitial alloying element in Fe-based alloys, being contained in almost all technically applied steels. By thermochemical surface treatments [1], additional amounts of interstitially dissolved elements can be introduced into a zone close to the surface of the treated material. Nitriding and nitrocarburising are two of those thermochemical surface treatment procedures widely applied in industry, during which N (and during nitrocarburising also C) are incorporated into the specimen. During the treatment, a diffusion zone and, if the chemical potentials of N and C are sufficiently high, a compound layer form close to the surface of the specimen, see Figure 1.1.

Nitriding and nitrocarburising are performed in order to improve e.g. the mechanical, tribological and anti-corrosion properties of the area close to the surface of a material. The main advantage of these processes is the low treatment temperature, leading only to minor changes of the microstructure and, therefore, of the properties of the bulk material. Both processes can be performed in different media, i.e. in a salt bath, in plasma or, as discussed here, in an atmosphere containing different gas species supplying N and/or C to the specimen, usually in a temperature range of 723 K to 863 K [1, 2].

1.1 Phases in the binary Fe–C and Fe–N systems and the ternary Fe–N–C system

The terminal solution phases in the binary Fe–C (Figure 1.2a) [3] and Fe–N (Figure 1.2b) [4] systems are the α/δ (bcc Fe) and γ (fcc Fe) phases. In the stable state, no other phases than those and N_2 gas and graphite exist. However, there are several metastable intermediate phases that can be formed by e.g. implying sufficiently high chemical potentials of N and C (see Section 1.2). In the binary Fe–C system, metastable cementite (θ) exists with a small solubility range with the formula Fe_3C_{1-z} [5–16], see also Chapter 5. In the phase diagram in Figure 1.2a,

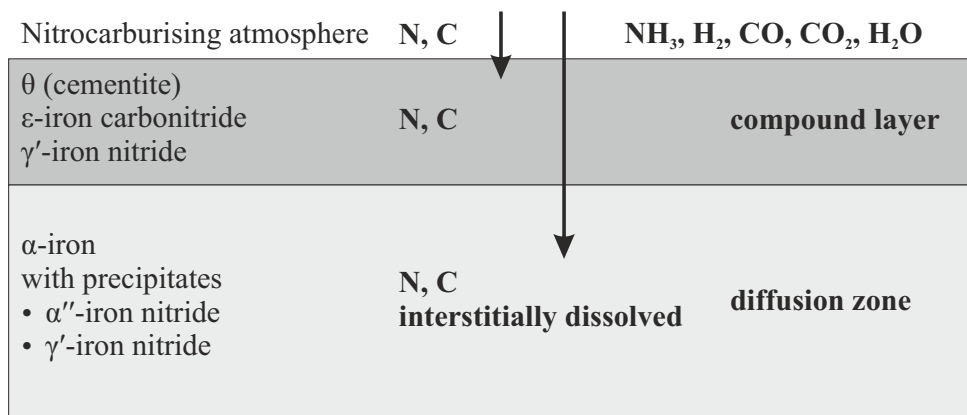


Figure 1.1: Schematic illustration of the process of nitrocarburising of iron. In the diffusion zone, N and C are interstitially dissolved into α -Fe. During cooling, precipitates of α'' -iron nitride and γ' -iron (carbo)nitride form. On top, a compound layer can form that consists of θ -iron carbide (cementite), ε -iron carbonitride and γ' -iron (carbo)nitride.

this homogeneity range is not shown. Until today, only trace amounts of N have been found in θ [17, 18]. Higher metastable carbides [19] as χ - Fe_5C_2 also exist in the Fe–C system but are not considered here.

In the Fe–N system (Figure 1.2b), the role of cementite is taken by the metastable γ' phase with the formula $\text{Fe}_4\text{N}_{1-x}$, showing a modest homogeneity range [20–22]. γ' is formed by N occupying only one octahedral site in each unit cell of an fcc-type Fe lattice, leading to L1₂-type order. γ' can dissolve small but significant amounts of C, see also Chapter 6. The ε phase can be considered as an interstitial solution of N and C in hcp Fe. Depending on the composition, varying degrees of ordering can be observed. The ε phase shows a large homogeneity range in the binary Fe–N system and extends to the ternary Fe–N–C system with N being replaced by C. In contrast to the binary Fe–N system, in the ternary Fe–N–C system, an equilibrium of α and ε can be observed at intermediate temperatures. This is discussed in detail in Chapter 4. No additional phases of essential ternary character exist in the ternary Fe–N–C system.

1.2 Thermodynamics of gaseous nitriding and nitrocarburising of iron

The thermodynamics of gaseous nitriding and nitrocarburising can be described following the approach in References 1 and 23–25. N can theoretically be taken up into the specimen from N_2 gas according to

$$\frac{1}{2}\text{N}_2 \rightleftharpoons [\text{N}] \quad (1.1)$$

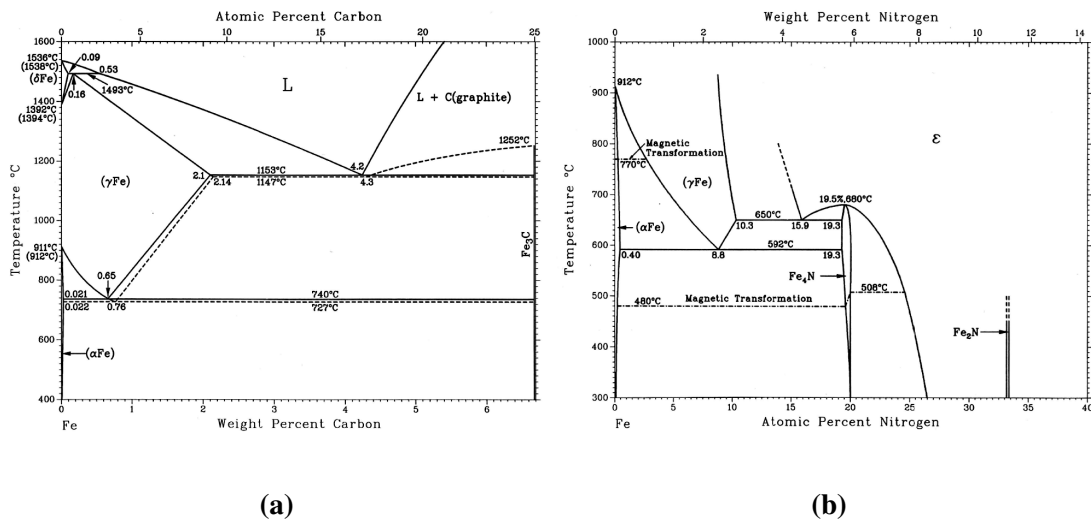


Figure 1.2: a) Phase diagram of the binary Fe–C system, taken from Reference 3, showing both the stable (solid lines) and metastable (dashed lines) equilibria. In the stable system, the α/δ , γ , graphite and liquid phase are in equilibrium with each other. In the metastable system, graphite formation is suppressed. Therefore, the cementite (Θ) phase is formed, here approximated by stoichiometric Fe_3C . b) Phase diagram of the metastable Fe–N system, taken from Reference 4. In the shown temperature range, only the solid phases α , γ , γ' (here shown as Fe_4N), ε and the not further considered Fe_2N exist.

with $[N]$ denoting N dissolved in Fe. The chemical potential of N μ_N can then be calculated as

$$\mu_N = {}^\circ\mu_N + RT \ln \left(\frac{p_{N_2}}{}^\circ p \right)^{1/2} = {}^\circ\mu_N + RT \ln a_N, \quad (1.2)$$

with the standard chemical potential of N μ_N° , the partial pressure of N₂ p_{N_2} , the standard pressure p° and the activity of nitrogen a_N , assuming ideal behaviour of the gas phase. However, at technically achievable pressures, the resulting chemical potentials of N are too low in order to obtain significant N contents in the specimen. Furthermore, formation of nitride phases is not possible due to their metastable character. Therefore, usually mixtures of NH₃ and H₂ are applied for technical nitriding. The equilibrium



then controls the chemical potential of N in equilibrium with the surface of the specimen. Using Equation 1.2 and the equilibrium constant K_N of the reaction



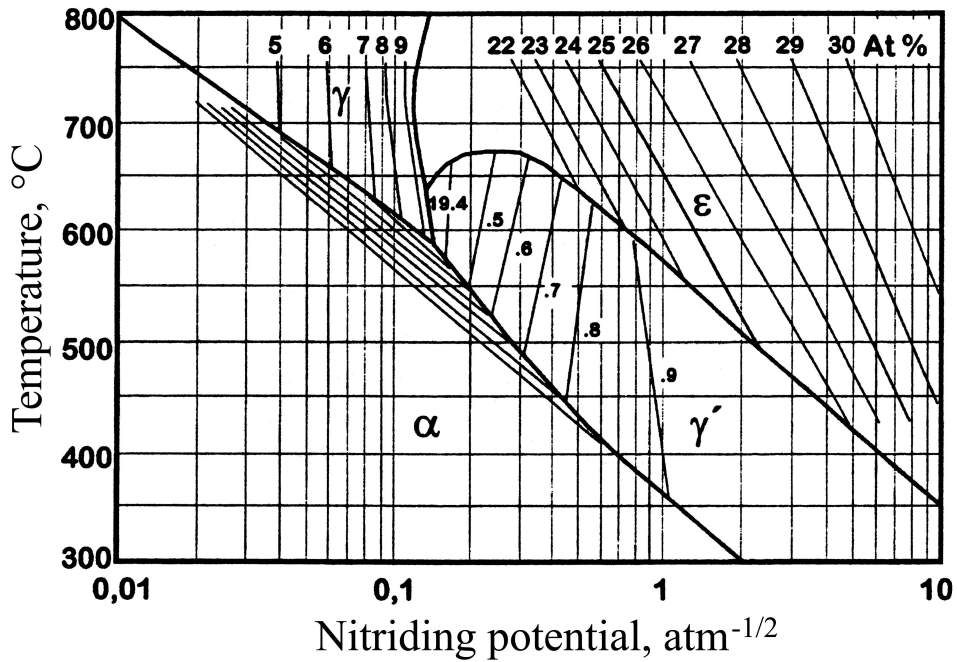


Figure 1.3: Lehrer diagram [28] taken from Reference 27, showing which phase is formed at the surface of a pure Fe specimen upon gas nitriding at a certain temperature and nitriding potential $r_N = p_{NH_3} p_{H_2}^{-3/2}$ together with lines of constant N content.

it follows

$$\mu_N = {}^\circ\mu_N + RT \ln \frac{p_{NH_3} {}^\circ p^{1/2}}{p_{H_2}^{3/2}} K_N. \quad (1.5)$$

with the partial pressure of NH_3 p_{NH_3} and the partial pressure of H_2 p_{H_2} . K_N can be calculated from standard Gibbs energies of the gas species, e.g. given in Reference 26. The ratio $r_N = p_{NH_3} / p_{H_2}^{3/2}$ as a process parameter is often called the nitriding potential. Because r_N is directly proportional to the nitrogen activity ($a_N = {}^\circ p^{1/2} K_N r_N$), it can be used as an axis variable in a potential phase diagram (Lehrer diagram) as shown in Figure 1.3 (taken from Reference 27) as first done by Lehrer [28], here shown with added lines of equal N content.

For carburising and nitrocarburising, a large variety of different gas mixes can be applied, leading to different equilibria governing the chemical potential of carbon. In the following, only the relevant equilibria are dealt with. CO in the gas phase leads to an uptake of C according to the reaction



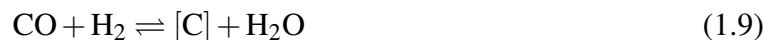
with $[C]$ denoting carbon dissolved in iron. Following similar arguments as above, the chemical potential in the gas phase can be calculated as

$$\mu_{C1} = {}^\circ\mu_C + RT \ln \frac{p_{CO}^2}{p_{CO_2} {}^\circ p} K_{C1} \quad (1.7)$$

with the equilibrium constant K_{C1} of the Boudouard reaction



and the partial pressures of CO and CO_2 , p_{CO} and p_{CO_2} . Due to the presence of H_2 in the atmosphere, furthermore the heterogeneous water gas reaction



has to be considered, defining a chemical potential in the gas phase after

$$\mu_{C2} = {}^\circ\mu_C + RT \ln \frac{p_{CO} p_{H_2}}{p_{H_2O} {}^\circ p} K_{C2}. \quad (1.10)$$

with the equilibrium constant K_{C2} of the heterogeneous water gas reaction



and the partial pressure of H_2O p_{H_2O} .

The gas-phase composition is adjusted that a unique chemical potential of C, $\mu_C = \mu_{C1} = \mu_{C2}$ is defined. Therefore, control of the partial pressures of NH_3 , H_2 , CO, CO_2 and H_2O is necessary. It is also possible to consider a large variety of other carburising reactions, e.g. involving methane or other hydrocarbons. In detail, this is dealt with in Reference 1 and 24.

On a laboratory scale, nitriding and nitrocarburising can be performed in a fused silica tube furnace. A schematic illustration of the furnace used for the experiments performed in the present work is shown in Figure 1.4. The furnace is equipped with gas supplies for NH_3 , H_2 , CO, CO_2 , CH_4 (not used in this work), H_2O and N_2 (the latter as a filler gas). The partial pressure of each gas can be precisely controlled by mass-flow controllers. In order to keep the gas composition constant, a high flow rate is used. The specimen is suspended from the specimen rod by a fused silica fibre. Before the start of the experiment, the specimen is located in the upper cool zone of the furnace until a constant gas composition can be assured. The specimen is then lowered into the hot zone of the furnace, defining the start of the treatment. At the end of the treatment, the valve is opened and the specimen is quenched in N_2 -flushed water

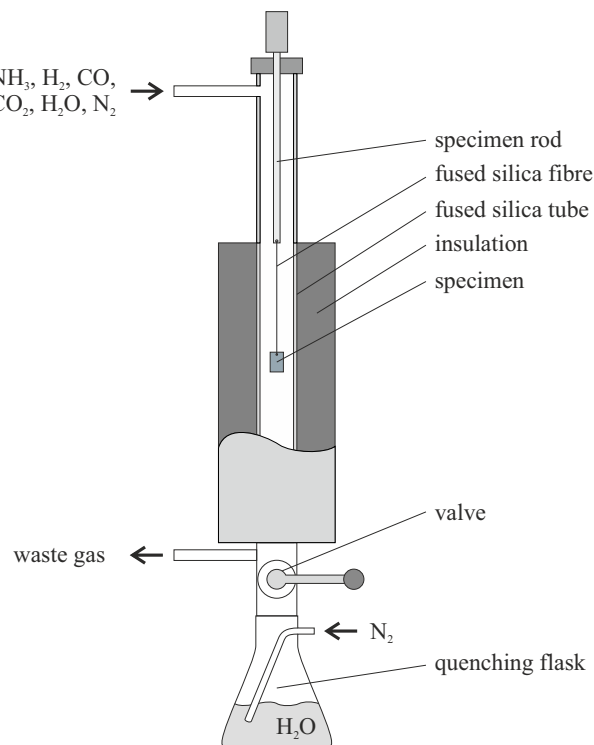


Figure 1.4: Fused silica tube furnace used in the present work with gas supplies for NH_3 , H_2 , CO , CO_2 , H_2O and N_2 . The specimen is suspended on a fused silica fibre that can be destroyed, quenching the specimen in N_2 -flushed water and defining the end of the treatment.

(to prevent oxidation) by destroying the fused silica fibre. Lower cooling rates can be realised by either lifting the specimen to the cool zone of the furnace or setting the heating power of the furnace to zero.

In theory, if the chemical potentials of N and/or C in the gas phase are controlled as described above, an equilibrium at the surface of the nitrided/nitrocarburised specimen can be established. However, in reality, often only a steady state is reached, leading to kinetically controlled constant N and/or C contents at the surface of the specimen [1, 25, 29, 30].

1.3 Thermodynamic modelling – the CALPHAD approach

Thermodynamic modelling has been performed in the past for the Fe–C system in References 31–34 and for the Fe–N system in References 31 and 35–43. For the ternary Fe–N–C system, thermodynamic models are available in References 39, 41 and 43–47.

The CALPHAD approach has been developed since the early 1970s [48]. The CALPHAD approach is based on thermodynamic descriptions of the Gibbs energy of each single phase occurring in the considered system. Therefore, starting from the Gibbs energies of the elements,

as published in Reference 49, the Gibbs energy for the binary alloys can be obtained by extrapolation. Then, by introducing additional parameters, the model for the binary system is fitted on the basis of experimental data. For ternary systems, the same steps are followed. Often, the description of ternary systems already gives a good extrapolation of the behaviour of higher order systems, e.g. technically applied steels [50]. In principle, however, it is possible to introduce parameters of arbitrary order.

The compound energy formalism [51] is the most frequently used approach to model the Gibbs energy of solution phases. In principle, it is capable of handling any number of sublattices. A purely substitutional solution phase would be described by mixing on only one sublattice. With two sublattices, then also called Hillert-Staffansson approach [52], it is possible to describe e.g. interstitial solutions or reciprocal salt systems. Depending on the crystal structure, the sublattices can have different numbers of sites relative to each other, resulting in a general formula of the phase ϕ of e.g. $(A,B)_a(C,D)_c$ for a quaternary solution with elements A and B on the first sublattice with a sites and C and D on the second sublattice with c sites. When order is considered, often more sublattices are needed. Each combination of components for which the sublattices are fully occupied is called an end-member. Those end-members can be pure metals or compounds for which the Gibbs energy can easily be described by fitting for experimental data of any thermodynamic quantities. However, often the end-members will be metastable in a large temperature range or even experimentally inaccessible hypothetical states. The Gibbs energy of e.g. the end member A_aD_c in its non-magnetic state, ${}^\circ G_{A:D}^\phi$ (with A:D denoting sublattices fully occupied by A and D), is then modelled with a temperature-dependent series after [50]

$${}^\circ G_{A:D}^\phi - a {}^\circ G_A^{\text{ref}} - c {}^\circ G_D^{\text{ref}} = a + bT + cT \ln T + d_1 T^2 + d_2 T^{-1} + d_3 T^3 \dots \quad (1.12)$$

with the reference Gibbs energy of A and D, ${}^\circ G_A^{\text{ref}}$ and ${}^\circ G_D^{\text{ref}}$ and any number of model parameters $a, b, c, d_1, d_2, d_3 \dots$ that is needed describe the experimental data. For the reference Gibbs energy, often the so-called SER state is chosen, which is the enthalpy of the element in its stable state at 298 K and 1×10^5 Pa [49]. However, it is also possible to refer the Gibbs energy of the end members to the Gibbs energy of the elements. If then only the parameters a and b are used, this is identical with the application of the Neumann-Kopp rule [53, 54] for the heat capacities.

The total Gibbs energy per formula unit of any phase ϕ can be formulated as [50]

$$G_m^\phi = G_m^{\phi,\text{srf}} + G_m^{\phi,\text{phys}} - TS_m^{\phi,\text{cnf}} + G_m^{\phi,\text{ex}} \quad (1.13)$$

with the Gibbs energy of the surface of reference $G_m^{\phi,\text{srif}}$, i.e. a mechanical mixture of the end members, the physical contribution $G_m^{\phi,\text{phys}}$ which considers especially, but not only magnetic ordering, the ideal configurational entropy $S^{\phi,\text{cnf}}$ as estimated by the Stirling formula and the excess Gibbs energy $G_m^{\phi,\text{ex}}$ considering all other contributions.

The most important contribution to $G_m^{\phi,\text{phys}}$ in Equation (1.13) considered in this work is due to magnetic ordering. Most frequently, the Inden model [55, 56] is applied. Accordingly, the magnetic contribution $G^{\phi,\text{mag}}$ to the phase ϕ can be described by

$$G^{\phi,\text{mag}} = RT f(\tau) \ln(\beta^\phi + 1) \quad (1.14)$$

with the reduced temperature $\tau = T/T_{\text{Curie}}^\phi$ or $\tau = T/T_{\text{Neel}}^\phi$, whereby T_{Curie}^ϕ and T_{Neel}^ϕ denote the Curie temperature and the Neel temperature of the magnetic order/disorder transformation, respectively, and the magnetic moment β^ϕ , and [50]

$$f(\tau) = \begin{cases} 1 - \frac{1}{A} \left[\frac{79\tau^{-1}}{140p} + \frac{474}{497} \left(\frac{1}{p} - 1 \right) \left(\frac{\tau^3}{6} + \frac{\tau^9}{135} + \frac{\tau^{15}}{600} \right) \right] & \tau < 1 \\ -\frac{1}{A} \left(\frac{\tau^{-5}}{10} + \frac{\tau^{-15}}{315} + \frac{\tau^{-25}}{1500} \right) & \tau \geq 1 \end{cases} \quad (1.15)$$

with

$$A = \frac{518}{1125} + \frac{11692}{15975} \left(\frac{1}{p} - 1 \right). \quad (1.16)$$

The constant p depends on the crystal structure: $p = 0.4$ can be used for bcc materials and $p = 0.28$ for materials with other crystal structures [55].

Both, the ideal configurational entropy and the excess Gibbs energy contributions will be explained in the following by a few examples in the ternary Fe–N–C system.

The liquid phase is in a state of no long-range order. Therefore, a substitutional solution model can be applied. The end members are then liquid Fe, liquid N and liquid C. Therefore, the total Gibbs energy of the liquid phase can be written as

$$G_m^l = x_{\text{Fe}}^l \circ G_{\text{Fe}}^l + x_{\text{N}}^l \circ G_{\text{N}}^l + x_{\text{C}}^l \circ G_{\text{C}}^l + RT(x_{\text{Fe}}^l \ln x_{\text{Fe}}^l + x_{\text{N}}^l \ln x_{\text{N}}^l + x_{\text{C}}^l \ln x_{\text{C}}^l) + G_m^{\text{l,ex}} \quad (1.17)$$

with the molar fractions of Fe, N and C in the liquid phase, x_{Fe}^l , x_{N}^l and x_{C}^l , and

$$G_m^{\text{l,ex}} = x_{\text{Fe}}^l x_{\text{N}}^l L_{\text{Fe},\text{N}}^l + x_{\text{C}}^l x_{\text{Fe}}^l L_{\text{C},\text{Fe}}^l + x_{\text{C}}^l x_{\text{N}}^l L_{\text{C},\text{N}}^l + x_{\text{C}}^l x_{\text{Fe}}^l x_{\text{N}}^l L_{\text{C},\text{Fe},\text{N}}^l. \quad (1.18)$$

The binary interaction parameters $L_{\text{Fe},\text{N}}^1$, $L_{\text{C},\text{Fe}}^1$ and $L_{\text{C},\text{N}}^1$ can be concentration dependent, most frequently expressed by a Redlich-Kister series [57], e.g.

$$L_{\text{Fe},\text{N}}^1 = \sum_k k L_{\text{Fe},\text{N}}^1 (x_{\text{Fe}}^1 - x_{\text{N}}^1)^k. \quad (1.19)$$

where the convention is that the elements are taken in alphabetic order of their symbol. The coefficients of this series $k L_{\text{Fe},\text{N}}^1$ are called the k -th order interaction parameter. If all interaction parameters equal zero, the model is called an ideal-solution model. With the zeroth (first) order interaction parameter the model is called a (sub-)regular-solution model. For the ternary interaction parameter $L_{\text{C},\text{Fe},\text{N}}^1$, a concentration-dependent value can be modelled by using the relations presented in Reference 58.

For the γ phase in the Fe–N–C system, N and C are interstitially dissolved in the octahedral sites of the fcc Fe lattice (one octahedral site per Fe atom). Therefore, in the compound energy formalism, it can be considered as a solution phase of the compounds FeVa (with Va denoting vacancies), FeN and FeC. Therefore, the Gibbs energy per mole formula unit can be written as

$$G_m^\gamma = y_{\text{Va}}^\gamma \circ G_{\text{Fe:Va}}^\gamma + y_{\text{N}}^\gamma \circ G_{\text{Fe:N}}^\gamma + y_{\text{C}}^\gamma \circ G_{\text{Fe:C}}^\gamma + RT(y_{\text{Va}}^\gamma \ln y_{\text{Va}}^\gamma + y_{\text{N}}^\gamma \ln y_{\text{N}}^\gamma + y_{\text{C}}^\gamma \ln y_{\text{C}}^\gamma) + G_m^{\gamma,\text{ex}}, \quad (1.20)$$

with the site fractions of Va, N and C in γ , y_{Va}^γ , y_{N}^γ and y_{C}^γ , taking into account that $y_{\text{Fe}}^\gamma = 1$ in all cases, and with e.g. a regular-solution model for the excess interactions, i.e.

$$G_m^{\gamma,\text{ex}} = y_{\text{N}}^\gamma y_{\text{Va}}^\gamma {}^0 L_{\text{Fe:N,Va}}^\gamma + y_{\text{C}}^\gamma y_{\text{Va}}^\gamma {}^0 L_{\text{Fe:C,Va}}^\gamma + y_{\text{C}}^\gamma y_{\text{N}}^\gamma {}^0 L_{\text{Fe:C,N}}^\gamma. \quad (1.21)$$

Because the first sublattice is only occupied by Fe, only interactions on the second sublattice are considered. Other phases in the Fe–N–C system can be modelled using similar expressions for the Gibbs energy. However, for the α phase, a sublattice model with the formula unit $\text{Fe}(\text{C},\text{N},\text{Va})_3$ and for the θ phase, a sublattice model with the formula unit $\text{Fe}_3(\text{C},\text{Va})$ (see Chapter 5) is used.

The γ' phase can be described by a sublattice model with the formula unit $\text{Fe}_4(\text{C},\text{N},\text{Va})$. However, in order to transform e.g. the Wagner-Schottky-type [59] and Gorsky-Bragg-Williams-type [60–63] models as applied for a thermodynamic description of this phase in References 20–22, introducing disorder of N, into the compound energy formalism, more sublattices are necessary: in principle, the γ' phase is a solution of N in an fcc-type Fe lattice, in which N and Va are ordered. Thus, a model according to the formula unit $\text{Fe}_4(\text{N},\text{Va})(\text{N},\text{Va})(\text{N},\text{Va})(\text{N},\text{Va})$, i.e. using five sublattices, would give a complete description of binary γ' . If only L_{12} ordering is considered, three of the interstitial sublattices are equivalent and the resulting model is de-

scribed by the formula unit $\text{Fe}_4(\text{N},\text{Va})(\text{N},\text{Va})_3$. Therefore, four different Gibbs energies of end members are needed to describe the model: ${}^\circ G_{\text{Fe:N:Va}}^{\gamma'}$ (stoichiometric γ' - Fe_4N), ${}^\circ G_{\text{Fe:Va:N}}^{\gamma'}$ (Fe_4N_3 with L1₂-ordered vacancies), ${}^\circ G_{\text{Fe:Va:Va}}^{\gamma'}$ (pure Fe in the same arrangement as in γ' , i.e. fcc Fe with an expanded lattice) and ${}^\circ G_{\text{Fe:N:N}}^{\gamma'}$ (NaCl-type FeN). For the Gorsky-Bragg-Williams-type model from Reference 22, also a binary interaction parameter on the third sublattice is needed.

Ordering can also be considered for ε as performed in References 64–66. In the CALPHAD-type thermodynamic description, however, a simpler sublattice model with the formula unit $\text{Fe}_2(\text{C,N},\text{Va})$ [41, 45–47] (see also Chapter 6) or $\text{Fe}(\text{C,N},\text{Va})$ [39, 43] with several interaction parameters describing the non-ideal behaviour is used.

1.3.1 Software for thermodynamic calculations

In principle, equilibrium calculations can be performed for any system by hand or by using any software that is capable of solving non-linear systems of equations. However, several commercial and non-commercial software packages are available [67–71], which are particularly suited to deal with the special mathematical problems associated with the usually employed Gibbs-energy functions and which can be used together with commercial thermodynamic databases or with Gibbs-energy functions from the literature. In all cases, in the work presented in Chapters 2, 3, 4, 5 and 6, the Thermo-Calc software [70] has been applied.

1.4 Ternary interstitial diffusion

The thickness of the compound layer formed upon nitriding and nitrocarburising of iron and steels increases with the treatment time. In an *ideal* case, the layer growth of a compound layer is diffusion controlled. Upon nitriding of C-containing steel or nitrocarburising of any Fe alloy, simultaneous diffusion of N and C occurs.

In a hydrostatic state of stress, a diffusional flux of a component k j_k is caused by a gradient in its chemical potential [72, 73]

$$j_k = -L_{kl}RT\nabla\mu_l. \quad (1.22)$$

with the Onsager coefficients L_{kl} . Because the concentration of a component is much more accessible by experiment than its chemical potential, more often, Fick's first law

$$j_k = -D_{kl}\nabla c_l \quad (1.23)$$

is used with the in general concentration dependent diffusivity matrix D_{kl} , considering the influence of the chemical potential of component k by the other components. The diffusivity matrix

can be related to the self-diffusion coefficients of each component D_k^* by the thermodynamic factor ϑ_{kl}

$$D_{kl} = D_k^* \frac{c_k}{RT} \frac{\partial \mu_k}{\partial c_l} = D_k^* \vartheta_{kl}, \quad (1.24)$$

resulting from setting Equations (1.22) and (1.23) equal. If the self-diffusion coefficients are independent of concentration, the concentration dependence of the diffusivity can be calculated by applying thermodynamic models for the relevant phases describing the chemical potential. Two properties of the thermodynamic factor are worth mentioning here: (i) the diagonal components must be positive, but the off-diagonal components can also be negative; (ii) the off-diagonal components must have the same sign, recognising that the concentrations are always positive and since $\partial \mu_k / \partial c_l = \partial \mu_l / \partial c_k$ because of the symmetry of partial derivatives.

The resulting concentration profile can then be calculated by integrating Fick's second law, given in one spatial dimension as

$$\frac{\partial c_k}{\partial t} = \frac{\partial}{\partial x} \left(D_{kl} \frac{\partial c_l}{\partial x} \right). \quad (1.25)$$

1.5 Outlook of the thesis

In the recent past, the Fe–N–C system has been studied extensively [29, 74–82]. However, this research on the Fe–N–C system also showed that the recently obtained experimental data can only be described partly by each of the models from the literature [39, 41, 43, 45–47]: e.g. when comparing the most recent complete models [41, 43], it was found that one [41] is superior describing the invariant temperatures [82], the other [43] for the phase boundaries [82] and thermodynamics of the ϵ phase [81]. This recognition provided the impetus for the research in the present work.

A study on simultaneous diffusion of N and C in the ϵ phase has already been performed in Reference 81. In Chapter 2, a different set of microstructures and a different temperature were applied in order to confirm the results from Reference 81. Because of the differently shaped concentration-depth profiles, the evaluation method had to be modified. A completely new approach has been used to determine the components of the diffusivity matrix. The main conclusions support the informations presented in Reference 81: the off-diagonal components of the diffusivity matrix have significantly positive values. This result gives important thermodynamic information about the ϵ phase: these data are only compatible with the thermodynamic model from Reference 43 and incompatible with the thermodynamic model from Reference 41.

Most of the nitriding and nitrocarburising experiments in the present work were terminated by quenching the specimen in water to room temperature in order to preserve the microstructure

present at the treatment temperature. Chapter 3 is dedicated to investigating the decomposition microstructures forming in Fe–N–C compound layers upon slow cooling or quenching and subsequent annealing at a temperature lower than the treatment temperature. Thereby, a lamellar $\gamma' + \epsilon$ microstructure emerged due with a strict orientation relationship which has been determined and reported.

The $\alpha + \epsilon$ equilibrium in the Fe–N–C system is of great importance for nitrocarburising of iron and steels: a pure ϵ layer is desired in contact with the substrate, leading to improved anti-corrosion, wear and tribological properties [1]. However, the equilibrium of α and ϵ was not recognised by early studies [83, 84] of the system, in contrast to later works [29, 75, 82, 85–96]. In Reference 75 a temperature range for the temperature of the $\alpha + \epsilon \rightleftharpoons \gamma' + \theta$ invariant reaction has been determined. In Chapter 4, systematic microstructure analyses were performed in order to refine and complement the findings in Reference 75. It was shown that the reaction $\alpha + \epsilon \rightleftharpoons \gamma' + \theta$ is not the only possibility of how the $\alpha + \epsilon$ equilibrium appears in the Fe–N–C system upon increasing temperature. The microstructural analysis was accompanied by thermodynamic calculations, comparing all of the models for the Fe–N–C system from the literature [39, 41, 43–47] to each other and the experimental data.

The cementite (θ) phase is treated as stoichiometric Fe_3C by many works from the literature [3, 31–34, 97, 98]. However, for a long time there is strong evidence [5–15] that in equilibrium, the actual C content of cementite is below 25 at.%. A new study [16] provided for the first time accurate data for the composition of cementite in equilibrium with α and γ . These data have been used in Chapter 5 in order to develop a new thermodynamic CALPHAD-type thermodynamic description for the cementite phase, considering its non-stoichiometric character.

In Chapter 6, new CALPHAD-type thermodynamic descriptions for both the Fe–N and Fe–N–C systems are presented. For the sub-system Fe–C, the description obtained in Chapter 5 was used. The model for the Fe–N system improves the agreement with experimental data, especially for the γ'/ϵ equilibrium. The new description of the Fe–N–C system excellently agrees with the recently obtained experimental data obtained in Reference 82 and in Chapter 4 for both the invariant temperatures and the phase boundaries, data that could not be reproduced using the thermodynamic descriptions of this system from the literature. Furthermore, the sign of the thermodynamic factors agrees with the experimentally obtained results in Reference 81 and Chapter 2.

Chapter 2

N and C interstitial diffusion and thermodynamic interactions in ϵ -iron carbonitride

Holger Göhring, Andreas Leineweber, Eric Jan Mittemeijer

The simultaneous diffusion of N and C over the interstitial sites of the Fe-sublattice of ϵ -iron carbonitride was studied. To this end, gas nitrocarburising experiments of pure Fe and Fe–C alloys were performed at 853 K (580 °C), leading to two different types of microstructures containing ϵ (sub)layers. These microstructures were investigated by light microscopy, electron probe micro analysis and X-ray diffraction in order to evaluate the components of the (N and C) diffusivity matrix. The off-diagonal components of the diffusivity matrix were shown to have significant, non-negligible values. These results provided insight into the thermodynamics of the Fe–N–C system.

2.1 Introduction

Nitriding and nitrocarburising are common thermo-chemical heat treatment processes used in order to improve e.g. the corrosion, wear and fatigue resistances of iron-based alloys [25]. In view of nitriding and nitrocarburising being widely applied in industry, there is a surprising lack of knowledge regarding the constitution of the ternary system Fe–N–C, whereas such

Table 2.1: Characteristics of the Fe–N–C phases relevant for the present work. Volume per mole Fe was calculated from the lattice-parameter data presented in the cited literature.

phase	space group	composition	$V_{m,Fe}/(10^{-6} \text{ m}^3 \text{ mol}^{-1})$
α -iron, ferrite	$Im\bar{3}m$	very low N and C contents	7.3 [99]
γ' -Fe ₄ N	$Pm\bar{3}m$	almost stoichiometric	8.2 [100]
ϵ -Fe ₃ (N,C) _{1+x}	$P6_322$	wide N and C ranges	8.4 [101]
θ -Fe ₃ C, cementite	$Pnma$	stoichiometric	7.8 [102]

knowledge is a prerequisite to arrive at fundamental understanding of the effects of nitriding and nitrocarburising of steels (normally containing carbon).

For predictions of the growth of compound layers forming upon nitriding and nitrocarburising of iron and steel it is necessary to understand the *simultaneous* diffusion of the interstitially dissolved components N and C in the resulting phases. For an overview of the phases considered, see Table 2.1. In the following, these phases will be abbreviated by the small Greek letters defined in Table 2.1.

Diffusion of N and C, separately, in Fe and the corresponding nitrides and carbides has been studied thoroughly in the past [103–117]. However, either upon nitriding or upon nitrocarburising, as soon as the system contains C, which may already originate from the substrate (e.g. steel) and/or from the treatment medium (in case of nitrocarburising), the role of this additional interstitially diffusing component C, next to the interstitially diffusing component N, has to be taken into account.

Diffusion of each of multiple components can be described by Fick's first law,

$$j_k = -D_{kl}\nabla c_l. \quad (2.1)$$

For the case of interstitial diffusion, the components of the diffusivity matrix, D_{kl} , read

$$D_{kl} = D_k^* \frac{c_k}{RT} \frac{\partial \mu_k}{\partial c_l} = D_k^* \vartheta_{kl}, \quad (2.2)$$

with the self diffusion coefficient D_k^* , the concentrations of the diffusing components k and l , c_k and c_l , the gas constant R , the temperature T , the chemical potential of component k , μ_k and the so-called thermodynamic factor ϑ_{kl} , relating the intrinsic diffusion coefficients to thermodynamics [72, 73]. The cross(off-diagonal)-terms of this diffusivity matrix express the influence of the concentration gradient of one diffusing species on the flux of another one. The thermodynamic factors can be calculated if a thermodynamic description is available. In

literature, several of these (partially incompatible) descriptions for the system Fe–N–C exist [41, 43, 45, 46].

A first theoretical treatment of simultaneous diffusion of N and C in an ϵ/γ' double layer system offered an analytical solution of Fick's second law by assuming concentration-independent diffusion coefficients [118]. However, the occurrence of a large solubility range of both N and C in ϵ -iron carbonitride, leading to large concentration variations in compound layers formed upon nitriding or nitrocarburising of iron or steel, already indicates that the assumption of concentration-independent diffusivities of N and C is unacceptable. By avoiding a such affected, analytical solution of Fick's second law in a later work and only using Fick's first law, the first experimental analysis of simultaneous interstitial diffusion of N and C in ϵ -iron carbonitride was made possible [81]: the diffusivity matrix of N and C was evaluated at 823 K (550 °C) for ϵ/γ' double layers growing upon nitriding and nitrocarburising of pure Fe using a linear fit for the concentration-depth profiles of N and C.

The present work is devoted to the evaluation of the diffusivity matrix of N and C in ϵ -iron carbonitride at 853 K (580 °C) on the basis of an approach provided in Reference 81. It will be demonstrated that the proposed method can be applied to a variety of microstructures, essentially different from those examined in Reference 81. Thus, the kinetics of growth of θ/ϵ double layers and of pure ϵ layers, containing considerably less N and considerably more C than in Reference 81, have been investigated. Further, the method has been expanded to incorporate the curved nature of the concentration-depth profiles occurring in some of these (sub)layers. Moreover, a graphical evaluation method is proposed for determining the values of the components of the diffusivity matrix, giving direct information about the accuracy of the measurements. The data obtained on the thermodynamic factors have been compared with thermodynamic descriptions of the Fe–N–C system to obtain decisive information about the thermodynamic interaction of N and C in the ϵ phase.

2.2 Evaluation method

The applied method is based on the following assumptions for interstitial diffusion in the Fe–N–C systems at constant temperature and pressure. The only mobile species considered here are N and C. Fe is immobile and forms a lattice with a volume that is taken to be independent of the amount of interstitials dissolved. The interfaces between the phases formed upon diffusion are planar. The shape of the concentration-depth profiles remains constant with increasing treatment time, i.e. the concentration-depth profile normalized with respect to the (sub)layer thickness is time-independent, which implies that the concentrations at the (sub)layer interfaces

are constant over time. The surface concentration is constant as determined by the treatment atmosphere. Local equilibrium is adopted at the solid-solid interfaces.

Fick's first law written explicitly for two diffusing components N and C reads

$$j_N = -D_{NN} \frac{dc_N}{dx} - D_{NC} \frac{dc_C}{dx}; \quad j_C = -D_{CN} \frac{dc_N}{dx} - D_{CC} \frac{dc_C}{dx}, \quad (2.3)$$

which can also be written as

$$D_{NC} = -D_{NN} \frac{dc_N}{dx} \cdot \frac{dx}{dc_C} - j_N \cdot \frac{dx}{dc_C}; \quad D_{CN} = -D_{CC} \frac{dc_C}{dx} \cdot \frac{dx}{dc_N} - j_C \cdot \frac{dx}{dc_N}. \quad (2.4)$$

Hence, for known fluxes (j_N and j_C) and known concentration gradients (dc_N/dx and dc_C/dx) all mathematically (not necessarily physically) possible solutions of D_{NC} (D_{CN}) are linearly dependent on D_{NN} (D_{CC}). These solutions can be represented by straight lines in a plot of D_{NC} versus D_{NN} and in a plot of D_{CN} versus D_{CC} . The fluxes and the concentration gradients needed for the proposed evaluation method can be determined experimentally by measuring concentration-depth profiles in the considered (sub)layers and their corresponding thicknesses. This is explained in Section 2.3.

It is obvious that for values of the fluxes and concentration gradients of N and C measured at one specific set of conditions as defined by the employed gas atmosphere, treatment temperature and time (and the constant, atmospheric pressure), the solution of Equation (2.4) is not possible, but straight lines (D_{NC} (D_{CN}) as a function of D_{NN} (D_{CC})) can be constructed in the above-mentioned plots. At the same temperature and pressure, but for a different treatment time and gas atmosphere, different values of the fluxes and concentration gradients of N and C will be found. The corresponding straight lines in the above-mentioned plots intersect the first mentioned straight lines. The intersection points define the solution of Equation (2.4) for the four components of the diffusivity matrix. Adding the results of a third set of conditions, the additional straight lines in both plots should ideally have the same intersection points with the earlier two sets of straight lines. In reality this need not occur: the values of the components of the diffusivity matrix represent effective diffusivities, i.e. a mean value of the diffusivities over the concentration range that is covered by the concentration-depth profile in the considered (sub)layer. Since the N and C concentration-depth profiles for each set of conditions are different, the resulting, corresponding effective diffusivities for the various sets of experimental conditions are (somewhat) different. Furthermore, all experimentally determined values and therefore also the parameters of the straight lines are prone to experimental errors. Hence, the intersection points of the straight lines in each of the plots of D_{NC} versus D_{NN} and D_{CN} versus D_{CC} for three different sets of conditions enclose a triangle. The coordinates of the geometric

centres of both triangles then represent a solution of Equation (2.4) that is approximately valid for all three cases. The area covered by the triangles indicates the ranges of possible values for the components of the diffusivity matrix, i.e. provides corresponding error estimates.

Data obtained from experiments at (even) more sets of experimental conditions can be added. This leads to an increase of intersection points of the straight lines in the plots of D_{NC} versus D_{NN} and D_{CN} versus D_{CC} . These intersection points may also occur in areas that do not have a physical meaning (i.e. correspond to negative values for D_{NN} or D_{CC}). Then, the area for the possible solutions of Equation (2.4) must be limited to the physically meaningful intersection points. The centroid of this area then gives the (at this stage) most likely solution of Equation (2.4). The extent of the area of physically meaningful intersection points in the plots indicates the ranges of possible values for the components of the diffusivity matrix, i.e. provides corresponding error estimates. In a second step, this solution found for the values of the diffusivity matrix can be refined by minimizing the differences between the experimentally determined fluxes and those calculated from Fick's first law.

2.3 Modelling of interstitial diffusion

Consider a double layer (cf. Figure 2.1) with an upper sublayer of phase III and a lower sublayer of phase II growing into a substrate of phase I at the time $t_1 = t$ and at the time $t_2 = t + dt$ between which the sublayer boundaries at the positions $x_1^{III/II}$ and $x_1^{II/I}$ at the time t_1 move by the amounts $v^{III/II}dt$ and $v^{II/I}dt$ to the positions $x_2^{III/II}$ and $x_2^{II/I}$ at the time t_2 . Here, $v^{III/II} = dx^{III/II}/dt$ and $v^{II/I} = dx^{II/I}/dt$ describe the velocities of the positions of the sublayer boundaries. The flux difference of component k at the layer boundary between the phases III and II is given by

$$\left(j_k^{III/II} - j_k^{II/III} \right) (t_2 - t_1) = \left(c_k^{III/II} - c_k^{II/III} \right) (x_2^{III/II} - x_1^{III/II}), \quad (2.5)$$

corresponding to the shaded area labelled 1 in Figure 2.1. The flux difference of component i at the layer boundary between the phases II and I complies with

$$\left(j_k^{II/I} - j_k^{I/II} \right) (t_2 - t_1) = \left(c_k^{II/I} - c_k^{I/II} \right) (x_2^{II/I} - x_1^{II/I}), \quad (2.6)$$

corresponding to the shaded area labelled 3 in Figure 2.1. For the fluxes j_k and the concentrations c_k , the superscript I/II denotes a quantity *in* phase I *at* the boundary between I and II, etc.

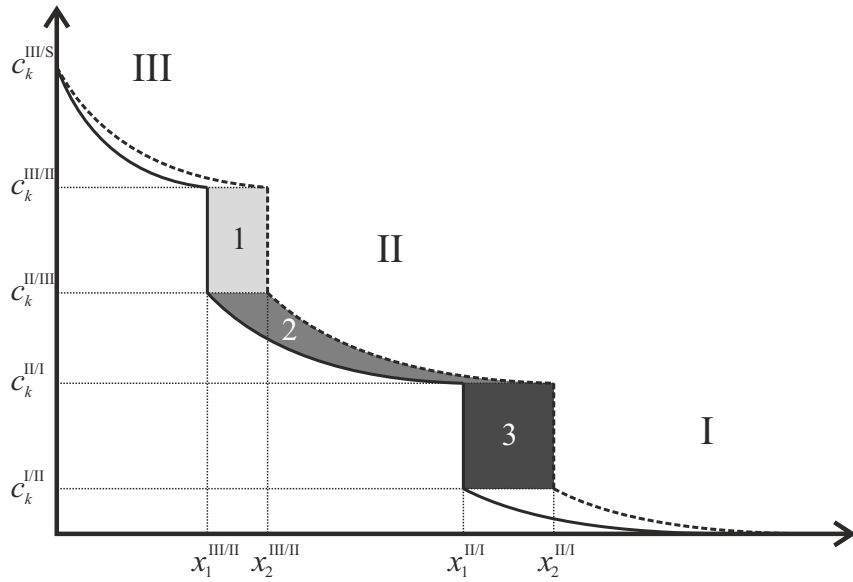


Figure 2.1: Schematic concentration-depth profile of component k in a III/II double layer growing into a substrate I at the time t_1 (solid lines) with the interfaces $x_1^{\text{III/II}}$ and $x_1^{\text{II/I}}$ and at the time $t_2 = t_1 + dt$ (dashed lines) with the interfaces $x_2^{\text{III/II}}$ and $x_2^{\text{II/I}}$. The shaded areas labelled with 1, 2 and 3 correspond to Equations (2.5), (2.7) and (2.6)

The flux difference between the upper and lower boundaries of layer II can be calculated by

$$(j_k^{\text{II/III}} - j_k^{\text{II/I}})(t_2 - t_1) = \int_{x_2^{\text{III/II}}}^{x_2^{\text{II/I}}} c_k(x, t_2) dx - \int_{x_1^{\text{III/II}}}^{x_1^{\text{II/I}}} c_k(x, t_1) dx, \quad (2.7)$$

corresponding with the shaded area labelled 2 in Figure 2.1. Note that these equations are valid regardless of the shape of the concentration-depth profile.

In case of a linear concentration-depth profile in layer II

$$c_k(x, t) = c_k^{\text{II/III}} - (c_k^{\text{II/III}} - c_k^{\text{II/I}}) \frac{x - S^{\text{III}}(t)}{S^{\text{II}}(t)}, \quad (2.8)$$

with S^{III} and S^{II} denoting the layer thicknesses of layers III and II, it follows from Equation (2.7)

$$j_k^{\text{II/III}} - j_k^{\text{II/I}} = \frac{1}{2}(c_k^{\text{II/III}} - c_k^{\text{II/I}})(v^{\text{III/II}} + v^{\text{II/I}}). \quad (2.7a)$$

In case of an arbitrary error-function shaped profile in layer II

$$c_k(x, t) = c_k^{\text{II/III}} - \frac{c_k^{\text{II/III}} - c_k^{\text{II/I}}}{\operatorname{erf} w_k} \operatorname{erf} \left(w_k \frac{x - S^{\text{III}}(t)}{S^{\text{II}}(t)} \right), \quad (2.9)$$

with w_k as fitting parameter, it follows from Eq. (2.7)

$$j_k^{\text{II/III}} - j_k^{\text{II/I}} = \left[v^{\text{III/II}} + \frac{1}{\sqrt{\pi}} \frac{1 - \exp(-w_k^2)}{w_k \operatorname{erf} w_k} (v^{\text{II/I}} - v^{\text{III/II}}) \right] (c_k^{\text{II/III}} - c_k^{\text{II/I}}). \quad (2.7b)$$

By replacing III by the surface S and setting $v^{\text{II/S}} = 0$ the above treatment directly provides similar expressions for the flux difference between the upper and lower interfaces of the surface layer.

Now, by assuming certain fluxes (of N and C) into the substrate, the above-indicated flux difference equations for layers II and III can be used to straightforwardly calculate the flux of each component in each phase at each layer boundary. In the present work, two different approaches for such calculations will be used, depending on the microstructure of the substrate. In the first case, the flux of N and C into the substrate is assumed to be zero, which holds if the substrate is already saturated before the beginning of the experiment. In the second case, the following numerical approximation is adopted for the flux of N into the substrate I of thickness $2L$ at the boundary with layer II at the time t [109, 114],

$$j_N^{\text{I/II}} = D_N^{\text{I}} \frac{2(c_N^{\text{I/II}} - c_N^{\text{I},0})}{L} \cdot \sum_{n=1}^{\infty} \exp\left(-\frac{(2n-1)^2 \pi^2 D_N^{\text{I}} \cdot t}{4L^2}\right) \quad (2.10)$$

with $c_N^{\text{I},0}$ denoting the concentration of N in the centre of the specimen. The intrinsic diffusion coefficient D_N^{I} of N in phase I is taken from the literature. As in the first case, the flux of C into the substrate can be neglected.

The difference of flux equations (2.5–2.7) considered here are independent of the diffusion mechanism (i.e. interstitial or substitutional) in the considered phases. However, the values for the concentrations, i.e. the amount of atoms of a component considered per *volume unit*, in contrast with values for the (e.g. molar) fractions, are not easily accessible by experiments. By assuming constant volume of a substitutional solid solution, the concentration variable c_k is directly proportional to the molar fraction $x_k = n_k/n$ (with the amount of atoms of component k , n_k , and the total amount of atoms $n = \sum_k n_k$). However, by similarly assuming the volume of an interstitial solid-solution phase, as ϵ -iron carbonitride, to be independent of the amount of interstitials (i.e. the (hcp) Fe sublattice without interstitially dissolved atoms has the same volume as the fully occupied lattice), the concentration variable c_k now is proportional to the so-called *u*-fraction

$$u_k = \frac{n_k}{n_{\text{host}}} \quad (2.11)$$

with n_{host} denoting the amount of the atoms forming the host lattice for the interstitially dissolved atoms [119]. If Fe, N and C are the only components of the solid solution, the u -fraction can be calculated from the molar fractions by

$$u_k = \frac{x_k}{1 - x_N - x_C}. \quad (2.12)$$

Then, the proportionality constant in order to obtain c_k from u_k is the inverse volume of one mole Fe atoms in the corresponding crystal structure, $V_{\text{m},\text{Fe}}$, i.e.

$$c_k = \frac{u_k}{V_{\text{m},\text{Fe}}} \quad (2.13)$$

Table 2.1 lists the phases considered in the present work and the corresponding volumes of one mole Fe atoms, $V_{\text{m},\text{Fe}}$, as calculated from the lattice-parameter data given in References 99–102.

The velocities of the sublayer boundaries are obtained by adopting a parabolic growth law (experimentally verified; see Section 2.5.1) for the position, x , of the sublayer boundary,

$$x^2(t) = k \cdot t, \quad (2.14)$$

and subsequently solving for x and taking the derivative. Note that, in an ideal case of such parabolic growth, the growth constant k contains a combination of the components of the diffusivity matrix, see Reference 118. This, however, requires that the Boltzmann transformation [72, 73] is applicable which is not necessarily the case in the present work. Thus, here the growth constant k is considered as a model parameter without that a physical interpretation is given.

It is possible to extend the kinetic model, especially for incubation effects in the early stage of the layer-growth process, by introducing a hypothetical initial squared layer thickness S_0^2 , like in Reference 81, i.e.

$$x^2(t) = k \cdot t + S_0^2. \quad (2.15)$$

For reasons discussed in Section 2.6.1, the latter approach was avoided in the present work.

2.4 Experimental

Two different types of substrates were used, one consisting of an Fe–N alloy and one consisting of an Fe–C alloy.

For preparing the Fe–N specimens, a pure iron (Alfa Aesar, 99.98 wt.%) ingot of 80 mm \times 30 mm \times 10 mm was cold-rolled to a thickness of about 1 mm and cut into plates with a size of 20 mm \times 12 mm. The plates were then ground and polished (down to 1 μm diamond suspension) to a final thickness of 0.5 mm. The specimens were then recrystallized in pure H₂ at 973 K (700 °C) for 2 h, polished again and presaturated with N over night (approx. 18 h) at 853 K (580 °C) in an atmosphere containing 10.6 vol.% NH₃ and 89.4 vol.% H₂ (corresponding to a N activity of 69 relative to pure N₂ gas, i.e. a nitriding potential r_N of $3.93 \times 10^{-4} \text{ Pa}^{-1/2}$ ($0.125 \text{ atm}^{-1/2}$)). This results in pure α -iron, verified by X-ray diffraction, with a N content between 0.36 at.% and 0.38 at.%, determined gravimetrically. These N contents are very close to the maximum solubility of N in α -iron in equilibrium with γ' -Fe₄N [4,30,41]. For recrystallization and N pre-saturation, the same furnace as for the nitrocarburising experiments described below was used.

The Fe–C substrates were prepared by casting an Fe–C alloy with nominal composition corresponding to the composition in the binary system Fe–C [32], into an ingot of the same dimensions as indicated above for the Fe–N specimens. The real C content of the Fe–C ingot was determined by chemical analysis as 0.63 wt.% (2.86 at.%), smaller than the eutectoid composition of approx. 0.8 wt.%, due to loss of C during casting. Cold-rolling, cutting, grinding and polishing was performed similar as for the preparation of the Fe–N substrates and as described above. The substrates were then fused in quartz vials containing $2 \times 10^4 \text{ Pa}$ Ar at room temperature to prevent oxidation. The specimens were treated at 1273 K (1000 °C) and afterwards cooled by putting the quartz vial on a metallic surface in air at room temperature, resulting in a very fine pearlitic microstructure.

The nitriding (upon preparing the Fe–N substrates) and nitrocarburising treatments were performed in a quartz-tube furnace at atmospheric pressure. This furnace is equipped with supplies for H₂, NH₃, CO, CO₂, CH₄ (not used in the present work), H₂O and N₂ (as an inert filler gas). The partial pressures of these gases can be controlled by mass-flow controllers. By using a high flow rate of 500 ml min⁻¹ (determined at room temperature) in the furnace, the equilibria in the gas phase can be controlled. In an ideal case, equilibrium at the surface of the specimen or at least a steady state [29, 30] leading to constant N (and C) concentration(s) in the substrate at the surface can therefore be achieved. The equilibria are thermodynamically characterized by the N and C activities or in technical terms the nitriding and carburising potentials which are proportional to the activities [23, 24].

The N-saturated iron specimens were treated in a so-called *uncontrolled* nitrocarburising atmosphere, i.e. a certain amount of CO gas was added to a nitriding (NH₃/H₂) atmosphere. In this way the N activity is well-defined, whereas the C activity cannot be defined [74]. This

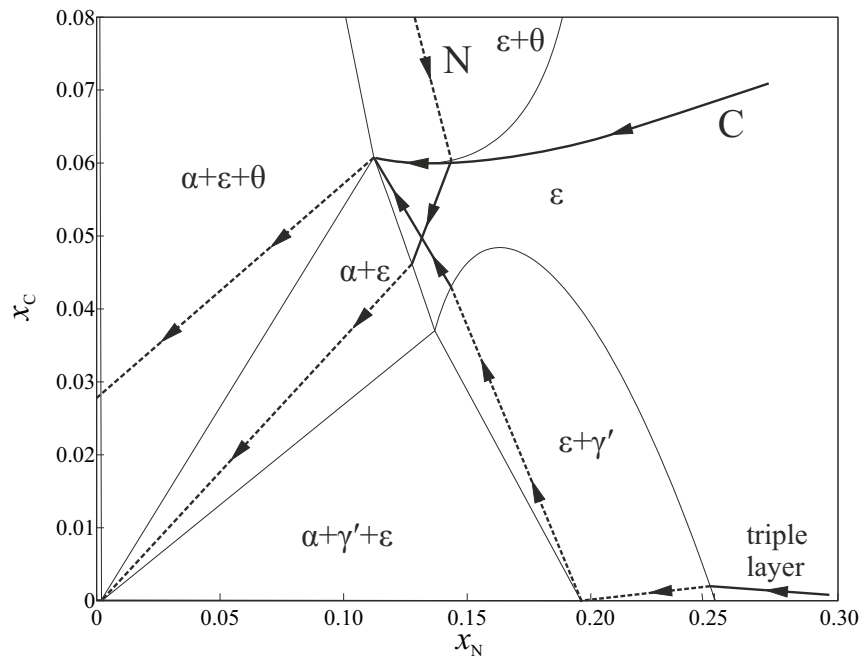


Figure 2.2: Schematic diffusion paths for the N and C experimental series and the $\epsilon/\gamma'/\epsilon$ layer discussed in Section 2.6.3 drawn in the phase diagram of the system Fe–N–C at 853 K (580 °C). Dashed lines indicate skipping of a two-phase or three-phase field. The phase diagram was calculated using the model described in Reference 43.

type of atmospheres is known to produce pure cementite (θ) layers on pure iron [74] and, at the N activities also applied in the present work, θ/ϵ double layers on N-saturated α -iron [29]. The concentration variation in these double layers complies with the schematic diffusion path¹ labelled N in Figure 2.2 (drawn in a phase diagram calculated with data from Reference 43): starting at the surface with θ and proceeding to larger depths, i.e. skipping the $\epsilon+\theta$ two phase field along a tie line, progressing steeply through the ϵ single phase field and skipping the $\alpha+\epsilon$ two phase field along a tie line to arrive at the α substrate. The atmospheres used for these experiments and the resulting N activities are shown in Table 2.2. The parameters for each experiment ($N1$ to $N4$) have been gathered in Table 2.3.

The Fe–C specimens were treated in *controlled* nitrocarburising atmospheres in which all relevant nitriding and nitrocarburising equilibria are adjusted such that the C activities pertaining to the Boudouard reaction



¹Diffusion paths indicate the change of (laterally averaged) composition and constitution in a diffusion couple at constant temperature and pressure. Often, they are drawn by superposition on an isothermal section of the phase diagram of the considered system [72, 120–122].

Table 2.2: Gas atmospheres used for nitrocarburising of the Fe–N and Fe–C specimens at 853 K (580 °C). All partial pressures have been expressed as a fractions of the total pressure $p^\circ = 101\,325 \text{ Pa}$ (1 atm). The reference state for the activities is the corresponding element in its stable state at the treatment temperature and at 101 325 Pa (1 atm).

substrate	$\frac{p(\text{NH}_3)}{p^\circ}$	$\frac{p(\text{H}_2)}{p^\circ}$	$\frac{p(\text{CO})}{p^\circ}$	$\frac{p(\text{CO}_2)}{p^\circ}$	$\frac{p(\text{H}_2\text{O})}{p^\circ}$	$\frac{p(\text{N}_2)}{p^\circ}$	a_{N}	a_{C}
Fe–N	0.13	0.58	0.20	–	–	0.09	166	∞
Fe–N	0.18	0.58	0.20	–	–	0.04	222	∞
Fe–C	0.15	0.45	0.34	0.05	0.02	–	277	50
Fe–C	0.15	0.45	0.36	0.03	0.01	–	277	100
Fe–C	0.15	0.34	0.42	0.07	0.02	–	415	50
Fe–C	0.20	0.34	0.38	0.06	0.02	–	554	50
Fe–C	0.20	0.34	0.41	0.03	0.01	–	554	100
Fe–C	0.51	0.49	–	–	–	–	831	0

Table 2.3: Overview of experimental parameters of the nitrocarburising experiments at 853 K (580 °C) of the N and C series. The reference state for the activities is the corresponding element in its stable state at the treatment temperature and at 101 325 Pa (1 atm). The phases resulting from this treatment have been given in the sixth column. The u -fractions (cf. Equation (2.12)) of N and C at the upper and lower interfaces ($j = \theta$ for $N1$ to $N4$, $j = S$ for $C1$ to $C5$) and the curvature parameter w_C of the C profile (if applicable) have also been indicated.

label	substrate	t/h	a_{N}	a_{C}	phases	$u_{\text{N}}^{\varepsilon/j}$	$u_{\text{N}}^{\varepsilon/\alpha}$	$u_{\text{C}}^{\varepsilon/j}$	$u_{\text{C}}^{\varepsilon/\alpha}$	w_{C}
$N1$	Fe–N	4	166	∞	θ/ε	0.183	0.171	0.065	0.044	–
$N2$	Fe–N	6	166	∞	θ/ε	0.183	0.175	0.063	0.049	–
$N3$	Fe–N	16	166	∞	θ/ε	0.184	0.175	0.063	0.053	–
$N4$	Fe–N	4	222	∞	θ/ε	0.194	0.168	0.067	0.048	–
$C1$	Fe–C	4	277	50	ε	0.253	0.177	0.069	0.050	–
$C2$	Fe–C	4	277	100	ε	0.236	0.175	0.088	0.048	–
$C3$	Fe–C	4	415	50	ε	0.228	0.182	0.125	0.055	2.30
$C4$	Fe–C	4	554	50	ε	0.261	0.161	0.080	0.051	1.70
$C5$	Fe–C	4	554	100	ε	0.264	0.175	0.113	0.055	1.95

and the heterogeneous water-gas reaction



(with $[\text{C}]$ denoting C dissolved into iron) are all (forced to be) equal [23, 24]. This treatment results in thick, almost pure ϵ layers growing evenly into the substrate at the N and C activities used in the present work. The schematic diffusion path (labelled C in Figure 2.2) starts in the ϵ single phase field and progresses through it until reaching the corner of the $\alpha+\epsilon+\theta$ three phase field. At the specific temperature concerned, 853 K (580 °C), only at this single point in an isothermal section of the ternary Fe–N–C phase diagram, defining the N and C concentrations in the ϵ phase, the three-phase equilibrium of the ϵ layer with the $\alpha+\theta$ substrate is possible. Thus, if ϵ is in equilibrium with the $\alpha+\theta$ substrate, the diffusion path *must* pass through this point (at a single depth in the specimen; the $\alpha+\epsilon+\theta$ equilibrium is non-variant at constant pressure and temperature) before skipping over the three phase field to reach the $\alpha+\theta$ two phase field at the (original) bulk composition of the substrate. The atmospheres used for these experiments and the corresponding N and C activities are also shown in Table 2.2. The parameters for each experiment (labelled $C1$ to $C5$) have been gathered in Table 2.3.

Qualitative phase analysis of the specimens was performed by XRD, Bragg-Brentano $\theta-\theta$ geometry, employing a Philips X’Pert MPD equipped with a Co tube and a secondary monochromator, selecting the Co K_α radiation. The resulting diffractograms were analysed by Rietveld refinement using structure models for all considered phases (see Table 2.1). This was done in favour of using peak-position databases because of the strongly varying composition-dependent values of the lattice parameters of the ϵ phase.

For light-microscopic analysis of the nitrocarburised specimens, a part cut from each specimen was electrolytically coated with Ni in a Watt’s bath, to produce a ductile protective layer on top of the brittle compound layer, embedded in resin, ground and polished (final stage 1 μm diamond suspension) and finally etched with 1 % Nital containing some HCl according to References 90 and 123. Some specimens were also treated with Groesbeck solution, i.e. an alkaline KMnO_4 solution which stains C-rich phases [124]. Thereby, the distinction of θ , ϵ and γ' (in decreasing order of C content) is facilitated. From the micrographs, the positions of the (sub)layer boundaries, corresponding to the difference of flux equations (2.5–2.7), were measured following a procedure provided by the software Olympus Stream. This measurement process involved manual selection of the surface and the sublayer boundaries. About 100 laterally equidistant measurements of these boundary positions (relative to the defined surface) were made on each micrograph. For each specimen, at least three micrographs were used in this process, resulting

in at least 300 single measurements for the determination of each averaged sublayer-boundary position value.

For EPMA measurements, the same cross-sectional specimens as used for the light microscopic analysis were used but the etching steps were left out. The instrument used was a Cameca SX 100 equipped with five WDS spectrometers. The three elements Fe, N and C were determined simultaneously, using pure α -Fe, a γ' - Fe_4N layer and a θ - Fe_3C layer as standards. Inclusions of small, single γ' grains in the ϵ (sub)layer, visible in the SEM image taken from the cross-section prior to the EPMA measurement, were avoided during the measurement. In order to reduce the C contamination from decomposition of organic molecules in the residual gas by the electron beam, an oxygen jet was applied to the cross-sectional specimen surface for 40 s before each point measurement and a cold plate was present in the specimen chamber [125]. Even with these decontamination methods the amount of C determined by EPMA is still too high and has to be corrected. The correction factor is determined by measuring the apparent C concentration on the C-free centre of the N-saturated α -Fe specimens and on the pure Fe standard for the Fe–C specimens. From the ratios of the intensities of the characteristic X-ray lines of the considered elements (corrected by a background measurement) and the corresponding intensities measured from the standards (pure Fe for Fe, γ' - Fe_4N for N and θ - Fe_3C for C), the mass fractions of Fe, N and C were calculated using the $\Phi(\rho z)$ approach [126]. The step size of the scans perpendicular to the original surface of the specimen was chosen 1 μm to 2 μm , depending on the thickness of the layers. For every specimen at least three concentration-depth profiles for Fe, N and C, each, were measured.

2.5 Results

2.5.1 Microstructure, layer thickness and kinetics

Exemplary micrographs of cross-sections of the compound layers resulting from nitrocarburising treatments of both types of substrates are presented in Figure 2.3. For the N series the resulting microstructure consisted of a θ/ϵ double layer in direct contact with the N-saturated α -iron substrate. For the C series the resulting microstructure consisted of a pure ϵ layer in contact with the pearlitic $\alpha+\theta$ substrate; sometimes inclusions of tiny γ' grains occurred in the middle of the compound layer, which were neglected in the evaluation. A variation of treatment parameters of the C series (increase of a_{C} , decrease of a_{N}) led to decomposition of the ϵ -iron carbonitride especially in the surface-adjacent regions and a porous carbide (mainly θ) sublayer emerged close to the surface of the specimen (cf. Reference 92). These specimens were not included in the evaluation.

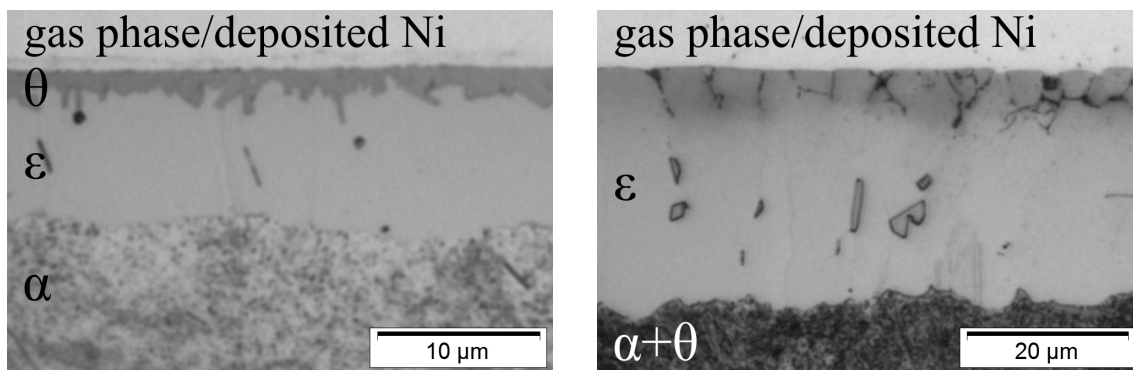


Figure 2.3: Light-microscopical micrographs of cross-sections of compounds layers resulting from the nitrocarburising treatments in the present work, after etching with Groesbeck's reagent. a) *N* series. The compound layer consists of a θ sublayer on top of an ϵ sublayer in direct contact with the N-saturated α -iron substrate. b) *C* series. The compound layer solely consists of an ϵ layer in contact with the fine pearlitic ($\alpha+\theta$) substrate. In some cases, a few tiny γ' grains had formed in the middle of the compound layer.

The values determined for the positions (depths) of the sublayer boundaries have been gathered in Table 2.4. By solving Equation (2.14) for k and inserting the determined corresponding values of treatment times and layer-boundary positions, the (parabolic) growth constants were determined. This last procedure was also performed for the experiments *N1* to *N3* to sensitively account for a possible change in the conditions between the experiments although a common parabolic growth constant was found to provide an acceptable fit to the experimental data by a straight line in Figure 2.4. Hence, the velocities of the layer boundaries, at the treatment times of the (sub)layer-depth measurements, could then be determined by differentiating Equation (2.14). These kinetic data are also shown in Table 2.4.

2.5.2 Concentration-depth profiles in the ϵ (sub)layers

From the mass fractions of Fe, N and C determined by EPMA as function of depth in the ϵ (sub)layer, the molar fractions were calculated by assuming that the only constituents of the examined layer material are Fe, N and C. From these values, the C correction, typically around 1.6 at.%, was subtracted (cf. Section 2.4)². After normalizing the values again to 100 at.%, the u -fractions were calculated (cf. Equation (2.12)) and plotted.

The (sub)layer boundaries are represented by steps in the u -fraction-depth profiles of both N and C. Thus, by inspection of the plots of the u -fraction-depth profiles, the positions of the (sub)layer boundaries can be defined. Additionally, for determining the position of the surface,

²The authors are aware that a C-correction on the basis of mass fractions or X-ray counts would in principle be a better approach. For the concentration range considered here, however, the difference is marginal.

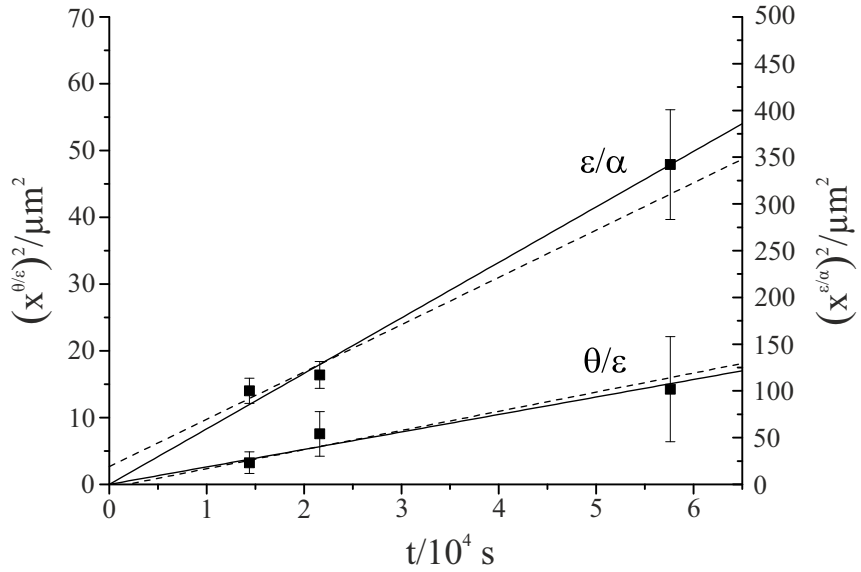


Figure 2.4: Plot of the squared positions of the θ/ϵ and ϵ/α interfaces $(x^{\theta/\epsilon})^2$ and $(x^{\theta/\epsilon})^2$, as measured from specimens $N1$ to $N3$, versus the treatment time t . Note the different scale for $(x^{\theta/\epsilon})^2$ and $(x^{\theta/\epsilon})^2$. The solid lines represent a fit of the data according to a parabolic growth law (cf. Equation (2.14)); the dashed lines describe the experimental data according to a modified parabolic growth law (cf. Equation (2.15))

Table 2.4: Interface positions $x^{\theta/\epsilon}$ and $x^{\epsilon/\alpha}$ as determined for the N and C series experiments, parabolic growth constants k (assuming $x^2 = k \cdot t$, cf. Equation (2.14)) and boundary velocities $v = dx/dt$ at the time of the end of the experiments.

label	$x^{\theta/\epsilon}$ /μm	$x^{\epsilon/\alpha}$ /μm	$k^{\theta/\epsilon}$ /(10 ⁻¹⁵ m ² s ⁻¹)	$k^{\epsilon/\alpha}$ /(10 ⁻¹⁵ m ² s ⁻¹)	$v^{\theta/\epsilon}$ /(10 ⁻¹⁰ ms ⁻¹)	$v^{\epsilon/\alpha}$ /(10 ⁻¹⁰ ms ⁻¹)
$N1$	1.80	10.0	0.23	6.94	0.63	3.47
$N2$	2.75	10.8	0.35	5.40	0.64	2.50
$N3$	3.78	18.5	0.25	5.94	0.33	1.61
$N4$	2.37	12.1	0.39	10.17	0.82	4.20
$C1$	—	23.0	—	36.73	—	7.99
$C2$	—	21.7	—	32.70	—	7.53
$C3$	—	21.3	—	31.51	—	7.40
$C4$	—	28.2	—	55.23	—	9.79
$C5$	—	27.1	—	51.00	—	9.41

the sum of the mass fractions of the determined elements Fe, N and C can be taken as an indicator, being below 100 wt.% in the protective Ni layer.

For the (at least) three plots of the u -fraction-depth profiles of N and C, these layer-boundary positions may differ somewhat as the layer boundaries are not truly flat (see Figure 2.3). To handle this problem, the depth coordinate of each single u -fraction-depth profile of N and C was normalized with respect to the local layer thickness.

Typical u -fraction-depth profiles for the N and the C series are shown in Figure 2.5. For the N series, the u -fraction of N is almost constant over the whole layer. The u -fraction of C decreases with increasing depth. The profiles of both elements depend linearly on depth, allowing application of Equation (2.7a).

For the C series, the u -fraction-depth profiles of both elements show a distinct, negative depth gradient. This is remarkable recognizing that the substrate initially is already (relatively) rich in C. For the fit of the u -fraction-depth profile of N, in all cases a linear function could be fitted justifiably, allowing application of Equation (2.7a). The u -fraction-depth profile of C shows a strong curvature in some cases. Therefore, the error function with curvature parameter w_C (cf. Equation (2.9)) was fitted in these cases, allowing application of Equation (2.7b).

Values derived from the fits to the u -fraction-depth profiles of the ϵ (sub)layers have been gathered in Table 2.3. For the N series, this includes the u -fractions of N and C in ϵ at the θ/ϵ interface and at the ϵ/α interface; for the C series, the u -fractions of N and C in ϵ at the specimen surface and at the $\epsilon/\alpha+\theta$ interface and, if applicable, the curvature parameter w_C of the C u -fraction-depth profile have been determined.

2.5.3 Fluxes at upper and lower boundaries of the ϵ (sub)layers

By using the flux-difference equations (2.5), (2.6), (2.7a) and (2.7b) given in Section 2.3 and the measured data for the concentrations of N and C at both boundaries of the ϵ (sub)layer, (if applicable) for the curvature parameter w_C , and for the interface velocities, the flux differences *at* and *between* the upper and the lower boundary of the ϵ (sub)layer can be calculated for each specimen/experiment. Then, from these data, the fluxes of N and C in ϵ at the upper and lower (sub)layer boundaries can be determined by departing from the flux into the substrate (see what follows directly below) and subsequently adding up the previously calculated flux differences.

For the N series, the flux of N into the substrate is zero because the substrate was already initially saturated with N; the flux of C into the substrate can be assumed to be zero in all cases because of the very small C solubility in α -iron. For the N concentration in the substrate the maximum solubility of N in the binary Fe–N system in equilibrium with γ' as calculated with data from Reference 41 was used ($x_N = 0.0036$ at 853 K (580 °C) and 101 325 Pa (1 atm), being

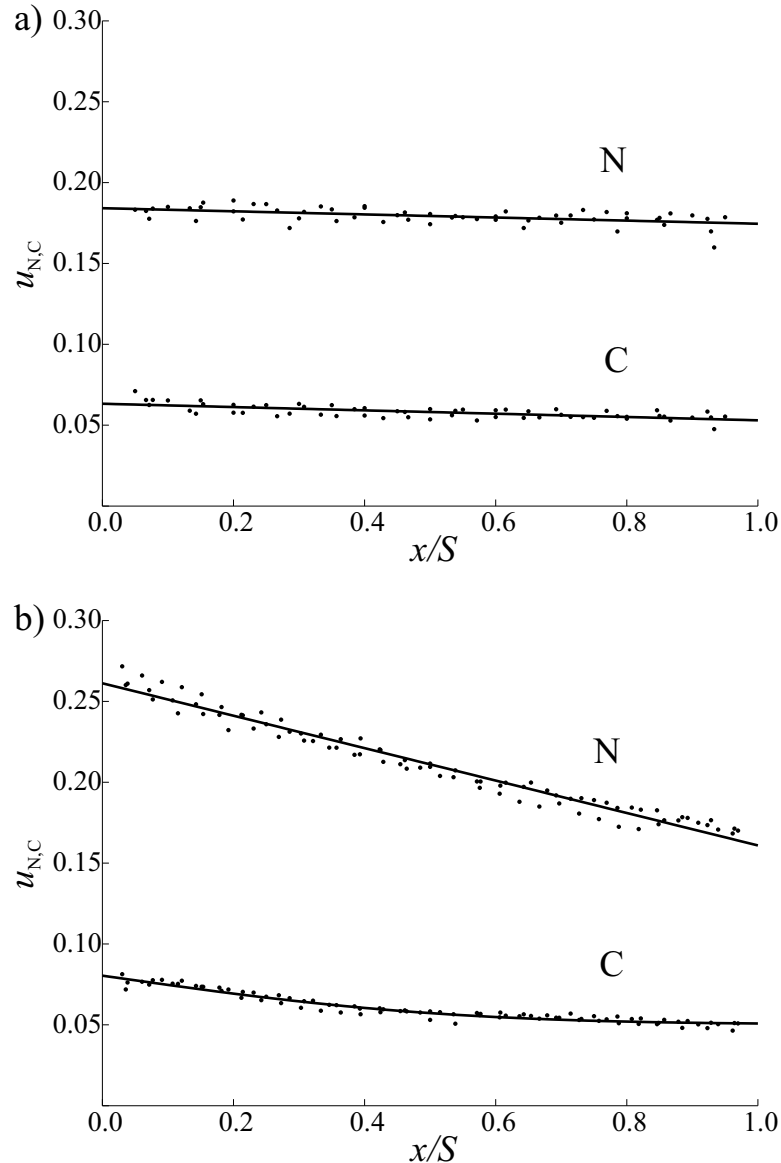


Figure 2.5: Typical u -fraction-depth profiles of N and C in the ϵ (sub)layer calculated (cf. Equation (2.12)) from the mass-fraction-depth profiles as measured by EPMA. The full lines drawn through the experimental data points are the plots of the (linear or error) functions which were fitted to the experimental data. The depth coordinate was normalized with respect to the local layer thickness. a) N series. The N and C contents depend linearly on depth. b) C series. The N profile depends linearly on the depth; the C profile shows strong curvature. The N and C u -fraction-depth profiles show pronouncedly negative depth gradients.

Table 2.5: The fluxes of N and C at the top and the bottom interfaces of the ϵ layer ($j = \theta$ for $N1$ to $N4$, $j = S$ for $C1$ to $C5$) as determined for the N and C series experiments in $10^{-6} \text{ mol m}^{-2} \text{ s}^{-1}$ and average molar fractions of N and C in the corresponding ϵ (sub)layers.

label	$j_N^{\epsilon/j}$	$j_N^{\epsilon/\alpha}$	$j_C^{\epsilon/j}$	$j_C^{\epsilon/\alpha}$	x_N	x_C
$N1$	7.53	7.23	2.44	1.91	0.144	0.044
$N2$	5.48	5.31	1.79	1.53	0.145	0.045
$N3$	3.52	3.41	1.18	1.06	0.145	0.047
$N4$	9.38	8.56	3.11	2.52	0.146	0.047
$C1$	21.13	17.34	2.57	1.6	0.169	0.047
$C2$	19.07	16.20	3.21	1.34	0.162	0.053
$C3$	18.65	16.54	3.53	1.96	0.160	0.056
$C4$	25.38	19.27	3.26	2.11	0.166	0.047
$C5$	25.36	20.16	4.47	2.55	0.170	0.056

closer to the gravimetrically determined N contents of the substrate than the value for the phase boundary $\alpha/\alpha+\gamma'$ in Reference 30.

For the C series, the C concentration in the substrate was assumed to remain constant at the initial value, i.e. at $x_C = 0.0286$, implying zero flux of C into/out of the substrate. The N flux into the substrate was calculated using Equation (2.10) adopting a value for the diffusion coefficient of N in α -iron according to Reference 106. Hereby, the reduction of the diffusion cross-section due to the volume fraction of θ in the substrate (approx. 10 %) was ignored and the volume per mole Fe of the $\alpha+\theta$ substrate (used for calculating the concentrations after Equation 2.13) was assumed to be equal to the volume per mole Fe of pure α -iron.

The thus obtained values for the fluxes at the upper and lower layer boundaries of the ϵ (sub)layers (pertaining to the finishing time of the corresponding experiment) for both the N and C series experiments have been listed in Table 2.5.

2.5.4 Diffusivity matrix

With the calculated fluxes for each specimen at the ϵ (sub)layer interfaces and the corresponding concentration gradients (determined by differentiation of either Equation (2.8) or Equation (2.9)), the coefficients of the straight lines as defined by Equation (2.4) can be calculated. Then the graphical evaluation as described in Section 2.2 can be performed. Such results for the upper interface of the ϵ (sub)layer, i.e. the θ/ϵ interface for the N series and the surface for the C series, are presented in Figure 2.6.

Looking at the plots of D_{NC} vs. D_{NN} and D_{CN} vs. D_{CC} in Figure 2.6, containing one straight line for each experiment of both the N and the C series, there appears no single well-defined

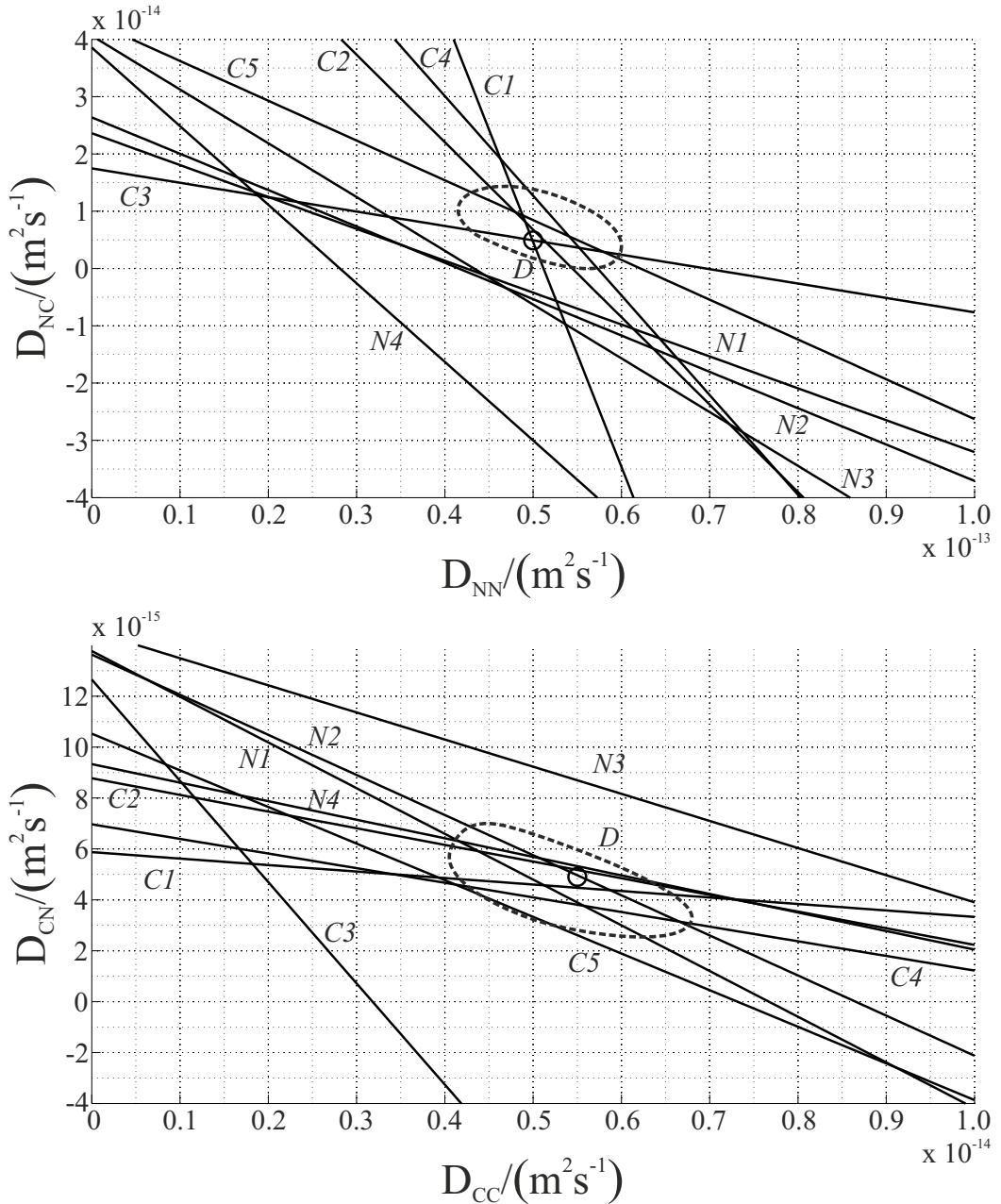


Figure 2.6: Plots of D_{NC} vs. D_{NN} and D_{CN} vs. D_{CC} . The straight lines represent relationships (cf. Equation (2.4)) as determined for all experiments of the N and C experimental series, following the evaluation method as proposed in Section 2.2. The evaluation was performed at the upper boundary of the ϵ (sub)layer, i.e. the boundary with the θ sublayer for the N series and the surface of the specimen for the C series. The likely possible values for the components of the diffusivity matrix pertaining to the concentration range covered by all experiments of the N and C series have been indicated by the dashed encircling lines. In a second stage, these components were refined, starting with values of the components given as the centroids of the encircled areas, see Section 2.5.4. The final values for the components of the diffusivity matrix have been indicated with circles.

solution for all four components of the diffusivity matrix owing to the strong concentration dependence of the effective values of the components of the diffusivity matrix and also the experimental errors accumulating over the process of the evaluation (see Section 2.2). However, as also made clear in Section 2.2, it is possible to define a point in each plot that represents *approximate* values for the corresponding components of the diffusivity matrix, valid for the concentration range comprised by *all* experiments. Thus, the *area of most probable possible solutions*, i.e. the area in which most of the (physically meaningful) intersection points of the straight lines accumulate, has been indicated with dashed encircling lines in each of the two plots in Figure 2.6. The coordinates of the centroids of these areas have been taken as the most likely values of the components of the diffusivity matrix. Note that in Figure 2.6a, all intersection points with a negative value of D_{NC} have been excluded. This is due to a physical restriction: since D_{CN} is clearly positive (cf. Figure 2.6b), the mathematical sign of D_{NC} must also be positive due to the equality of mixed partial derivatives, cf. Equation (2.2). This is discussed in detail in Section 2.6.2.

In a second step, the preliminary values of the components of the diffusivity matrix were further refined by iteratively minimizing the difference of (i) the fluxes calculated, using Fick's first law, with the (to be refined) components of the diffusivity matrix and the experimentally determined concentration-depth gradients of N and C and (ii) the fluxes calculated using the equations given in Section 2.3 and the experimentally determined boundary concentrations, and, if applicable, the curvature parameter of the C concentration-depth profiles and growth constants. The thus determined final values for the diffusivity matrix, as given by

$$D(853\text{ K}) = \begin{pmatrix} D_{NN} & D_{NC} \\ D_{CN} & D_{CC} \end{pmatrix} = \begin{pmatrix} 50 & 4.9 \\ 4.9 & 5.5 \end{pmatrix} \times 10^{-15} \text{ m}^2 \text{ s}^{-1}, \quad (2.18)$$

have been indicated in Figure 2.6.

A similar evaluation for the lower boundary of the ϵ layer, i.e. the interface with the substrate for both experimental series, did not lead to well-defined results. This is due to the very small concentration gradient of C at the lower boundary for the profiles which were described with an error function (cf. Equation (2.9)), leading to extremely steep slopes of the straight lines in the plot of D_{NC} versus D_{NN} and extremely flat slopes of the straight lines in the plot of D_{CN} versus D_{CC} .

The graphical evaluation method used in the present work is mathematically equivalent to numerical solution of the system of linear equations defined by Equation (2.4) with D_{NN} , D_{NC} , D_{CN} and D_{CC} as the unknown, independent variables. The advantage of the proposed graphical evaluation is the simplicity of performing a test for the validity of the assumptions and a corre-

sponding estimation of the error in the obtained values. This error estimation can be done in (at least) two ways: (i) By introducing variations of the parameters in Equation (2.4), the straight line of possible solutions for each set of conditions becomes a set of straight lines comprising an area of possible solutions. (ii) Already the area of accumulation of intersection points, as indicated in both plots in Figure 2.6, as a result of experimental over-determination (more than two sets of experimental conditions subject to the same values of the intrinsic diffusion coefficients), allows error estimation from the size of these accumulation areas.

Thus, following approach (ii), looking at the indicated areas in Figure 2.6, for D_{NN} and D_{CC} , an error of approx. 20 % can be estimated, leading to $D_{NN} = (50 \pm 10) \times 10^{-15} \text{ m}^2 \text{s}^{-1}$ and $D_{CC} = (5.5 \pm 1.0) \times 10^{-15} \text{ m}^2 \text{s}^{-1}$. For D_{CN} , the error can be estimated at approx. 20 % or less, leading to $D_{CN} = (4.9 \pm 1.0) \times 10^{-15} \text{ m}^2 \text{s}^{-1}$. Figure 2.6 indicates that D_{CN} has the most well-defined solution; D_{NC} is the least well-defined component in the present evaluation (note the scales of the coordinates of Figure 2.6).

2.6 Discussion

2.6.1 Merits and limitations of the model and the evaluation method

The concentration-depth profiles especially in the thick pure ϵ layers growing into the pearlitic substrates (C series) show relatively large gradients in both the N and C content at the surface (e.g. see Figure 2.5). The strong curvature in the C concentration-depth profiles of the C series is a consequence of the high C content of the substrates used for the C series: This high C content results in a small C concentration difference at the $\epsilon/\alpha+\theta$ interface, leading to a small C flux difference/total flux in ϵ at the $\epsilon/\alpha+\theta$ interface. Thus, the total flux in ϵ at the surface of the specimen is mainly controlled by the flux difference between the upper and lower boundary of the ϵ layer. Fick's first law relates these significantly different fluxes in ϵ at the surface and at the $\epsilon/\alpha+\theta$ interface to significantly different depth gradients of the C concentration-depth profile in ϵ at both interfaces. The thus resulting large difference of the concentration gradients in ϵ at the surface and at the $\epsilon/\alpha+\theta$ interface implies a significant curvature of the C concentration-depth profile. This curvature was well described in the present work by an error-function shaped profile with only one profile-shape, fit parameter w_C . On this basis the concentration-depth profiles in case of diffusion in the ϵ phase of high-C, low-N contents were evaluated, whereas until now only the ϵ phase of high-N content (and variable C content) could be analysed [81]; see also below.

In the present work parabolic growth with $S_0^2 = 0$ (cf. Equations (2.14) and (2.15)) was adopted to describe the (macroscopic) layer-growth kinetics. Then the possible occurrence

of, e.g. an incubation time (i.e. $S_0^2 < 0$), would be a cause of error. The conditions used for the experiments *N1* to *N3*, cf. Table 2.3, are identical except for the treatment time. The squared values of the θ/ϵ and ϵ/α sublayer-boundary positions measured for these specimens (cf. Section 2.4) are shown in Figure 2.4. The error bars shown were calculated from the standard deviation of the single measurement points. If a parabolic growth law holds for this series *N1* to *N3*, the experimental data can be represented by straight lines through the origin in a plot of x^2 versus t (cf. Equation (2.14)), which holds for the experiments *N1* to *N3* within the accuracy of the measurements: see the solid straight lines in Figure 2.4. A modified parabolic growth law, i.e. fitting the experimental data according to Equation (2.15), does not increase the quality of the fit significantly: cf. the dashed and solid lines in Figure 2.4. This indicates that also for experiment *N4* with similar conditions and the same substrate as used for experiments *N1* to *N3* a parabolic growth law holds. Additional experiments not shown here with the same conditions as used for the experiment *C4* but for different treatment time led to a similar result, indicating that also for the conditions of experiments *C1* to *C3* and *C5* the description of the layer-growth kinetics by a parabolic growth law is justified. The validity of the ideal parabolic growth has two advantages. Firstly, it is possible to use every specimen investigated by EPMA in the evaluation without the need to collect additional kinetic data (e.g. to determine S_0^2). Secondly and more importantly, a single experiment suffices to determine the velocities of the migrating interfaces between sublayers and between (sub)layer and substrate, thereby avoiding the problems caused by irreproducible surface conditions: The gas-solid equilibrium at the specimen surface (if established at all, cf. References 25, 29 and 30) is found to be rather labile as compared to the solid-solid equilibria established at interfaces within the solid, leading to the formation of different phases (e.g. cementite, Hägg carbide) upon decomposition of interstitial-rich ϵ close to the surface of the specimen; see also Reference 92.

Growth kinetics could also be affected by the formation of pores, nucleating at the grain boundaries in the region of the compound layer that is close to the surface and eventually forming channels through which N and C can be taken up from the gas atmosphere [92]. Figure 2.3b indicates that such pores have formed during the nitrocarburising treatment. However, own experiments and literature data [96] show that severe pore formation in C-rich ϵ is always connected with formation of Fe carbides, e.g. θ or Hägg carbide. There has been no indication in XRD for the formation of such phases. Furthermore, due to etching the porosity appears much more pronounced than it actually is. Therefore, the effect of porosity on the nitrocarburising kinetics can be neglected.

The interface, of the (sub)layer considered, for which the evaluation is performed, is determining for the results of the evaluation (i.e. the components of the diffusivity matrix). It has

been made clear in Reference 114 that the diffusivities obtained from (the growth rates of) layers with concentration depth gradients are always *effective* diffusivities. Performing the evaluation at another interface (in the present work the top interface of the ϵ (sub)layer was chosen in a considerate manner; cf. Section 2.5.4) implies that other effective diffusivities are determined, i.e. the way the mean value of the diffusivities is defined changes then, cf. Equation (3b) in Reference 114. Therefore, the values of the components of the diffusivity matrix determined at the top interface/surface and those determined at the bottom interface are principally different.

2.6.2 N and C diffusion in the ϵ phase; comparison with literature data

Various temperature dependencies for the effective diffusion coefficient of N in binary ϵ -iron nitride have been summarized in Reference 115 using data from References 105, 108, 112 and 113. Using these data, it follows for the diffusion coefficient of N in pure ϵ -iron nitride that at 853 K (580 °C) values are obtained between $21 \times 10^{-15} \text{ m}^2 \text{s}^{-1}$ and $52 \times 10^{-15} \text{ m}^2 \text{s}^{-1}$. The experimentally determined value at 853 K (580 °C) equals $39.8 \times 10^{-15} \text{ m}^2 \text{s}^{-1}$ as determined in Reference 115. The here-determined value for D_{NN} is at the high end of this range.

Values for the diffusivities at 823 K (550 °C) had been presented in Reference 81:

$$D(823 \text{ K}) = \begin{pmatrix} 21.2 & 19.6 \\ 3.6 & 0.9 \end{pmatrix} \times 10^{-15} \text{ m}^2 \text{s}^{-1}. \quad (2.19)$$

The values of the diagonal components of the diffusivity matrix as determined in the present work at 853 K (580 °C) are larger than those at 823 K (550 °C) (cf. Eqs. (2.18) and (2.19)), which is in accordance with the expected Arrhenius-type temperature dependence of diffusion coefficients. The difference of the off-diagonal elements at 823 K (550 °C) and 853 K (580 °C), however, cannot be understood on the basis of the temperature difference, 823 K (550 °C) vs. 853 K (580 °C); note the decrease of D_{NC} upon going from 823 K to 853 K (550 °C to 580 °C). This phenomenon can be understood looking at the concentration range covered by the experiments in the present work and in Reference 81. The average molar fractions of N and C in each ϵ (sub)layer were determined from the fit of the measured u -fraction-depth profiles, as shown in Figure 2.5, and applying Equation (2.12) solved for x_k . The results have been listed in Table 2.5 for each profile incorporated in the evaluation. The molar fraction range of N and that of C covered by all these u -fraction-depth profiles together and the molar fractions of N and C averaged over all these u -fraction-depth profiles are shown in Table 2.6. The diffusivities at 853 K (580 °C) presented in Section 2.5.4 pertain to these molar fraction (range) values. The concentration range covered in the experiments considered in Reference 81 extends to much larger N

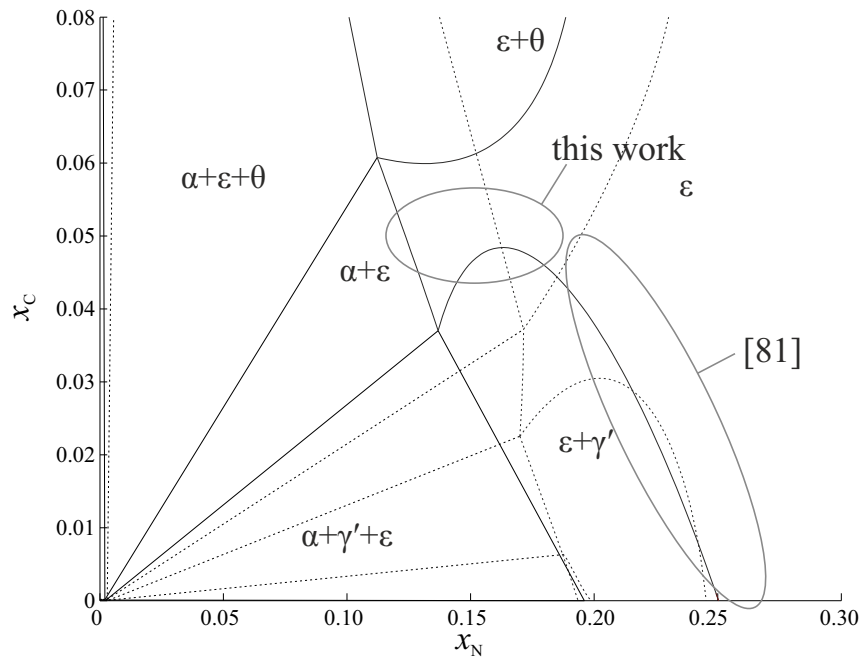


Figure 2.7: Comparison of the N and C concentration ranges for which the diffusivity matrix was determined in the present work and in Reference 81, superimposed on the Fe–N–C phase diagrams at 853 K (580 °C) and at 101 325 Pa (1 atm) using the model described in Reference 41 (dotted lines) and as calculated using the model described in Reference 43 (solid lines). Note that the data from Reference 81 were determined at 823 K (550 °C). The $\epsilon + \gamma'$, two-phase area, however, has a very similar shape at both temperatures.

contents and to smaller C contents than as in the present work (see the data in Table 2.6): a comparison of the concentration ranges investigated in the present work and in Reference 81 is provided by Figure 2.7, where these concentration ranges have been superimposed on the phase diagrams of the system Fe–N–C at 853 K (580 °C) calculated with data from either Reference 41 or 43.

Both, the results obtained in the present work and those obtained in Reference 81, prove that the N (C) flux caused by the concentration-depth gradient of C (N) significantly contributes to the total flux of N (C), indicating strong interactions of N and C in ϵ -iron carbonitride. Actually,

Table 2.6: Approximate concentration ranges (cf. Figure 2.7) and average concentrations corresponding to the N and C series experiments performed in the present work, and those pertaining to the experiments in Reference 81.

	T / K	range of x_N	\bar{x}_N	range of x_C	\bar{x}_C
present work	853	0.14...0.17	0.156	0.04...0.06	0.049
[81]	823	0.19...0.25	0.222	0.00...0.06	0.026

such interactions are already the consequence of only ideal mixing entropy of the interstitially dissolved components, as shown in Reference 81. Thus, for interstitial diffusion of N and C in Fe, the off-diagonal values of the diffusivity matrix cannot be neglected.

Another approach was used in Reference 127. There, the thermodynamic interactions of N and C during interstitial diffusion in γ -Fe based alloys (expanded austenite) in technical steels were expressed by introducing *effective* concentrations, i.e. the hypothetical N (C) concentration that would lead to the same chemical potential of N (C) in a solution of only N (C) in the material as occurring in reality for the real solution of *both* elements in the material. This enabled the authors of Reference 127 to apply a model [128] that describes the concentration dependence of the diffusion coefficient of C in γ to ternary diffusion of both N and C in γ . However, this requires the assumption of a thermodynamic model for the Fe–N–C phase considered. The main conclusion drawn in Reference 127 is compatible with that of a preceding work [81] and the present rigorous approach: the chemical potentials of each, N and C and thus the diffusivities of each interstitially dissolved component are largely influenced by the other element, originating mainly from entropic [81] interactions. Ternary diffusion in the system Fe–N–C cannot be described neglecting these interactions.

Values for the thermodynamic factors connecting the here-determined diffusivities to the self diffusion coefficients of N and C in ϵ -iron carbonitride (cf. Equation (2.2)) can be calculated, using e.g. Thermo-Calc [70], adopting a concentration-dependent thermodynamic description for the ϵ phase in the Fe–N–C system as given in Reference 41 or 43. The values of the thermodynamic factors calculated using the average N and C concentrations pertaining to this study and as listed in Table 2.6 are shown in Table 2.7. From the data obtained in the present work, it is not possible to directly obtain experimental values of the thermodynamic factors, owing to D_N^* and D_C^* being unknown. However, experimental values for the ratios of the average thermodynamic factors can be calculated by (cf. Equation 2.2):

$$\frac{\vartheta_{NC}}{\vartheta_{NN}} = \frac{D_{NC}}{D_{NN}} \quad \frac{\vartheta_{CN}}{\vartheta_{CC}} = \frac{D_{CN}}{D_{CC}}. \quad (2.20)$$

The experimental values for these ratios have also been given in Table 2.7. Evidently, the experimental results support the thermodynamic model for the ϵ phase as presented in Reference 43. The description in Reference 41 leads to even negative values of the off-diagonal components of the diffusivity matrix, which is not at all compatible with the results obtained here. This important conclusion regarding the thermodynamics of ϵ -iron carbonitride is consistent with the results presented in Reference 81. Moreover, as follows from Figure 2.7, if the Fe–N–C phase diagram as calculated on the basis of Reference 41 is adopted, the experimentally determined concentration-depth profiles in the ϵ phase would overlap with the $\alpha+\epsilon+\theta$ three phase

Table 2.7: Thermodynamic factors, ϑ_{kl} , and their corresponding ratios, as calculated adopting the model description of either Reference 41 or 43 for the average concentrations $\bar{u}_N = 0.197$ and $\bar{u}_C = 0.062$. Values from the present work were experimentally determined from the *N* and *C* series.

source	ϑ_{NN}	ϑ_{NC}	ϑ_{CN}	ϑ_{CC}	$\vartheta_{NC}/\vartheta_{NN}$	$\vartheta_{CN}/\vartheta_{CC}$
[41]	3.29	-2.84	-0.89	2.84	-0.86	-0.31
[43]	3.09	1.65	0.52	1.70	0.53	0.31
present work					0.10	0.89

field, which is physically impossible. Hence, the thermodynamic description of the ϵ phase according to Reference 43 is the physically more realistic one.

On the bases of Figure 2.6a, one might argue that the value of D_{NC} could have a negative sign. However, as briefly mentioned in Section 2.5.4, since D_{CN} is evidently positive, the mathematical sign of D_{NC} also *must* be positive, as follows upon inspection of Equation (2.2): Since all other quantities (D_k^* , c_k) are necessarily positive, the mathematical sign of D_{kl} is defined by $\partial \mu_k / \partial c_l$. This quantity represents is a second derivative of the Gibbs energy and therefore the equality of mixed partial derivatives holds, immediately leading to the important restriction of equal mathematical signs for the off-diagonal components of the diffusivity matrix.

The ratio of the off-diagonal entries of the diffusivity matrix only contains the ratio of the self diffusion coefficients of both N and C and the (known) ratio of the N and C concentrations (as $\partial \mu_N / \partial c_C = \partial \mu_C / \partial c_N$; see above):

$$\frac{D_{NC}}{D_{CN}} = \frac{D_N^*}{D_C^*} \frac{c_N}{c_C}. \quad (2.21)$$

As a first approximation, the self diffusion coefficients of N and C in ϵ -iron carbonitride can be taken to be equal. Then, the ratio of the off-diagonal values of the diffusivity matrix D_{NC}/D_{CN} equals the ratio of the average u -fractions (or concentrations) $u_N/u_C \approx 3$ (cf. Table 2.6). The experimental value for D_{NC}/D_{CN} is 1. However, considering the experimental error in D_{NC} and D_{CN} the range of experimental values for this ratio is compatible with the above theoretical prediction. Note that an (about) equality of the off-diagonal values of the diffusivity matrix, as determined above, is only by chance; it does not result from physical requirements.

2.6.3 Application to other microstructures

Upon pure nitriding at conditions characterized with $a_N = 831$, $a_C = 0$ (cf. Table 2.2) of the same Fe–C alloy as used for the experiments of the *C* series, an $\epsilon/\gamma/\epsilon$ triple layer was found to grow into the $\alpha+\theta$ substrate. In the following, the ϵ sublayer adjacent to the surface will be

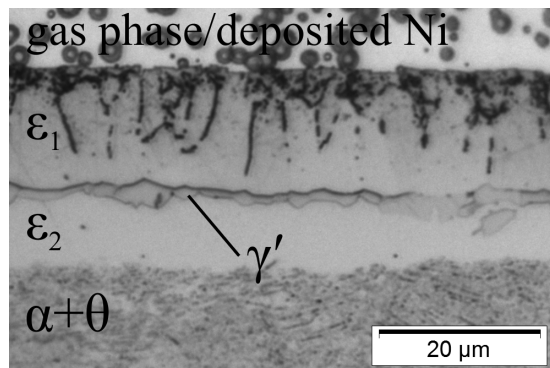


Figure 2.8: Light microscopical micrograph (after Groesbeck staining) of a cross-section through the $\epsilon/\gamma'/\epsilon$ triple layer growing into the $\alpha+\theta$ substrate upon pure nitriding. In order to distinguish the upper and lower ϵ sublayer, they have been labelled ϵ_1 and ϵ_2 .

Table 2.8: N and C fluxes in $10^{-6} \text{ mol m}^{-2} \text{ s}^{-1}$ in the upper (ϵ_1) and lower (ϵ_2) ϵ sublayer of the $\epsilon/\gamma'/\epsilon$ triple layer growing into a pearlitic Fe–C substrate upon pure nitriding. See text for fluxes with index Fick, which were calculated from the diffusivities determined from the N and C series experiments.

component	$j_{\text{fleq}}^{\epsilon_1/S}$	$j_{\text{Fick}}^{\epsilon_1/S}$	$j_{\text{fleq}}^{\epsilon_2/\gamma'}$	$j_{\text{Fick}}^{\epsilon_2/\gamma'}$
N	21.7	111.9	17.8	27.5
C	-1.9	8.1	2.9	4.3

designated as ϵ_1 , whereas the ϵ sublayer adjacent to the substrate will be designated as ϵ_2 . A micrograph of a cross-section through this layer structure is shown in Figure 2.8. The corresponding N and C u -fraction-depth profiles, as measured by EPMA, are shown in Figure 2.9. In principle, these u -fraction-depth profiles and the additionally measured distances of the layer boundaries to the surface of the specimens can be used to calculate the fluxes of N and C at the layer boundaries of the ϵ sublayers, applying the procedure described in Section 2.3. The results are shown in Table 2.8³. This specimen was not used for the evaluation of the diffusivity matrix because of the high porosity of the ϵ_1 layer, leading to inaccurate concentration measurements by EPMA. Also, due to the formation of channels [92] due to pores that open during the nitriding treatment, N uptake can be influenced. The layer-growth kinetics was found to be less regular than those pertaining to the experiments of the N and C series. However, the data obtained from this specimen can be used to look for consistency with the values of the diffusivity matrix presented in Section 2.5.4, as determined from the N and C series of experiments.

³The fluxes listed in Table 2.8 were calculated with the assumption of zero flux of C from the substrate in the direction of the surface. This is justified since both recent models for the system Fe–N–C [41, 43] predict a higher chemical potential of C in the ϵ_2 layer than in the $\alpha+\theta$ substrate.

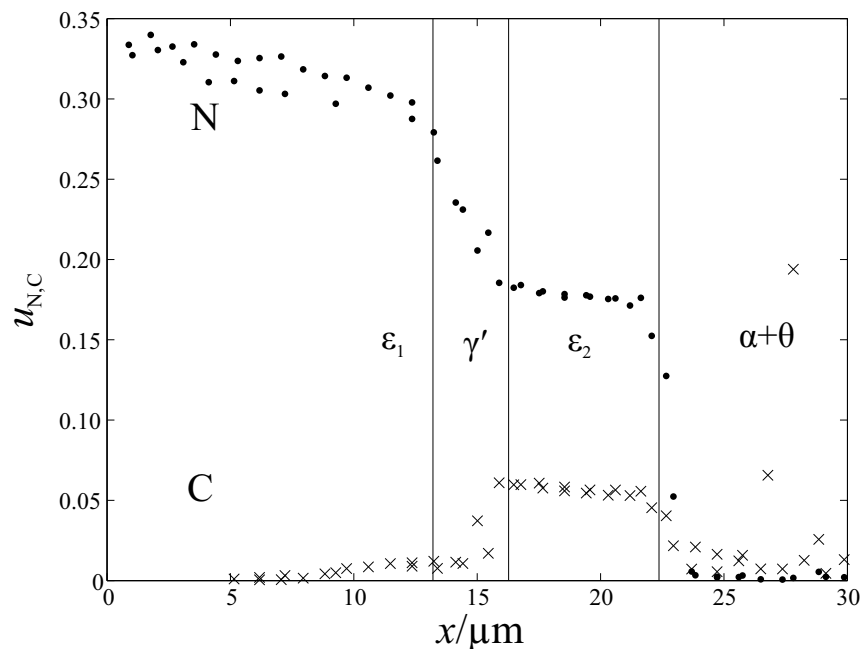


Figure 2.9: N and C u -fraction-depth profiles as measured by EPMA on a cross-section of the $\epsilon/\gamma'/\epsilon$ triple layer specimen produced by pure nitriding ($a_N = 831$; $a_C = 0$) of pearlitic Fe–C substrates identical to those used for the C series of experiments. As in Figure 2.8, the upper and lower ϵ sublayer have been labelled ϵ_1 and ϵ_2 . The x coordinate, i.e. the total local layer thickness, was scaled with respect to the average total compound layer thickness as measured by light microscopy. The vertical lines have been drawn at the average position of the corresponding interfaces between the sublayers.

The N and C concentration-depth profiles of the lower ϵ layer, labelled ϵ_2 in Figure 2.9, depend linearly on depth within experimental accuracy. Recognizing that the purely nitriding atmosphere applied in this experiment has a strong decarburising character, due to its H₂ content (formation of CH₄), the occurrence of a negative gradient for also the component C is surprising. This phenomenon can be explained as a consequence of the rejection of C by the γ' sublayer growing on top of the ϵ_2 sublayer as the solubility of C in γ' is very low (max. 0.63 at.% at 853 K (580 °C) as calculated using the model in Reference 41; the model given in Reference 43 assumes that C cannot be dissolved in γ'). This effect is also revealed by the positive value of the flux of C in this lower sublayer, see Table 2.8.

The fluxes (i) as calculated from the experimental data for the $\epsilon_1/\gamma/\epsilon_2$ specimen using the flux equations from Section 2.3, and those (ii) as calculated by Fick's first law, using the N and C concentration-depth gradients pertaining to the ϵ_2 sublayer and the values for the diffusivity matrix as determined in the present work from experiments of the N and C series, can be compared in Table 2.8. It follows that the both sets of flux values are comparable for the lower, ϵ_2 sublayer. The average N and C concentrations in this ϵ_2 sublayer ($x_N = 14.4$ at.% and $x_C = 4.7$ at.%) are close to the average concentrations in the ϵ layers of the N and C series, so that it can be expected that the diffusivities of Equation (2.18) are good approximations for also those of the ϵ_2 sublayer (cf. discussion on *effective diffusion coefficient* in Section 2.6.2).

In the upper ϵ sublayer, labelled ϵ_1 in Figure 2.9, the N content is very high and the C content is very low (on average $x_N = 23.7$ at.% and $x_C = 0.3$ at.%). The depth gradient of the C content is positive, i.e. the C content increases from the surface to the substrate. This corresponds with a negative flux of C as derived from the experimental data of the $\epsilon_1/\gamma'/\epsilon_2$ specimen (see flux data in Table 2.8). The fluxes calculated by application of Fick's first law, using the N and C concentration-depth gradients pertaining to the ϵ_1 sublayer and the values for the diffusivity matrix as determined in the present work from the experiments of the N and C series, now largely deviate from the fluxes calculated from the experimental data for the $\epsilon_1/\gamma'/\epsilon_2$ specimen using the flux equations from Section 2.3. This is an obvious consequence of the average N and C concentrations in this ϵ_1 sublayer being incompatible with the concentration ranges pertaining to the values compatible with the diffusivity matrix (cf. Table 2.6). For such low values of C concentration as in the ϵ_1 sublayer, the component D_{CN} should be close to zero (see Equation (2.2)). Hence, the flux of C in the ϵ_1 sublayer is predominated by the C concentration-depth gradient and not the N concentration-depth gradient, explaining the negative sign of the C flux.

On the other hand, in the ϵ_1 sublayer, the flux of N as calculated using Fick's first law is much higher than the flux of N as calculated using the flux equations, see Table 2.8. At such

low C concentrations the component D_{NC} of the diffusivity matrix is expected to reach a value so high that already the small *positive* gradient present in the C concentration-depth profile significantly decreases the flux of N. This interpretation is supported by the magnitude of the value of D_{NC} as determined in Reference 81 (cf. Equation (2.19)) resulting from an analysis of ϵ layers containing much less C than the ϵ layers examined in the present work: in that case D_{NC} was nearly as large as D_{NN} in Reference 81.

2.7 Conclusions

1. A straightforward, graphical procedure to determine the four intrinsic diffusion coefficients governing the simultaneous diffusion of N and C in a host lattice is possible utilizing experimentally determined concentration-depth profiles of N and C (e.g. measured by EPMA) and (parabolic) layer-growth constants (e.g. determined by light microscopy).
2. The diffusivity matrix thus determined for the diffusion of N and C in ϵ -iron carbonide, for N contents of approximately 14...17 at.% and C contents of 4...6 at.%, at 853 K (580 °C) and at 101 325 Pa (1 atm) is given by $D_{NN} = 50 \times 10^{-15} \text{ m}^2 \text{s}^{-1}$, $D_{NC} = 4.9 \times 10^{-15} \text{ m}^2 \text{s}^{-1}$, $D_{CN} = 4.9 \times 10^{-15} \text{ m}^2 \text{s}^{-1}$ and $D_{CC} = 5.5 \times 10^{-15} \text{ m}^2 \text{s}^{-1}$.
3. The here-determined values of the off-diagonal components of the diffusivity matrix imply a pronounced influence of the N (C) concentration-depth profile on the C (N) flux: the off-diagonal values of the diffusivity matrix cannot be neglected at all for diffusional calculations, e.g. simulations of layer-growth kinetics.
4. Analysis of (ratios of) thermodynamic factors derived from the components of the diffusivity matrix indicates that the thermodynamic interaction of N and C on the same sublattice for the Fe–N–C system is better described by the thermodynamic model of Reference 43 than that of Reference 41.

Acknowledgments

The authors would like to thank Mrs S. Haug from the Stuttgart Center for Electron Microscopy (Max Planck Institute for Intelligent Systems) for her help with performing the EPMA analysis.

Chapter 3

Microstructural development and crystallographic properties of decomposing Fe–N–C compound layers

Holger Göhring, Stefan Kante, Andreas Leineweber, Eric Jan Mittemeijer

The microstructural development of Fe–N–C compound layers resulting from nitrocarburising and heat treatments applied to Fe–N and Fe–C alloys was investigated. Slow cooling or secondary annealing, instead of quenching, after the end of the nitrocarburising treatment causes decomposition of $\gamma\text{-Fe[N,C]}$ and $\epsilon\text{-Fe}_3(\text{N,C})_{1+x}$ in the compound layer. The resulting decomposition microstructures were analysed by, in particular, light microscopy and electron backscatter diffraction, and X-ray diffraction and electron probe micro-analysis, revealing their constitution and crystallographic properties. The results are discussed in comparison to data obtained from undecomposed, i.e. quenched specimens and to data reported in the literature.

3.1 Introduction

Nitriding and nitrocarburising are thermochemical surface treatments widely applied in industry in order to improve the mechanical, tribological and corrosion properties of iron and steel [1]. In recent years, a number of studies have been devoted to the nitrocarburising of Fe, Fe–N and Fe–C alloys, involving subsequent quenching of the specimens to preserve the high-temperature

microstructure [29, 75, 81, 82], see also Chapter 2. A major focus of these works was the investigation of the treatment-time dependent evolution of the carbonitride compound-layer microstructures. Layer-thickness data can in particular be used to determine the interstitial elements' diffusivities [81], see also Chapter 2. Such diffusivities, in turn, can then be used to simulate the layer-growth kinetics, which is of cardinal importance for optimisation of the nitrocarburising process.

The microstructural analyses performed in the above mentioned investigations have all been performed on specimens subjected to (fairly) fast cooling after the nitrocarburising so that the microstructure resulting from only the nitrocarburising treatment was quenched in. Such high cooling rates, as applied in References 29, 75, 81 and 82 and in Chapter 2, do not occur in the case of the nitrocarburising of technical components. This implies that microstructural developments induced by and during the cooling are highly relevant for the resulting mechanical, tribological and anti-corrosive properties.

In the present work, nitrocarburising treatments, similar to those in References 29, 75, 81 and 82 and in Chapter 2, were conducted focussing on the effect of furnace cooling and the thus evoked phase transformations. In particular, *secondary* annealing experiments were also performed. The resulting microstructures are investigated using light microscopy, X-ray diffraction and electron backscatter diffraction in order to obtain insight in their constitution and crystallographic properties. On this basis important thermodynamic knowledge on the Fe–N–C system is acquired.

3.1.1 Phases in the Fe–N–C system

All phases considered in the Fe–N–C system and as produced by a nitrocarburising treatment are, at normal temperature and pressure, metastable with respect to decomposition into almost pure α -Fe (or γ -Fe[C] at elevated temperature), N₂ gas and graphite. Nevertheless, different solid Fe–N–C phases can be in metastable (local) equilibrium with each other at inter-phase boundaries. When using the term *equilibrium* in the present work, it refers to such metastable solid-state equilibria at inter-phase boundaries. Every phase in the Fe–N–C system corresponds to a ternary extension of either a binary Fe–N or a binary Fe–C phase, i.e. there is no phase that only exists in the ternary Fe–N–C system. Some characteristics [19, 25] of the phases relevant for the present work have been summarised in Table 3.1. In the following, the lower-case Greek letters defined in Table 3.1 will be used to denote the single phases.

The sequence of invariant reactions (at 1 atm) in the Fe–N–C system has been subjected to extensive, also controversial discussion. Thus, in contrast to the binary systems, in the ternary system, the ϵ phase can exist in equilibrium with the α phase at typical nitriding/nitrocarburising

Table 3.1: Crystal structures, typical N and C content x_N and x_C , of phases relevant for the present work according to References 19 and 25.

phase	space group	structure description	x_N /at.%	x_C /at.%
α -Fe[N,C]	Im $\bar{3}$ m	bcc Fe lattice, N and C on octahedral sites	<0.4	<0.1
α' -Fe[N,C]	I4/mmm	bct Fe lattice, N and C ordered on octahedral sites	<10	<8.3
α'' -Fe ₁₆ N ₂	I4/mmm	bct Fe lattice, N ordered on octahedral sites	≈ 12.5	≈ 0
γ -Fe[N,C]	Fm $\bar{3}$ m	fcc Fe lattice, N and C on octahedral sites	<10.3	<9.1
γ' -Fe ₄ N _{1-z}	Pm $\bar{3}$ m	fcc Fe lattice, N ordered on octahedral sites	19.4–20	<0.7
ϵ -Fe ₃ (N,C) _{1+x}	P6 ₃ 22	hcp Fe lattice, N and C ordered on octahedral sites	15–33	<8
	P6 ₃ /mmc	simpler hcp cell used for EBSD analysis with $a_{\text{hcp}} = a_{\epsilon}/\sqrt{3}$ and $c_{\text{hcp}} = c_{\epsilon}$		
θ -Fe ₃ C	Pnma	orthorhombic, C in trigonal prisms of Fe	≈ 0	25
χ -Fe ₅ C ₂	C12/c1	monoclinic, C in trigonal prisms of Fe	≈ 0	28.6

temperatures. In this case, it contains relatively large amounts of C and remarkably small amounts of N in comparison to the typical N content of binary ϵ nitride at the same temperature [41, 43, 46, 75]. This $\alpha+\epsilon$ equilibrium was not included in early publications covering the constitution of the system Fe–N–C [84, 129]. Moreover, we have shown [81, 82] (see also Chapter 2) that the equations of the Gibbs energies of the relevant phases as given in Reference 43 lead to a description of the system Fe–N–C that fits considerably better with most of the experimental data than the description given in Reference 41. Isothermal sections of the phase diagram of the system Fe–N–C at the here-considered temperatures (and at 1 atm) have been calculated in the present project by implementing the equations for the relevant Gibbs energies as given in Reference 43 into a database readable by the software Thermo-Calc [70] and are shown in Figure 3.1. Note that in Figure 3.1c and d the phase boundary $\alpha+\epsilon/\epsilon$ and in Figure 3.1d the phase boundary $\gamma/\gamma+\epsilon$ show a strikingly small curvature. This is a feature directly resulting from the model parameters of the Gibbs-energy functions from Reference 43.

3.1.2 Phase transformations in Fe–N–C compound layers

Nitrocarburising leads to the uptake of atomic N and C into a substrate. At a certain temperature, the equilibrium constitution is then predicted by applying the lever rule in the appropriate isothermal section of the phase diagram at the point defined by the gross composition (see Figure 3.1) [130]. However, to reach this true (metastable) equilibrium state, very long holding times at the desired temperature are needed in order to flatten out the concentration gradients,

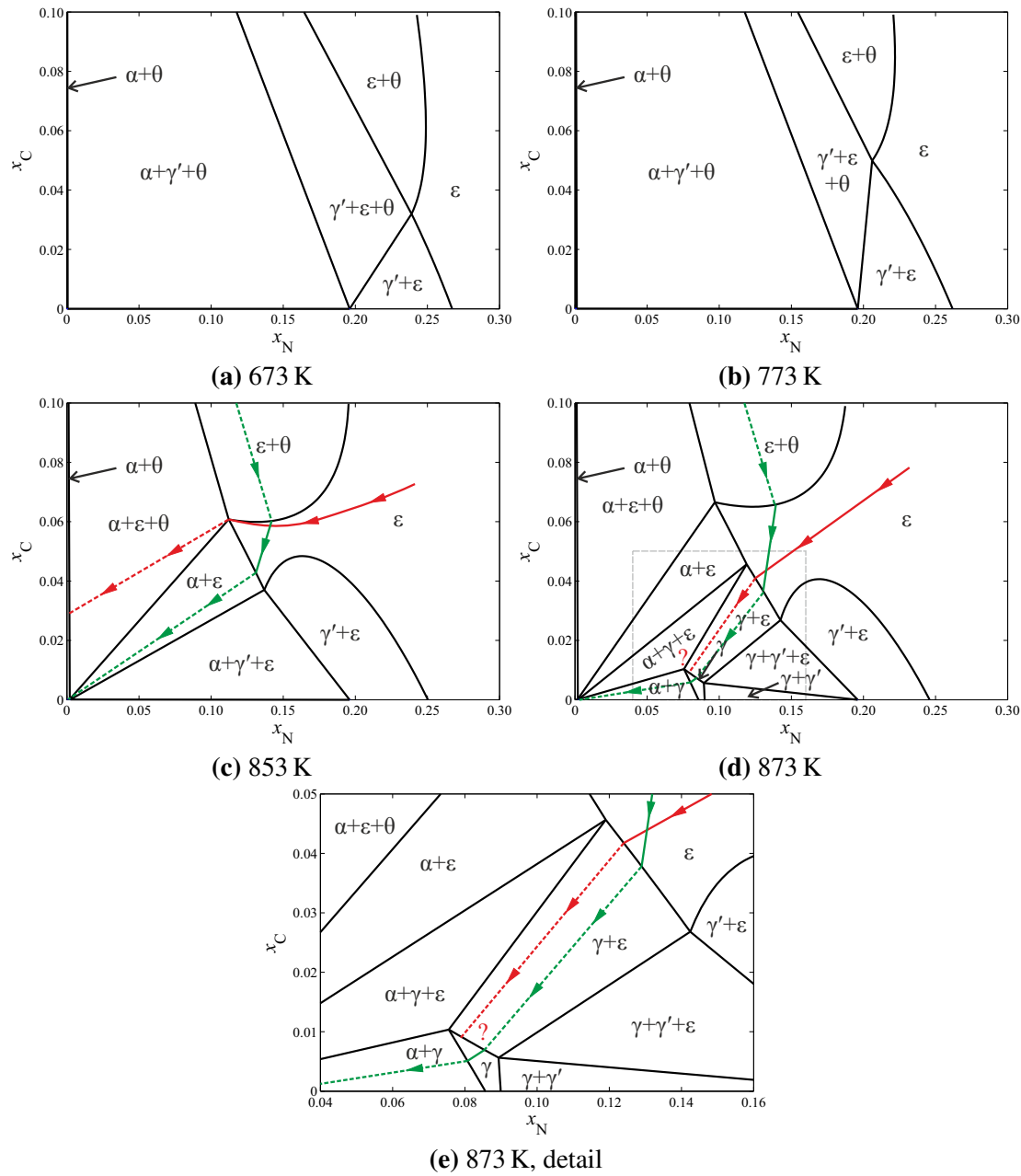


Figure 3.1: Isothermal sections of the phase diagram of the system Fe–N–C at the indicated temperatures (and at 1 atm), calculated by implementing the equations for the relevant Gibbs energies as given in Reference 43 into a database readable by the software Thermo-Calc [70]. The schematic diffusion paths drawn in (c) (853 K) correspond with the microstructures in Figure 3.2a (green, Fe–N substrate) and 3.2b (red, Fe–C substrate); those in (d) and the enlarged section in (e) (cf. grey rectangle in (d)) correspond with the microstructures in Figure 3.2c (green, Fe–N substrate) and 3.2d (red, Fe–C substrate). Hereby, dashed lines denote skipping over a two- or three-phase field. The diffusion path of the Fe–C specimen nitrocarburised at 873 K is incompatible with the phase diagram calculated using the data from Reference 43, since the equilibrium between γ , α and θ found at the interface with the substrate is not possible, as indicated by the question mark in (d) and the enlarged section in (e).

while avoiding changes in composition due to outward diffusion of N and C due to decomposition of metastable phases.

In growing compound layers, the phase constitution as a function of depth can be predicted using the concept of diffusion paths [72, 120–122]: the evolution of the (laterally averaged) composition as a function of depth yields the diffusion path. If local equilibrium at each point of the diffusion path and thus at each depth in the specimen *separately*, prevails, this then also holds at the solid–solid interphase boundaries in the compound layer and at the interface with the substrate. Then the sequence of the phases developing within the compound layer and the diffusion path can be related with the corresponding phase diagram [72, 120, 122].

The (high-temperature) microstructure at the nitrocarburising treatment temperature is the microstructure predicted by the diffusion path in the phase diagram at the treatment temperature. Water quenching of the specimens normally suffices to preserve this high-temperature microstructure of the specimens at the end of the nitrocarburising treatment. An exception occurs if any $\gamma\text{-Fe[N,C]}$ has formed: this austenite will at least partly transform to tetragonally distorted α' martensite, showing a characteristic lath- or plate-like microstructure in the metallographic cross-sections [131–133].

Upon slow cooling with cooling rates of e.g. 2 K min^{-1} to 3 K min^{-1} as in the nitrocarburising furnace used in the present work (between the treatment temperature and approximately 673 K), there is only a marginal change in local composition since there is not enough time for long-range diffusion and local equilibria cannot be established. Yet, at the lower temperatures occurring during cooling, phase diagrams can still predict which phases, different from those at the nitrocarburising temperatures, would be stable at the *local* composition. Thus the tendencies and possible initiation of phase transformations on a *local* scale can be indicated.

The solubility of N in α in equilibrium with γ' decreases with decreasing temperature. Furthermore, at lower temperatures, the ordered phase α'' can form. Thus, upon slow cooling or upon secondary annealing at lower temperatures one or both phases precipitate from the, at this temperature super-saturated, α of the substrate [4, 134].

At lower temperature, there is often a tendency of decomposition of intermediate phases. Upon cooling, α has been found to precipitate in the γ' sub-layer of nitrided $\alpha\text{-Fe}$ specimens [135]. In the case of Fe–C austenite, lamellar pearlite ($\alpha+\theta$) forms upon slow cooling, and in the case of Fe–N austenite, a microstructure consisting of $\alpha+\gamma'$ is formed, usually called braunite. Braunite can show a similar lamellar morphology to pearlite. Often, however, γ' in braunite shows an abnormal granular morphology which has a strong tendency for coarsening [136, 137]. Decomposition of the ε phase could be thought to lead to similar morphologies to braunite or pearlite: thermodynamic calculations using the equations for the Gibbs energy

of the Fe–N–C phases from Reference 43 predict a eutectoid decomposition of ϵ at 825 K, following $\epsilon \rightleftharpoons \alpha + \gamma' + \theta$. One aim of the present work involves production and investigation of the microstructures (morphology and crystallographic properties) resulting from such ϵ decomposition.

3.2 Experimental

3.2.1 Specimen preparation

Two different substrates were used for the nitrocarburising treatments, an Fe–N alloy and an Fe–C alloy. For the Fe–N alloy, pure Fe (Alfa Aesar, 99.98 wt.%) granulate was molten and cast into ingots of 80 mm \times 25 mm \times 10 mm. The ingots were cold-rolled to obtain sheets with a thickness of approximately 1 mm, which were subsequently cut into foils with lateral dimensions of 12 mm \times 20 mm. These foils were ground and polished (final stage 1 μm diamond suspension) to a final thickness of approximately 0.5 mm. The foils were recrystallised in H₂ at 973 K for 2 h and presaturated with N in a nitriding atmosphere containing 10.6 vol.% NH₃ and 89.4 vol.% H₂ at 853 K overnight (16 h to 18 h), resulting in homogeneous specimens with gravimetrically determined N contents between 0.36 at.% and 0.37 at.%, very close to the solubility limit of N in α -Fe in equilibrium with γ' -Fe₄N at 853 K, ranging from 0.36 at.% to 0.42 at.% according to literature [4, 30, 41]. The recrystallisation and prenitriding treatments were performed in the same quartz-tube furnace as described in Section 3.2.2.

The Fe–C specimens were manufactured by casting an Fe–C alloy with a C content corresponding to the eutectoid composition in the Fe–C system [32] with the same dimensions as for the Fe–N alloys. The ingots used in the present work had actual C contents of 0.71 wt.%, 0.81 wt.% and 0.82 wt.% as determined by chemical analyses, close to the value of 0.77 at.% in accordance with Reference 32. The cold-rolling, cutting, grinding and polishing steps were the same as for the Fe–N specimens. Thereafter, the specimens were annealed in a crucible furnace at 1273 K for 2 h. To prevent oxidation, the specimens were encapsulated into quartz vials containing Ar at a pressure corresponding to 1×10^5 Pa at the above indicated annealing temperature. The anneal was terminated by cooling the specimens in the quartz vial in air on a metal surface. This resulted in a fine, purely pearlitic microstructure.

3.2.2 Nitrocarburising treatment

The nitrocarburising treatments were performed in a vertical quartz-tube furnace equipped with mass-flow controllers determining the composition of the nitrocarburising atmosphere. The

Table 3.2: Composition of gas atmospheres applied for nitrocarburising treatments. $\phi_i = p_i / {}^\circ p$, with p_i as partial pressure of component i and ${}^\circ p = 101\,325 \text{ Pa}$.

substrate	T / K	ϕ_{NH_3}	ϕ_{H_2}	ϕ_{CO}	ϕ_{CO_2}	$\phi_{\text{H}_2\text{O}}$	ϕ_{N_2}
Fe–N	853/873	0.13	0.58	0.20	—	—	0.09
Fe–C	853	0.20	0.34	0.38	0.06	0.02	—
	873	0.20	0.34	0.41	0.04	0.01	—

furnace was equipped with gas supplies for NH_3 , H_2 , CO, CO_2 , H_2O , N_2 and CH_4 (not used in the present work). A total flux of 500 ml min^{-1} as determined at room temperature was applied in all cases. Various different treatments were performed both at 853 K and at 873 K. By varying the composition of the gas atmosphere the N and C uptake during the nitrocarburising treatment could be varied. The applied gas atmospheres are listed in Table 3.2. In an ideal case, an equilibrium or at least a stationary state is established at the gas-solid interface (see, e.g. Chapter 1 in Reference 1), thereby controlling the resulting phase(s) and (their) composition at the surface of the specimen.

The Fe–N specimens were treated with atmospheres known to produce θ/ϵ double layers [29]. The approach used involved adding a certain amount of CO gas to a mild nitriding (NH_3/H_2) atmosphere (see Table 3.2), resulting in no definable C activity, but a well-defined N activity [1, 23, 24]. The Fe–C specimens were treated with atmospheres that control the most important carburising reactions, neglecting formation of CH_4 and other organic compounds. By setting the C activity pertaining to these governing reactions equal, a unique C activity can be assigned to the gas phase [1, 23, 24]. At 853 K, nitrocarburising of pearlitic specimens using the atmospheres listed in Table 3.2 results in pure ϵ layers as shown in Chapter 2.

The nitrocarburising treatment was terminated by either quenching in N_2 -flushed water or reducing the heating power of the furnace to zero. Preliminary experiments showed that changing the furnace atmosphere to pure N_2 during slow cooling leads to severe formation of pores, especially for the nitrocarburised Fe–C substrates. Therefore, in the experiments presented and discussed here the atmosphere was kept constant during cooling until a temperature of 573 K was reached. Using data from the thermocouples of the nitrocarburising furnace and assuming that they (also) indicate the temperature of the specimen (i.e. thermal equilibrium prevails), the temperature of 573 K was reached approximately 2.5 h after the end of the nitrocarburising treatment. During the early phase of slow cooling (down to 673 K), a cooling rate of 2 K min^{-1} to 3 K min^{-1} occurred.

3.2.3 Secondary annealing

Secondary annealing experiments were applied to nitrocarburised and water-quenched specimens. These anneals were performed in a crucible furnace at (approximate) temperatures of 673 K and 773 K. The specimens were encapsulated into quartz tubes containing Ar at a pressure of 4×10^4 Pa to prevent oxidation. After the secondary annealing treatments, the quartz tubes were destroyed in water at room temperature, defining the end of the treatment.

3.2.4 Microstructure characterisation

X-ray diffraction (XRD) patterns were recorded in Bragg–Brentano θ – θ geometry from the surface of the specimens using a Philips X’Pert MPD diffractometer equipped with a Co tube and a monochromator in the diffracted beam selecting Co-K α radiation. The diffraction patterns were analysed by Rietveld refinement [138] using the software TOPAS [139] for qualitative phase analysis of the compound layer.

Cross-sectional specimens were prepared and analysed as follows. Prior to cross-sectioning, a piece of each specimen was electrolytically coated with Ni in order to protect the brittle compound layer. The piece was then embedded in resin and ground and polished (final stage 1 μm diamond suspension). For light-microscopical analysis, the cross-sections were etched for 15 s in 1 % Nital containing some HCl [90, 123]. To increase the contrast, some specimens were treated with Groesbeck solution, staining C-rich phases (approximately 10 min at 323 K to 333 K) [124]. The light-microscopical analyses were performed using a Zeiss Axiophot microscope.

For electron backscatter diffraction (EBSD) analysis of the cross-sections, the etching step was replaced by an additional oxide polishing step using Struers OPS suspension, followed by ultrasonic cleaning in isopropyl alcohol for 15 min. Examination of the fine plate-like ϵ + γ' microstructures (see Section 3.3.2) was performed on areas in which the plates are cut by the surface of the cross-sectioned specimen in directions inclined with respect to the plate faces, implying appearance of a coarser plate-like morphology in the cross-section than observed with the plates oriented edge-on with respect to the cross-section. These areas were chosen in the light microscope and marked with an indenter in the protective Ni layer prior to EBSD analysis. EBSD analysis was performed using a LEO 438VP SEM, equipped with a W filament cathode. The smallest possible step size of 50 nm was used. Evaluation was performed with the software EDAX OIM Analysis 7 [140]. Analysis of the ϵ phase was performed on the basis of the strong intensity bands in the Kikuchi patterns caused by the hcp Fe substructure. Thus, a simpler unit

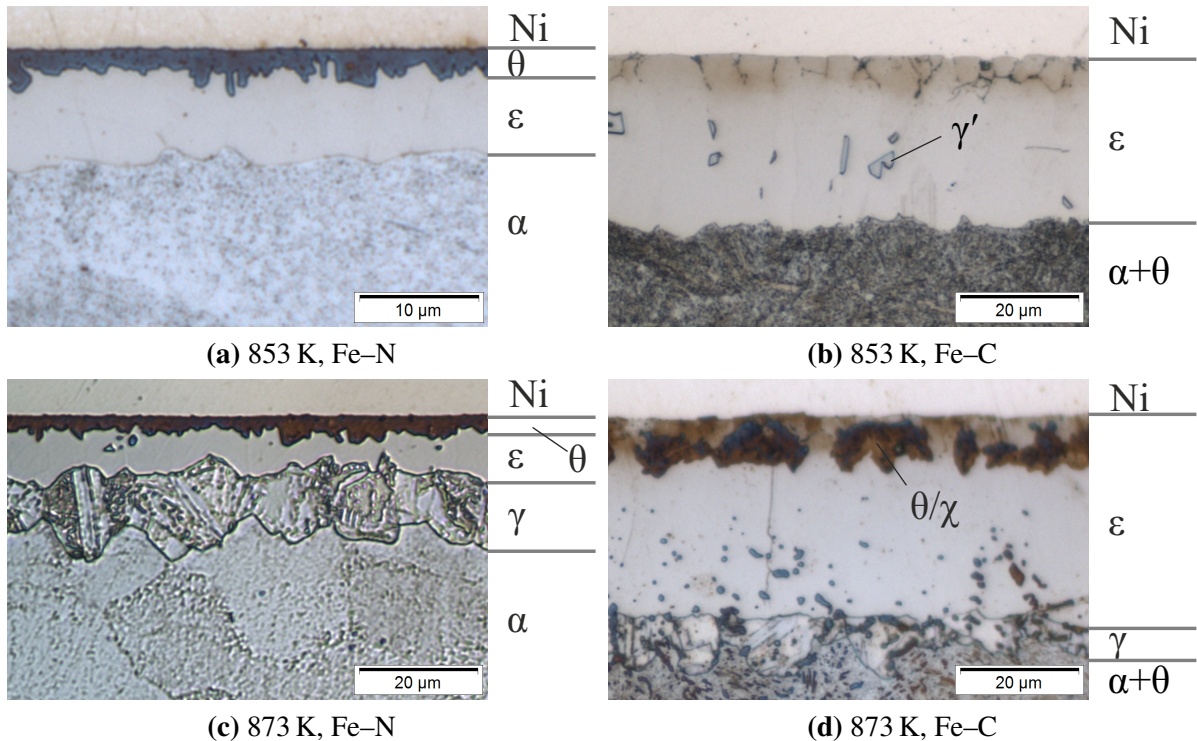


Figure 3.2: Micrographs of Groesbeck-stained cross-sections showing the microstructures resulting from nitrocarburising treatments of the indicated specimens at the indicated temperatures after quenching in water, with schematic representation of the layer structure at the treatment temperature, recognising that γ partially transforms to α' upon quenching. After nitrocarburising at 853 K, on the Fe–N substrates a θ/ϵ double layer and on the Fe–C substrates a pure ϵ layer is found. At 873 K ϵ is separated from the substrate by a γ sublayer.

cell, referring to the hcp structure of the Fe atoms (space group $P6_3/mmc$), ignoring ordering of interstitially dissolved N and C, was used with $a_{\text{hcp}} = a_{\epsilon}/\sqrt{3}$ and $c_{\text{hcp}} = c_{\epsilon}$, see Table 3.1.

3.3 Results

3.3.1 Quenched high-temperature microstructure

Light micrographs of metallographic cross-sections of the quenched specimens (see Figure 3.2) confirm the presence of the phases detected by XRD analysis. Upon nitrocarburising of the Fe–N specimens at 853 K with the parameters shown in Table 3.2 a thin θ/ϵ double layer forms as shown in Figure 3.2a. Under the same conditions, but at a higher temperature of 873 K a $\theta/\epsilon/\gamma$ triple layer¹ forms, as shown in Figure 3.2c.

After nitrocarburising at 853 K with the parameters shown in Table 3.2 the Fe–C specimens show a pure ϵ layer, sometimes containing some γ' grains (see Figure 3.2b). At 873 K with the

parameters shown in Table 3.2 an ϵ/γ double layer¹ forms as shown in Figure 3.2d. On some specimens formation of θ or χ carbides (as verified by XRD) in conjunction with pores (caused by N₂ development [141]) was observed close to the surface due to decomposition of the original, interstitial-rich ϵ . During the nitrocarburising treatment, spheroidisation (coarsening) of the θ lamellae in the substrate, as originally present in the untreated material, occurs. Therefore, it is difficult to dissolve, upon nitrocarburising, all initially present θ into γ or ϵ . The remnants of these θ grains are visible as artefacts [96] in the compound layer (see Figure 3.2d).

3.3.2 Microstructure development upon slow cooling and upon secondary annealing

The microstructures resulting from the nitrocarburising treatments of the different substrates and subsequent *slow, furnace cooling* (see Section 3.2.2) are shown in Figure 3.3 and in detail in Figure 3.4. It was observed that, for both the Fe–N and Fe–C substrates, the columnar ϵ grains formed at 853 K and 873 K exhibit upon slow cooling a plate-like subdivided inner microstructure. EBSD analysis of such transformed ϵ grains in the furnace-cooled specimens revealed that the plate-like microstructure consists of parallel γ' plates which had formed inside the original columnar ϵ grains: see the EBSD phase and orientation maps in Figure 3.5. The parallel orientation of the γ' plates in each columnar originally pure ϵ grain suggests occurrence of a preferred crystallographic orientation relationship of ϵ and γ' (see the analysis in Section 3.3.3). Further, the mostly planar nature of the ϵ/γ' interfaces suggests that the ϵ/γ' interfaces are coherent or at least partially coherent.

The ϵ phase formed on Fe–N substrates almost completely transforms into this $\epsilon+\gamma'$ microstructure (see the micrographs in Figure 3.3a and c and the EBSD maps in Figure 3.5a and c), whereas for the Fe–C substrates only the part of the ϵ layer adjacent to the substrate decomposes (see the micrographs in Figure 3.3b and d and the EBSD maps in Figure 3.5b and d). For the compound layers formed on the Fe–C substrates, the plate-like microstructure is penetrated by coarse γ' grains; see the examples indicated with arrows in Figure 3.5b and d.

The γ phase formed at 873 K in the Fe–N and Fe–C specimens (see Figure 3.2c and d) upon cooling transforms into a three-phase microstructure consisting of α , γ' and θ as validated by EBSD analysis, of partly granular, partly lamellar morphology; see the enlarged section of a micrograph in Figure 3.4, in which the prominent lamellar part has been encircled. By EBSD analysis (see Figure 3.5b and d), a few ϵ grain were also found in this decomposition microstructure. Further, the decomposition of ϵ upon cooling of the Fe–C specimens treated at 873 K also

¹Note that the γ sublayer transforms into an $\alpha'+\gamma_R$ (=retained austenite) two-phase microstructure upon quenching.

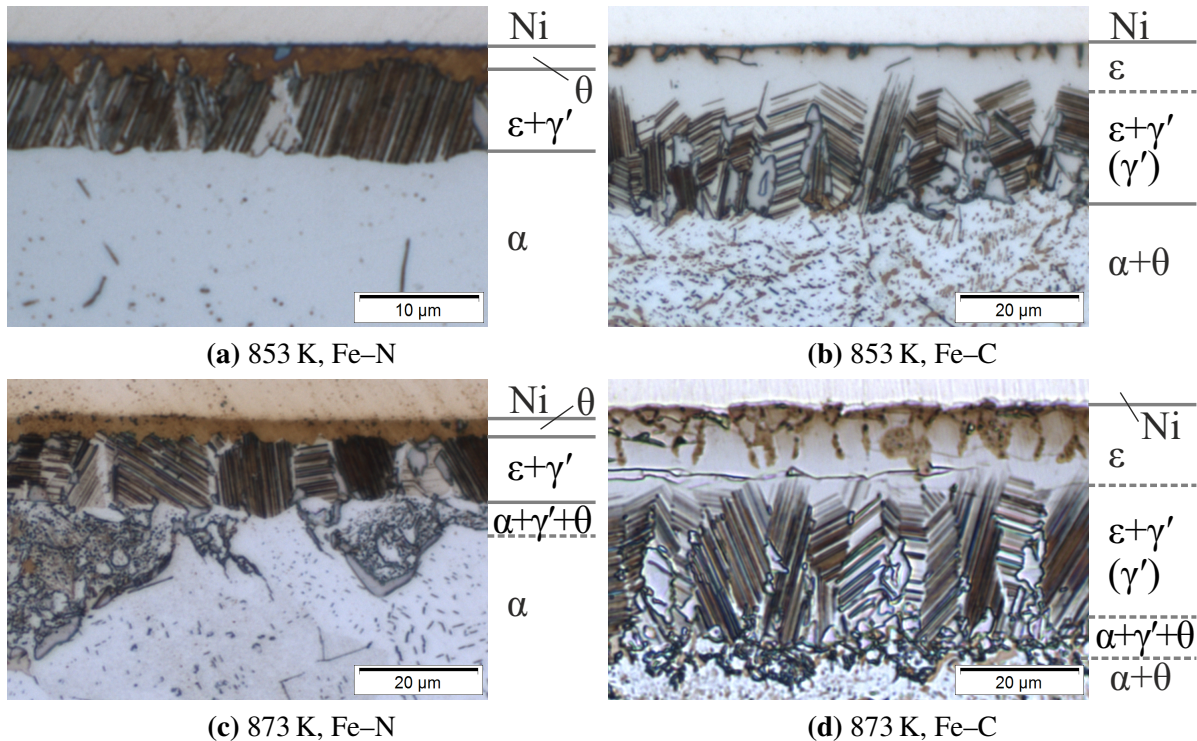


Figure 3.3: Micrographs of Groesbeck-stained cross-sections showing the microstructures resulting from nitrocarburising treatments of the indicated specimens at the indicated temperature and after subsequent slow (furnace) cooling, with schematic representation of the layer structure (dashed lines indicating no clear (sub)layer boundary). Upon cooling, the ϵ phase transforms into a plate-like microstructure that consists of ϵ and γ' grains as identified by EBSD, see Figure 3.5. Larger γ' grains are also found, across grain boundaries of the former ϵ sublayer. The original γ sublayer of the specimens treated at 873 K transforms into a lamellar/granular microstructure labelled as $\alpha+\gamma'+\theta$ with large γ' precipitates at the interface with the substrate; see Figure 3.4 for an enlarged section revealing this morphology. The θ sublayer formed on the Fe–N specimens remains unchanged by the slow cooling. In the substrate of the Fe–N specimens precipitates of γ' are visible.

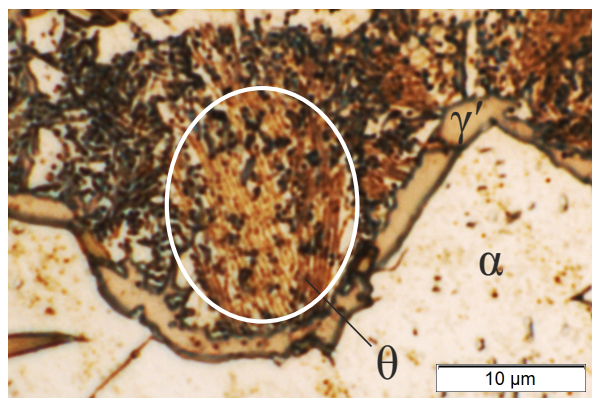


Figure 3.4: Enlarged part of a micrograph with enhanced contrast revealing the microstructure resulting from eutectoid decomposition of the former γ sublayer upon slow (furnace) cooling of an Fe–N specimen nitrocarburised at 873 K; see Figure 3.3c for an overview. A prominent area showing the lamellar pearlite-like morphology has been encircled (θ appears brown because of Groesbeck staining). Other parts of the microstructure show a more granular morphology, resembling a morphology often found for braunite. At the former boundary between γ and the substrate, coarsened γ' grains are present.

causes formation of some α precipitates at the former ϵ grain boundaries (see the EBSD phase map in Figure 3.5d).

At some places the γ' plates seem to grow out of their parent ϵ grains (i.e. cross a grain boundary between the originally pure ϵ grains); see the encircled examples in the EBSD phase maps in Figure 3.5b and d. A very prominent example is shown in the magnified part of Figure 3.5b with the former ϵ/ϵ grain boundary marked in red.

Specimens nitrocarburised at 853 K and afterwards quenched were subjected to *secondary annealing* treatments for 1 h at 673 K or 1 h at 773 K. Micrographs of the cross-sections of the compound layers on these specimens are presented in Figure 3.6. Evidently, the microstructures resulting from secondary annealing (see Figure 3.6) are similar to those of the slowly cooled specimens nitrocarburised at the same temperature (see Figure 3.3a and b): the original ϵ sublayer of the θ/ϵ compound layers (see Figure 3.6a and b) on the Fe–N specimens had completely decomposed into the same lamellar microstructure consisting of ϵ and γ' plates as already observed for the slowly cooled specimens. The plates resulting from the anneal at 673 K are finer than those resulting from the anneal at 773 K. For the original ϵ layers on the Fe–C specimens (see Figure 3.6c and d), only a part of the ϵ layer adjacent to the substrate had decomposed into a plate-like $\epsilon+\gamma'$ microstructure.

In case of the Fe–C specimens, the coarse γ' grains appearing in the transformed zone of the compound layer upon slow cooling (Figure 3.3b) are not visible in the similarly nitrocarburised and subsequently quenched specimens after the secondary anneals for 1 h at 673 K or 773 K

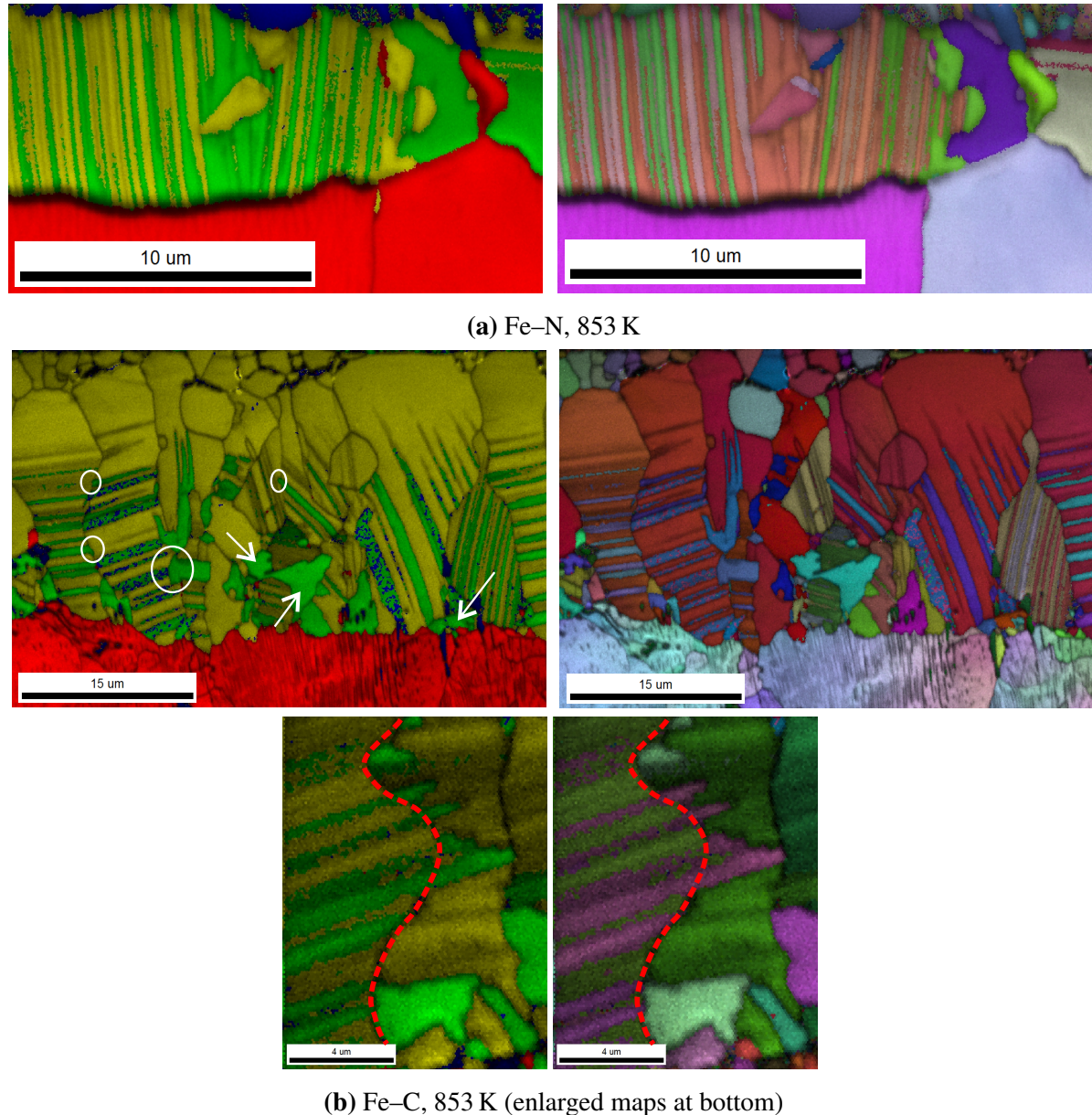


Figure 3.5: (continued on page 64)

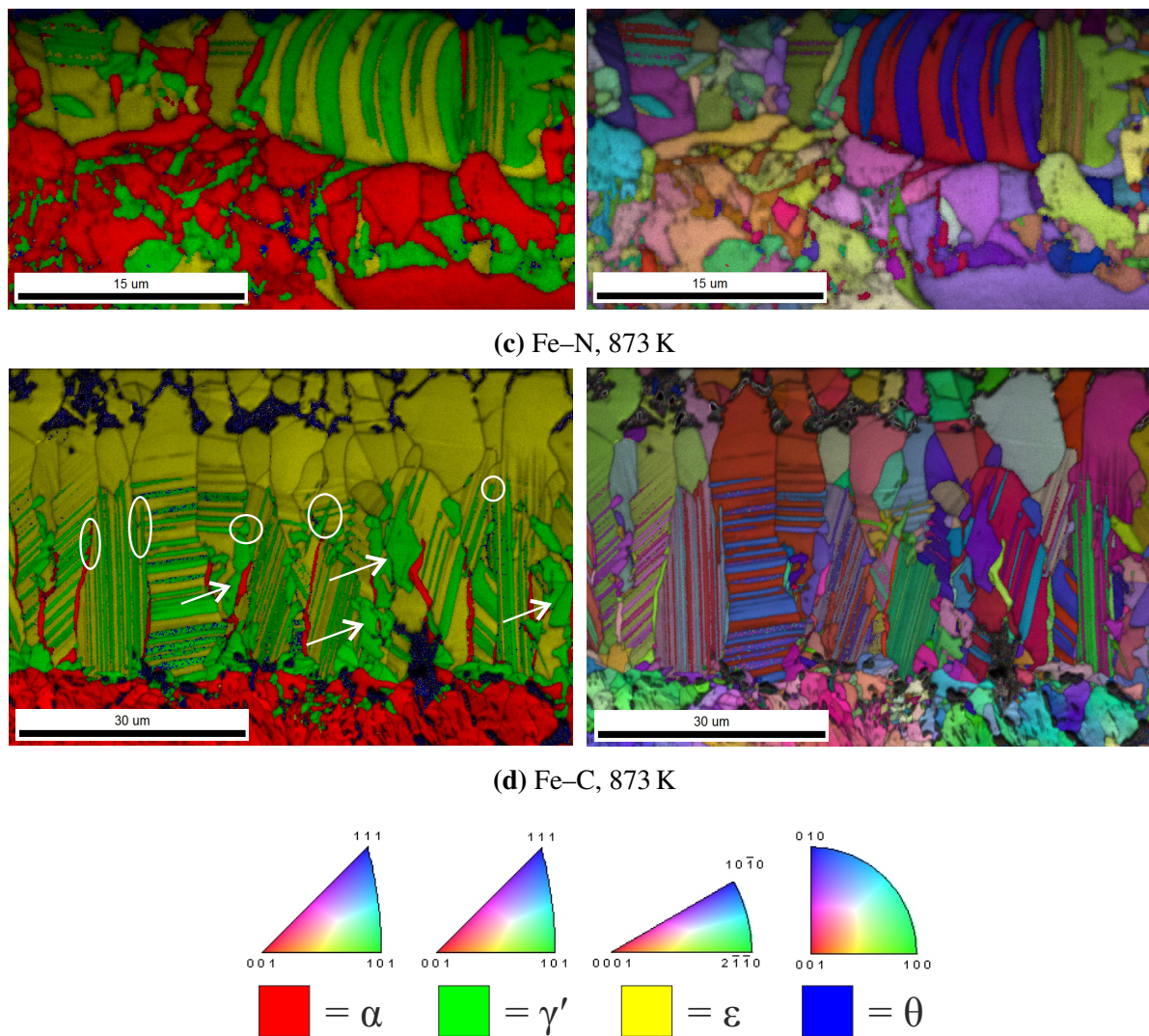


Figure 3.5: (continued from page 63) EBSD phase maps (left) and orientation maps (right) of Fe–C and Fe–N specimens nitrocarburised for 4 h at the indicated temperature and after slow (furnace) cooling; see Figure 3.3. In the orientation map, colours are mapped according to orientations in the standard stereographic triangle as shown for each crystal structure. Both EBSD maps are overlaid with indication of the image quality: dark shaded areas represent areas of bad quality of the recorded Kikuchi patterns used for phase identification. Note the significantly deviating magnification for the Fe–N specimen nitrocarburised at 853 K (very fine microstructure). The plate-like structure visible in the light micrographs of Figure 3.3 is identified as $\varepsilon+\gamma'$. Thereby, in some γ' grains the Kikuchi patterns were misinterpreted by the evaluation software as belonging to the θ phase, shown in blue on the EBSD phase maps. Some of the γ' plates have started to grow out of their respective original ε grain (marked with white circles in (b) and (d)). One prominent example has been enlarged in (b) with the former ε/ε grain boundary marked in red. Examples of massive γ' grains growing across grain boundaries of the original ε grains have been marked with white arrows in (b) and (d). For the Fe–C specimen nitrocarburised at 873 K shown in (d) α precipitates had formed at the former ε grain boundaries (red colour). For both specimens nitrocarburised at 873 K ((c) and (d)), the granular/lamellar structure below the original ε (sub)layer consists of α , γ' , ε and θ (blue in the EBSD phase map) resulting from the eutectoid decomposition of the original γ sublayer (see Section 3.4.2). Curved phase boundaries in (c) are probably caused by a curvature of the specimen due to polishing.

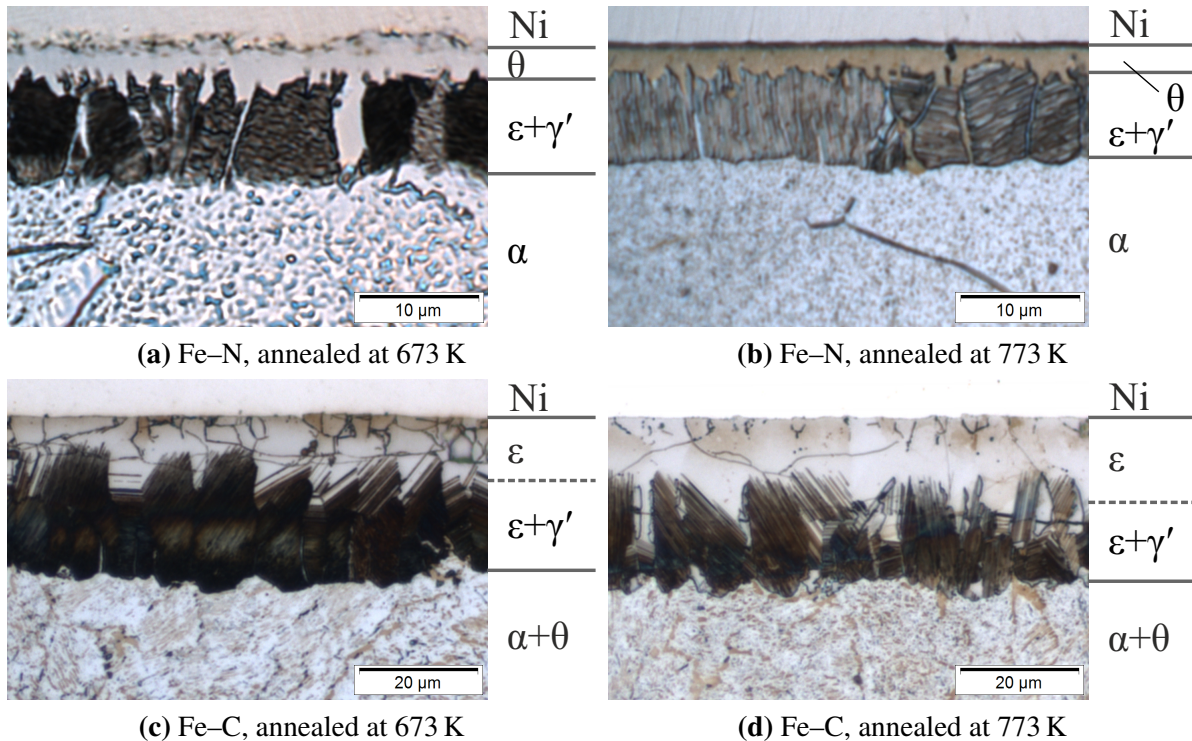


Figure 3.6: Micrographs of Groesbeck-stained cross-sections showing the microstructures resulting from nitrocarburising treatments of the indicated specimens at the 853 K, after quenching and subsequent secondary annealing for 1 h at the indicated temperatures, with schematic representation of the layer structure (dashed lines indicating no clear (sub)layer boundary). As for the case of slow furnace cooling (see Figure 3.3), ϵ decomposes into a plate-like $\epsilon+\gamma'$ structure. The plates formed during secondary annealing at 673 K are finer than those formed during secondary annealing at 773 K. For the Fe–N specimens, the whole ϵ sublayer has transformed. The θ sublayer remains unchanged. For the Fe–C specimens, the transformation occurs in a part of the originally pure ϵ layer adjacent to the substrate. This transformation zone is larger for the specimen annealed at 773 K than for the specimen annealed at 673 K.

(Figure 3.6c and d). The emergence of (coarse) γ' grains by secondary annealing depends on the annealing time: Fe–C specimens nitrocarburised at 853 K and subsequently quenched were annealed at 773 K for different times between 5 min and 16 h; see Figure 3.7 for light micrographs and Figure 3.8 for EBSD phase and orientation maps of cross-sections of these specimens. After 5 min the $\epsilon+\gamma'$ plate-like microstructure is clearly visible. The $\epsilon \rightarrow \epsilon+\gamma'$ decomposition zone propagates in the direction of the surface of the specimen with increasing annealing time at 773 K. After 2 h, coarse γ' grains occur in the decomposed part of the original ϵ layer, which grow with increasing annealing time. After annealing for 16 h, the lower zone of the compound layer has completely transformed into a γ' sublayer. γ' forming the eventually practically closed γ' sublayer appears in two distinctive morphologies: massive grains of γ' with a single orientation, and areas within an original ϵ grain formed by γ' plates with varying orientation; see the orientation maps in Figure 3.8 (examples of the latter morphology encircled in white). Between the γ' grains, θ grains form after long annealing times, as a cause of dissolved C rejected by γ' , seen as the dark blue spots in the EBSD phase maps in Figure 3.8.

During the secondary annealing treatment in Ar pore formation occurs in the part of the ϵ layer of highest supersaturation (i.e. the surface adjacent part) [141] leading to loss of nitrogen and the emergence of θ . This process becomes visible after approximately 2 h, see Figure 3.7d. After 16 h, the area of the compound layer adjacent to the surface thus has decomposed into α -Fe, θ (both confirmed by EBSD) and N_2 (which has left the specimen), see Figure 3.8c.

3.3.3 Orientation relationship of ϵ and γ'

By comparing the orientation of many γ' plates with respect to the parent ϵ grain, applying the EBSD maps taken during the microstructure investigation, it was found that the following ϵ (hcp Fe sublattice)/ γ' (fcc Fe sublattice) orientation relationship holds within 1° :

$$\{0001\}_{\text{hcp}} \parallel \{111\}_{\gamma'}, \langle \bar{2}110 \rangle_{\text{hcp}} \parallel \langle 1\bar{1}0 \rangle_{\gamma'} \quad (3.1)$$

This orientation relationship of ϵ and γ' was reported before in References 142–144. A relation for the dependence of the lattice parameters of ϵ on the N content is given in Reference 101. It can approximately be applied to ϵ in the ternary Fe–N–C system by assuming that C has the same effect on the lattice parameters as N, i.e. using the total interstitial content to determine the lattice parameters. According to the EPMA data shown in Chapter 2, obtained from specimens treated at the same conditions as in the present work, close to the interface with the substrate in both Fe–N and Fe–C specimens treated at 853 K, approx. 0.24 interstitial atoms have been taken up per Fe atom. This interstitial content corresponds with $a_\epsilon \approx 4.63 \text{ \AA}$ or $a_{\text{hcp}} \approx 2.67 \text{ \AA}$.

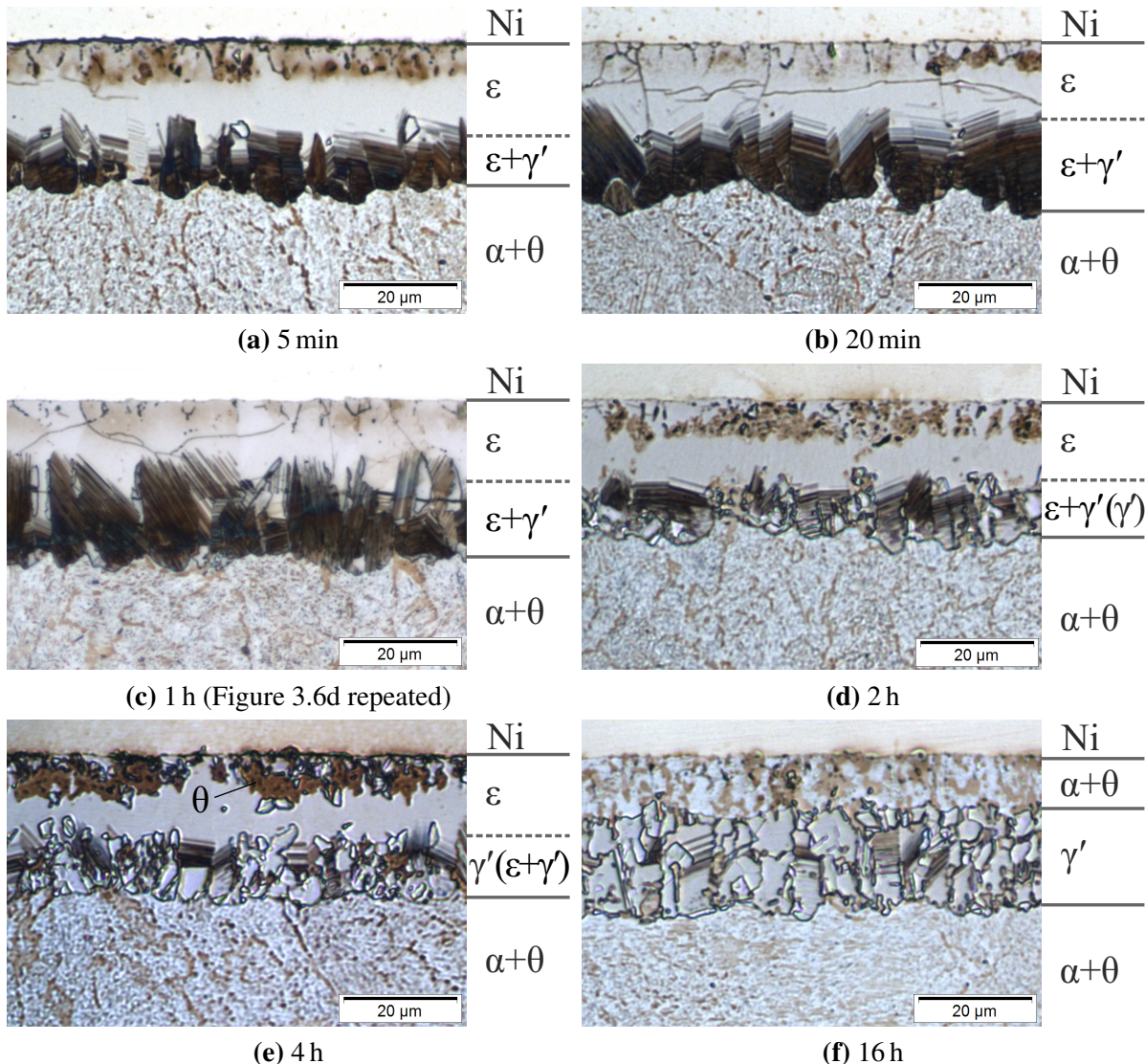


Figure 3.7: Micrographs of Groesbeck-stained cross-sections showing the microstructures resulting from nitrocarburising treatments of the Fe–C specimens at 853 K, after quenching and subsequent secondary annealing at 773 K for the indicated times, with schematic representation of the layer structure (dashed lines indicating no clear (sub)layer boundary). The transformation of ϵ into a plate-like $\epsilon+\gamma'$ microstructure initiates at the zone adjacent to the substrate and propagates through the ϵ layer in the direction of the surface. At longer annealing times, massive γ' grains grow until a γ' sublayer develops. In the region adjacent to the surface decomposition of ϵ occurs, leading to the formation of pores and θ . After 16 h, the outermost ϵ sublayer has completely decomposed into a porous $\alpha+\theta$ sublayer as identified by EBSD, see Figure 3.8.

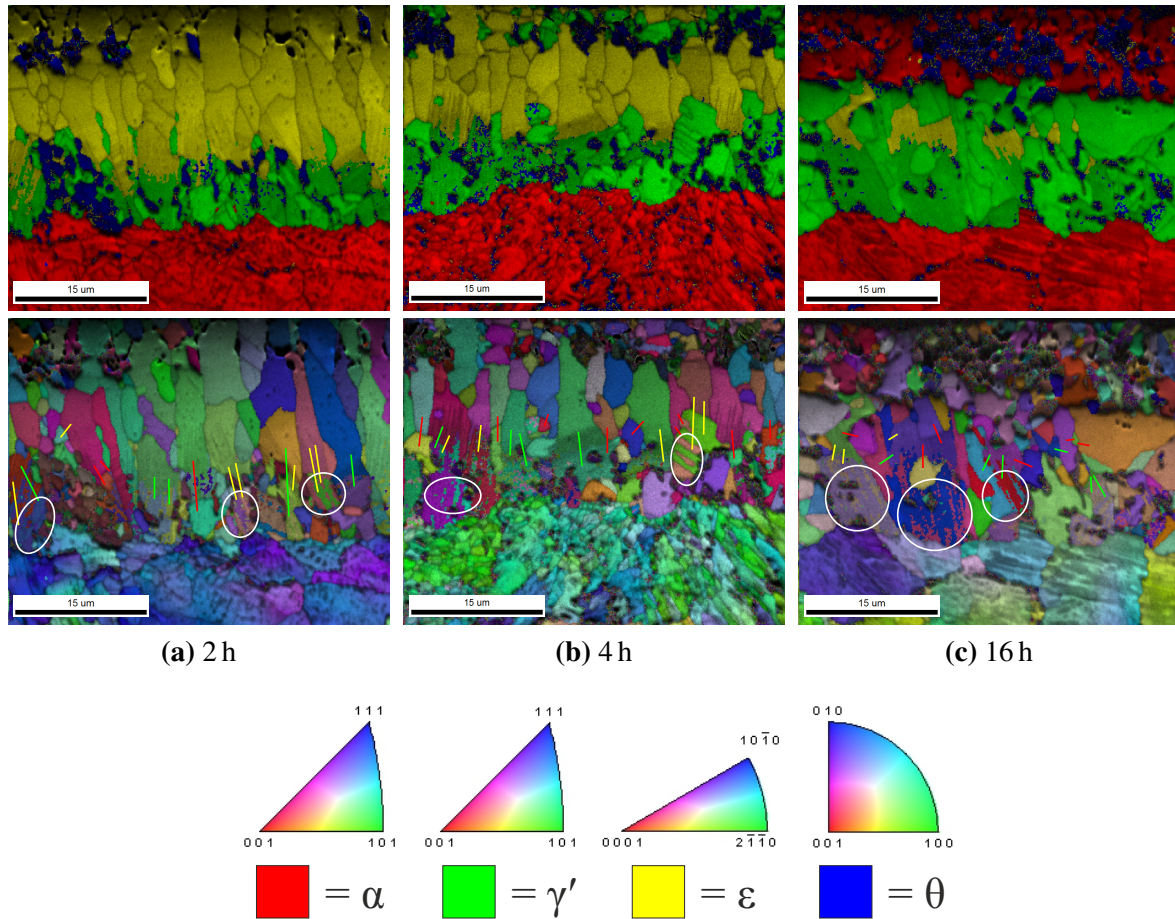


Figure 3.8: EBSD phase (top) and orientation maps of Fe–C specimens nitrocarburised for 4 h at 853 K, after quenching and subsequent secondary annealing at 773 K for the indicated times (see Figure 3.7). In the orientation map, colours are mapped according to orientations in the standard stereographic triangle as shown for each crystal structure. Both EBSD maps are overlaid with indication of the image quality: dark shaded areas represent areas of bad quality of the recorded Kikuchi patterns used for phase identification. With increasing annealing time a γ' sublayer develops close to the substrate. Throughout the γ' sublayer, θ precipitates form (dark, due to poor image quality, blue spots), taking up the C rejected by γ' . Green and yellow lines connecting neighbouring ϵ and γ' grains in the orientation maps indicate fulfilment of the orientation relationship after Equation (3.1) (green: within 1°, yellow: within a few degrees); red lines indicate clear deviation from the orientation relationship. Examples of areas of γ' plates with twin orientation with respect to each other within a single original ϵ grain have been encircled. With increasing annealing time, ϵ decomposes (also) close to the surface, leaving a porous $\alpha+\theta$ sublayer after 16 h of annealing.

(and $c_\epsilon \approx 4.34 \text{ \AA}$). Hence, the misfit of the closest Fe–Fe distances in the ϵ (hcp Fe sublattice) and γ' (fcc Fe sublattice) crystal structures can be calculated as

$$\left| \frac{a_{\text{hcp}} - a_{\gamma'}/\sqrt{2}}{a_{\gamma'}/\sqrt{2}} \right| \approx 0.5 \% \quad (3.2)$$

using the lattice-parameter data for γ' given in Reference 100. This low misfit value suggests full coherency of the interfaces between ϵ and γ' .

Considering only Fe atoms, both ϵ and γ' are close packed structures only differing by the stacking sequence of the close packed planes parallel to $\{0001\}_\epsilon$ and $\{111\}_{\gamma'}$. By trace analysis of the straight interfaces between ϵ and γ' it was found that all these interfaces are compatible with $\{0001\}_\epsilon$ (or $\{111\}_{\gamma'}$) as habit plane. From a mechanistic point of view, the Fe sublattices of the crystal structure of both the ϵ and γ' can be transformed into each other by the glide of Shockley partial dislocations [133]. This process has already been proposed by the authors of Reference 142. For a single ϵ orientation, two γ' orientations exist which comply with Equation (3.1), which can be chosen randomly during the transformation. The two variants of the orientation relationship have indeed been observed: see the differently oriented γ' plates in the orientation maps in Figure 3.5. If two of those differently oriented γ' plates impinge, e.g. by thickening of the γ' plates, a coherent $\Sigma 3$ twin is formed with a former $\{0001\}_{\text{hcp}}$ lattice plane as the twinning plane.

Indeed, in the areas of γ' composed of γ' plates with varying orientation within a former ϵ grain (see the encircled areas in the EBSD orientation maps in Figure 3.8), the γ' plates have a twin relationship to each other. Furthermore, those γ' plates and the grains of ϵ sitting above them fulfil the orientation relationship after Equation (3.1) (see the green and yellow lines connecting those grains in the EBSD orientation maps in Figure 3.8), supporting the interpretation that the areas of γ' with varying orientation have been formed by impingement of γ' plates within a single former ϵ grain.

3.4 Discussion

3.4.1 Microstructure after quenching

The microstructures developed at 853 K (as observed after quenching) are compatible with the phase diagram shown in Figure 3.1c, calculated as described in Section 3.1.1 EPMA measurements performed for the research presented in Chapter 2 on cross-sections of similar specimens allow sketching of the corresponding diffusion paths in Figure 3.1c. Evidently, these diffusion

paths are compatible with the calculated phase diagram. Thus, the concentrations of N and C in ϵ fall within the bottleneck-shaped area of the phase diagram. The occurrence of small γ' grains in the ϵ layer on Fe–C specimens nitrocarburised at 853 K as shown in Figure 3.2b and as also observed in the literature [96] and in Chapter 2 is possibly due to passing of the diffusion path through the $\gamma'+\epsilon$ two-phase field of the phase diagram.

In the above sense, the $\theta/\epsilon/\gamma$ triple layer on the α substrate of the Fe–N specimens nitrocarburised at 873 K and quenched thereafter, also complies with the calculated phase diagram (see the sketched, green diffusion path in Figure 3.1d and the enlarged part in Figure 3.1e). However, the ϵ/γ double layer growing into the $\alpha+\theta$ substrate of the Fe–C specimens at 873 K (as observed after quenching) is incompatible with the phase diagram as calculated using the data from Reference 43 (see the sketched, incomplete red diffusion path in Figure 3.1d and the enlarged part in Figure 3.1e), as this observation implies occurrence of a (local) equilibrium of γ , α and θ at the $\gamma/\alpha+\theta$ interface, which is impossible as long as the $\alpha+\epsilon$ two-phase field exists. This microstructure is only explainable if the temperature of the invariant reaction $\gamma+\theta \rightleftharpoons \alpha+\epsilon$ is lower than 873 K which is compatible with the very recent experimental results presented in Reference 82 (according to that work the temperature of the invariant reaction is between 868 K and 873 K) and the prediction of Reference 41 (867 K). In contrast, according to the model from Reference 43, the invariant reaction $\gamma+\theta \rightleftharpoons \alpha+\epsilon$ occurs at a temperature as high as 952 K.

It is noted that it has been suggested in a recent study dealing with plasma nitrocarburising of steels that $\gamma\text{-Fe[N,C]}$ would be a stable phase at a temperature as low as 843 K [145], which is in striking conflict with recent models of the system Fe–N–C [41, 43], the above mentioned recent experimental study [82] and the results of the present work. The authors of Reference [145] argue on the basis of Reference 146, based on Reference 147, which in turn is based on early experimental work on the system Fe–N–C [84]. However, there has been no evidence for the formation of γ at temperatures as low as 853 K and below both in the present work and in the various studies on the system Fe–N–C in the recent past [29, 75, 81, 82] (see also Chapter 2). It is suggested here that the temperature measurement during the plasma nitrocarburising treatments conducted in Reference 145 has been flawed.

3.4.2 Microstructure after cooling slowly

The morphology of the γ decomposition microstructure as observed in the present work for the slowly cooled specimens nitrocarburised at 873 K (Figure 3.3c and d; similar microstructures have been reported in References 143 and 145) can be interpreted as a combination of typical lamellar pearlite in the Fe–C system [136] and coarsened granular braunite in the Fe–N system [137]; in particular, see the enlarged micrograph in Figure 3.4. This microstructure sug-

gests a eutectoid decomposition of the ternary γ phase. Considering the sequence of invariant reactions as predicted by the data from References 41 and 43, eutectoid decomposition of γ occurs according to $\gamma \rightleftharpoons \alpha + \gamma' + \epsilon$ at 859 K [41] or 857 K [43], yielding a microstructure consisting of α , γ' and ϵ , explaining the formation of some ϵ grains in the decomposition microstructure. Formation of θ in a morphology that usually only occurs upon eutectoid decomposition (see Figure 3.4) could be explained by inhibition of ϵ formation. Theoretically, a metastable invariant reaction according to $\gamma \rightarrow \alpha + \gamma' + \theta$ could occur at 851 K [41] or 848 K [43].

The plate-like $\epsilon + \gamma'$ microstructure as an ϵ decomposition microstructure observed in the slowly cooled specimens (Figures 3.3 and 3.5) has already been reported by various authors in the past as resulting from slow cooling of Fe–N–C compound layers [143, 148–151]. The reason for the formation of the plate-like $\epsilon + \gamma'$ microstructure is the decreasing stability of ϵ with decreasing temperature: ϵ formed in equilibrium with α or $\alpha + \theta$ at 853 K (Figure 3.2a and b) or with γ at 873 K (Figure 3.2c and d) has a relatively low N content, as compared to typical N contents of the binary ϵ phase, and a high C content. The concentrations of N and C in the original pure ϵ (sub)layer adjacent to either the substrate or the γ sublayer lie in the bottleneck-shaped area of the phase diagram, illustrated by the diffusion paths superimposed on the isothermal sections of the phase diagram in Figure 3.1c and d. Additional EPMA measurements performed on these slowly cooled specimens showed that, as compared to the corresponding quenched specimens, the concentration-depth profiles and thus the composition along the diffusion path, i.e. the laterally averaged composition, had not changed significantly. Upon decreasing temperature, the composition of the originally pure ϵ (sub)layer comes to lie in a two- or three-phase field (Figure 3.1a and b versus Figure 3.1c and d), inducing decomposition of ϵ : the N and C concentration ranges of ϵ formed on the Fe–N substrates become located entirely in the $\gamma' + \epsilon$ two- or the $\alpha + \gamma' + \epsilon$ or $\gamma' + \epsilon + \theta$ three-phase fields, whereas the N and C concentration ranges of ϵ formed on the Fe–C substrates become only partially located in these two- or three-phase fields, leading to complete and incomplete decompositions in the first case and the latter case, respectively (as observed; see Figure 3.3a and c versus Figure 3.3b and d).

Formation of α was only observed in the decomposing (upon slow cooling) ϵ sublayer formed by nitrocarburising of the Fe–C substrates at 873 K (see Figure 3.5d). The models of References 41 and 43 predict that the total interstitial content of ϵ can be slightly lower at 873 K than at 853 K (see the bottleneck-shaped part of the ϵ single phase region in Figure 3.1c and d). Thus, cooling after nitrocarburising at 873 K can make the ϵ , which developed at this temperature, more or less instantaneously prone to decomposition in ϵ and α even before a poly-phase field involving the γ' phase is entered (see Figure 3.1d, c and b, in that order).

It is noted that a eutectoid microstructure resembling either pearlite or braunite clearly originating from decomposition of the ϵ phase has not been found (cf. end of Section 3.1.2). Thus, eutectoid decomposition of ϵ as predicted by the model from Reference 43 is improbable.

3.4.3 Microstructure after secondary annealing

The above interpretation of the microstructure after slowly cooling is confirmed by the secondary annealing experiments: for the original ϵ layers on the Fe–C specimens (see Figure 3.6c and d), *also only the part* of the ϵ layer adjacent to the substrate decomposes into a plate-like $\epsilon+\gamma'$ microstructure. The decomposed zone in ϵ is larger upon secondary annealing at 673 K than at 773 K. Indeed, the $\epsilon+\gamma'$ two-phase field extends to somewhat larger N contents at 673 K than at 773 K (as seen in the phase diagrams in Figure 3.1a and b). Thus, at 673 K the part of the originally pure ϵ sublayer with a composition falling in this two-phase field is larger, making a larger fraction of the originally pure ϵ (sub)layer unstable.

Formation of γ' plates requires diffusion of N and C in ϵ since ϵ contains less N than necessary for the formation of γ' and the solubility of C in γ' is very low (see Table 3.1). This necessity of diffusion explains the development of the fine morphology of the resulting microstructure: then the diffusion lengths are short. The plates in the Fe–N and Fe–C specimens resulting from secondary annealing at 673 K (Figure 3.6a and c) appear finer than those resulting from secondary annealing at 773 K (Figure 3.6b and d), which then is an obvious consequence of slower diffusion of N and C at lower temperatures.

The above discussion has been restricted to the stage of ϵ decomposition where all γ' plates are formed *within* a single ϵ grain. However, upon slow cooling and especially after long times of secondary annealing, massive γ' grains can also be observed that appear to extend across grain boundaries of the originally pure ϵ layer (see the grains marked with an arrow in the EBSD phase maps in Figure 3.5b and d). In contrast to the massive γ' grains formed by growth of γ' plates *within* the originally pure ϵ grains as described in Section 3.3, the morphology of γ' described here does *not* consist of plates. Furthermore, in this case, the orientation relationship given by Equation (3.1) is *not* satisfied between neighbouring γ' and ϵ grains (see the grains connected by red lines in the EBSD orientation maps in Figure 3.8): if, upon growing out of their parent ϵ grain (see the areas encircled in the EBSD phase maps in Figure 3.5b and d and the magnified example in Figure 3.5b) the orientation relationship is obeyed with the first ϵ grain, the orientation relationship is obviously not obeyed for the neighbouring ϵ grain and the grown-out γ' plate. These ϵ/γ' interface will be incoherent and thus relatively mobile. The grown-out parts of the γ' plates can thus relatively rapidly grow out to a more equiaxial (rounded) morphology and thus massive γ' grains develop.

According to the phase diagrams, it is not possible that the ϵ phase of compositions considered here upon cooling or secondary annealing transforms into γ' without that a carbon-rich phase, here θ , forms as well; see the diffusion paths in Figure 3.1. Indeed, upon prolonged secondary annealing, θ precipitates can be observed in the developed γ' sublayer (see the EBSD phase maps in Figure 3.8). Also upon slow cooling, an early stage of θ formation can already be detected, see the EBSD phase maps in Figure 3.5b and d.

Upon long secondary annealing times, eventually a closed γ' layer is formed underneath the ϵ layer and growing back into it, see the time-dependent development in Figures 3.7 and 3.8. This is comparable to the back-growth of γ' sublayers upon annealing of ϵ/γ' double layers formed by nitriding of pure Fe [152, 153]. Even in this very late stage of ϵ decomposition, the different growth rates of γ' grains formed by the coarsening of γ' plates within the original ϵ grain and of the massive γ' grains can be observed (see above discussion and Figure 3.8).

3.5 Conclusions

The constitution and microstructures of the carbonitride compound layer formed upon nitrocarburising of Fe–N and Fe–C specimens has been investigated for the nitrocarburised condition and for states of decomposition upon cooling and annealing at lower temperatures, in particular with a view to existing, fragmentary knowledge on the Fe–N–C phase diagram. The following conclusions can be drawn:

1. The diffusion paths determined on the as-quenched microstructures of the Fe–N specimens nitrocarburised at 853 K and 873 K and of the Fe–C specimens nitrocarburised at 853 K are compatible with the phase diagrams calculated using either the data from Reference 41 or the data from Reference 43. The microstructure formed upon nitrocarburising of Fe–C at 873 K is compatible with the thermodynamic description from Reference 41 and incompatible with the thermodynamic description from Reference 43.
2. Upon slow cooling or upon secondary annealing after quenching, ϵ decomposes into a fine plate-like microstructure consisting of ϵ and γ' with a strict orientation relationship. Formation of γ' plates is caused by the instability of ϵ at lower temperatures since its composition then lies in the $\gamma'+\epsilon$ two-phase or in the $\alpha+\gamma'+\epsilon$ or $\gamma'+\epsilon+\theta$ three-phase fields. Eventually, a closed γ' layer forms underneath the ϵ layer, growing back in the direction of the surface.
3. Upon slow cooling of Fe–C specimens nitrocarburised at 873 K, α forms at the former ϵ grain boundaries because upon cooling the composition of ϵ passes through the $\alpha+\epsilon$ two-

phase field (this is unlikely to happen for Fe–N specimens and for the Fe–C specimens nitrocarburised at lower temperature in view of the composition of the ϵ (sub)layer).

4. Due to slow precipitation kinetics, the thermodynamically required θ formation is only observed after long secondary annealing times, allowing rejection of (dissolved) C by γ' . After long annealing times, ϵ decomposes into a porous $\alpha+\theta$ microstructure due to development of N_2 (and its subsequent loss to the outer atmosphere).
5. Formation of γ has only been observed upon nitrocarburising at 873 K. Upon slow cooling, the γ phase undergoes eutectoid decomposition, leading to a microstructure of a morphology combining features of lamellar pearlite and coarsened granular braunite.

Acknowledgements

The authors would like to thank Dr. E. Bischoff and Dipl.-Ing. T. Steiner (both with the Max Planck Institute for Intelligent Systems) for performing the SEM and EBSD measurements.

Chapter 4

The $\alpha+\epsilon$ two-phase equilibrium in the Fe–N–C system – experimental investigations and thermodynamic calculations

Holger Göhring, Andreas Leineweber, Eric Jan Mittemeijer

The present work is dedicated to investigating the occurrence of the $\alpha+\epsilon$ equilibrium at temperatures typically applied for nitrocarburising treatments. To this end, pearlitic Fe–C specimens were treated between 823 K (550 °C) and 863 K (590 °C) in gaseous nitriding and gaseous nitrocarburising atmospheres, allowing control of the chemical potentials of N and C. Subsequently, the resulting compound-layer microstructures were investigated using light microscopy and X-ray diffraction. Thermodynamic calculations, adopting several models for the Fe–N–C system from the literature, were performed, showing significantly different predictions for both the sequence of the invariant reactions and their temperatures. Comparison of the experimental data and the theoretical calculations led to the conclusion that none of the models from the literature is able to realistically describe the experimentally observed constitution in the Fe–N–C system in the considered temperature range. Values/value ranges for the temperatures of the invariant reactions were obtained.

Table 4.1: Crystal structures and (ranges of) N and C content, x_N and x_C , of phases relevant for the present work according to References 19 and 25.

phase	space group	structure description	x_N /at.%	x_C /at.%
α -Fe[N,C]	$I\bar{m}\bar{3}m$	bcc Fe lattice, N and C on octahedral sites	<0.4	<0.1
γ -Fe[N,C]	$Fm\bar{3}m$	fcc Fe lattice, N and C on octahedral sites	<10.3	<9.1
γ' -Fe ₄ N _{1-z}	$Pm\bar{3}m$	fcc Fe lattice, N ordered on octahedral sites	19.4–20	<0.7
ϵ -Fe ₃ (N,C) _{1+x}	$P6_322$	hcp Fe lattice, N and C ordered on octahedral sites	15–33	<8
θ -Fe ₃ C	$Pnma$	orthorhombic, C in trigonal prisms of Fe	≈ 0	25

4.1 Introduction

4.1.1 Equilibrium, metastable equilibrium, local equilibrium

Phase equilibria of the Fe–N–C system have been studied extensively in the past. The first attempt to determine an isothermal section of the phase diagram (at 723 K (450 °C) and at 1×10^5 Pa) was performed by Jack [129]. Probably the most influential study on solid-state equilibria in this ternary system was performed by Naumann and Langenscheid [84]. They presented isothermal sections of the Fe–N–C phase diagram at 1×10^5 Pa between 773 K and 973 K (500 °C to 700 °C). This work was the main reference to the later reviews in References 147, 154, 155.

For an overview of the relevant phases in the system Fe–N–C, indicating crystallographic and compositional characteristics, as assembled from References 19 and 25, see Table 4.1. These phases have in common that at 1×10^5 Pa they are metastable with respect to decomposition into α -Fe or β -Fe (with low interstitial content), graphite and nitrogen gas. They can be stabilised *at the surface* of specimens by imposing specific chemical potentials of N and C at the surface of the specimen, e.g. by gaseous nitriding/nitrocarburising. Thus, in the sequel, with the term *equilibrium*, always a metastable equilibrium is meant. Note that similar remarks hold for the established Fe–N [4] and Fe–C [3] binary phase diagrams [1, 25, 133].

As in the present work, the experimental data for the phase constitution of the Fe–N–C system is usually obtained from gas nitrided or gas nitrocarburised specimens consisting originally of pure Fe or of Fe–N or Fe–C alloys. During these thermochemical surface treatment processes, and as a consequence of specific imposed chemical potentials of N and C in the gas phase, (further) N and C can be taken up into the specimen from the gas atmosphere. At intermediate stages, a diffusion zone, and if sufficiently high chemical potentials of N and C in the gas atmosphere prevail, as in the present work, a compound layer on top develop [1, 25]. Thus N and C concentration gradients occur in both the compound layer and the diffusion zone.

The corresponding microstructures do not represent the true equilibrium state for the entire specimen, as prescribed by its gross composition, the temperature and the pressure. However, it can be assumed [29] that at each depth below the surface local equilibrium with respect to the local, lateral gross composition, the temperature and the pressure is established, especially at the interfaces between the Fe–N–C solid-solution phases, i.e. the sublayer boundaries and the interface with the substrate. The phase constitution as a function of depth can be predicted using the concept of diffusion paths [72, 120–122]: the evolution of the (laterally averaged) composition as a function of depth allows to plot these composition data in a phase diagram at the temperature (and pressure) concerned, which data together constitute the diffusion path. If local equilibrium at each point of the diffusion path and thus at each depth in the specimen *separately*, prevails, the sequence of the phases developing within the compound layer and the diffusion path can be related with the corresponding phase diagram [72, 120, 122], e.g. see Reference 29.

4.1.2 Constitution and invariant reactions in the Fe–N–C system

At least at typical nitriding/nitrocarburising temperatures, an $\alpha+\epsilon$ equilibrium does not exist in the binary Fe–N phase diagram. However, in the additional presence of C, α/ϵ phase boundaries are often observed, indicating the presence of a local $\alpha+\epsilon$ equilibrium. Considering the experimental results presented in the “old” References 83 and 84, it is possible to deduce in retrospect that ϵ can occur in direct contact with α . In Reference 83, a micrograph (their Figure 3) was given, showing ϵ forming a network along α grain boundaries after prolonged nitrocarburising of Fe at 843 K (570 °C). In Reference 84, the conclusion that an $\alpha+\epsilon$ equilibrium does not occur is based on a single specimen treated at 853 K (580 °C), interpreted to contain γ . All other experimental data presented in Reference 84 at temperatures of 873 K (600 °C) and below can be compatible with the occurrence of an $\alpha+\epsilon$ equilibrium. In both references a possible occurrence of an $\alpha+\epsilon$ equilibrium was not recognized.

In later works [29, 75, 82, 85–96] (see also Chapter 2), microstructures with α and ϵ in direct contact were frequently found and recognized as such. On this basis, at present an equilibrium of α and ϵ is accepted and included in all recent thermodynamic models of the Fe–N–C system [39, 41, 43, 45–47]. The $\alpha+\epsilon$ equilibrium is of pronounced relevance for nitrocarburising of ferritic steels: by appropriate choice of the process parameters, it is possible to obtain a single phase ϵ layer in contact with the substrate, which corresponds to improved anti-corrosion, wear and tribological properties [1].

The sequence of invariant reactions in the Fe–N–C system possibly met upon cooling at $T \leq 1000$ K (727 °C) can be visualized in a Scheil reaction scheme [156–158] as shown in Fig-

ure 4.1. From the binary systems, the congruent transition c ($\text{Fe}-\text{N}$, $\epsilon \rightleftharpoons \gamma'$, 953 K (677 °C) [4]) as well as the well-established eutectoid reactions e_1 ($\text{Fe}-\text{C}$, $\gamma \rightleftharpoons \alpha+\theta$, 1000 K (727 °C) [3]), e_2 ($\text{Fe}-\text{N}$, $\epsilon \rightleftharpoons \gamma+\gamma'$, 923 K (650 °C) [4]) and e_3 ($\text{Fe}-\text{N}$, $\gamma \rightleftharpoons \alpha+\gamma'$, 865 K (592 °C) [4]) are inherited, giving rise to two-phase ($\gamma'+\epsilon$) and three-phase ($\alpha+\gamma+\theta$, $\gamma+\gamma'+\epsilon$, $\alpha+\gamma+\gamma'$; in that order upon decreasing temperature) fields in the ternary system. In the ternary system, at high temperatures, an equilibrium between γ and θ exists, vanishing upon cooling and being replaced by the $\alpha+\epsilon$ equilibrium via the U_1 invariant reaction, $\gamma+\theta \rightleftharpoons \alpha+\epsilon$. Upon further cooling, the γ phase vanishes via the ternary eutectoid reaction E_1 , $\gamma \rightleftharpoons \alpha+\gamma'+\epsilon$. Both reactions (U_1 and E_1) involving the γ phase have been investigated recently in an experimental study of the $\text{Fe}-\text{N}-\text{C}$ system [82]¹; the temperature of the invariant reaction U_1 , as first determined in Reference 82 to occur between 868 K and 873 K (595 °C to 600 °C) was confirmed in Chapter 3.

At even lower temperatures, the $\alpha+\epsilon$ equilibrium is replaced by an equilibrium between γ' and θ . This can occur via the invariant reaction U_2 . This sequence of invariant reactions is illustrated in the Scheil reaction scheme in Figure 4.1a and in the left part of Figure 4.2. However, in principle, this is only *one* of only *two* possibilities to realize the transition from the $\alpha+\epsilon$ equilibrium at higher temperature to the $\gamma'+\theta$ equilibrium at lower temperature, assuming that ϵ is the only phase existing in this temperature range with a considerable homogeneity range and that γ does not participate in the considered invariant reactions. The second possibility is shown in the Scheil reaction scheme in Figure 4.1b, which can be discussed considering the right part of Figure 4.2. Upon cooling, the ϵ single-phase field is divided into two separate ϵ single-phase fields at the temperature of the pseudo-binary eutectoid reaction [159] e_4 , $\epsilon \rightleftharpoons \gamma'+\theta$, giving rise to the $\gamma'+\theta$ two-phase field upon continued cooling. The ϵ single-phase field at relatively low interstitial content (see middle right part of Figure 4.2), with the $\alpha+\epsilon$ two-phase field, vanishes at lower temperature via the ternary eutectoid reaction E_2 , $\epsilon \rightleftharpoons \alpha+\gamma'+\theta$. In the following, the first series of invariant reactions is referred to as type I and the latter one as type II.

In Reference 75, pure α -Fe specimens nitrocarburised at 823 K (550 °C), resulting in a $\gamma'/\gamma'+\theta$ layer on top of the substrate, were subsequently annealed at higher temperatures (in steps of 10 K), leading to a microstructure with α in direct contact with ϵ at 843 K (570 °C) and above. Also, α -Fe specimens nitrocarburised at 853 K (580 °C), resulting in a γ'/ϵ layer on top of the substrate, were subsequently annealed at lower temperatures (in steps of 10 K). Thereby, the $\alpha+\epsilon$ equilibrium vanished at annealing temperatures of 833 K (560 °C) and below. It was concluded that the transitional reaction $\alpha+\epsilon \rightleftharpoons \gamma'+\theta$ occurs at a single temperature between 833 K and 843 K (560 °C to 570 °C) (reaction U_2 in Figures 4.1a and 4.2).

¹In Reference 82, the numbering of reactions U_1 and U_2 has been inverted.

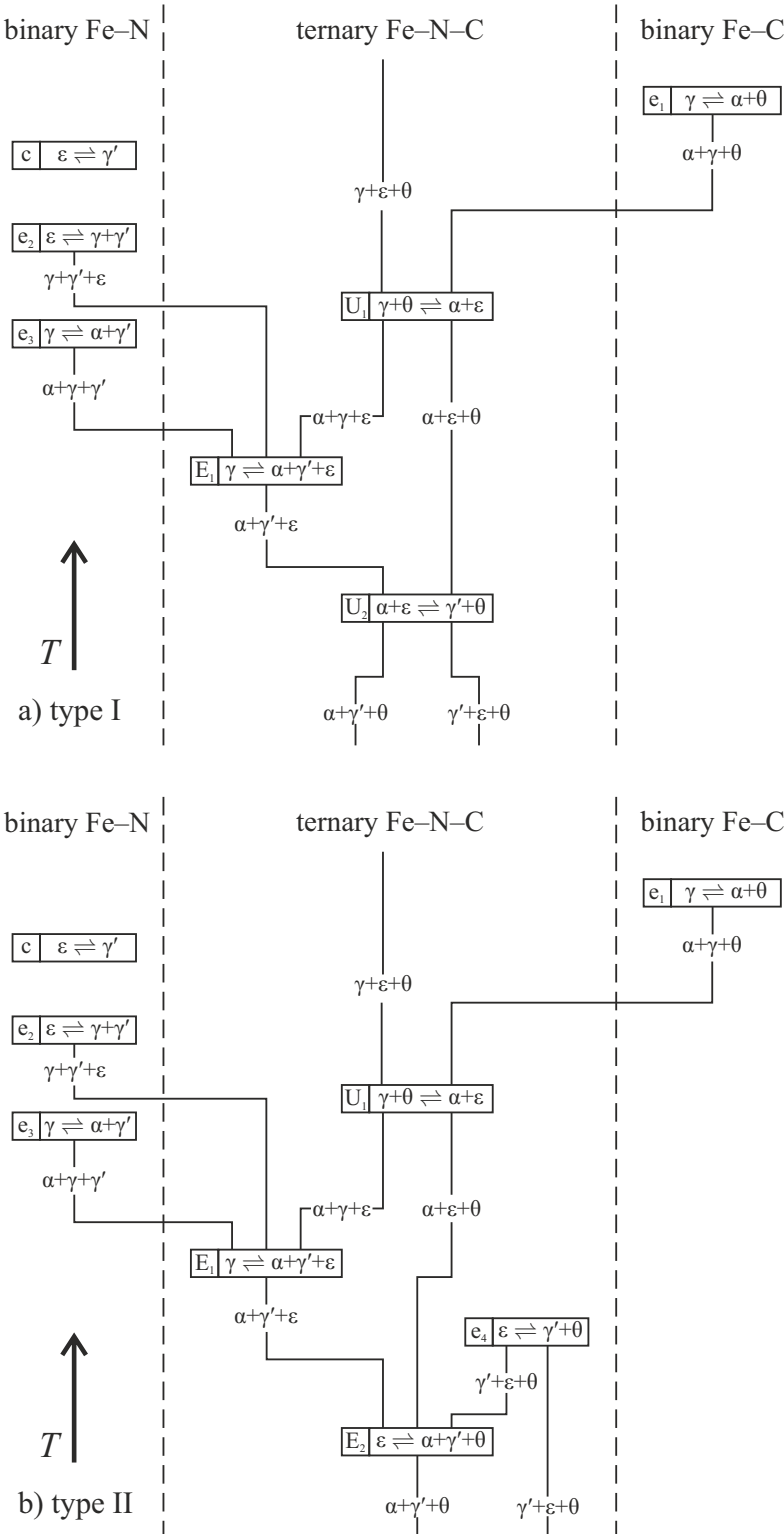


Figure 4.1: Schematic Scheil reaction schemes showing the two possibilities for the (sequence of) invariant reaction(s) leading from the $\alpha+\epsilon$ equilibrium to the $\gamma'+\theta$ equilibrium upon cooling, cf. Figure 4.2. Both Scheil reaction schemes comprise the c , e_1 , e_2 , e_3 , E_1 and U_1 invariant reactions. The invariant reaction U_2 is unique to the type I Scheil reaction scheme (a), whereas it is replaced by the reactions e_4 and E_2 in the type II Scheil reaction scheme (b).

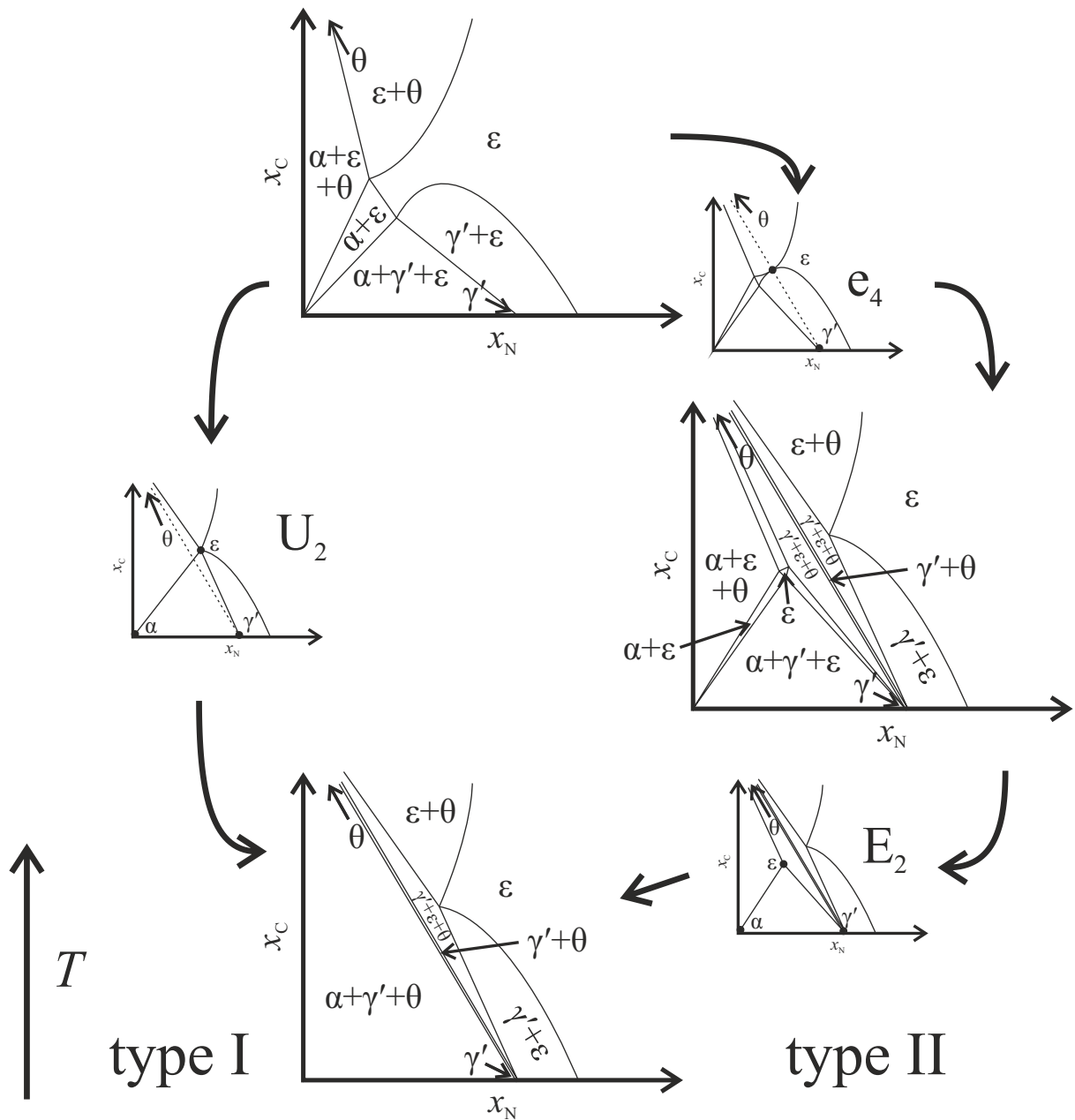


Figure 4.2: Schematic isothermal sections of the Fe–N–C phase diagram illustrating the two possibilities for the (sequence of) invariant reaction(s) in the system Fe–N–C leading to the replacement of the $\alpha+\epsilon$ equilibrium by the $\gamma'+\theta$ equilibrium upon cooling. At the temperatures of the invariant reactions e_4 , E_2 and U_2 , the compositions of the phases in equilibrium (e_4 : three phases; E_2 and U_2 : four phases; except the θ phase) have been indicated by solid dots. At these temperatures, two-phase equilibria existing above and below the invariant temperature have been indicated by solid and dashed lines, respectively. Left part: in the type I sequence of invariant reactions, the $\alpha+\epsilon$ equilibrium is directly replaced by the $\gamma'+\theta$ equilibrium via the transitional reaction U_2 , $\alpha+\epsilon \rightleftharpoons \gamma'+\theta$. Right part: in the type II sequence of invariant reactions, upon cooling, the $\gamma'+\theta$ equilibrium is introduced via the pseudo-binary eutectoid reaction e_4 , $\epsilon \rightleftharpoons \gamma'+\theta$, dividing the ϵ single-phase field into two separate ϵ single-phase fields, see the isothermal section of the phase diagram in the middle right part of the figure. The second ϵ single-phase field at low interstitial content vanishes via the ternary eutectoid reaction E_2 , $\epsilon \rightleftharpoons \alpha+\gamma'+\theta$.

The present work is a follow-up and distinct extension of the work performed in Reference 75. Deliberately, significantly different types of microstructures distinctly different from those produced in Reference 75 were generated in the current project by nitriding and nitrocarburising of pearlitic Fe–C alloys. The experimentally obtained results were compared to predictions from several existing thermodynamic models of the system Fe–N–C [39, 41, 43, 45–47]. Since the present work focuses on the $\alpha+\epsilon$ equilibrium, two informations are of paramount interest: (i) at which temperature the $\alpha+\epsilon$ equilibrium disappears and the $\gamma'+\theta$ equilibrium appears upon cooling (reaction U_2 or e_4 and E_2), and (ii) which sequence of invariant reactions (type I or type II) occurs upon cooling establishing the disappearance of the $\alpha+\epsilon$ equilibrium and appearance of the $\gamma'+\theta$ equilibrium. The temperature at which the $\alpha+\epsilon$ equilibrium disappears can be determined by choosing conditions that lead to unambiguous microstructures proving the presence of the $\gamma'+\theta$ equilibrium below and the $\alpha+\epsilon$ equilibrium above that temperature. To distinguish occurrence in reality of the sequence of invariant reactions of type I from the sequence of invariant reactions of type II is difficult: in principle, all microstructures featuring an $\alpha+\epsilon$ equilibrium are compatible with phase diagrams corresponding to the sequence of invariant reactions of type I above the temperature of the U_2 reaction, but also with phase diagrams corresponding to the sequence of invariant reactions of type II above the temperature of the E_2 reaction. The sequence of invariant reactions of type II can only be proven by the presence of both the $\alpha+\epsilon$ equilibrium and the $\gamma'+\theta$ equilibrium at a range of temperatures, i.e. between the temperatures of the e_4 and E_2 invariant reactions (see middle right part of Figure 4.2), whereas according to the sequence of invariant reactions of type I this can only occur at one temperature (the temperature of the U_2 invariant reaction). With this in mind, the experiments performed in the present work had been designed.

4.2 Thermodynamic considerations

4.2.1 Thermodynamics of interstitial solid solutions

The thermodynamics of the system Fe–N–C can be described by modelling the temperature and composition dependence of the Gibbs energy of each phase, e.g. using the Calphad approach [50]. In the past, this has been performed several times [39, 41, 43–47]. In the following, the Gibbs-energy models employed in these works [39, 41, 43–47] are introduced.

The phases in the system Fe–N–C can be regarded as interstitial solid solutions of N and C in an Fe lattice. Thus, the Gibbs energy of one formula unit of such a phase φ , $Fe_a(C,N,Va)_c$, where Va denotes a vacant site on the interstitial sublattice, and with integers a and c , the ratio of

which is determined by the crystal structure, can be described as (Hillert-Staffansson approach, also called compound-energy formalism [51, 52, 160])

$$G_m^\varphi = y_C^\varphi {}^o G_{Fe:C}^\varphi + y_N^\varphi {}^o G_{Fe:N}^\varphi + y_{Va}^\varphi {}^o G_{Fe:Va}^\varphi + cRT(y_C^\varphi \ln y_C^\varphi + y_N^\varphi \ln y_N^\varphi + y_{Va}^\varphi \ln y_{Va}^\varphi) + G^{\varphi,ex} + G^{\varphi,mag} \quad (4.1)$$

with y_C^φ , y_N^φ and y_{Va}^φ as the site fractions of C, N and Va on the interstitial sublattice, ${}^o G_{Fe:C}^\varphi$, ${}^o G_{Fe:N}^\varphi$ and ${}^o G_{Fe:Va}^\varphi$ as the standard Gibbs energy of the real or hypothetical compounds (“end members”) Fe_aC_c , Fe_aN_c and Fe_aVa_c with the crystal structure of the phase φ and in the state of no magnetic order (with Fe:C, Fe:N and Fe:Va denoting that the second, interstitial sublattice is fully occupied by C, N and Va, respectively), $G^{\varphi,ex}$ as the excess Gibbs energy and $G^{\varphi,mag}$ as the magnetic contribution.

The excess Gibbs energy can be modelled as

$$G^{\varphi,ex} = y_C^\varphi y_N^\varphi L_{Fe:C,N}^\varphi + y_C^\varphi y_{Va}^\varphi L_{Fe:C,Va}^\varphi + y_N^\varphi y_{Va}^\varphi L_{Fe:N,Va}^\varphi + y_C^\varphi y_N^\varphi y_{Va}^\varphi L_{Fe:C,N,Va}^\varphi \quad (4.2)$$

with the binary interaction parameters $L_{Fe:C,N}^\varphi$, $L_{Fe:C,Va}^\varphi$ and $L_{Fe:N,Va}^\varphi$ and the ternary interaction parameter $L_{Fe:C,N,Va}^\varphi$ ². Thereby, the binary interaction parameters can be expressed by a concentration-dependent Redlich-Kister series [57], e.g. for $L_{Fe:C,N}^\varphi$:

$$L_{Fe:C,N}^\varphi = \sum_{k=0}^n k L_{Fe:C,N}^\varphi (y_C - y_N)^k. \quad (4.3)$$

For the ternary interaction parameter $L_{Fe:C,N,Va}^\varphi$ a concentration dependence can also be introduced, which was, however, not applied in the cited thermodynamic models [39, 41, 43–47].

4.2.2 Comparison of thermodynamic descriptions – invariant reactions

The previous thermodynamic descriptions of the system Fe–N–C [39, 41, 43–47] provide values for the parameters as defined by Equations (4.1)–(4.3) obtained by fitting the model to experimental data. The differences between the various descriptions [39, 41, 43–47] boil down to different values (including the temperature dependence) adopted for some of the model parameters (e.g. equating them to values for corresponding parameters for the binary systems; for Fe–N from References 31, 37, 38, 40; for Fe–C from References 31, 32) and different numbers of to be fitted parameters.

²In References 39 and 43, the model for the ϵ phase has been formulated in the compound-energy formalism. Afterwards, the equations for the chemical potentials of Fe, N and C have been simplified. In order to correctly re-formulate the resulting model in the compound-energy formalism as done in the current work, a ternary interaction parameter is needed.

The first complete thermodynamic description of the system Fe–N–C [44] has been assembled from existing parameters for the binary and ternary systems from the literature [31, 161, 162] together with estimated parameters for the ternary system. This model was not intended as a stand-alone model for the system Fe–N–C, but rather as only a building stone for a thermodynamic model of the quaternary Fe–Cr–N–C system. Furthermore, this study was focused only at a single temperature of 1273 K (1000 °C), i.e. far out of the range of temperatures relevant for nitrocarburising (say, 773 K to 923 K (500 °C to 650 °C)). It is therefore perhaps not surprising that, adopting this model, a sequence of invariant reactions is predicted that differs pronouncedly from (especially recent) experimental data and from predictions obtained from more recent models [39, 41, 43, 45–47]. Thus, this model is not further considered in the present work.

Using values for the parameters of the Gibbs-energy equations, i.e. the Gibbs energies of the end members and the interaction parameters as defined by Equations (4.1)–(4.3), given in each of the References 39, 41, 43, 45–47, isothermal sections were calculated using Thermo-Calc [70] in the present work for each model [39, 41, 43, 45–47] at different temperatures in order to determine the sequence of invariant reactions. Subsequently, the temperatures of the invariant reactions were calculated by setting the amounts (and not the compositions) of the three or four phases participating in each of the invariant equilibria to a fixed value. It was found that the models from References 41, 45, 46 and 47³ lead to a type I series of invariant reactions, and the models from References 39 and 43 lead to a type II series of invariant reactions (cf. Section 4.1.2 and Figures 6.4 and 4.2). The temperatures of the invariant reactions as calculated using the models of References 39, 41, 43, 45–47 have been summarised in Table 4.2.

4.3 Experimental

The substrates used for the investigations in the present work were manufactured by casting an Fe–C alloy with a nominal composition corresponding to the eutectoid composition of the Fe–C system (approximately 3.5 at.%, see Reference 32 and Chapter 5) into ingots of dimensions 80 mm × 30 mm × 10 mm. The ingots were cold-rolled to a thickness of approximately 1 mm. The resulting sheets were cut into rectangular specimens of lateral dimensions of 20 mm × 12 mm and ground and polished (final step 1 µm diamond suspension). The specimens were encapsulated into fused silica tubes containing Ar at a pressure of 2×10^5 Pa in order to prevent

³Another series of invariant reactions than stated here was shown in the Scheil reaction scheme given in Reference 47, with the reactions U₁ and E₁ being degenerated, i.e. occurring at exactly the same temperature. However, using the actual Gibbs-energy equations of Reference 47 leads to the type I series of invariant reactions, albeit the calculated temperatures of the reactions U₁ and E₁ lie within 1 K.

Table 4.2: Temperatures in K of the invariant reactions (cf. Figure 4.1) as predicted by models for the system Fe–N–C in the literature and as experimentally determined in Reference 82 (invariant reactions c, e₂, E₁ and U₁), Reference 30 (invariant reaction e₃) and in the present work (invariant reaction U₂ for type I model, invariant reactions e₄ and E₂ for type II model). Matches between the calculated and experimentally determined data are marked with an asterisk.

	Slycke [45]	Kunze 1990 [39]	Du/Hillert [46]	Du [41]	Kunze 1996 [43]	SGTE [47]	experimental data
Type	I	II	I	I	II	I	I/II
c	964	954 ^(*)	970	971	955 ^(*)	972	938–948 [82]
e ₁	1000	1000	1000	1000	1000	1000	—
e ₂	922 [*]	921	923 [*]	923 [*]	923 [*]	917	923–925 [82]
e ₃	865 [*]	868 [*]	863 [*]	863 [*]	867 [*]	864 [*]	866 ^a [30]
e ₄		832			833	840–844	this work
E ₁	858 [*]	858 [*]	849	859 [*]	857 [*]	848	853–863 [82]
E ₂		825			825	840–844	this work
U ₁	863	954	853	867 [*]	952	849	868–873 [82]
U ₂	824		821	783		841 [*]	842±2 this work

^aNo error margin given

oxidation during the subsequent heat treatment. The specimens were treated at 1273 K (1000 °C, in the γ phase-field range) and cooled by putting the fused silica tube on a metallic surface at room temperature. Thereby, a fine pearlitic microstructure with a lamella spacing < 1 μm was achieved.

The pearlitic specimens were nitrided or nitrocarburised in a fused silica tube furnace which is equipped with mass-flow controllers for the gas supplies of NH₃, H₂, CO, CO₂, H₂O and CH₄ (the latter not used in the present work). The composition of the gas atmosphere can be varied precisely in order to control the chemical potentials of N and C in the gas atmosphere recognizing the simultaneous occurrence of several nitriding and carburising reactions [23–25]. By applying a high flow rate (500 ml min⁻¹), the composition of the gas atmosphere remains constant. In an ideal case, thus, a local equilibrium at the surface of the specimen is achieved. Often, however, a steady state [1, 29, 30] prevails at the surface.

The experimental conditions applied in the present work were selected in order to investigate which solid-state equilibria are established at the treatment temperature. Temperatures between 823 K and 863 K (550 °C to 590 °C) were applied. In the most interesting temperature range of 838 K to 848 K (565 °C to 575 °C) (see Section 4.4), a temperature increment of 1 K was chosen and multiple experiments were performed at each temperature. The temperature was controlled within 1 K. Two different types of atmospheres were chosen, leading to distinctly

Table 4.3: Temperatures, treatment times, composition of gas atmospheres applied for nitrocarburising (series NC) and nitriding (series N) treatments and resulting N activity (reference state N₂ gas at 1×10^5 Pa) and C activity (reference state graphite at 1×10^5 Pa) as calculated using the data from Reference 26. $\phi_i = p_i / {}^\circ p$, with p_i as partial pressure of component i and ${}^\circ p = 1 \times 10^5$ Pa.

series	T /K	t /h	ϕ_{NH_3}	ϕ_{H_2}	ϕ_{CO}	ϕ_{CO_2}	$\phi_{\text{H}_2\text{O}}$	a_{N}	a_{C}
NC	863	4, 16	0.20	0.34	0.40	0.05	0.01	605	50
	858	4, 16	0.20	0.34	0.39	0.05	0.02	579	50
	853	4, 16	0.20	0.34	0.38	0.06	0.02	554	50
	848	4, 16	0.20	0.34	0.37	0.07	0.02	506	50
	847	4	0.20	0.34	0.37	0.07	0.02	525	50
	846	4	0.20	0.34	0.32	0.10	0.03	520	25
		4	0.20	0.34	0.37	0.07	0.02	520	50
	845	4	0.20	0.34	0.32	0.10	0.03	525	25
		4	0.20	0.34	0.37	0.07	0.02	515	50
	844	4	0.20	0.34	0.32	0.10	0.04	511	25
		4	0.20	0.34	0.37	0.07	0.02	511	50
	843	4	0.20	0.34	0.32	0.11	0.04	506	25
		4, 6, 16	0.20	0.34	0.37	0.07	0.02	506	50
	842	4	0.20	0.34	0.31	0.11	0.04	501	25
		4	0.20	0.34	0.36	0.07	0.02	501	50
	841	4	0.20	0.34	0.31	0.11	0.04	497	25
		4	0.20	0.34	0.31	0.11	0.04	497	50
	840	4	0.20	0.34	0.36	0.08	0.02	492	50
	839	4	0.20	0.34	0.36	0.08	0.02	488	50
	838	4, 16	0.20	0.34	0.36	0.08	0.02	483	50
	833	4, 16	0.20	0.34	0.35	0.08	0.02	461	50
	828	4, 16	0.20	0.34	0.34	0.09	0.03	440	50
	823	4, 16	0.20	0.34	0.33	0.10	0.03	420	50
N	848–838	4	0.51	0.49				794–725	

different types of compound-layer microstructures. The values of the experimental parameters for all experiments, together with the resulting thermodynamic activities of N (reference state N₂ gas at 1×10^5 Pa) and C (reference state graphite at 1×10^5 Pa) [24, 25] as calculated using the data for the Gibbs energies of the gaseous species given in Reference 26, have been given in Table 4.3. Except for a few cases, a treatment time of 4 h was applied.

The first experimental series (labelled NC in Table 4.3) was performed using nitrocarburising atmospheres at temperatures in the range 838 K to 848 K (565 °C to 575 °C) with specific activities of N (400–600) and C (25–50). At 853 K (580 °C) the formation of pure ϵ layers in contact with the pearlitic substrate was observed (see Chapter 2), corresponding to the (schematic) dif-

fusion path labelled NC in Figure 4.3a. Additional experiments with lower N activities in the temperature range of 838 K to 848 K (565 °C to 575 °C) led to thin, inhomogeneous compound layers that could not be investigated.

The second experimental series (labelled N in Table 4.3) was performed at temperatures in the range of 838 K to 848 K (565 °C to 575 °C) using a pure nitriding atmosphere ($\text{NH}_3\text{-H}_2$ mixture), corresponding to N activities between 720 and 800. At 853 K (580 °C), this led to the formation of an $\epsilon/\gamma'/\epsilon$ triple layer on the pearlitic substrates (see Chapter 2), corresponding to the diffusion path labelled N in Figure 4.3a.

Qualitative phase analysis of the specimens was performed by X-ray diffraction in Bragg-Brentano $\theta\text{-}\theta$ geometry, employing a Philips X'Pert MPD equipped with a Co tube and a secondary monochromator, selecting the Co K_α radiation. The resulting diffraction patterns were analysed by Rietveld refinement using the appropriate crystal-structure models for all considered phases (see Table 4.1), applying the software TOPAS [139]. This was done in favour of using the fixed peak-position values from databases as e.g. provided by ICDD that cannot be applied to the ϵ phase which has strongly varying (composition-dependent) values of the lattice parameters.

For light-microscopic analysis of the nitrocarburised specimens, cross-sectional samples were prepared by cutting a part from each specimen. This sample was electrolytically coated with Ni in a Watt's bath, to produce a ductile protective layer on top of the brittle compound layer. This sample was then embedded in resin, ground and polished (final stage 1 μm diamond suspension) and finally etched with 1 % Nital containing some HCl according to Reference 90 and 123. The specimens were treated with Groesbeck solution, i.e. an alkaline KMnO_4 solution which stains C-rich phases [124]. Thereby, the distinction of θ , ϵ and γ' (in order of decreasing C content) is facilitated. The light-microscopical analysis was performed using a ZEISS Axiophot microscope. In all cases, the presence of phases as recognized in the optical micrographs was verified by analysing the X-ray diffraction patterns.

4.4 Results of experimental investigation

4.4.1 Nitrocarburizing of Fe–C alloys

The compound layer resulting from nitrocarburising of the Fe–C alloy at $T > 848\text{ K}$ (575 °C) consists of a pure ϵ layer growing into the $\alpha+\theta$ substrate, corresponding to the schematic diffusion path labelled NC in Figure 4.3a. Even after the treatments at 863 K (590 °C), no sign of γ formation was observed. By gaseous nitrocarburising at $T < 838\text{ K}$ (565 °C), an $\epsilon/\gamma'+\theta$ double layer growing into the $\alpha+\theta$ substrate is induced, corresponding to the schematic diffusion path

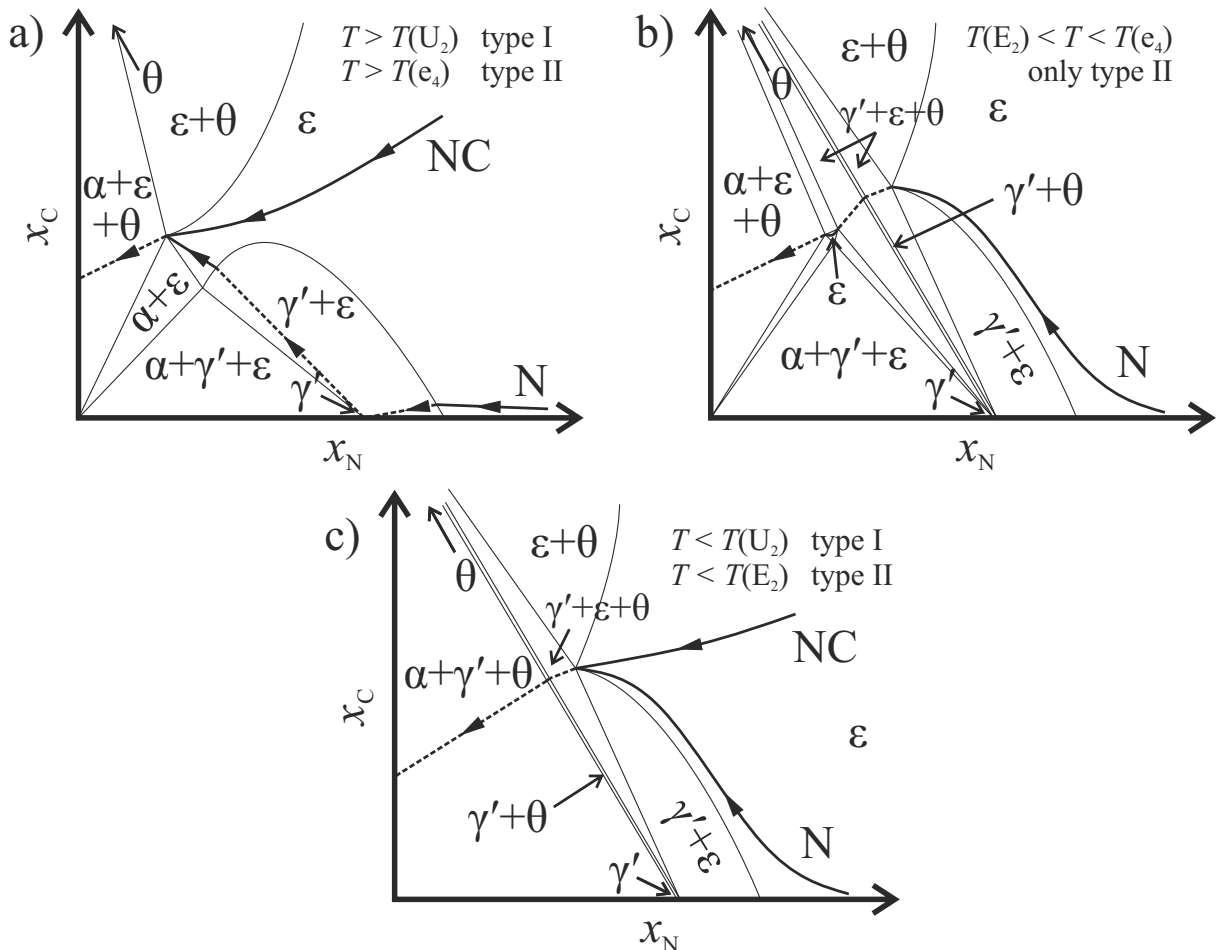


Figure 4.3: Schematic diffusion paths superimposed on isothermal sections of the phase diagram of the Fe–N–C system (cf. Figure 4.2). Hereby, dashed lines indicate skipping over a two- or three-phase field. a) Diffusion paths corresponding with the microstructures resulting from nitrocarburising of the Fe–C alloy above 848 K (NC) and nitriding of the Fe–C alloy above 847 K (N) superimposed on an isothermal section of the phase diagram at a temperature above the temperature of the U_2 (type I) or e_4 (type II) invariant reaction. b) Hypothetical, schematic diffusion path corresponding with an $\epsilon/(\gamma'+\theta)/\epsilon$ triple layer microstructure which is only possible for a type II series of invariant reactions between the temperatures of the e_4 and the E_2 invariant reactions. c) Diffusion paths corresponding with the microstructure resulting from nitrocarburising (NC) or nitriding (N) of the Fe–C alloy below 838 K superimposed on an isothermal section of the phase diagram at a temperature below the temperature of the U_2 (type I) or E_2 (type II) invariant reactions.

labelled NC in Figure 4.3c. At intermediate temperatures between 838 K and 848 K (565 °C to 575 °C), transitional microstructures, i.e. in-between the two described ones, occur. Thus, the microstructures were classified into five types on the basis of the observations made for increasing nitrocarburising temperature (from 838 K to 848 K (565 °C to 575 °C)). Representative examples of all types of microstructures are shown in Figure 4.4. Type A (Figure 4.4a) refers to the microstructure that *also* occurs below 838 K (565 °C, see above): an ϵ sublayer separated from the substrate by a $\gamma' + \theta$ sublayer. Type B microstructures (Figure 4.4b) show isolated locations where the $\gamma' + \theta$ sublayer becomes penetrated by ϵ grains (see e.g. the encircled area in Figure 4.4b), which has been pronouncedly realized in type C microstructures (Figure 4.4c), where many ϵ grains are in direct contact with the substrate. In the type D microstructure (Figure 4.4d) the original $\gamma' + \theta$ sublayer then has become a $\gamma' + \epsilon$ sublayer. Finally (see also above), a single phase ϵ layer results (type E, Figure 4.4e), possibly containing some (retained) γ' and θ “impurities”.

In contrast to what is suggested by the above presentation of a transitional series of microstructures of the compound layer, microstructural analysis (in lateral directions) of the whole cross section of the compound layers, obtained by nitrocarburising at temperatures from 838 K to 848 K (565 °C to 575 °C), revealed that the microstructure of the compound layer, also over the substrate of a single specimen, was often found to vary in lateral directions, i.e. more than one type of microstructure then could be identified in a single compound layer⁴. Therefore, for each compound layer, all detected microstructure types were recorded. The results of this analysis have been listed in Table 4.4. Thereby, it becomes clear, despite the microstructural variation in each compound layer, that starting from lower temperatures and going to higher temperatures, the microstructure of the compound layer gradually changes from type A to type E.

4.4.2 Nitriding of Fe–C alloys

In general, the microstructure of the compound layer resulting from nitriding of the Fe–C alloy is much more laterally uniform than that obtained upon nitrocarburising (see discussion in Section 4.5.1). The compound-layer microstructures after nitriding at 838 K, 841 K, 844 K and 848 K (565 °C, 568 °C, 571 °C and 575 °C) are shown in Figure 4.5. The microstructure obtained at 838 K (565 °C) resembles the type A microstructure resulting from nitrocarburising of the Fe–C alloy, see Figure 4.5a: a (in this case of pure nitriding, more porous) ϵ sublayer is

⁴A section adjacent to the edge of the specimen was ignored due to the possibility of inward diffusion of N and C from more than one side, leading to edge effects [29]. However, the microstructural transitions present there were compatible with those found in the investigated part of the specimen.

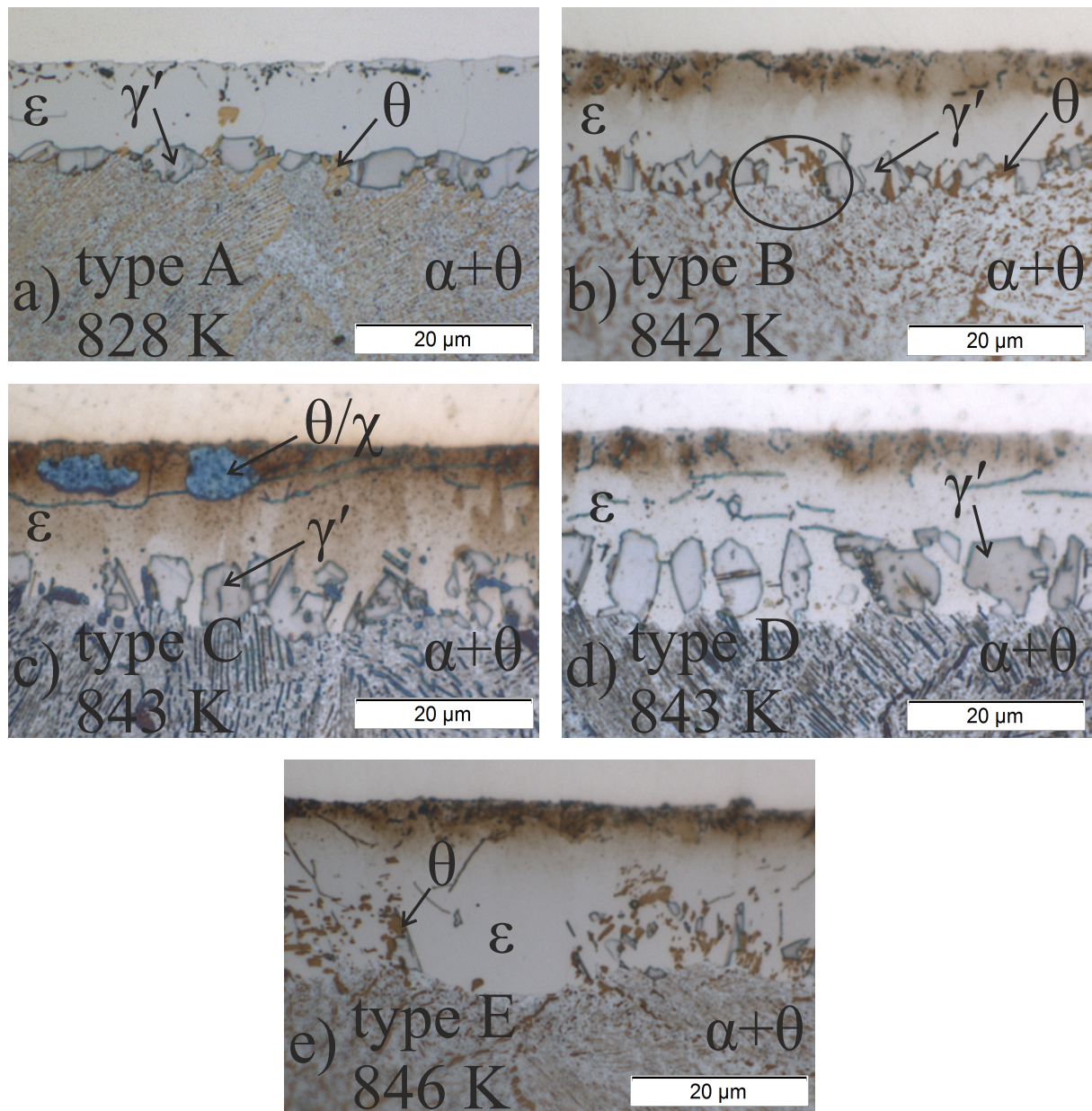


Figure 4.4: Micrographs of cross-sections showing examples of the typical microstructures occurring upon nitrocarburising between 838 K and 848 K. The treatment temperature of the specimens from which the shown examples were taken has been indicated in each micrograph. All specimens were treated for 4 h. a) ϵ separated from substrate by a $\gamma'+\theta$ sublayer. b) The $\gamma'+\theta$ sublayer becomes penetrated by ϵ grains at some places, e.g. in the encircled area. c) γ' , ϵ and θ in contact with the substrate. d) ϵ growing around γ' grains, no θ present. e) ϵ layer, possibly containing γ' and θ impurities.

Table 4.4: Microstructure types (cf. Figure 4.4 and its discussion) obtained by nitrocarburising of Fe–C substrates at different temperatures.

T/K	number of specimens	A	B	C	D	E
848	3			(x) ^a	x	x
847	1					x
846	2				x	x
845	1				x	x
844	2			x	x	x
843	5	(x) ^b	x	x	x	
842	2		x	x	x	
841	2	x	x	x		
840	1	x	x	x		
839	1	x	x			
838	3	x	x			

^a1 of 3 specimens

^b2 of 5 specimens

separated from the substrate by a γ' + θ sublayer, corresponding to the diffusion path labelled N in Figure 4.3c. In contrast to the nitrocarburising experiments, only at temperatures of 840 K (567 °C) and higher single ϵ grains penetrate the γ' + θ sublayer (Figure 4.5b). The penetration of ϵ into the γ' + θ sublayer at temperatures of 840 K (567 °C) and higher (cf. Figure 4.5b) appears to be the initiation of the development of a final $\epsilon/\gamma'/\epsilon$ microstructure with a closed γ' sublayer at $T \geq 847$ K (574 °C, Figure 4.5d) in agreement with results obtained at 853 K (580 °C) in Chapter 2, corresponding to the schematic diffusion path labelled N in Figure 4.3a. At an intermediate stage, an $\epsilon/(\gamma'+\epsilon)/\epsilon$ compound layer is found (see Figure 4.5c), comparable to the microstructures presented in Reference 88, featuring already a closed ϵ sublayer in contact with the $\alpha+\theta$ substrate.

4.5 Discussion

4.5.1 Development of the compound-layer microstructure between 823 K and 863 K (550 °C and 590 °C)

As an ageing phenomenon, formation of pores in the oldest part of the compound layer, i.e. in the surface adjacent region [25], occurs by decomposition of the metastable ϵ phase into N_2 and/or Fe carbides such as θ or monoclinic χ (Hägg carbide) [19] and/or the formation of

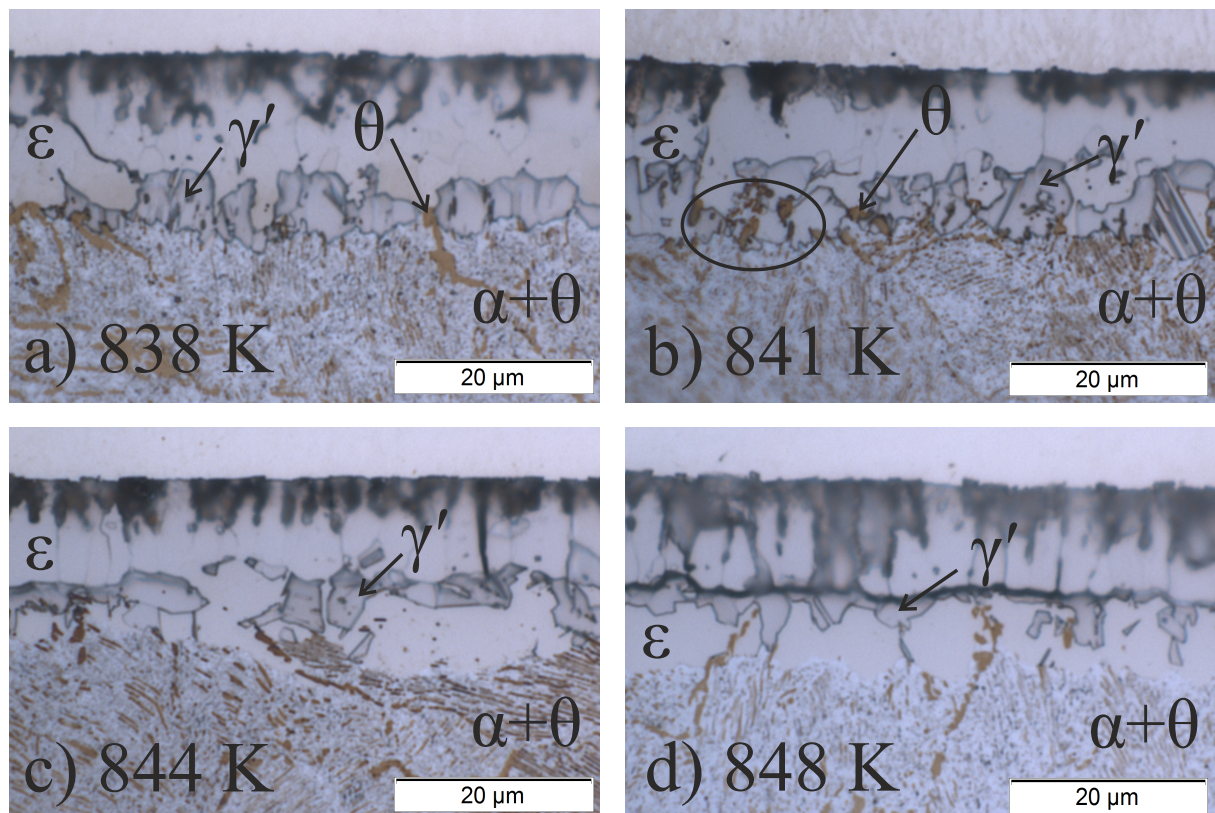


Figure 4.5: Micrographs of cross-sections showing examples of the typical microstructures resulting from nitriding of the Fe–C alloy at 838 K, 841 K, 844 K and 848 K. a) porous ϵ separated from the substrate by a $\gamma'+\theta$ sublayer. b) The $\gamma'+\theta$ sublayer becomes penetrated by ϵ at some places, e.g. in the encircled area. c) An $\epsilon/\alpha+\theta$ interface microstructure, showing establishment of $\alpha+\epsilon$ equilibrium; γ' sublayer forming in the middle of the compound layer. d) An $\epsilon/\gamma'/\epsilon$ triple layer microstructure.

channels and subsequent further reactions with the nitrocarburising atmosphere [92] (see also Chapters 2 and 3). This decomposition process needs no further discussion here.

As discussed elsewhere [25, 29], whereas local solid-solid equilibria can occur at each depth, corresponding to the local gross (laterally averaged) composition, within the compound layer, this may not occur at the gas-solid interface, i.e. at the surface of the compound layer, where moreover at most a stationary state may be established [1, 30]. Then, recognizing that in gaseous nitrocarburising, as compared to gaseous nitriding, distinctly more reactions participate at the gas/solid interface [23, 24], it may be understood that the microstructures obtained upon nitriding are more uniform than those obtained upon nitrocarburising (cf. Sections 4.4.1 and 4.4.2).

Above the temperature of 848 K (575 °C) for the nitrocarburising experiments and 844 K (571 °C) for the nitriding experiments, the compound layer contains a continuous ϵ layer (sometimes with small inclusions of γ' and/or θ) in contact with the $\alpha+\theta$ substrate over the whole specimen, see Figure 4.4e, Figure 4.5d and Table 4.4. This is compatible with an $\alpha+\epsilon+\theta$ three-phase equilibrium at the layer/substrate interface. Since the $\alpha+\epsilon+\theta$ three-phase field must be bounded by three two-phase fields, including the $\alpha+\epsilon$ two-phase field, this implies the occurrence of the $\alpha+\epsilon$ equilibrium. These microstructures correspond to the schematic diffusion paths labelled NC (nitrocarburising) or N (nitriding) in Figure 4.3a. They are qualitatively in agreement with the phase diagram resulting from any of the considered models [39, 41, 43, 45–47], i.e. at a temperature both (i) above the temperature of the invariant reaction U_2 for type I models and above the temperature of the invariant reaction e_4 for type II models and (ii), for both types of models, below the temperature of the invariant reaction U_1 . The here observed lowest values of the temperatures at which pure ϵ layers occur on the $\alpha+\theta$ substrate are compatible with the temperatures of the U_2 (type I) or e_4 (type II) reactions of all models from the literature [39, 41, 43, 45–47] (cf. Table 4.2).

Theoretically, it seems possible that a pure ϵ layer in contact with the $\alpha+\theta$ substrate already occurs at a temperature between the temperature of the E_2 and the e_4 invariant reactions of the type II models; see the second, small triangularly shaped ϵ single-phase field, appearing upon heating through the invariant reaction E_2 (see right part of Figure 4.2). Then, the concentrations of N and C in the entire ϵ layer must be at least within a compositional triangle connecting pure Fe and the (hypothetical) stoichiometric compounds Fe_4N and Fe_3C , being the upper limits of the homogeneity ranges of the binary γ' and θ phase, respectively. EPMA data collected from ϵ layers growing into Fe–C substrates at 853 K (580 °C), as presented in Chapter 2, rule out this possibility: the measured diffusion path starts at high N and C contents and passes through the bottle-neck shaped area of the phase diagram (see the diffusion path labelled NC in Figure 4.3a), thereby crossing the line connecting the Fe_4N and Fe_3C compositions. Therefore, at least at the

temperature of 853 K (580 °C), one large ϵ single-phase field (i.e. not two separate ones as for a type II model between the temperatures of the e_4 and E_2 invariant reactions; see the middle right part of Figure 4.2) must be present.

The microstructure of the compound layer resulting from nitrocarburising of Fe–C below 838 K (565 °C) and from nitriding of Fe–C at 838 K (565 °C) consists of an ϵ sublayer separated from the $\alpha+\theta$ substrate by a $\gamma'+\theta$ sublayer in contact with the $\alpha+\theta$ substrate (see Figure 4.4a, Figure 4.5a and Table 4.4). This is compatible with an $\alpha+\gamma'+\theta$ three-phase equilibrium at the layer/substrate interface, and, following the same considerations as above, also implies the existence of a $\gamma'+\theta$ two-phase field. This microstructure corresponds to the schematic diffusion path labelled NC in Figure 4.3c and thus is qualitatively in agreement with the phase diagram resulting from any of the investigated models for the system Fe–N–C [39, 41, 43, 45–47] at a temperature below the temperature of the U_2 invariant reaction (type I model) or the E_2 reaction (type II model), cf. Section 4.1.2 and Figures 4.1 and 4.2. However, also considering the as-predicted values for the temperatures of these invariant reactions (see Table 4.2), the occurrence of this microstructure at 838 K (565 °C) is only compatible with the model from Reference 47 with a predicted U_2 invariant reaction temperature of 841 K (568 °C) and incompatible with the models from References 39, 41, 43, 45, 46. Upon cooling the $\alpha+\epsilon$ equilibrium (see the $\alpha+\epsilon$ two-phase field in the top part of Figure 4.2) disappears already at higher temperatures than predicted by most of the models from the literature [39, 41, 43, 45, 46], which is in agreement with earlier findings by our group as presented in Reference 75.

The microstructures of type B, C and D (cf. Figures 4.4b–d and Table 4.4) resulting from nitrocarburising of the Fe–C alloy at temperatures between 838 K and 848 K (565 °C to 575 °C) are intermediates of type A and type E microstructures. The same holds for the microstructures obtained by nitriding of the Fe–C alloy between 840 K and 844 K (567 °C to 571 °C). Hence in the temperature range between 840 K and 844 K (567 °C to 571 °C), at the (more or less defined) interface between the compound layer and the substrate four phases (α , γ' , ϵ , θ) are in contact with each other. However, according to Gibbs' phase rule [133, 163], an $\alpha+\gamma'+\epsilon+\theta$ four-phase equilibrium is only possible at a single temperature (and at constant pressure), which here is the temperature of either the invariant reaction U_2 for type I models or the invariant reaction E_2 for type II models (see Figure 4.2). It is therefore concluded that the microstructures of types B, C and D represent *non-equilibrium* states. The difficulty of establishing equilibrium so close to the temperature of an invariant reaction is obvious: in that case, the Gibbs energy of the four-phase microstructure differs only a little from the Gibbs energy of the genuine two-phase or three-phase equilibrium states, and thus, the driving force and consequently the transformation rates are vanishingly small. By performing additional experiments in this

project, where the specimens were treated over night, no equilibrium microstructure was established (i.e. microstructures of the types B, C, D occurred with four phases in contact at the compound-layer/substrate interface).

4.5.2 The $\alpha+\epsilon$ two-phase field – nature of the invariant reactions and their temperatures

Grains of γ' in contact with θ occur at or below a temperature of 846 K (573 °C) in the nitrocarburised specimens (microstructure type D, for an example see Figure 4.4d, cf. Table 4.4) and at or below a temperature of 844 K (571 °C, see Figure 4.5c) in the nitrided specimens. Assuming local equilibrium at the compound-layer/substrate interface this then is the highest possible value of the temperature of either the invariant reaction U_2 (type I models) or the invariant reaction e_4 (type II models).

Grains of ϵ in contact with the $\alpha+\theta$ substrate appear at or above 838 K (565 °C) according to the results from the nitrocarburising experiments (microstructure type B, for an example see Figure 4.4b, cf. Table 4.4), and at or above 840 K (567 °C) according to the results from the nitrided specimens. On the basis of a similar reasoning as above, this then is the lowest possible value for the temperature of either the U_2 invariant reaction (type I model) or the E_2 invariant reaction (type II model).

The results from the nitriding experiments imply that the invariant reaction(s), U_2 (type I models) or e_4 and E_2 (type II models), leading upon decreasing temperature to the disappearance of the $\alpha+\epsilon$ equilibrium and the occurrence of the $\gamma'+\theta$ equilibrium, occur within the range of 840 K to 844 K (567 °C to 571 °C). The equivalent temperature range resulting from the nitrocarburising experiments is larger (838 K to 846 K (565 °C to 573 °C)). However, in principle, the only few places where ϵ is in contact with the substrate for the non-equilibrium microstructures of type B (see Figure 4.4b) and the only few places in which γ' is in contact with the substrate for the non-equilibrium microstructures of type D (see Figure 4.4d) can be considered as kinetic artefacts (see discussion in Section 4.5.1). This leaves the temperatures at which type C microstructures occur as the temperature range in which the invariant reactions U_2 (type I models) or e_4 and E_2 (type II models) occur (840 K to 844 K (567 °C to 571 °C)), see Table 4.4, confirming the results from the nitriding experiments.

A conclusive proof of a type II series of invariant reactions would be the occurrence of two separate $\gamma'+\epsilon+\theta$ three-phase equilibria, which is only compatible with the phase diagram for a type II model between the temperatures of the invariant reactions E_2 and e_4 . This could, under the assumption of local equilibrium, be indicated by e.g. the occurrence of the an $\epsilon/(\gamma'+\theta)/\epsilon$ triple-layer microstructure as illustrated by the diffusion path in Figure 4.3b: starting in and

passing through (full line) the ϵ single-phase field at high interstitial content, it skips over the first $\gamma'+\epsilon+\theta$ three-phase field (dashed line), reaching the $\gamma'+\theta$ two-phase field. After passing through the narrow $\gamma'+\theta$ two-phase field (full line), it skips over the second $\gamma'+\epsilon+\theta$ three-phase field (dashed line), passes through the second ϵ single-phase field (full line) and finally ends by skipping over the $\alpha+\epsilon+\theta$ three-phase field (dashed line) to the $\alpha+\theta$ two-phase field (close to the abscissa in Figure 4.3b). Such a microstructure could not be obtained experimentally, as any other conceivable microstructure pointing to exclusively a sequence of invariant reactions of the type II model. Moreover, and as mentioned in Section 4.5.1, under the assumption of local equilibrium, the available EPMA data from specimens treated at 853 K (580 °C) are incompatible with the presence of an isolated second ϵ single-phase field in the phase diagram at least at that temperature, as would be possible between the temperature of the E_2 and e_4 invariant reactions according to the type II models. On the other hand, the actual concentration values close to the compound-layer/substrate interface, as determined in Chapter 2, lie clearly within the already mentioned compositional triangle Fe–Fe₄N–Fe₃C. This could then be explained with a phase diagram of a type II model only a few K above the temperature of the e_4 invariant reaction.

If local equilibrium prevails, the transitional microstructure obtained upon nitriding of the Fe–C alloy at 844 K (571 °C, see Figure 4.5c) also indicates that at this temperature, two isolated ϵ single-phase fields cannot exist: under local equilibrium conditions, the sublayer morphology $\epsilon/(\gamma'+\epsilon)/\epsilon$ is only possible if the $\gamma'+\theta$ two-phase field in the Fe–N–C phase diagram has already vanished at this lower temperature.

All results in the present work show that it is difficult to reach equilibrium under the applied conditions, especially in the temperature range of 838 K to 848 K (565 °C to 575 °C) in which transitional microstructures occurred, clearly deviating from equilibrium. In general, also if a microstructure complies with Gibbs' phase rule, an equilibrium state is thereby not proven. Thus, the above observations pointing towards either a type I or type II series of invariant reactions could also be explained by kinetic effects.

Thermodynamics can predict a sharp transition between microstructures in which α is in contact with ϵ at higher temperature to microstructures in which γ' is in contact with θ at lower temperature (in this work at the compound-layer/substrate interface). This means a transition at a single temperature via the U_2 invariant reaction (type I model) or via invariant reactions at two temperatures, i.e. the e_4 and E_2 (type II model) invariant reactions. In reality, due to kinetic limitations (see above), this transition occurs gradually over a narrow range of temperatures: approaching an invariant temperature, the driving force for the transition is very small, becoming nil at the invariant temperature.

In view of the results obtained in this work and the above discussion, it is not possible to draw unambiguously a final conclusion which of both types of models better describes the physical reality. In case of a type I model as predicted by References 41, 45, 46 and 47, the temperature of the invariant reaction U_2 , $\alpha + \epsilon \rightleftharpoons \gamma' + \theta$, can be given as 842 ± 2 K (569 ± 2 °C); in case of a type II model as predicted by References 39, 43, the reactions e_4 and E_2 must occur subsequently within the temperature range from 840 K to 844 K (567 °C to 571 °C).

All microstructures that emerged as a result of the nitriding and nitrocarburising treatments performed in the present work are compatible with the observations of Reference 75. However, in the present work, the $\alpha + \epsilon$ equilibrium was not clearly established at 843 K (570 °C) as in Reference 75, but at a slightly higher temperature: the temperature of the U_2 invariant reaction as determined in the present work (if a type I model is assumed), and as due to smaller steps in temperature in the performed series of experiments, is close to the higher end of the temperature range of 833 K to 843 K (560 °C to 570 °C) as proposed for the U_2 reaction in Reference 75.

4.5.3 Compatibility of experimental data with the models from the literature

The temperatures of the invariant reactions as calculated in the present work by application of the models for the Fe–N–C system given in the literature [39, 41, 43, 45–47] have been gathered in Table 4.2. Experimentally determined data from recent works [30, 82] and the temperature of the invariant reaction U_2 (if a type I model is assumed) or the temperature range for the invariant reactions E_2 and e_4 (if a type II model is assumed) as determined in the present work have also been given in Table 4.2. Matches of the experimental and calculated data have been marked with an asterisk.

Considering the temperatures of the invariant reactions in the binary Fe–N system (c , e_2 and e_3), all models except the model of Reference 47 give an acceptable but varying degree of agreement with the experimentally determined data.

The temperature of the ternary invariant reaction E_1 (cf. Figure 6.4) is also reproduced accurately by most [39, 41, 43, 45] models. For the invariant reaction U_1 , only the model of Reference 41 gives a value which is close to the experimentally determined range [82]. Strikingly, the values predicted by the models of Reference 39 and 43 are almost 100 K higher than the experimental value provided by Reference 82. The other models [45–47] give a too low value, disagreeing with both the results from the present work and from Reference 82.

The temperature of the invariant reaction U_2 that was determined experimentally in the present work is only reproduced well by the model of Reference 47. For all other invariant temperatures in the ternary system, however, this model [47] gives inaccurate values. The

values for the temperature of the invariant reaction U_2 as calculated using the models of References 45 and 46 are about 20 K too low. The model from Reference 41 gives a value which is much too low in view of the here determined experimental result. Also note that the type II models [39, 43] give a slightly too low temperature range for the transition between the $\gamma'+\theta$ and the $\alpha+\epsilon$ equilibria (reactions e_4 and E_2).

Considering all invariant reactions in the system Fe–N–C, the model from Reference 41 agrees best with the experimental data, but note the huge discrepancy with the experimental value for the invariant reaction U_2 (see above). The model from Reference 43 also gives an overall fair agreement with the experimental data for the invariant temperatures if a type II model is assumed. Moreover, it has already been shown by our group that the model from Reference 43 agrees better with the experimental data for phase boundaries [29, 82] and the thermodynamics of the ϵ phase [81] (see also Chapter 2).

The above evaluation suggests that development of a new model for the system Fe–N–C is timely. Such a model must yield good agreement with the experimental data pertaining to the invariant temperatures and the phase boundaries and the thermodynamics of especially the ϵ phase.

4.6 Conclusions

- Inspection of all models for the Fe–N–C system available in the literature indicates two different possibilities for the (series of) invariant reaction(s) leading to the transition from the $\alpha+\epsilon$ two-phase field in the Fe–N–C system at higher temperatures to the $\gamma'+\theta$ two-phase field at lower temperatures. Models of type I realize this transition via the invariant reaction $\alpha+\epsilon \rightleftharpoons \gamma'+\theta$ (U_2). Models of type II realize this transition via the invariant reactions $\epsilon \rightleftharpoons \gamma'+\theta$ (e_4) and $\epsilon \rightleftharpoons \alpha+\gamma'+\theta$ (E_2).
- Microstructural analyses of the compound layer developing on Fe–C substrates upon nitriding and nitrocarburising for a series of temperatures showed that both types of models are qualitatively compatible with the experimental results. A sharp transition from the $\alpha+\epsilon$ to the $\gamma'+\theta$ equilibrium upon cooling is not found due to kinetic reasons.
- The minimum temperature at which the $\alpha+\epsilon$ equilibrium of the Fe–N–C system is established has been determined at 844 K (571 °C). The maximum temperature at which the $\gamma'+\theta$ equilibrium is established has been determined at 840 K (567 °C). This corresponds to a temperature of the invariant reaction U_2 of 842 ± 2 K (569 ± 2 °C) if a type I model is assumed and a temperature range of 844 K to 840 K (567 °C to 571 °C) in which upon

cooling the e_4 and E_2 invariant reactions must occur subsequently according to a type II model.

- Comparison of the available experimental data of temperatures of the invariant reactions and the phase boundaries with the predictions calculated by applying models presented in the literature shows that none of the published models provides a satisfactory description of the experimental data. A remodelling of the Fe–N–C system is required.

Acknowledgements

The authors are very grateful to Dr. B. Hallstedt, RWTH Aachen, Germany for assistance with formulating the models from References 39 and 43 in terms of the compound-energy formalism and implementing them into a Thermo-Calc database, and also for supplying Thermo-Calc databases for the thermodynamic descriptions given in References 46 and 41.

Chapter 5

A thermodynamic model for non-stoichiometric cementite; the Fe–C phase diagram

Holger Göhring, Andreas Leineweber, Eric Jan Mittemeijer

On the basis of recently published experimental data a new thermodynamic model for the cementite phase was developed, accounting for its non-stoichiometry in equilibrium with α , γ and liquid solution phases. The predictions from the model were discussed in the context of experimental and ab-initio data from the literature. Further, the model was compared to existing models for stoichiometric and non-stoichiometric cementite. It was shown that the resulting description is consistent with thermodynamic descriptions of the Fe–C system, excluding the non-stoichiometry of cementite, from the literature. Thus, the new model is suitable as a basis for multi-component systems correctly predicting the constitution of technically applied alloys.

5.1 Introduction

The system Fe–C has been studied extensively in the past. A review of experimental data is given in Reference 3. Thermodynamic modelling has been performed in References 31–34, 97 and 98. The solid Fe–C equilibrium phases at 1 atm pressure are α -Fe[C] (ferrite) with bcc

Table 5.1: Phases considered in the present work, their crystal structure and designations.

phase	space group	formula unit $\text{Fe}_a(\text{C}, \text{Va})_c$
ferrite, α	$I\bar{m}\bar{3}m$	$\text{Fe}(\text{C}, \text{Va})_3$
austenite, γ	$Fm\bar{3}m$	$\text{Fe}(\text{C}, \text{Va})$
cementite, θ	$Pnma$	$\text{Fe}_3(\text{C}, \text{Va})$
graphite	$P6_3/mmc$	C
diamond	$Fd\bar{3}m$	C
liquid phase	–	(Fe,C)

Fe lattice structure, $\gamma\text{-Fe}[\text{C}]$ (austenite) with fcc Fe lattice structure and graphite (hexagonal crystal structure), with [C] denoting C dissolved in Fe, cf. Table 5.1. In the following, small Greek letters will be used to denote the solid-solution phases. Since graphite only forms slowly upon solidification of Fe–C melt and even slower in the solid state (e.g. from metastable iron carbides upon annealing at elevated temperatures), the metastable cementite phase, $\theta\text{-Fe}_3\text{C}_{1-z}$, is relevant for most technically used Fe–C alloys. An exception is the case of grey cast iron where the decomposition of θ is promoted in particular by presence of Si [164]. The metastable Fe–C system, i.e. neglecting graphite formation, is considered in the following.

All the cited studies [3, 31–34, 97, 98] treat cementite as a stoichiometric compound Fe_3C . However, there is strong evidence [5–16] that cementite has a solubility range that extends to C contents smaller than the stoichiometric composition, i.e. < 25 at.%, i.e. with positive z in the formula $\text{Fe}_3\text{C}_{1-z}$, due to introduction of vacancies on the C sublattice¹. Thus, cementite should rather be treated as an interstitial solid solution of C in Fe with a very specific Fe sublattice structure.

Lattice-parameter variations of cementite which has been equilibrated with α or at different temperatures have been ascribed to a variation of the cementite’s composition due to C vacancy formation as early as 1944 [5]. The same trend has been observed in a later work but on the basis of rather inaccurate chemical analyses [6]. Still later works from the same group present phase diagrams of the Fe–C system exhibiting rough estimates for the homogeneity range for cementite [7–10].

Upon decreasing temperature, $\alpha\text{-Fe}$ has been found to precipitate from cementite [11], indicating that the C content of cementite in metastable equilibrium with $\alpha\text{-Fe}[\text{C}]$ increases with decreasing temperature². The equilibrium composition of cementite at room temperature has

¹A similar case pertains to γ' iron nitride, $\gamma'\text{-Fe}_4\text{N}_{1-x}$, where N contents smaller than the stoichiometric composition are possible, i.e. < 20 at.%, i.e. with positive x in the formula $\gamma'\text{-Fe}_4\text{N}_{1-x}$ [22].

²Again note the similarity with $\gamma'\text{-Fe}_4\text{N}_{1-x}$: $\alpha\text{-Fe}$ (needles) precipitate in $\gamma'\text{-Fe}_4\text{N}_{1-x}$ upon decreasing temperature [135].

been quantified in Reference 12. Also in non-equilibrium solid Fe–C specimens as obtained upon fast quenching of Fe–C melts, non-stoichiometric cementite has been found [13]. The temperature-dependent composition of cementite stabilised by Mn has been studied by neutron diffraction in Reference 14. However, the C vacancy fractions determined in that study (up to $z \approx 0.6$) seem unrealistically high. The homogeneity range of cementite at elevated pressures (> 1 GPa) and temperatures around 1400 K was obtained from EPMA data presented in Reference 15. All these studies [5–15] have in common that the data cannot be applied for developing a thermodynamic model of cementite predicting the equilibrium vacancy content of cementite in equilibrium with α or γ as function of temperature at ambient pressure, because of either incompatible/inadequate experimental conditions or low data quality due to impurities, inaccurate measurements or an only estimative character of the study concerned. A big problem thus is that, although the occurrence of a homogeneity range of cementite is generally acknowledged, reliable estimates for the C contents of non-stoichiometric cementite as function of temperature at 1 atm cannot be given on the basis of the data in References 5–15.

Recently, the vacancy content of pure Fe–C cementite in equilibrium with α or in equilibrium with γ was quantitatively determined at temperatures between 823 K and 1323 K and at ambient pressure utilising high-temperature equilibrated and subsequently quenched Fe–C specimens [16]. To this end, after extraction of the cementite, X-ray diffraction analysis on the resulting cementite powder was applied, leading to values of the equilibrium C contents of cementite with a much higher accuracy than in past works [5–15].

The aim of the present work is to extend the thermodynamic model for the system Fe–C given in Reference 32, until now only incorporating a stoichiometric cementite phase, by allowing for non-stoichiometry of cementite and including the new data presented in Reference 16.

5.2 Thermodynamic models for Fe–C solution phases

The solid solution phases in the system Fe–C can be described as interstitial solid solutions of C, on a partially occupied (by C) interstitial sublattice, in a sublattice completely occupied by Fe, with a formula unit given by $\text{Fe}_a(\text{C},\text{Va})_c$ with a and c being small integers the ratio of which is determined by the crystal structure. The Gibbs energy of one formula unit of this phase $\varphi = \alpha, \gamma, \theta$ can be described as [50–52]

$$G_m^\varphi = y_C^\circ G_{\text{Fe:C}}^{\varphi,\text{non-mag}} + y_{\text{Va}}^\circ G_{\text{Fe:Va}}^{\varphi,\text{non-mag}} + cRT(y_C \ln y_C + y_{\text{Va}} \ln y_{\text{Va}}) + G^{\varphi,\text{ex}} + G^{\varphi,\text{mag}} \quad (5.1)$$

with the site fractions of C and vacancies (Va) y_C and y_{Va} , the standard Gibbs energies of the hypothetical compounds Fe_aC_c and Fe_aVa_c in the structure of the phase φ and in the state of

no magnetic order (so-called end-members), ${}^{\circ}G_{\text{Fe:C}}^{\phi,\text{non-mag}}$ and ${}^{\circ}G_{\text{Fe:Va}}^{\phi,\text{non-mag}}$ (with Fe:C and Fe:Va denoting that the second sublattice is fully occupied by C and Va, respectively), the excess Gibbs energy

$$G^{\phi,\text{ex}} = y_{\text{C}}y_{\text{Va}} \sum_{k=0}^n k L_{\text{Fe:C,Va}}^{\phi} (y_{\text{C}} - y_{\text{Va}})^k \quad (5.2)$$

with the k -th order interaction parameter $L_{\text{Fe:C,Va}}^{\phi}$, and the magnetic contribution $G^{\phi,\text{mag}}$. Without the excess term, the model is called the ideal interstitial solution model. A model with $n = 0$ ($n = 1$) is referred to as a (sub-)regular interstitial solution model [54, 165].

The Gibbs energies of the end members, ${}^{\circ}G_{\text{Fe:C}}^{\phi,\text{non-mag}}$ and ${}^{\circ}G_{\text{Fe:Va}}^{\phi,\text{non-mag}}$, are usually expressed as a power series relative to the so-called stable element reference (SER) state as defined in Reference 49, i.e. relative to the enthalpy of the elements in their stable state at 298 K, denoted as H^{SER} . If no information about the shape of the temperature dependence of the Gibbs energy at 1 atm pressure is available (e.g. heat-capacity data), one typically models the Gibbs energy of formation of the end members relative to the Gibbs energy of the elements, using a constant enthalpy of formation and a constant entropy of formation. Then, the heat capacity of the non-magnetic end member (compound) is an atomic fraction weighted average of the heat capacities of the corresponding non-magnetic elements, which is nothing else than adoption of the Neumann-Kopp rule [53, 54].

The magnetic contribution can be described according to the Inden model [55, 56] as

$$G^{\phi,\text{mag}} = RT f(\tau) \ln(\beta^{\phi} + 1) \quad (5.3)$$

with the reduced temperature $\tau = T/T_{\text{Curie}}^{\phi}$ or $\tau = T/T_{\text{Neel}}^{\phi}$, whereby T_{Curie}^{ϕ} and T_{Neel}^{ϕ} denote the Curie temperature and the Neel temperature of the magnetic order/disorder transformation, respectively, and the magnetic moment β^{ϕ} , and [50]

$$f(\tau) = \begin{cases} 1 - \frac{1}{A} \left[\frac{79\tau^{-1}}{140p} + \frac{474}{497} \left(\frac{1}{p} - 1 \right) \left(\frac{\tau^3}{6} + \frac{\tau^9}{135} + \frac{\tau^{15}}{600} \right) \right] & \tau < 1 \\ -\frac{1}{A} \left(\frac{\tau^{-5}}{10} + \frac{\tau^{-15}}{315} + \frac{\tau^{-25}}{1500} \right) & \tau \geq 1 \end{cases} \quad (5.4)$$

with

$$A = \frac{518}{1125} + \frac{11692}{15975} \left(\frac{1}{p} - 1 \right). \quad (5.5)$$

The constant p depends on the crystal structure: $p = 0.4$ can be used for bcc materials and $p = 0.28$ for materials with other crystal structures [55].

Since the magnetic moment β^φ pertains to one formula unit of phase φ [166], it can be related to the magnetic moment per Fe atom $\beta^{\varphi,*}$ (ignoring the contributions by C atoms) according to

$$\beta^\varphi = (\beta^{\varphi,*} + 1)^a - 1 \quad (5.6a)$$

or, if β^φ is known, $\beta^{\varphi,*}$ can be calculated as

$$\beta^{\varphi,*} = (\beta^\varphi + 1)^{1/a} - 1. \quad (5.6b)$$

In summary, the magnetic contribution can be modelled using only two parameters, namely the magnetic moment β^φ and the Curie or Neel temperature $T_{\text{C/N}}^\varphi$. These parameters can be concentration dependent. The parameters for a certain composition (y_C^φ , y_{Va}^φ) are determined by linear interpolation (or a similar series as in Equation (5.2)). Similar to the standard Gibbs energies of the non-magnetic end members, the parameters of the magnetic model for each end member are indicated by an index, Fe:Va or Fe:C.

5.3 The employed experimental data set

After choosing a suitable thermodynamic model for each phase, the set of model parameters yielding the best description for the experimental data is determined. These model parameters are e.g. the coefficients of the power series describing the T -dependence of the Gibbs energy of the end members of each phase (cf. Section 5.2). In the present work, the optimisation, i.e. finding out the appropriate set of model parameters in the above sense, has been performed using the PARROT module of the Thermo-Calc software [70]. During the optimisation process, it is necessary to modify the weights assigned to the experimental data. Moreover, it might be necessary to modify the model for a phase itself if it proves to be unsuitable to describe the experimental data of the system.

The evaluation shows that the existing description [32, 49] of the system Fe–C appears satisfactory regarding the α , γ , liquid, graphite and diamond phases. In the present work it was necessary to develop a new model for the cementite solid solution phase, which, moreover, incorporates its ferromagnetic character at low temperatures. Thus, only data considering pure cementite in equilibrium (at each T and at a pressure of 1 atm) or equilibria of other phases with cementite are considered.

5.3.1 Gibbs energy of cementite

Essentially two sources of thermodynamic data for cementite in the relevant temperature range of $T > 298\text{ K}$ exist. One early experimental work [167] has been thoroughly reviewed and analysed in Reference 168 and later in Reference 169. The data published in Reference 167 have been obtained from calorimetric measurements on dual-phase Fe–C alloys with varying gross composition. Thus, depending on the temperature, both the phase fractions and the compositions of α or γ and cementite vary. Unfortunately, the evaluations of these data in References 168, 169 have been performed under the assumption that cementite is stoichiometric; the thus resulting heat-capacity data are consequently error affected.

For the present work, the data from Reference 170 are more suitable: pure extracted cementite was employed in Reference 170 instead of dual phase alloys with temperature-dependent phase fractions as in the works referred to above. The cementite investigated in Reference 170 was extracted from a dual-phase Fe–C alloy equilibrated at 973 K. According to the experimental data in Reference 16, this temperature corresponds to a vacancy content on the C, interstitial sublattice of only approximately 1% and thus a C content of 24.8 at.%, which is close to stoichiometry. The c_p data from Reference 170 have been used in the current optimisation to determine both the coefficients for the isobaric molar heat capacity c_p of stoichiometric cementite and the magnetic moment used in the magnetic model (cf. Equation (5.3)). Relatively recent data for the c_p of cementite have been presented in Reference 171. However, as compared to the other sources [167–170], the data from Reference 171 seem too large.

The enthalpy of formation of cementite at room temperature has been determined in Reference 172. This value has been included in the evaluation with a low weight because of its relatively large uncertainty. For the entropy of cementite at room temperature, the value from Reference 169 was used, which is identical to the value from Reference 97.

For the Curie temperature of cementite, several values have been reported in the literature, e.g. 480 K [169], 483 K [171] or 485 K [33, 34]. It may be suggested that the Curie temperature of cementite decreases slightly with decreasing C content [13, 173]. As the magnetic contribution to the Gibbs energy of cementite has an only very small influence on the thermodynamics of the Fe–C system, especially as compared to the magnetic contribution to the Gibbs energy of α , for simplicity, the constant value of the Curie temperature given in References 33 and 34 has been adopted in the present work.

5.3.2 Mono-variant (at 1 atm) equilibria

The solubility of C in α -Fe in equilibrium with cementite has been experimentally determined in References 174–183 and modelled in References 97, 98 and 184. These data are *not* included in the present optimisation in view of their pronounced scatter. This scatter is partially due to an apparent considerable dependence of the C solubility in α -Fe on the microstructure [3, 185]. Another work [186] is devoted to the determination of the C solubility in ferritic steels containing elements other than Fe and C as well and therefore, these data cannot be used in the present investigation of the binary Fe–C system.

The solubility of C in γ -Fe in equilibrium with cementite has been determined in References 168 and 187–190, additionally to early works from before 1940 cited in these references. The measurement method applied in Reference 188 allows direct determination of the C content of γ -Fe and is thus independent of the assumption of a stoichiometric composition of cementite. Therefore, these data have been included in the present optimisation process.

The vacancy content of cementite in equilibrium with α -Fe or with γ -Fe has been recently determined by application of XRD by using a relationship between the vacancy content and the unit cell volume resulting from DFT-based first-principles calculations [16]. These data were directly used in the present optimisation process.

The equilibrium of cementite and the liquid phase is not accessible by experiment due to the instability of cementite at elevated temperature and 1 atm [3]. The only available data are results from thermodynamic calculation. Thus, they are not included in the present optimisation.

5.3.3 Invariant (at 1 atm) equilibria

For the metastable eutectoid ($\gamma \rightleftharpoons \alpha + \theta$) and metastable eutectic ($L \rightleftharpoons \alpha + \theta$) reactions, the well-established values of the invariant temperatures and the compositions of all phases *other than cementite* have been adopted from Reference 97.

In the present evaluation, values for the metastable melting point of cementite and the invariant temperature of the cementite-diamond peritectic reaction as given in Reference 169 have been included with a low weight due to the only estimative character of these values.

5.4 Optimisation of the thermodynamic model

The thermodynamic parameters used for the pure elements are taken from Reference 49. For the solution phases α , γ and the liquid phase, the models and the corresponding parameters from previous evaluations have been gathered in Table 5.2.

Table 5.2: Thermodynamic model parameters for solution phases, taken from cited literature and for the non-stoichiometric model for the cementite solid solution as determined in the present work. T in K, values of Gibbs energy in J mol^{-1} .

liquid phase, model (Fe,C) [32]
${}^0L_{\text{C},\text{Fe}}^{\text{L}} = -124320 + 28.5T$
${}^1L_{\text{C},\text{Fe}}^{\text{L}} = 19300$
${}^2L_{\text{C},\text{Fe}}^{\text{L}} = 49260 - 19T$
α/δ , model $\text{Fe}(\text{C},\text{Va})_3$ [32]
${}^\circ G_{\text{Fe:Va}}^{\alpha/\delta,\text{non-mag}} = {}^\circ G_{\text{Fe}}^{\alpha/\delta,\text{non-mag}}$
${}^\circ G_{\text{Fe:C}}^{\alpha/\delta,\text{non-mag}} - {}^\circ G_{\text{Fe}}^{\alpha/\delta,\text{non-mag}} - 3{}^\circ G_{\text{C}}^{\text{gra}} = 322050 + 75.667T$
${}^0L_{\text{Fe:C,Va}}^{\alpha/\delta} = -190T$
$\beta_{\text{Fe:Va}}^{\alpha/\delta} = \beta_{\text{Fe:C}}^{\alpha/\delta} = \beta_{\text{Fe}}^{\alpha/\delta} = 2.22$
$T_{\text{Curie,Fe:Va}}^{\alpha/\delta} = T_{\text{Curie,Fe:C}}^{\alpha/\delta} = T_{\text{Curie,Fe}}^{\alpha/\delta} = 1043$
γ , model $\text{Fe}(\text{C},\text{Va})$ [32], adding magnetic model [49]
${}^\circ G_{\text{Fe:Va}}^{\gamma,\text{non-mag}} = {}^\circ G_{\text{Fe}}^{\gamma,\text{non-mag}}$
${}^\circ G_{\text{Fe:C}}^{\gamma,\text{non-mag}} - {}^\circ G_{\text{Fe}}^{\gamma,\text{non-mag}} - {}^\circ G_{\text{C}}^{\text{gra}} = 77207 - 15.877T$
${}^0L_{\text{Fe:C,Va}}^{\gamma} = -34671$
$\beta_{\text{Fe:Va}}^{\gamma} = \beta_{\text{Fe:C}}^{\gamma} = \beta_{\text{Fe}}^{\gamma} = 0.7$
$T_{\text{Néel,Fe:Va}}^{\gamma} = T_{\text{Néel,Fe:C}}^{\gamma} = T_{\text{Néel,Fe}}^{\gamma} = 67$
$\theta\text{-Fe}_3\text{C}_{1-z}$, model $\text{Fe}_3(\text{C},\text{Va})$, present work
${}^\circ G_{\text{Fe:C}}^{\theta,\text{non-mag}} - 3H_{\text{Fe}}^{\text{SER}} - H_{\text{C}}^{\text{SER}} =$
$-8983 + 658.38T - 113.578T \ln T - 3.059 \times 10^{-3}T^2 + 6.105 \times 10^5T^{-1}$
${}^\circ G_{\text{Fe:Va}}^{\theta,\text{non-mag}} - 3{}^\circ G_{\text{Fe}}^{\alpha,\text{non-mag}} = 44782 - 11.59T$
$\beta_{\text{Fe:C}}^{\theta} = \beta_{\text{Fe:Va}}^{\theta} = 1.51$
$T_{\text{Curie,Fe:C}}^{\theta} = T_{\text{Curie,Fe:Va}}^{\theta} = 485$ [33]

For cementite, an ideal interstitial solution model (cf. Equation (5.1) and text below) has been adopted, using two sublattices and the formula unit $\text{Fe}_3(\text{C},\text{Va})$. It was not attempted to model the composition-dependence of the magnetic properties of cementite [13, 173]. The magnetic contribution has been assumed to be independent of composition, with $T_{\text{Curie},\text{Fe:C}}^\theta = T_{\text{Curie},\text{Fe:Va}}^\theta = 485 \text{ K}$ as taken from Reference 33 and with $\beta_{\text{Fe:C}}^\theta = \beta_{\text{Fe:Va}}^\theta$ as a fitting parameter.

For the optimisation process, the experimental data gathered in Section 5.3 were implemented in a format readable by the PARROT module of the Thermo-Calc software [70]. During the optimisation process, the weights assigned to different experimental data (sets) were varied. Frequently, the model was checked for deviations of the instantaneous model prediction with the experimental data and for thermodynamic reasonableness.

During the optimisation process it was found that the expression

$${}^\circ G_{\text{Fe:C}}^{\theta,\text{non-mag}} - 3H_{\text{Fe}}^{\text{SER}} - H_{\text{C}}^{\text{SER}} = a_1 + b_1 T + c_1 T \ln T + d_1 T^2 + e_1 T^{-1} \quad (5.7)$$

suffices to describe the Gibbs energy of non-magnetic stoichiometric cementite. This is the same type of power series as used in Reference 33.

It is not the intention of the present work to present a correct description of highly hypothetical Fe in cementite configuration, but rather to find a simple but complete model correctly describing the thermodynamics of cementite with a low fraction of C vacancies by applying an ideal interstitial solution model. Thus, the Gibbs energy of Fe in cementite configuration has been modelled relative to pure α -Fe according to

$${}^\circ G_{\text{Fe:Va}}^{\theta,\text{non-mag}} - 3G_{\text{Fe}}^{\alpha,\text{non-mag}} = a_2 + b_2 T. \quad (5.8)$$

Doing so, pure Fe of the crystal structure as its arrangement in cementite incorporates the heat capacity of non-magnetic α -Fe.

The optimisation of the parameters for the thermodynamic model of cementite was performed using the PARROT module of the Thermo-Calc software [70]. As start values for the parameters of the power series for the Gibbs energy of stoichiometric cementite (Equation (5.7)), the values for the highest temperature interval from Reference 33 have been used. The final results of the model fitting, the values of the model parameters, have been listed in Table 5.2.

5.5 Discussion

5.5.1 Thermodynamics of cementite

The enthalpy of formation of one mole stoichiometric cementite (Fe_3C) at 298 K as calculated using the new model, 26.3 kJ mol^{-1} , is as close to the value determined calorimetrically in Reference 172 of $18.8 \pm 4.4 \text{ kJ mol}^{-1}$ as the values of 25.2 kJ mol^{-1} [32], 26.9 kJ mol^{-1} [33] and 26.3 kJ mol^{-1} [34] as calculated from the models in the literature. The entropy of one mole cementite at 298.15 K is $104.6 \text{ J mol}^{-1} \text{ K}^{-1}$ as calculated with the current model. This accurately reproduces the also calculated values for the entropy of cementite at 298.15 K as given in References 33, 34, 97 and 169, and in particular agrees well with the experimental value of $106.9 \text{ J mol}^{-1} \text{ K}^{-1}$ determined in Reference 191.

c_p of stoichiometric cementite as calculated using the Gibbs-energy function determined in the present work can be compared in Figure 5.1 with corresponding experimental data from Reference 170 and the calculated results from References 33, 34, 169 and Reference 192 (first-principles calculation). The model developed in the present work agrees well with the experimental data for c_p [170] and also with the data from the assessment from Reference 169. The descriptions of the experimental c_p data by the Calphad-type models from References 33, 34 and the ab-initio data [192] are also reasonable, with varying degrees of fit.

In view of the above indicated good agreement of the Gibbs energy of formation at 298 K of stoichiometric cementite and of its heat capacity with experimental and calculated literature data [32–34, 97, 169, 170, 172, 192], it is not surprising that the temperature dependence of the Gibbs energy of formation of *stoichiometric* cementite agrees well with the available calculated literature data [32–34, 97].

However, when comparing the temperature-dependent values of the Gibbs energy of formation of stoichiometric cementite, a systematic positive deviation between the model from the present work and the models from the literature [32–34, 97] is noticed (see at the composition of Fe_3C in Figure 5.2). This is a consequence of accounting for the non-stoichiometry of cementite in the present model: when performing the double tangent construction [54] for the $\alpha+\theta$ or $\gamma+\theta$ equilibrium (at e.g. 1400 K, see Figure 5.2) using the model from the present work, the Gibbs energy of θ in the equilibrium composition is different from the Gibbs energy of stoichiometric cementite due to the configurational entropy introduced by the C-vacancy content of cementite. However, the intersection of the equilibrium tangent and the vertical line at the composition Fe_3C agrees very well with the single data points for the Gibbs energy of formation calculated using the models from the literature [33, 34] (the point for the model from Reference 32 coincides with the point for the model from Reference 33) in Figure 5.2, i.e. the

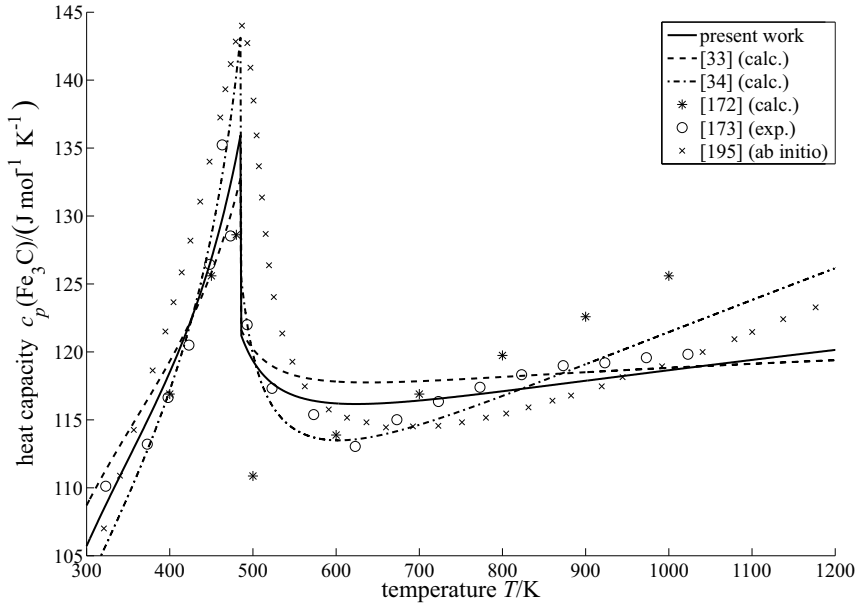


Figure 5.1: Comparison of the heat capacity c_p of stoichiometric cementite as calculated using the Gibbs-energy function as determined in the present work with the data from References 169 and 170, data obtained from first-principles calculations [192] and c_p as calculated using models from the literature [33, 34].

same equilibrium composition of γ and therefore the same chemical potentials of Fe and C result when using the models from the literature [32–34] treating cementite as a stoichiometric phase. This is not surprising since in the past models [32–34], the available thermodynamic data pertaining to *non-stoichiometric* cementite has been attributed to *stoichiometric* cementite due to the lack of reliable equilibrium vacancy content data. Therefore, taking an existing description of the Gibbs energy of (stoichiometric) cementite [32–34] and only optimise the coefficients of ${}^\circ G_{\text{Fe:Va}}^\theta$, instead of completely remodelling the cementite phase, would have been insufficient to correctly describe the two-phase equilibria in the Fe–C system.

It is important to note that the magnetic model leads to an unrealistically small magnetic moment of Fe: applying Equation (5.6b) and the data for β^θ in Table 5.2 yields $\beta_{\text{Fe}}^{\theta,*} = 0.36$. Typical experimental values for the average magnetic moment per Fe atom in cementite are 1.7–1.8 [193, 194]; ab-initio calculations yield values for the average magnetic moment per Fe atom between 1.8 and 2.0 [192, 195, 196]. The values for the magnetic moment of cementite from both recent, previous models [33, 34], both using the Inden model [55, 56] for the magnetic contribution to the Gibbs energy of cementite (cf. Equation (5.3)), are similarly small. This may suggest that in the case of cementite the Inden model [55, 56] can only be used for phenomenological, mathematical description of c_p , as in this work.

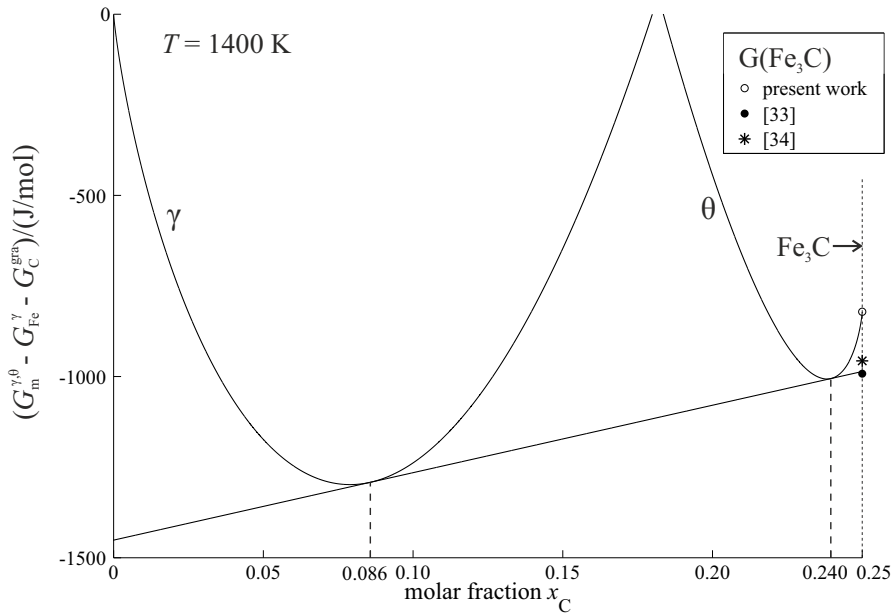


Figure 5.2: Common tangent construction [54] performed for the $\gamma+\theta$ equilibrium at 1400 K using the model from the present work. The Gibbs energies are given relative to γ -Fe and graphite. The compositions of the phases γ and θ at equilibrium have been indicated on the abscissa. For comparison, the Gibbs energy of stoichiometric cementite according to the model from the present work and the models from References 33 and 34 are given.

The melting point of metastable cementite is not accessible by experiments: at the relevant C contents, cementite decomposes upon heating; upon cooling of the melt, graphite precipitates. However, the melting point of cementite as predicted by the thermodynamic model can be compared to other similar predictions. The melting point of cementite as calculated with the thermodynamic model from the present work is 1484 K (pertaining to congruent melting at a non-stoichiometric C content of 24.6 at%). This is lower than the value predicted by References 98 and 197 (1525 K) and as accepted in Reference 3, the value calculated with the model in Reference 32 (1498 K) and the value estimated in Reference 169 (approximately 1520 K); in all cases only stoichiometric cementite was considered. By molecular dynamics simulations, the melting point of stoichiometric cementite has been predicted to be 1425 K [198], which is very close to the eutectic temperature of the Fe–C system, and therefore that value appears unrealistically low.

5.5.2 The Fe–C phase diagram

The metastable Fe–C phase diagram as calculated using the thermodynamic descriptions of α , γ and the liquid from Reference 32 as well as the new model for cementite is presented in Figure 5.3a. Thereby, both graphite, diamond and higher carbides (Fe_5C_2 , Fe_7C_3) have been excluded from the calculation. The distinct homogeneity range of cementite (θ) is clearly visible. Note that the second $\theta+\text{L}$ two-phase field (high C contents) and thus also the right phase-boundary limiting the homogeneity range of cementite are an artefact from excluding phases dissolving higher amounts of C and have no physical meaning. Similar phase diagrams with a certain homogeneity range of cementite have already been published in References 7–10 and 199. There, the problem addressed above has been solved by either including in the calculation the diamond phase or other Fe carbides with a higher C content than cementite. A similar, here calculated phase diagram, including diamond but excluding graphite, is shown in Figure 5.3b.

A comparison of a section of the calculated phase diagram with the experimental equilibrium data used in the optimisation process is provided by Figure 5.4a for the data from Reference 16 and in Figure 5.4b for the data from Reference 188 (with the mass fraction as a concentration variable), both showing the excellent agreement of the new model with these data.

In the present work, the description of the α phase was taken from Reference 32. Since the description of the θ phase was changed, the equilibrium between both phases could be affected. In Figure 5.5, the phase boundary $\alpha/\alpha+\theta$ as calculated using the model from the present work is shown in comparison with experimental data from References 174–183. As mentioned in Section 5.3.2, the experimental data show a pronounced scatter. The phase boundary as calculated using the model from the present work lies within the area determined by the scattered experimental data points. In Figure 5.5, the phase boundary $\alpha/\alpha+\theta$ as calculated using the model from either Reference 32 or 34 is not shown since they are almost indistinguishable from the phase boundary as calculated using the model from the present work.

The new model has been developed with the constraint of preserving the relevant equilibria as predicted by the model from Reference 32. The temperatures and compositions of each phase at the experimentally accessible metastable eutectic and eutectoid equilibria, as calculated using both the model from the present work and the models from References 32 and 34 are shown in Table 5.3; the values that have been accepted in the elaborate review in Reference 3 have also been included in Table 5.3. Both, the values calculated with the model from the present work and with the model from Reference 32 are in very good agreement with each other and in good agreement with the values from References 3 and 34.

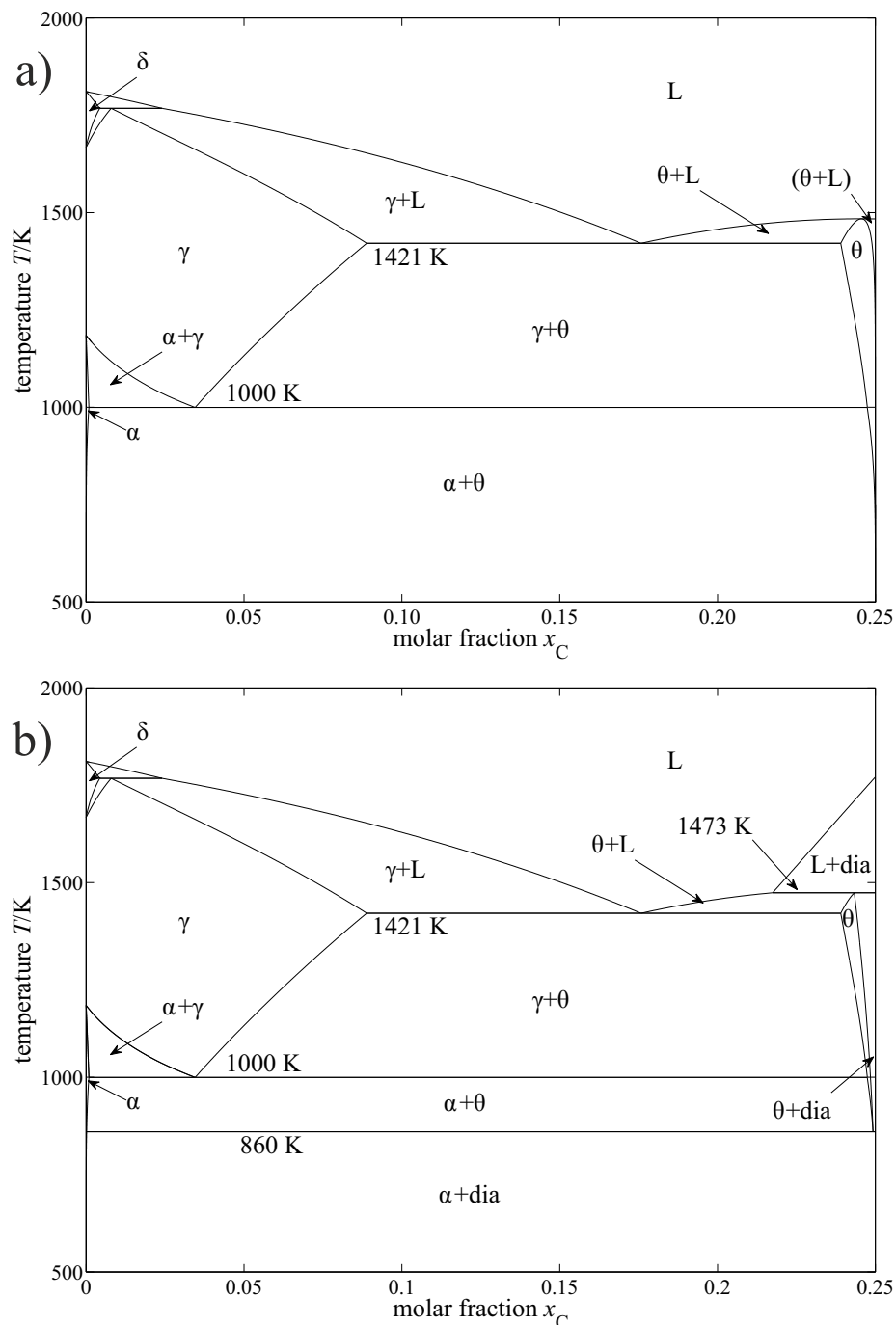


Figure 5.3: The metastable Fe–C phase diagram as calculated using the new model for cementite, showing a pronounced homogeneity range of the cementite (θ) phase. a) Calculated excluding both graphite and diamond. Note that the right (high-C) boundary of the θ single phase field is an unrealistic boundary with a $\theta+L$ two-phase field (denoted by brackets) which is a consequence of the exclusion of graphite, diamond and other carbides from the calculation and has no physical meaning. b) Calculated excluding only graphite. The diamond phase is abbreviated as dia in the figure annotations. As compared to the phase diagram in a), the cementite congruent melting point is replaced by a peritectic reaction with diamond and an additional eutectoid reaction $\theta \rightleftharpoons \alpha + dia$ occurs.

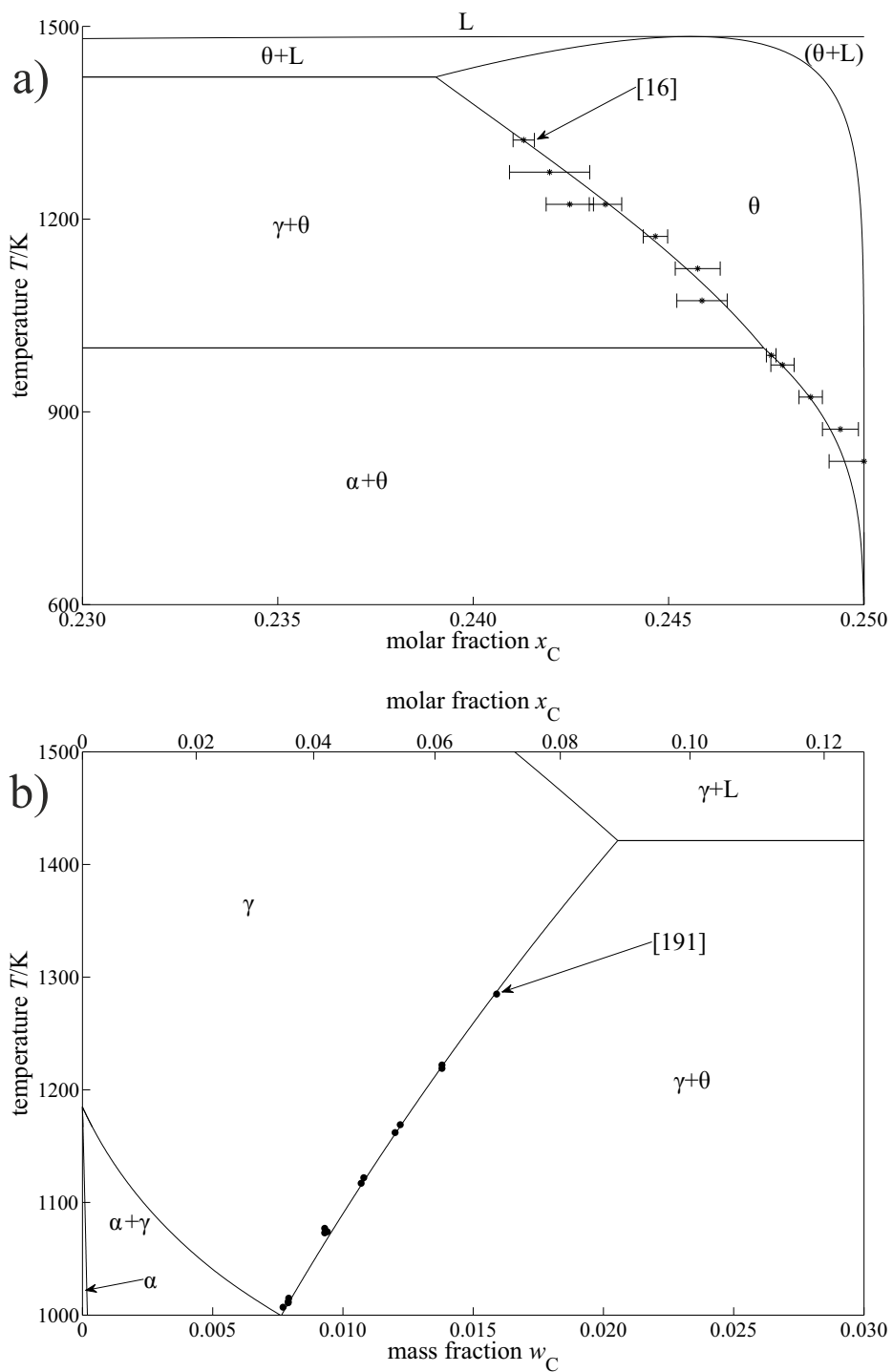


Figure 5.4: Parts of the metastable Fe–C diagram as calculated using the new model excluding both graphite and diamond (cf. Figure 5.3a) with experimental data from the literature superimposed. a) Detail showing the homogeneity range of cementite (the $\alpha+\theta/\theta$ and $\gamma+\theta/\theta$ phase boundaries) in comparison to the data from Reference 16. Note that the right (high-C) boundary of the θ single phase field is an unrealistic boundary to a $\theta+L$ two-phase field (denoted by brackets) which is a consequence of the exclusion of graphite, diamond and other carbides from the calculation and has no physical meaning. b) Detail showing the $\gamma/\gamma+\theta$ phase boundary in comparison to experimental data from Reference 188.

Table 5.3: Comparison of some metastable invariant equilibria of the Fe–C system which include the cementite phase, as calculated with the model of the present work and as stated in or as calculated using data from the cited literature. The calculated values of the temperatures have been given with a number of digits incompatible with possible experimental accuracy, in order to illustrate the marginal disagreement of such results.

reaction	reference	T/K	x_C^α /at.%	x_C^γ /at.%	x_C^L /at.%	x_C^θ /at.%
$\gamma \rightleftharpoons \alpha + \theta$	[3]	1000	0.104	3.46		25^a
	[32]	999.78	0.085	3.44		25^a
	[34]	1001.34	0.091	3.39		25^a
	present work	999.50	0.086	3.45		24.7
$L \rightleftharpoons \gamma + \theta$	[3]	1420		9.23	17.3	25^a
	[32]	1421.51		8.81	17.6	25^a
	[34]	1421.15		8.98	17.5	25^a
	present work	1421.17		8.89	17.6	23.9
$L + \text{diamond} \rightleftharpoons \theta$	[169]	1500				
	[32]	1484.09			21.9	25^a
	[34]	1492.17			21.6	25^a
	present work	1473.84			21.7	24.3
$L \rightleftharpoons \alpha + \theta$	[197]	1375	2.3		15.5	25^a
	[32]	1369.72	1.6		15.3	25^a
	[34]	1364.05	1.5		15.4	25^a
	[13]	1375 ^b	1.6		—	24.6
	present work	1372.90	1.6		15.3	23.6

^aCementite assumed as stoichiometric Fe_3C .

^bModel parameters only determined at 1375 K.

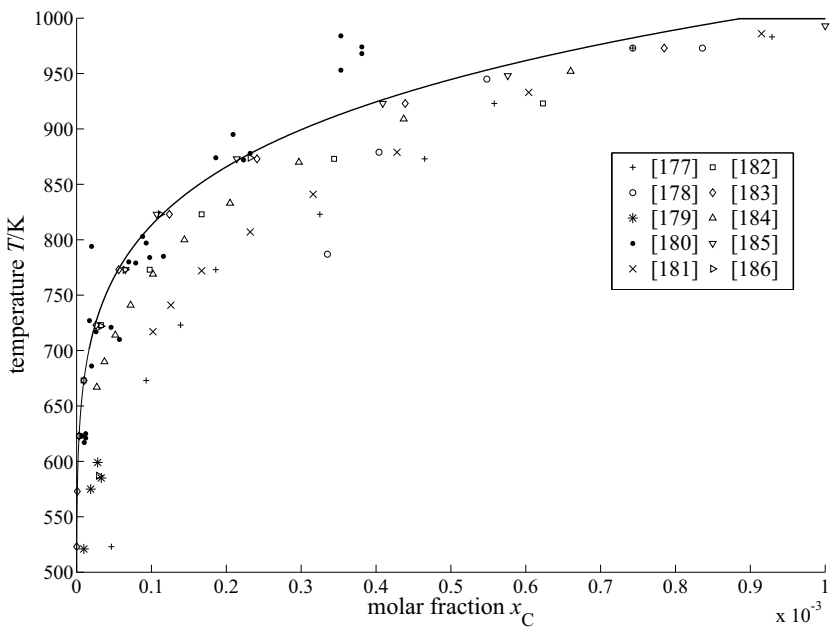


Figure 5.5: The $\alpha/\alpha+\theta$ phase boundary as calculated using the model from the present work in comparison to experimental data from References 174–183 up to the eutectoid temperature.

When excluding graphite, but including diamond, cf. the phase diagram in Figure 5.3b, the latter phase becomes stable at room temperature and ambient pressure. At elevated temperatures, however, cementite is formed from diamond and α in a eutectoid reaction, occurring at 860 K as calculated using the model from the present work (as compared to 861 K as calculated using the model from Reference 32). The metastable melting point of cementite (cf. Figure 5.3a) is replaced by a peritectic reaction with diamond (cf. Figure 5.3b). Evidently, the Fe–C system as described here is not accessible by experiments. It can be studied on the basis of thermodynamic calculations only [8–10, 199]. Such estimated values for the peritectic reaction of cementite with diamond are given in Table 5.3 (as given in Reference 169 and as calculated using the model from Reference 32).

A thermodynamic treatment of the metastable Fe–C system excluding the γ phase has been performed in Reference 197, including the eutectic reaction $L \rightleftharpoons \alpha + \theta$. This equilibrium has been helpful for understanding non-equilibrium or metastable microstructures occurring upon rapid solidification of molten Fe–C alloys [13]. The temperature and composition of the phases at the invariant $L \rightleftharpoons \alpha + \theta$ equilibrium as stated in Reference 197 and as calculated with the model of the present work and the models of References 32 and 34 have been given in Table 5.3. Both the compositions of the single phases and the temperature of the invariant reaction as

calculated using the model of the present work and the model of Reference 32 and the values stated in Reference 197 are in reasonable agreement with each other.

The model from Reference 32 was chosen as a basis in favour of the model from Reference 34. The model from Reference 34 especially improves the description of the Fe–C system in the low temperature range and describes certain phase transformations occurring during tempering of martensite. It does not improve the description of the phase equilibria in the temperature range where the non-stoichiometry of cementite is significant.

However, according to the model for the Fe–C system from Reference 32, the α phase reappears above approx. 4000 K and C contents of 30 at.% to 40 at.%, in equilibrium with the liquid phase. In Reference 34, this artefact does not occur due to a modification of the description of the α phase. However, in this temperature range, the appearance of a gaseous phase is expected which is not considered in any of the thermodynamic models of the Fe–C system [32–34]. The artefact has not been resolved in the present work. Nevertheless, it is possible to use the model for the α phase from Reference 34, i.e. the Gibbs-energy function for ${}^{\circ}G_{\text{Fe:C}}^{\alpha}$ and ${}^0L_{\text{Fe:C,Va}}^{\alpha}$, instead of the model from Reference 32 in order to avoid the artefact, leading to only insignificantly deviating results in the temperature range investigated in this paper.

5.5.3 Comparison to other models for non-stoichiometric cementite

Thermodynamic treatments of non-stoichiometric cementite have been presented before in References 13 and 16. In Reference 13, the model parameters for the adopted regular interstitial solution model with the sublattice model indicated by the formula unit $\text{FeVa}_{1/3}$ have been determined at a single temperature (1375 K, the invariant metastable $L \rightleftharpoons \alpha + \theta$ equilibrium [197]) using DSC data. Thereby, ${}^{\circ}G_{\text{Fe:Va}}^{\theta}$ was fixed at the Gibbs energy of hexagonal Fe [49] and for ${}^{\circ}G_{\text{Fe:C}}^{\theta}$ the Gibbs energy of stoichiometric cementite from Reference 32 was taken, while no magnetic contribution was modelled separately.

A thermodynamic treatment of the $\alpha + \theta$ equilibrium has also been performed in Reference 16, using an ideal interstitial solution model for both phases with the same sublattice models for α and cementite as applied in the present work. In Reference 16, for both phases, the magnetism was not modelled separately. It was shown [16] that for the C vacancy fraction of cementite (z in $\text{Fe}_3\text{C}_{1-z}$) in equilibrium with α , and recognising the very low C contents in the α phase, the following expression would hold:

$$z = \exp \left(-\frac{{}^{\circ}G_{\text{Fe}_3\text{Va}}^{\theta} - 3 {}^{\circ}G_{\text{FeVa}_3}^{\alpha}}{RT} \right) = \exp \left(\frac{{}^{\circ}S_{\text{Fe}_3\text{Va}}^{\theta} - 3 {}^{\circ}S_{\text{FeVa}_3}^{\alpha}}{R} \right) \exp \left(-\frac{{}^{\circ}H_{\text{Fe}_3\text{Va}}^{\theta} - 3 {}^{\circ}H_{\text{FeVa}_3}^{\alpha}}{RT} \right) \quad (5.9)$$

Thereby, ${}^{\circ}G_{\text{Fe}_3\text{Va}}^{\theta}$, ${}^{\circ}S_{\text{Fe}_3\text{Va}}^{\theta}$, ${}^{\circ}H_{\text{Fe}_3\text{Va}}^{\theta}$, and ${}^{\circ}G_{\text{FeVa}_3}^{\alpha}$, ${}^{\circ}S_{\text{FeVa}_3}^{\alpha}$ and ${}^{\circ}H_{\text{FeVa}_3}^{\alpha}$ stand for the Gibbs energy, entropy and enthalpy of the hypothetical magnetic Fe in cementite configuration, θ -Fe₃Va, and of magnetic α -Fe (FeVa₃), respectively. Thus, in view of the applied ideal solution model, the quantity ${}^{\circ}G_{\text{Fe}_3\text{Va}}^{\theta} - 3 {}^{\circ}G_{\text{FeVa}_3}^{\alpha} = \Delta_f^{\text{vac}} G^{\theta}$ can be regarded as the Gibbs energy of C vacancy formation in cementite according to $(1-z) \text{Fe}_3\text{C} + 3z \alpha\text{-Fe} \rightleftharpoons \text{Fe}_3\text{C}_{1-z}$ [16]. Note that, using the symbols of the present work, the quantities of equation (5.9) can be calculated as e.g. ${}^{\circ}G_{\text{Fe}_3\text{Va}}^{\theta} = {}^{\circ}G_{\text{Fe:Va}}^{\theta,\text{non-mag}} + G^{\theta,\text{mag}}$.

The Arrhenius-like behaviour (cf. Equation (5.9)) was observed indeed for the experimental data in Reference 16. Thus, the Gibbs energy of formation of vacancies in cementite was determined as

$$\Delta_f^{\text{vac}} G^{\theta} = {}^{\circ}G_{\text{Fe}_3\text{Va}}^{\theta} - 3 {}^{\circ}G_{\text{FeVa}_3}^{\alpha} = (69000 - 34T/\text{K}) \text{ J mol}^{-1}. \quad (5.10)$$

For the regular interstitial solution model applied for cementite in Reference 13, Equation (5.9) has to be modified to

$$z = \exp\left(-\frac{3 {}^{\circ}G_{\text{FeVa}_{1/3}}^{\theta} + 3 {}^0L_{\text{Fe:C,Va}}^{\theta} - 3 {}^{\circ}G_{\text{FeVa}_3}^{\alpha}}{RT}\right). \quad (5.11)$$

with ${}^{\circ}G_{\text{FeVa}_{1/3}}^{\theta}$ standing for the Gibbs energy of one mole iron in cementite configuration of the formula unit FeVa_{1/3} as applied in Reference 13. In this case, the expression

$$\Delta_f^{\text{vac}} G^{\theta} = 3 {}^{\circ}G_{\text{FeVa}_{1/3}}^{\theta} + 3 {}^0L_{\text{Fe:C,Va}}^{\theta} - 3 {}^{\circ}G_{\text{FeVa}_3}^{\alpha} \quad (5.12)$$

represents the Gibbs energy of C vacancy formation in cementite.

If, as in the present work, a regular interstitial solution model is applied only for α -Fe-[C], Equation (5.9) is also valid for low C contents of α . For the model from the present work, the Gibbs energy of C vacancy formation can then be determined as

$$\Delta_f^{\text{vac}} G^{\theta} = {}^{\circ}G_{\text{Fe}_3\text{Va}}^{\theta} - 3 {}^{\circ}G_{\text{FeVa}_3}^{\alpha} = {}^{\circ}G_{\text{Fe:Va}}^{\theta,\text{non-mag}} + G^{\theta,\text{mag}} - 3 {}^{\circ}G_{\text{Fe:Va}}^{\alpha,\text{non-mag}} - 3 G^{\alpha,\text{mag}}. \quad (5.13)$$

with the values for the corresponding model parameters as provided by Table 5.2, giving a physical interpretation of Equation (5.8) together with the magnetic model.

The T -dependences for the Gibbs energy of formation of C vacancies according to Equations (5.10) and (5.13) agree very well in the temperature range in which the $\alpha+\theta$ equilibrium prevails (up to 1000 K), see Figure 5.6. The deviations occurring for higher and (much less pronounced) for lower temperatures are due to the ferromagnetic-paramagnetic transitions oc-

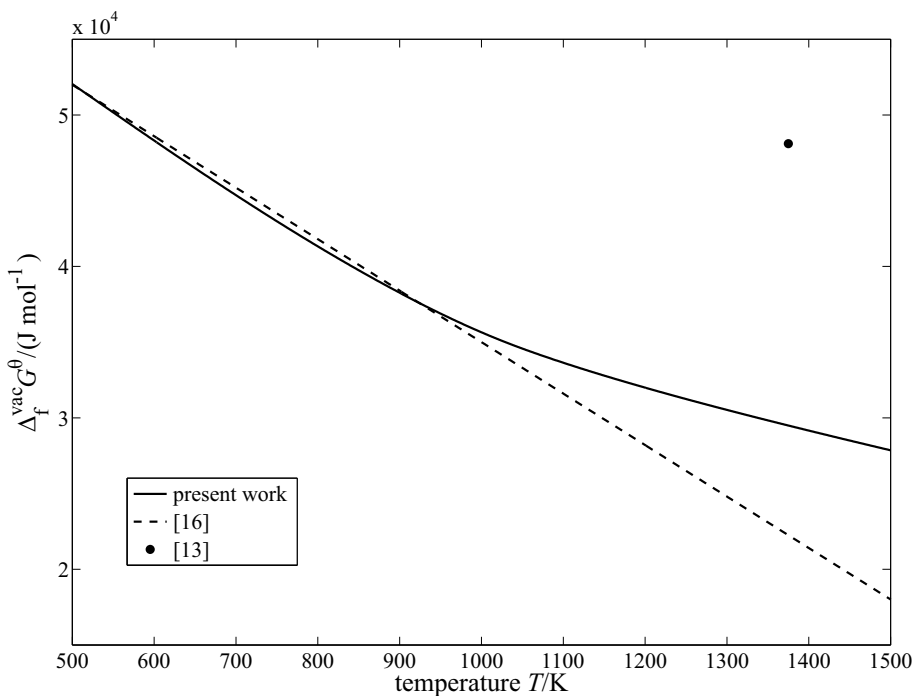


Figure 5.6: The Gibbs energy of vacancy formation in cementite in equilibrium with α , $\Delta_f^{\text{vac}} G^\theta$, as given by Equations (5.10), (5.12) or (5.13), as determined in the present work and as taken from Reference 16. The additional single data point is from Reference 13.

curing at 1043 K for α and at 485 K for cementite. The magnetic transition of α is not visible in the actual experimental data from Reference 16 (cf. Figure 5.4a) because of the occurrence of γ above 1000 K.

The value of the Gibbs energy of C vacancy formation in cementite from Reference 13 at 1375 K (also shown in Figure 5.6) is in strong disagreement with both the result of the present work (Equation (5.13)) and that of Reference 16 (Equation (5.10)). This is mainly due to the high temperature of 1375 K for which the model of Reference 13 was determined. At this high temperature, metastable α dissolves significant amounts of C in equilibrium with cementite according to both the model of the present work and the model of Reference 32. Thus, the assumptions that led to Equation (5.11) for the model of Reference 13 are not valid. Strictly speaking, Equations (5.9) (Reference [16] and present work) and (5.11) (Reference 13) only describe the equilibrium of non-stoichiometric cementite and pure α -Fe without C. Using e.g. Thermo-Calc [70], the equilibrium data at the temperature of the $L \rightleftharpoons \alpha + \theta$ invariant reaction as predicted by the model of the present work and by the model of Reference 13 can be compared. The data calculated using both models are shown in Table 5.3. The molar fractions of C in cementite correspond to a C vacancy fraction of 1.85 % [13] and 7.16 % (present work). The lower C content in cementite at the metastable eutectic as predicted by the present model (23.6 at.%) is in very

good agreement with the actual C content of cementite from the quenched melt (23.5 at.%) as estimated from experimental data (XRD and metallography) in Reference 13, as opposed to the prediction resulting from the model of Reference 13 (24.6 at.%).

5.6 Conclusions

1. Recently published data quantifying the vacancy content of $\theta\text{-Fe}_3\text{C}_{1-z}$ [16] has been successfully described by a new thermodynamic model for the cementite phase, considering cementite as an ideal interstitial solution of C in Fe.
2. The model predicts significant C-vacancy contents in cementite in equilibrium with α or γ over a distinct temperature range.
3. Incorporation of the non-stoichiometric model for cementite into existing models of multi-component systems of which the Fe–C system is a sub-system is possible with only minor modifications, as demonstrated here adopting the successful description of the system Fe–C from the literature [32], while preserving all relevant equilibria. With the help of such multi-component models, it will be possible to arrive at significantly more correct predictions of the constitution of technical Fe–C-based alloys.

Acknowledgements

The authors would like to thank Dr. O. Fabrichnaya, Institute for Materials Science, TU Bergakademie Freiberg, for the elaborate introduction to the PARROT module of the Thermo-Calc software and helpful advice during the modelling process.

Chapter 6

Thermodynamics of the Fe–N and Fe–N–C systems; the Fe–N and Fe–N–C phase diagrams revisited

Holger Göhring, Olga Fabrichnaya, Andreas Leineweber, Eric Jan Mittemeijer

Several thermodynamic descriptions of the Fe–N and Fe–N–C systems were proposed until now. The results of these descriptions significantly deviate from more recently obtained experimental data. The present work provides a revised thermodynamic description of these systems. The new description for the Fe–N system agrees distinctly better with the experimental data especially for the equilibrium of γ' -Fe₄N_{1-x} and ϵ -Fe₃N_{1+z}. The new thermodynamic description for the Fe–N–C system considering the Fe-rich part of the system with less than 33 at.% N and less than 25 at.% C excellently agrees with the new experimental data for both the temperatures of the invariant reactions and the phase boundaries. This in particular concerns the temperature range of typical technical nitriding and nitrocarburising treatments (723 K–923 K, 450 °C–650 °C), within which three invariant reactions occur in the ternary system.

6.1 Introduction

The Fe–C, Fe–N and Fe–N–C systems are highly relevant for Fe-based components, in particular if these are subjected to technically applied nitriding and nitrocarburising treatments [1].

Table 6.1: Phases considered in the present work, their crystal structure and formula units of their sublattice models.

phase	space group	structure	formula unit
ferrite, α -Fe[N,C]	$I\bar{m}\bar{3}m$	bcc Fe lattice with N and C on octahedral sites (3 per Fe atom)	$Fe(C,N,Va)_3$
austenite, γ -Fe[N,C]	$Fm\bar{3}m$	fcc Fe with N and C on octahedral sites	$Fe(C,N,Va)$
γ' -Fe ₄ N _{1-z}	$Pm\bar{3}m$	fcc-type Fe lattice, N and C ordered on one octahedral site per unit cell	$Fe_4(C,N,Va)$
ϵ -Fe ₃ (N,C) _{1+x}	$P6_{3}22, P312$	hcp-type Fe lattice, N and C on every second octahedral site with different types of order ^a	$Fe(C,N,Va)_{1/2}$
θ -Fe ₃ C _{1-δ}	$Pnma$	distorted hcp-type Fe lattice, C in trigonal prisms	$Fe_3(C,Va)$

^aThe chosen formula unit of the sublattice model does not assume a specific state of order. It is, however, noted that octahedral sites adjacent in the c direction cannot be occupied simultaneously [64, 65].

The Fe–N–C equilibrium phases considered in the present work have been listed in Table 6.1, as assembled from References 19 and 25.

The binary Fe–C system is the basis of all technically applied steels [133]. The stable phases in the binary Fe–C system [3] are the terminal interstitial solid solution phases α (ferrite) and γ (austenite), the liquid solution phase and graphite. However, due to kinetically obstructed precipitation of graphite, at carbon contents of up to 25 at.%, the iron carbide cementite, θ -Fe₃C_{1- δ} , occurs in metastable equilibria. Recently, the non-stoichiometry of θ in equilibrium with α and γ with positive values of δ , has been quantified [16]. On this basis, a new thermodynamic description for the cementite phase has been presented in Chapter 5, which, in contrast to the previous descriptions [31–34], recognizes and well describes its non-stoichiometric character.

The constitution of compound layers developing upon nitriding of Fe can be predicted by the Fe–N phase diagram [4], assuming local equilibrium in the solid state, featuring the interstitial solid solution phases α (ferrite) and γ (austenite) and the iron nitride phases γ' -Fe₄N_{1-x} and ϵ -Fe₃N_{1+z}. In order to identify such local equilibria, the Fe–N system to be considered, as discussed above for the Fe–C system, represents metastable equilibrium states, corresponding to suppression of the formation of N₂ gas. In genuine equilibria, iron-nitride phases as γ' and ϵ do not occur. Metastable equilibria in the Fe–N system can be investigated by gas-nitriding experiments using NH₃/H₂ atmospheres, defining a chemical potential of N in the gas phase [1]. For data obtained from such gas-nitrided specimens furthermore the establishment of a steady

state instead of a local equilibrium at the surface of the specimens, i.e. equality of the rate of N dissolution and recombination instead of equality of the chemical potential of N in the gas phase and in the solid, has to be considered: the N concentration will then be lower than that corresponding to local metastable equilibrium with the gas atmosphere [1, 30]. The effect becomes significant above approximately 853 K (580 °C) for nitrided ferrite (α) [30] and is more pronounced for increasing nitrogen content in the solid matrix and thus becomes significant at the surface of ϵ -iron nitride (containing > 30 at.% N) already at 723 K (450 °C) [65].

Until today, the experimental data set for the Fe–N system as compiled in Reference 4 is the most complete experimental description of the system and largely provides the basis for the optimisation of thermodynamic parameters in the present work. Recently, some additional data on the constitution of the system have been published [30, 82] that are also considered in the present work. CALPHAD-type thermodynamic descriptions for the Fe–N system have been published in References 31 and 35–43. In general, for the intermediate phases γ' and ϵ , these descriptions only consider random mixing of nitrogen on an interstitial sublattice and thus excess Gibbs energy parameters have to be introduced to describe the deviation of the real system from such ideal behaviour. Theoretical approaches to describe the thermodynamics of nitrogen ordering and disordering have been presented for γ' [20, 22, 200–202] and ϵ [64–66, 200, 203, 204].

Upon nitrocarburising of Fe, a simultaneous uptake of N and C into the substrate occurs [1]. Upon only nitriding of technical steels interactions of N and C already have to be considered as well, due to (initial) C present in the substrate. A first systematic study of the ternary Fe–N–C system has been provided in Reference 129. Subsequent work has been presented in References 83 and 84. All these early works have in common that they do not include the possibility of an $\alpha+\epsilon$ equilibrium. Furthermore, the appearance of γ is concluded to occur at a temperature as low as 838 K (565 °C) in Reference 84, in flagrant contrast with later experimental data [82].

In contrast to these early experimental works [83, 84, 129], the observation of microstructures forming upon nitriding of Fe–C alloys and C-containing steels and upon nitrocarburising of pure Fe, Fe–C alloys and C-containing steels which *do contain* interfaces between α and ϵ [85–92, 94, 96, 205] makes it very likely that equilibrium between α and ϵ does occur, albeit in a narrow temperature range. Later works [29, 75, 79, 82] (see also Chapters 2–4) confirmed the occurrence of such microstructures. Except for an early work [44], the $\alpha+\epsilon$ equilibrium is taken into account in all thermodynamic descriptions of the Fe–N–C system in the literature [39, 41, 43, 45–47]. However, systematic experimental work to investigate the occurrence of the $\alpha+\epsilon$ equilibrium in Reference 75 and Chapter 4 showed that the experimentally determined temperatures of the invariant reactions leading to the appearance of this equilibrium deviate

from the temperatures as predicted using each of the thermodynamic descriptions from the literature [39, 41, 43, 45–47]. Additionally, a recent experimental study of the constitution in the system Fe–N–C for the temperature range above 853 K (580 °C) [82], investigating both the phase boundaries and the temperatures of the invariant reactions involving γ , showed bad agreement with again each of the thermodynamic descriptions from the literature [39, 41, 43, 45–47]. Finally, analysis of the thermodynamic factors derived from N and C diffusivities in ternary ϵ at 823 K (550 °C) in Reference 81 and 853 K (580 °C) in Chapter 2 showed agreement with the thermodynamic descriptions of ϵ given in References 39 and 43 and disagreement with the one from Reference 41.

In the present work, new thermodynamic assessments of the Fe–N and Fe–N–C systems are presented, using the newly obtained data in the optimization process in order to eliminate the discrepancies associated with the previous thermodynamic descriptions. As a result, for the first time a description of the Fe–N–C system was obtained that is compatible with all experimental data and thus is suitable for nitriding and nitrocarburising applications. Furthermore, significant improvements in the description of the binary Fe–N system were achieved: (i) a simpler model for the γ' phase, accounting for its homogeneity range but using fewer parameters than the thermodynamic description from Reference 41 and (ii) an improved description of the $\gamma'+\epsilon$ equilibrium at high N contents.

6.2 Thermodynamic model of the Fe–N and Fe–N–C solid solution phases

The Fe–N and Fe–N–C solid solution phases can be described by the compound-energy formalism [50, 51], also called Hillert-Staffansson approach [52]. In the following, only an Fe–N–C solid solution phase is considered; a similar treatment is used for an Fe–N (and an Fe–C) solid solution phase.

The interstitial solution of N and C in a phase φ is considered as a mixture of the hypothetical compounds Fe_aC_c , Fe_aN_c and Fe_aVa_c (with Va standing for vacancies) with a and c being stoichiometric indices determined by the crystal structure of the phase φ . The total Gibbs energy of the phase φ with the formula $\text{Fe}_a(\text{C},\text{N},\text{Va})_c$ per formula unit reads

$$G_m^\varphi = y_C^\varphi G_{\text{Fe:C}}^\varphi + y_N^\varphi G_{\text{Fe:N}}^\varphi + y_{\text{Va}}^\varphi G_{\text{Fe:Va}}^\varphi + cRT(y_C^\varphi \ln y_C^\varphi + y_N^\varphi \ln y_N^\varphi + y_{\text{Va}}^\varphi \ln y_{\text{Va}}^\varphi) + G^{\varphi,\text{ex}} + G^{\varphi,\text{mag}}, \quad (6.1)$$

with y_C^φ , y_N^φ and y_{Va}^φ representing the fractions of sublattice occupancies of C, N and Va, respectively, recognizing that the first sublattice is always completely occupied by Fe, i.e. $y_{\text{Fe}}^\varphi = 1$,

the Gibbs energies ${}^\circ G_{\text{Fe:C}}^\varphi$, ${}^\circ G_{\text{Fe:N}}^\varphi$ and $\varphi {}^\circ G_{\text{Fe:Va}}^\varphi$ of the hypothetical non-magnetic compounds Fe_aC_c , Fe_aN_c and Fe_aVa_c , the so-called end-members, with Fe:C , Fe:N and Fe:Va denoting that the second sublattice is fully occupied by C, N and Va, respectively, the excess Gibbs energy $G^{\varphi,\text{ex}}$ and the magnetic contribution $G^{\varphi,\text{mag}}$.

The Gibbs energy of the end members is usually described as a temperature series according to e.g. for Fe_aN_c :

$${}^\circ G_{\text{Fe:N}}^\varphi - a {}^\circ G_{\text{Fe}}^{\text{ref}} - c {}^\circ G_{\text{N}}^{\text{ref}} = a + bT + cT \ln T + d_1 T^2 + d_2 T^{-1} + d_3 T^3 \dots \quad (6.2)$$

with the reference Gibbs energies for Fe and N, ${}^\circ G_{\text{Fe}}^{\text{ref}}$ and ${}^\circ G_{\text{N}}^{\text{ref}}$ and the model parameters a , b , c , d_i . The reference state is usually the SER state, i.e. the enthalpy of the elements in their most stable state at 298 K (25 °C) and 1×10^5 Pa.

The excess Gibbs energy is described as

$$G^{\varphi,\text{ex}} = y_{\text{C}}^\varphi y_{\text{N}}^\varphi L_{\text{Fe:C,N}}^\varphi + y_{\text{C}}^\varphi y_{\text{Va}}^\varphi L_{\text{Fe:C,VA}}^\varphi + y_{\text{N}}^\varphi y_{\text{Va}}^\varphi L_{\text{Fe:N,VA}}^\varphi, \quad (6.3)$$

only considering binary interaction parameters $L_{\text{Fe:C,N}}^\varphi$, $L_{\text{Fe:C,VA}}^\varphi$ and $L_{\text{Fe:N,VA}}^\varphi$, with their composition dependence described by a Redlich-Kister series [57]:

$$L_{\text{Fe:C,N}}^\varphi = \sum_k k L_{\text{Fe:C,N}}^\varphi (y_{\text{C}}^\varphi - y_{\text{N}}^\varphi)^k, \quad (6.4)$$

and analogously for $L_{\text{Fe:C,VA}}^\varphi$ and $L_{\text{Fe:N,VA}}^\varphi$. In the present work, interaction parameters of zeroth and first order are used (i.e. $k = 0, 1$). These treatments correspond to a regular and a sub-regular solution model, respectively, whereas $G^{\varphi,\text{ex}} = 0$ corresponds to an ideal solution model [54]. For the magnetic contribution $G^{\varphi,\text{mag}}$ of the α , γ and θ phases, the Inden model [55, 56] is used, taking the magnetic moment β^φ and the Curie (for α and θ) or Néel (for γ) temperature T_{Curie}^φ , or $T_{\text{Néel}}^\varphi$, as (potentially concentration-dependent) model parameters, as described in detail in Reference [50]. For γ' and ε no separate magnetic contribution is modelled (see Section 6.4).

6.3 Employed data for the thermodynamic parameter optimization

6.3.1 Binary Fe–N data

For the binary system Fe–N, the data as assembled in Reference 4 ([20, 21, 28, 83, 84, 174, 206–222]) was chosen according to the recommendations given there. The binary thermodynamic

descriptions of the α and γ phase were taken from Reference 41; for the choice of parameters to be optimized, see Section 6.4. Thus, only equilibrium data including the phases γ' or ϵ have been used, in particular the data for the $\alpha+\gamma'$, $\gamma+\gamma'$, $\gamma+\epsilon$ and $\gamma'+\epsilon$ two-phase equilibria. The available data are compositions and activities at the phase boundaries. If instead of activities the nitriding potential, a (technical) process parameter [1], was given, the activities were calculated using the Gibbs-energy equations for various gas species given in Reference 26. Newer data for the $\gamma \rightleftharpoons \alpha + \gamma'$ invariant equilibrium and the $\alpha + \gamma'$ two-phase equilibrium [30, 223, 224] and the $\gamma + \gamma'$ and $\gamma + \epsilon$ equilibria [82, 223] were also included. As an additional information, the activity curves for γ' from References 20 and 21 and for ϵ in References 36 and 225 were used. However, these so-called absorption isotherms obtained from gaseous nitriding of Fe specimens are affected by the establishment of steady states instead of true metastable equilibrium at the surface of the specimen at higher temperatures and N contents [1, 30, 65], making it impossible to use all data above 823 K (550 °C). Already at lower temperatures, but high N contents (> 30 at.%), a steady state instead of an equilibrium prevails at the surface. Therefore, such affected data have not been used during the optimization. Furthermore, during the optimization process, agreement of the model with the activity data has been considered less important than agreement with the information on solid-solid equilibria.

Based on this experimental information, the parameters ${}^0G_{\text{Fe:N}}^{\gamma'}$ and ${}^0G_{\text{Fe:Va}}^{\gamma'}$ of γ' and the parameters ${}^0L_{\text{Fe:N, Va}}^{\epsilon}$ and ${}^1L_{\text{Fe:N, Va}}^{\epsilon}$ of ϵ were optimized.

6.3.2 Ternary Fe–N–C data

For the optimization process of the model parameters for the ternary Fe–N–C system, almost only recently published data was used. During the optimization, care was taken that the resulting invariant temperatures comply with the ranges as determined experimentally in Reference 82 and Chapter 4. The second source of data was the location of the phase boundaries at 853 K (580 °C) and at 893 K (620 °C) as determined experimentally in Reference 82. The experimental information that in the considered C and N content ranges the off-diagonal components of the thermodynamic factor of ϵ are positive (see Reference 81 and Chapter 2) was used as a constraint for the model of the ϵ phase. Additionally, the N-solubility data in C-containing γ from Reference 226 was used.

For the C content of γ' , no reliable equilibrium data is available. EPMA investigations on specimens produced for the investigations in Chapters 2–4 and Reference 81 showed C contents in γ' which were always below 1 at.%. Therefore, during the optimization care was taken that this level of C content was not exceeded considerably. In θ only trace amounts of N have been found at temperatures ≤ 1073 K (800 °C) [17]. At lower temperatures, θ layers can be

produced on Fe substrates by heat treatment in an atmosphere containing CO, NH₃ and H₂ [74]. During the treatment, the substrate is gradually saturated with N that has diffused through θ [78], eventually leading to formation of an ε layer underneath the θ layer [29]. θ produced under these conditions has been investigated by atom probe tomography [18], revealing, nevertheless, a maximum total impurity content of only 0.01 at.%, also including N. This supports the above experimental results of Reference 17 and is in contrast with the prediction of N contents of > 1 at.% resulting from the thermodynamic description of Reference 41.

On the basis of these ternary experimental data, the binary parameters ${}^0G_{\text{Fe:C}}^{\gamma'}$ of γ' and ${}^0L_{\text{Fe:C,Va}}^{\epsilon}$ and ${}^1L_{\text{Fe:C,Va}}^{\epsilon}$ of ε, which are only relevant for the ternary system, and the ternary parameters ${}^0L_{\text{Fe:C,N}}^{\gamma}$ of γ and ${}^0L_{\text{Fe:C,N}}^{\epsilon}$ and ${}^1L_{\text{Fe:C,N}}^{\epsilon}$ of ε were optimized.

6.4 Applied models; optimization process

The descriptions for the Gibbs energy of the pure elements were taken from Reference 49. The formula units of the sublattice models applied in the present work for each phase have been listed in Table 4.1. The values for the parameters of the thermodynamic description for the α phase were taken from Reference 41. For the γ phase, only the parameter ${}^0L_{\text{Fe:C,N}}^{\gamma}$ was included in the optimization (see end of Section 6.3.2). The values of the binary parameters of γ were taken from References 32 and 41.

The thermodynamic parameters of γ' were completely reassessed (see end of Sections 6.3.1 and 6.3.2). In the model for γ' from Reference 41, ${}^0G_{\text{Fe:Va}}^{\gamma'}$ had been set equal to $4{}^0G_{\text{Fe:Va}}^{\gamma}$. In order to correctly model the thermodynamics of γ' , then the interaction parameters ${}^0L_{\text{Fe:N,Va}}^{\gamma'}$ and ${}^1L_{\text{Fe:N,Va}}^{\gamma'}$ (both T -dependent) had to be introduced in Reference 41. In the present work, ${}^0G_{\text{Fe:Va}}^{\gamma'}$ was used as an optimization variable, eliminating the need for any interaction parameters for γ' and thus reducing the number of parameters as compared to the model of Reference 41. Due to lack of accurate data for the C solubility in γ' , the parameter ${}^0G_{\text{Fe:C}}^{\gamma'}$ was fixed to a value giving a reasonable homogeneity range of γ' in the ternary Fe–N–C system. The γ' phase shows ferromagnetic ordering with a somewhat concentration-dependent Curie temperature around 763 K (490 °C) [4]. As there is no heat-capacity data available, which would allow to introduce the magnetic moment as a fitting parameter, no magnetic model is used¹.

The thermodynamic description for the θ phase was taken directly from Chapter 5. No N solubility had to be modelled as explained in Section 6.3.2.

¹It was shown in Chapter 5, providing a new thermodynamic description for θ, that the magnetic moments obtained from fitting, specifically of c_p curves, are far from experimentally obtained values. Therefore it was avoided to use such values for the thermodynamic descriptions of γ' and ε in the present work.

For the ϵ phase, the sublattice model of $\text{Fe}(\text{C},\text{N},\text{Va})_{1/2}$ as used in References 41 and 45–47 was also applied in the present work. The ϵ phase shows magnetic ordering with a Curie temperature strongly varying with, at least, the N content between 10 K and 550 K (-260°C – 280°C) [4]. As for the γ' phase, the lack of heat-capacity data prevents fitting for the magnetic moment, so no magnetic contribution was modelled¹. The value of the parameter ${}^0G_{\text{Fe:N}}^\epsilon$ was taken from Reference 41 as during re-optimization attempts on the basis of the available equilibrium data, the ϵ phase became unreasonably stable at high temperature. It was also attempted to include the parameter ${}^0G_{\text{Fe:C}}^\epsilon$ in the optimization. This led to the unreasonable appearance of the ϵ phase in the binary Fe–C system instead of θ for a large temperature range. Thus it was decided to keep the value from Reference 227 as also used in Reference 41. The optimization process revealed that several binary interaction parameters of zeroth and first order (sub-regular solution model) were necessary in order to obtain an acceptable description of the ϵ phase (see also the discussion in Sections 6.1 and especially 6.5.4). The introduction of ternary interaction parameters was not necessary.

The resulting model parameters as determined in this work and as taken from the literature are presented in Table 6.2. If desired, the model for the Fe–N–C liquid phase from Reference 46 can be included.

6.5 Discussion

6.5.1 The binary Fe–N phase diagram

The temperatures and the compositions of the phases at the invariant equilibria in the Fe–N system, as predicted by the thermodynamic description resulting from the present work, can be compared with the experimental data from References 4, 30 and 82 and the previous predictions from References 41 and 43 in Table 6.3. The agreement of these features of the Fe–N phase diagram with the experimental data is comparably good for the new and old [41, 43] thermodynamic descriptions.

The Fe–N phase diagram as calculated using the model parameters from the present work is shown in Figure 6.1. Various enlarged sections of the phase diagram are shown in Figure 6.2 to allow a more detailed comparison with both the experimental data [20, 21, 30, 82–84, 174, 206, 207, 209–214, 216–219, 221, 223, 224] and the previous predictions from References 41 and 43.

The homogeneity range of α agrees well with the experimental data and with the homogeneity range resulting from the thermodynamic description of Reference 41 (see Figure 6.2a). The newer experimental data from Reference 30 are better described by the thermodynamic description from Reference 43. This description, however, shows an $\alpha+\epsilon$ equilibrium below

Table 6.2: Thermodynamic model parameters for the solid solution phases as determined in the present work and as taken from the cited literature to be used with the unary Gibbs-energy functions from Reference 49. T in K, values of Gibbs energy and interaction parameters in J mol^{-1} .

α , model $\text{Fe}(\text{C},\text{N},\text{Va})_3$
${}^\circ G_{\text{Fe};\text{Va}}^{\alpha,\text{non-mag}} = {}^\circ G_{\text{Fe}}^{\alpha,\text{non-mag}}$
${}^\circ G_{\text{Fe};\text{C}}^{\alpha,\text{non-mag}} - {}^\circ G_{\text{Fe}}^{\alpha,\text{non-mag}} - 3 {}^\circ G_{\text{C}}^{\text{gra}} = 322050 + 75.667T$ [32]
${}^\circ G_{\text{Fe};\text{N}}^{\alpha,\text{non-mag}} - {}^\circ G_{\text{Fe}}^{\alpha,\text{non-mag}} - \frac{3}{2} {}^\circ G_{\text{N}_2}^{\text{gas}} = 93562 + 165.07T$ [40]
${}^0 L_{\text{Fe};\text{C},\text{Va}}^{\alpha/\delta} = -190T$ [32]
$\beta_{\text{Fe};\text{Va}}^\alpha = \beta_{\text{Fe};\text{C}}^\alpha = \beta_{\text{Fe};\text{N}}^\alpha = \beta_{\text{Fe}}^\alpha = 2.22$ [32, 40]
$T_{\text{Curie},\text{Fe};\text{Va}}^\alpha = T_{\text{Curie},\text{Fe};\text{C}}^\alpha = T_{\text{Curie},\text{Fe};\text{N}}^\alpha = T_{\text{Curie},\text{Fe}}^\alpha = 1043$ [32, 40]
γ , model $\text{Fe}(\text{C},\text{N},\text{Va})$
${}^\circ G_{\text{Fe};\text{Va}}^{\gamma,\text{non-mag}} = {}^\circ G_{\text{Fe}}^{\gamma,\text{non-mag}}$
${}^\circ G_{\text{Fe};\text{C}}^{\gamma,\text{non-mag}} - {}^\circ G_{\text{Fe}}^{\gamma,\text{non-mag}} - {}^\circ G_{\text{C}}^{\text{gra}} = 77207 - 15.877T$ [32]
${}^\circ G_{\text{Fe};\text{N}}^{\gamma,\text{non-mag}} - {}^\circ G_{\text{Fe}}^{\gamma,\text{non-mag}} - \frac{1}{2} {}^\circ G_{\text{N}_2}^{\text{gas}} = -20277 + 245.3931T - 21.2984T \ln T$ [41]
${}^0 L_{\text{Fe};\text{C},\text{Va}}^\gamma = -34671$ [32]
${}^0 L_{\text{Fe};\text{N},\text{Va}}^\gamma = -26150$ [35]
${}^0 L_{\text{Fe};\text{C},\text{N}}^\gamma = 8218$
$\beta_{\text{Fe};\text{Va}}^\gamma = \beta_{\text{Fe};\text{C}}^\gamma = \beta_{\text{Fe}}^\gamma = 0.7$ [32]
$T_{\text{Néel},\text{Fe};\text{Va}}^\gamma = T_{\text{Néel},\text{Fe};\text{C}}^\gamma = T_{\text{Néel},\text{Fe}}^\gamma = 67$ [32]
γ' , model $\text{Fe}_4(\text{C},\text{N},\text{Va})$
${}^\circ G_{\text{Fe};\text{C}}^{\gamma'} - 4 {}^\circ G_{\text{Fe}}^{\alpha,\text{non-mag}} - {}^\circ G_{\text{C}}^{\text{gra}} = 20000$
${}^\circ G_{\text{Fe};\text{N}}^{\gamma'} - 4 {}^\circ G_{\text{Fe}}^{\alpha,\text{non-mag}} - \frac{1}{2} {}^\circ G_{\text{N}_2}^{\text{gas}} = -37744 + 72.786T$
${}^\circ G_{\text{Fe};\text{Va}}^{\gamma'} - 4 {}^\circ G_{\text{Fe}}^{\alpha,\text{non-mag}} = 12066 + 3.691T$
ε , model $\text{Fe}(\text{C},\text{N},\text{Va})_{1/2}$
${}^\circ G_{\text{Fe};\text{Va}}^\varepsilon = {}^\circ G_{\text{Fe}}^\varepsilon$
${}^\circ G_{\text{Fe};\text{C}}^\varepsilon - {}^\circ G_{\text{Fe}}^\varepsilon - \frac{1}{2} {}^\circ G_{\text{C}}^{\text{gra}} = 52905 - 11.9075T$ [227]
${}^\circ G_{\text{Fe};\text{N}}^\varepsilon - {}^\circ G_{\text{Fe}}^\varepsilon - \frac{1}{4} {}^\circ G_{\text{N}_2}^{\text{gas}} = -13863 + 40.2123T$ [41]
${}^0 L_{\text{Fe};\text{C},\text{Va}}^\varepsilon = -53059$
${}^1 L_{\text{Fe};\text{C},\text{Va}}^\varepsilon = -38756$
${}^0 L_{\text{Fe};\text{N},\text{Va}}^\varepsilon = 8186 - 18.127T$
${}^1 L_{\text{Fe};\text{N},\text{Va}}^\varepsilon = -24378 + 24.959T$
${}^0 L_{\text{Fe};\text{C},\text{N}}^\varepsilon = -20772 - 32.504T$
${}^1 L_{\text{Fe};\text{C},\text{N}}^\varepsilon = -28839$
θ , model $\text{Fe}_3(\text{C},\text{Va})$
${}^\circ G_{\text{Fe};\text{C}}^{\theta,\text{non-mag}} - 3 H_{\text{Fe}}^{\text{SER}} - H_{\text{C}}^{\text{SER}} =$
$-8983 + 658.38T - 113.578T \ln T - 3.059 \times 10^{-3}T^2 + 6.105 \times 10^5T^{-1}$ (see Chapter 5)
${}^\circ G_{\text{Fe};\text{Va}}^{\theta,\text{non-mag}} - 3 {}^\circ G_{\text{Fe}}^{\alpha,\text{non-mag}} = 44782 - 11.59T$ (see Chapter 5)
$\beta_{\text{Fe};\text{C}}^\theta = \beta_{\text{Fe};\text{Va}}^\theta = 1.51$ (see Chapter 5)
$T_{\text{Curie},\text{Fe};\text{C}}^\theta = T_{\text{Curie},\text{Fe};\text{Va}}^\theta = 485$ [33]

Table 6.3: Comparison of temperatures and compositions of phases participating in the invariant reactions. “exp” = experimentally determined; “pred” = predicted by a thermodynamic description.

reaction	reference	T / K	$x_{\text{N}}^{\alpha} / \text{at.\%}$	$x_{\text{N}}^{\gamma} / \text{at.\%}$	$x_{\text{N}}^{\gamma'} / \text{at.\%}$	$x_{\text{N}}^{\epsilon} / \text{at.\%}$
$\epsilon \rightleftharpoons \gamma'$	present work (pred)	964			19.6	19.6
	[4] (exp)	953			19.5	19.5
	[82] (exp)	938–948			N/A	N/A
	[41] (pred)	971			19.4	19.4
	[43] (pred)	955			19.6	19.6
$\epsilon \rightleftharpoons \gamma + \gamma'$	present work (pred)	923		9.7	19.1	16.3
	[4] (exp)	923		10.3	19.3	15.9
	[82] (exp)	923–925			N/A	N/A
	[41] (pred)	923		9.7	19.1	16.1
	[43] (pred)	923		10.3	19.6	15.9
$\gamma \rightleftharpoons \alpha + \gamma'$	present work (pred)	865 (592)	0.39	9.0	19.2	
	[4] (exp)	865	0.40	8.8	19.3	
	[30] (exp)	866	0.44		N/A	N/A
	[41] (pred)	863	0.39	9.0	19.3	
	[43] (pred)	867	0.40	8.9	19.6	

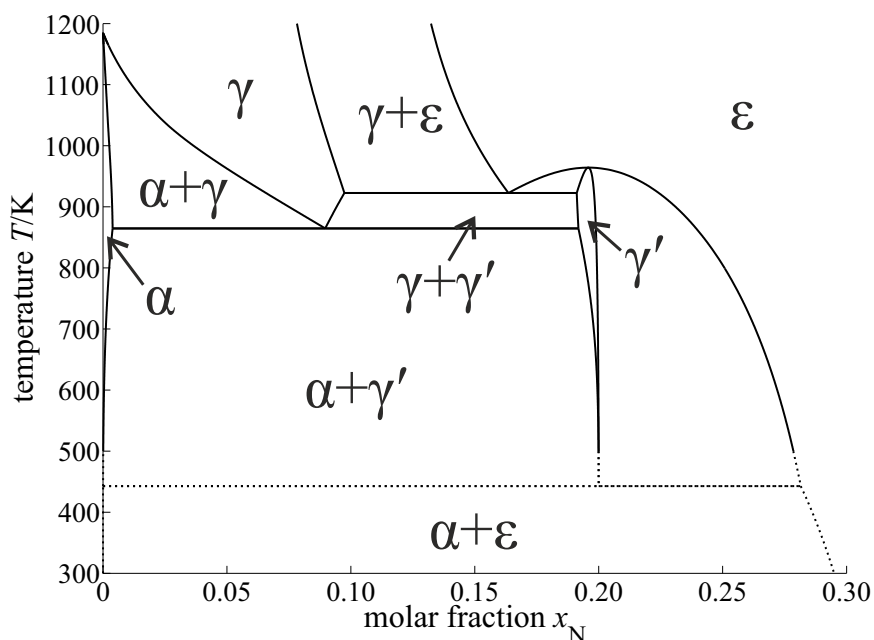


Figure 6.1: The Fe–N phase diagram as calculated using the thermodynamic description from the present work, suppressing formation of the N_2 gas phase. At a temperature below 443 K (170 °C), an $\alpha + \epsilon$ equilibrium is predicted, see the dotted lines (see discussion in Section 6.5.2)

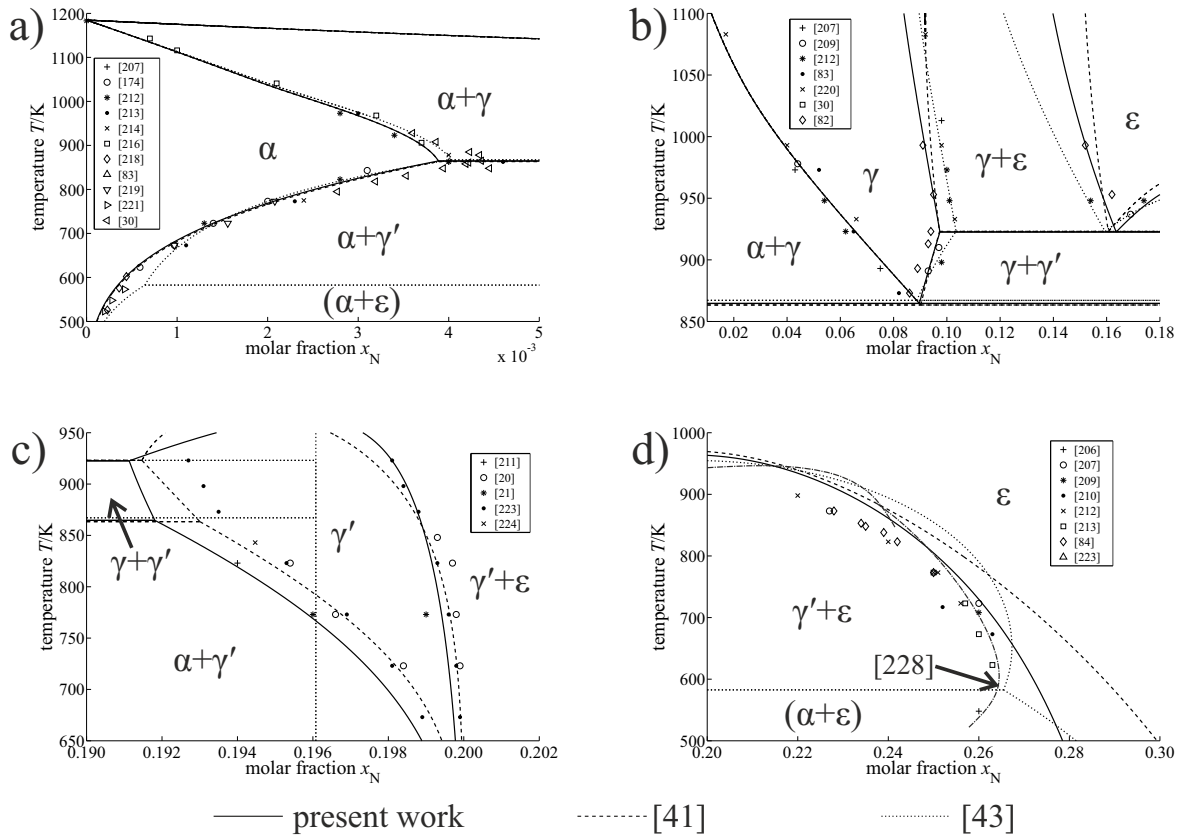


Figure 6.2: Magnified sections of the Fe–N phase diagram as calculated using the thermodynamic description from the present work (solid lines) in comparison to (i) the phase diagrams as calculated using the descriptions from Reference 41 (dashed lines) and 43 (dotted lines) and (ii) various experimental data. An $\alpha+\epsilon$ equilibrium is predicted using the description of Reference 43 in the shown temperature range. a) Low N-content range with experimental data from References 30, 83, 174, 207, 212–214, 216, 218, 219 and 221. b) Equilibria involving the γ phase compared with experimental data from References 30, 82, 83, 207, 209, 212 and 220. c) The homogeneity range of γ' compared with experimental data from References 20, 21, 211, 223 and 224. Note that the thermodynamic description of Reference 43 describes γ' as a stoichiometric compound with the formula $\text{Fe}_{4.1}\text{N}$. d) The $\gamma'+\epsilon/\epsilon$ phase boundary compared with experimental data from References 84, 206, 207, 209, 210, 212, 217 and 223. Also, the phase boundary redrawn from Figure 4 in Reference 228 (variant for low N content) is shown..

approximately 580 K (310 °C), a temperature at which the $\alpha+\gamma'$ equilibrium is observed experimentally (see also below) and therefore disagrees with the experimental phase-boundary data at low temperatures (cf. Figure 6.2a).

The calculated phase boundaries of the γ single-phase field agree well with the few available experimental data, see Figure 6.2b. Experimental data on the phase boundaries $\gamma/\gamma+\gamma'$ and $\gamma/\gamma+\epsilon$ is somewhat contradictory: recent investigations obtained by EPMA measurements on nitrided specimens [82] showed N contents of up to 1 at.% less than given in older works [207, 209, 212, 220]. For the phase boundary $\gamma/\gamma+\gamma'$, the predictions by the thermodynamic description from the present work lie between these values. For the phase boundary $\gamma/\gamma+\epsilon$, the data from Reference 82 is described better than the data from References 207, 209, 212 and 220. Overall, a good representation of all data employed in the optimisation is given, also accounting for the error margins of the usually applied EPMA method to determine these phase-boundary compositions.

The $\gamma'/\gamma+\epsilon$ phase boundary agrees well with the experimental data from Reference 223, whereas the N content at the phase boundary $\alpha+\gamma'/\gamma'$ is lower than indicated by most of the experimental data and by the phase boundary as calculated using the thermodynamic description from Reference 41, but still agrees within less than 0.1 at.% (see Figure 6.2c). Better agreement could be achieved by introducing a more advanced model considering N disorder, see Section 6.5.3.

The thermodynamic description from the present work reproduces the phase boundary $\gamma'+\epsilon/\epsilon$ significantly better than the previous descriptions [41,43] (see Figure 6.2d). The data point from Reference 206 and semi-quantitative investigations in Reference 134 suggest that the phase boundary $\gamma'+\epsilon/\epsilon$ might extend to lower N contents in the low- T range. In this low- T range, the agreement of the experimental data with the phase boundary from Reference 228, based on a thermodynamic description considering ordering of N on its sublattice, is better, which is also shown in Figure 6.2d. The thermodynamic description of Reference 228, however, gives multiple expressions for the phase boundary in order to cover the whole temperature range (see the overlap of the two curves in Figure 6.2d). Moreover, in the high- T range, the agreement with the experimental data is poor and there is a maximum in the proposed phase boundary. This is thermodynamically only possible if the congruent transition $\epsilon \rightleftharpoons \gamma'$ occurs at N contents as high as 21.2 at.%, which is impossible according to the model from the present work (maximum N content of γ' is 20 at.%) and also incompatible with the prediction according to the model for γ' from Reference 228.

A “potential phase diagram” using the activity of N (reference state N_2 gas at 1×10^5 Pa and at the considered temperature) as a variable is shown in Figure 6.3a, allowing comparison of the

phase boundaries as calculated using the thermodynamic description from the present work with the respective phase boundaries as calculated using the datasets from References 41 and 43, the phase boundary γ'/ϵ as calculated using the expressions given in Reference 228, and the phase boundaries as indicated by the experimental data [20, 21, 28, 30, 208, 210, 214, 215, 217, 222]. The same diagram using as a variable the often applied nitriding potential

$$r_N = \frac{P_{NH_3}}{P_{H_2}^{3/2}}, \quad (6.5)$$

a (technical process) parameter used for gaseous nitriding, which is a measure for the activity of N, but multiplied with ${}^{\circ}p^{1/2}$ (where ${}^{\circ}p = 1 \times 10^5$ Pa is the pressure of the reference state, to obtain a dimensionless variable [1]), is given in Figure 6.3b. For the phase boundary α/γ' , the thermodynamic dataset of the present work describes the experimental data equally well as the dataset published in Reference 41. For the γ range, the thermodynamic descriptions from the present work and from References 41 and 43 reproduce the experimental data well. However, the phase boundary γ'/ϵ as calculated using the thermodynamic dataset of the present work agrees significantly better with the experimental data than the phase boundaries resulting from the previous descriptions of References 41 and 43. The phase boundary γ'/ϵ is even better described with the expressions given in Reference 228. However, in that work direct least-squares fitting of the phase boundary was performed, yielding several expressions for different temperature ranges. The thermodynamics of both the binary and ternary γ' and ϵ phases are discussed in a comparative manner in Sections 6.5.3 and 6.5.4, respectively.

Including the thermodynamic description of the liquid Fe–N phase from Reference 40 peritectic melting of ϵ is predicted in the binary Fe–N system at 1654 K (1381 °C). A similar prediction is obtained from the thermodynamic descriptions of the Fe–N system of References 40 and 41. The thermodynamic descriptions from References 39 and 43, however, predict a congruent transition $\gamma'=\epsilon$. Since there is no corresponding experimental data available, no conclusion can be drawn which variant is correct. Nevertheless, the shape of the γ phase field as predicted by References 39 and 43 seems unrealistic. Thus, the thermodynamic description involving peritectic melting is the preferred one, at least until more experimental data is available.

At low temperatures, an $\alpha+\epsilon$ equilibrium is predicted by the presently obtained thermodynamic description, which disappears upon heating at 443 K (170 °C, see the dotted lines in Figure 6.1). The same feature at low temperature is predicted using the thermodynamic descriptions from References 39, 41 and 43. The appearance of an $\alpha+\epsilon$ equilibrium at low temperatures is not necessarily a modelling artefact: experimental investigations [229–231] suggested that ϵ was in equilibrium with α at low temperatures (approximately ≤ 550 K, 280 °C). Another work [134]

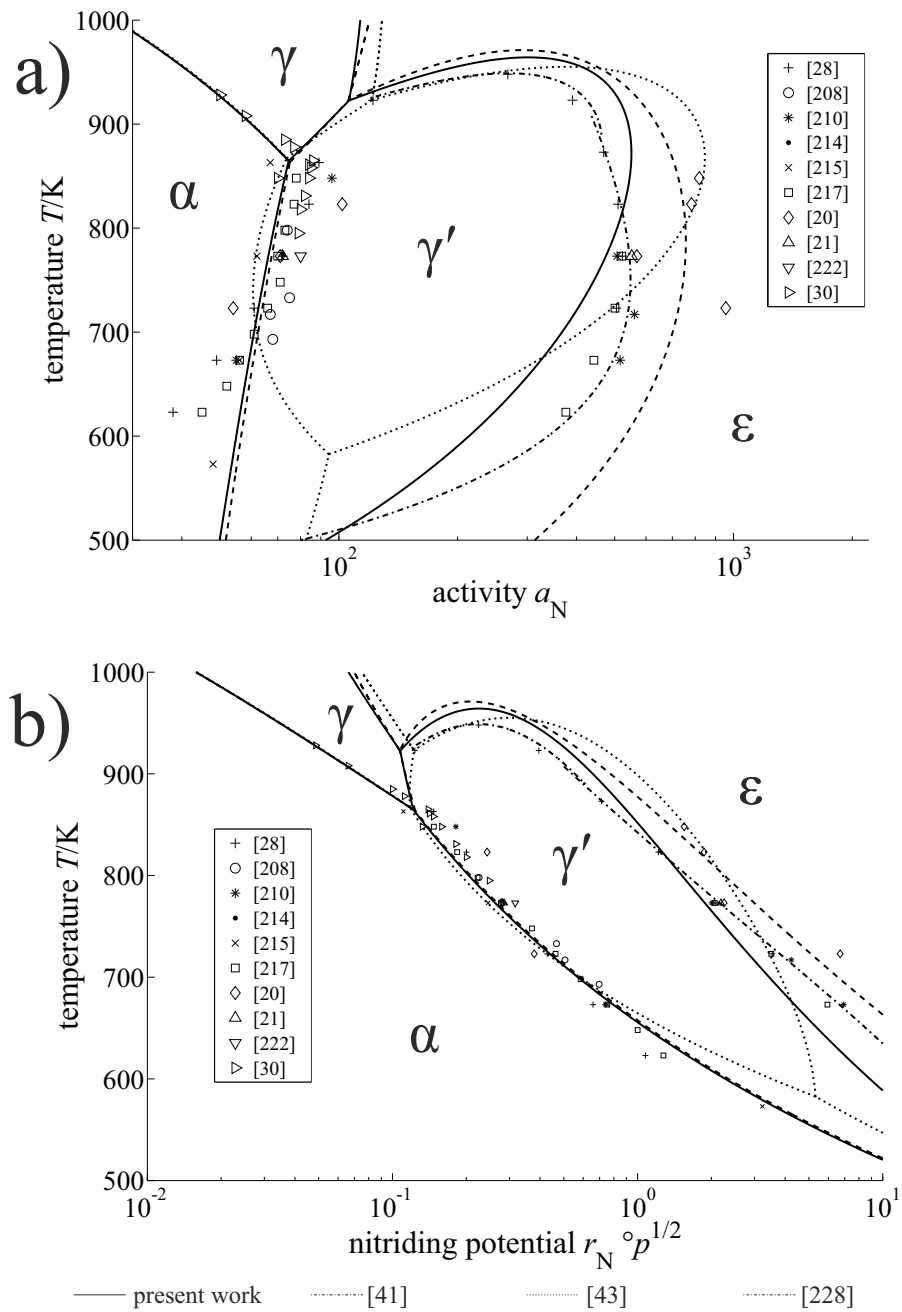


Figure 6.3: Potential phase diagrams as calculated using the thermodynamic description from the present work (solid lines), and as calculated using the descriptions from References 41 (dashed lines) and 43 (dotted lines). For comparison, the phase boundary γ'/ϵ as given by Equations [14b/c] in Reference 228 (dash-dot lines) and experimental data for the phase boundaries from References 20, 21, 28, 30, 208, 210, 214, 215, 217 and 222 are also shown. a) Using the activity of N as a variable (reference state N_2 gas at 1×10^5 Pa and the respective temperature). b) Using the nitriding potential $r_N = p_{NH_3}/p_{H_2}^{3/2}$ (multiplied with $p^{1/2}$ to obtain a dimensionless quantity) as a variable, which is a measure for the activity of N [1].

excluded the possibility of the $\alpha+\epsilon$ equilibrium in the binary Fe–N system at low temperatures and discussed the possible formation of the cubic $\alpha''\text{-Fe}_{16}\text{N}_2$ nitride as an equilibrium phase, which was not included in the present assessment. At least at 623 K (350 °C) (and at higher temperatures), precipitation of γ' from ϵ was still observed [232]. However, due to the very slow kinetics at those low temperatures it is difficult to reach a genuine equilibrium state and this prohibits to draw a final conclusion. Finally, as a fine point, recent ab-initio calculations pertaining to 0 K (−273 °C) [233, 234] indicate that a mechanical mixture of pure α -Fe and $\epsilon\text{-Fe}_3\text{N}$ with a gross N content of 20 at.% has a lower enthalpy than pure $\gamma'\text{-Fe}_4\text{N}$, supporting the occurrence of an $\alpha+\epsilon$ equilibrium at low temperature. It is noted that this point was not addressed specifically in these works [233, 234].

6.5.2 The ternary Fe–N–C system

A Scheil reaction scheme [156–158] illustrating the sequence of invariant reactions as resulting from the present thermodynamic description of the Fe–N–C system is shown in Figure 6.4. The temperatures of the invariant reactions in the Fe–N–C system as calculated using the thermodynamic description of the present work can be compared in Table 6.4 with the corresponding experimental data and the predictions as obtained using the thermodynamic descriptions from References 41 and 43, which are the two thermodynamic descriptions giving the best agreement with experimentally determined invariant temperatures (see Reference 82 and Chapter 4) according to the detailed discussion in Chapter 4. Both Figure 6.4 and Table 6.4 use the designations for the invariant reactions introduced in Chapter 4. The possibilities for the sequence of invariant reactions in the system Fe–N–C below 853 K (580 °C) have been discussed in detail in Chapter 4, offering two possibilities realized by the previous various thermodynamic descriptions for the Fe–N–C system [39, 41, 43, 45–47]. In the first case, upon cooling, the $\alpha+\epsilon$ equilibrium is replaced by the $\gamma'+\theta$ equilibrium via a single transition reaction U_2 , $\alpha+\epsilon \rightleftharpoons \gamma'+\theta$. In the second case, upon cooling, the $\gamma'+\theta$ equilibrium first appears via the pseudo-binary eutectoid reaction e_4 , $\epsilon \rightleftharpoons \gamma'+\theta$, dividing the ϵ single phase field into two separate ϵ single phase fields. Subsequently, the second ϵ single phase field vanishes via the ternary eutectoid reaction E_2 , $\epsilon \rightleftharpoons \alpha+\gamma'+\theta$. *The thermodynamic description of the present work reproduces the first sequence of invariant reactions (see Figure 6.4).*

The temperature of the transitional reaction U_2 as calculated using the dataset from the present work (839 K, 566 °C) is only slightly below the value of the temperature for this reaction as determined experimentally in Chapter 4 (842 ± 2 K, 569 ± 2 °C). The here predicted temperatures of the U_1 and E_1 invariant reactions are within the boundaries determined experimentally for these reactions in Reference 82. The previous thermodynamic descriptions for

Table 6.4: Comparison of the temperatures of the invariant reactions in the ternary Fe–N–C system, using the designations for the invariant reactions introduced in Chapter 4. All values in K; as predicted by the present thermodynamic description and the descriptions from References 41 and 43 and as experimentally determined in the cited literature.

reaction	experiment	this work	Reference 41	Reference 43
$U_1, \gamma+\theta \rightleftharpoons \alpha+\epsilon$	868–873 [82]	873	867	952
$E_1, \gamma \rightleftharpoons \alpha+\gamma'+\epsilon$	853–863 [82]	857	859	857
$U_2 \alpha+\epsilon \rightleftharpoons \gamma'+\theta$	842 ± 2 (see Chapter 4)	839	783	–
$E_2, \epsilon \rightleftharpoons \gamma'+\theta$	840–844 (see Chapter 4)	–	–	833
$e_4, \epsilon \rightleftharpoons \alpha+\gamma'+\theta$	840–844 (see Chapter 4)	–	–	825

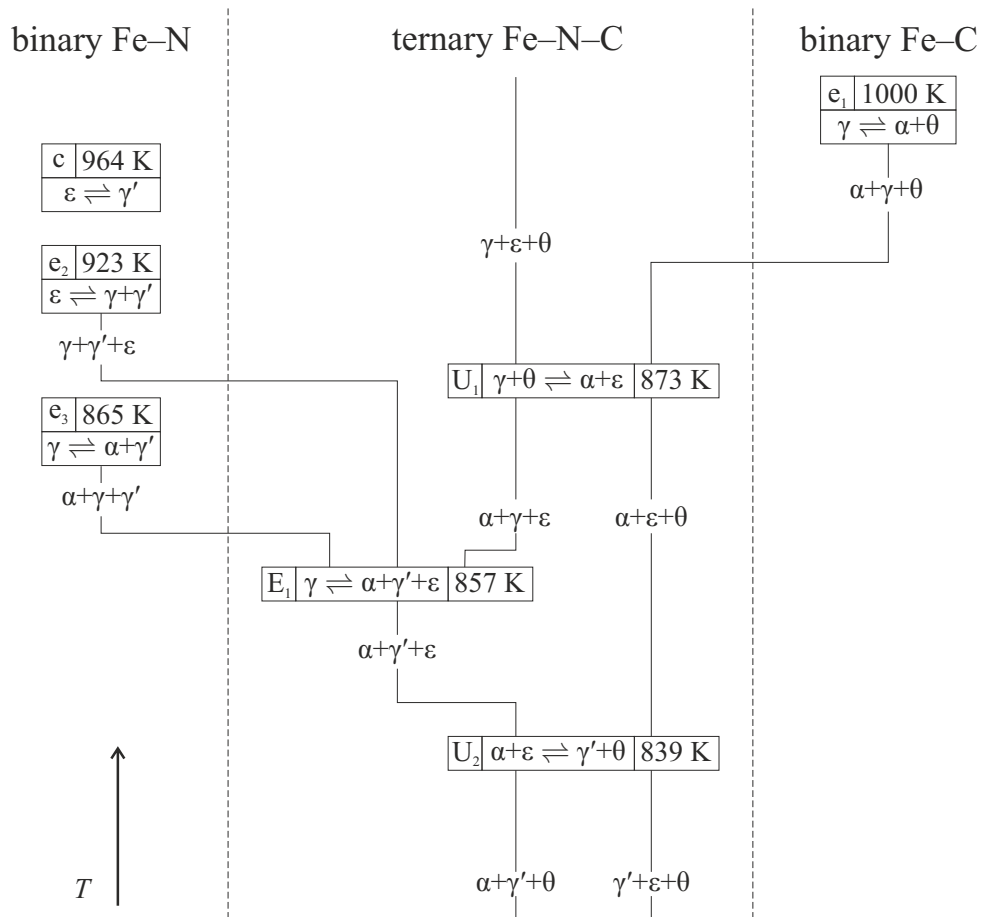


Figure 6.4: Scheil reaction scheme representing the sequence of invariant reactions predicted by the thermodynamic description from the present work, using the designations for the invariant reactions introduced in Chapter 4.

the system Fe–N–C [39, 41, 43–47] only describe a part of the invariant temperatures correctly and give significantly deviating values for other ones (see the discussion in Chapter 4 and the examples in Table 6.4). In contrast, the new thermodynamic description predicts correctly the values of *all* invariant temperatures, as recently determined experimentally.

Isothermal sections of the Fe–N–C phase diagram as calculated using the thermodynamic dataset derived in the present work at the (technologically relevant) temperatures of 853 K and 893 K (580 °C and 620 °C) are shown in Figure 6.5 together with the phase boundaries as proposed in Reference 82 on the basis of EPMA investigations on nitrocarburising Fe specimens. These experimental data have been used in the optimization process. It was not possible to obtain an even better fit of the phase boundaries without allowing the formation of a large miscibility gap in the ϵ phase. The agreement with the phase boundaries from Reference 82 at 853 K (580 °C) is significantly better than as obtained by the predictions from References 41 and 45 and comparable to the phase boundaries resulting from the prediction from Reference 43 as follows from Figure 8d in Reference 82. At the same temperature, according to the descriptions from References 46 and 47, the $\alpha+\epsilon$ equilibrium is non-existent or just disappearing. Therefore, the phase boundaries resulting from these descriptions cannot be compared to experimental data or to the phase boundaries resulting from the description from the present work. Further experimental data points have been given in Figure 6.5a: (i) the single data point from Reference 88 for the phase boundary $\alpha+\epsilon/\epsilon$ shows higher N and lower C contents than predicted here; (ii) the data points for the same phase boundary from Reference 94 (for 120 min and 240 min), however, agree well with the calculations from the present work; (iii) recent experimental data measured at 853 K (580 °C) for either the $\alpha+\epsilon/\epsilon$ or the $\alpha+\epsilon+\theta/\epsilon$ equilibrium as presented in Chapter 2 also agree well with the predictions from the present work.

At 893 K (620 °C), the agreement with the experimental data is also good, especially for the γ single phase field, with the deviations between the data from Reference 82 and the calculated phase boundaries being close to the accuracy of EPMA. There is a clear deviation at 893 K (620 °C) for the phase boundary $\gamma'+\epsilon/\epsilon$. However, the phase boundary given there is an estimation which is compatible with EPMA data presented in the same work but not based on a thermodynamic model. In principle, the phase boundary as predicted by the thermodynamic description from the present work is compatible with the EPMA data from Reference 82, see their Figure 8b. Thermodynamic calculations at the same temperature using the description from Reference 41 showed significantly higher N contents and lower C contents in ϵ for the equilibria with γ and especially θ than determined in Reference 82 and predicted by the thermodynamic description from the present work.

Table 6.5: The solubility of N in C-containing γ in equilibrium with N_2 gas at 1×10^5 Pa as experimentally determined in Reference 226 and as predicted by the model from the present work. Compositions expressed in mass fractions w_N and w_C .

$T/K (T/^\circ C)$	$w_C/\text{wt.\%}^a$	$w_N \cdot 10^2/\text{wt.\%}$ (exp, [226])	$w_N \cdot 10^2/\text{wt.\%}$ (calc, this work)
1323 (1050)	0.57	2.28	2.04
1373 (1100)	0.44	2.25	2.03
	0.75	2.12	1.82
1423 (1150)	0.43	2.18	1.95
	0.50	2.18	1.90
	0.76	2.00	1.75
	0.76	1.94	1.75
1473 (1200)	0.46	2.08	1.86
	0.50	2.07	1.84
	0.78	1.88	1.68

^aTheoretically, for the experiments considered in Reference 226, the activity of C is zero at the surface of the specimen. However, as there is no decarburizing medium in the gas phase, C remains in the substrate.

Both, at 853 K (580 °C) and at 893 K (620 °C), the phase boundaries of the γ' phase show excellent agreement with those shown in Reference 82. The ternary γ' single phase field given there is, however, not based on quantitative experimental data, but has only estimative character. The γ' single phase field resulting from the model from the present work agrees well with the EPMA data mentioned in Section 6.3.2.

The priority in the present work was to obtain a reasonable representation of the phase boundaries of γ at 893 K (620 °C) and to correctly describe the invariant temperatures. On this basis, the parameter ${}^0L_{\text{Fe:C,N}}^\gamma$ was optimized. In order to obtain a better description of γ in the range of higher temperatures, a temperature dependence of ${}^0L_{\text{Fe:C,N}}^\gamma$ could be introduced as soon as more experimental data is available. Even though systematically too low, the here determined prediction for the N solubility in carbon containing γ is already good, see the comparison of experimental data [226] and the values predicted by the thermodynamic description from the present work in Table 6.5.

6.5.3 The appropriateness of a model for the γ' phase

In the present work, a different approach for modelling the thermodynamics of γ' than in Reference 41 has been used. Instead of setting ${}^\circ G_{\text{Fe:Va}}^{\gamma'}$ equal to the Gibbs energy of γ -Fe and introducing interaction parameters, ${}^\circ G_{\text{Fe:Va}}^{\gamma'}$ has been used as a model parameter. Its value should, therefore, not be interpreted as the Gibbs energy of a hypothetical compound. The physical

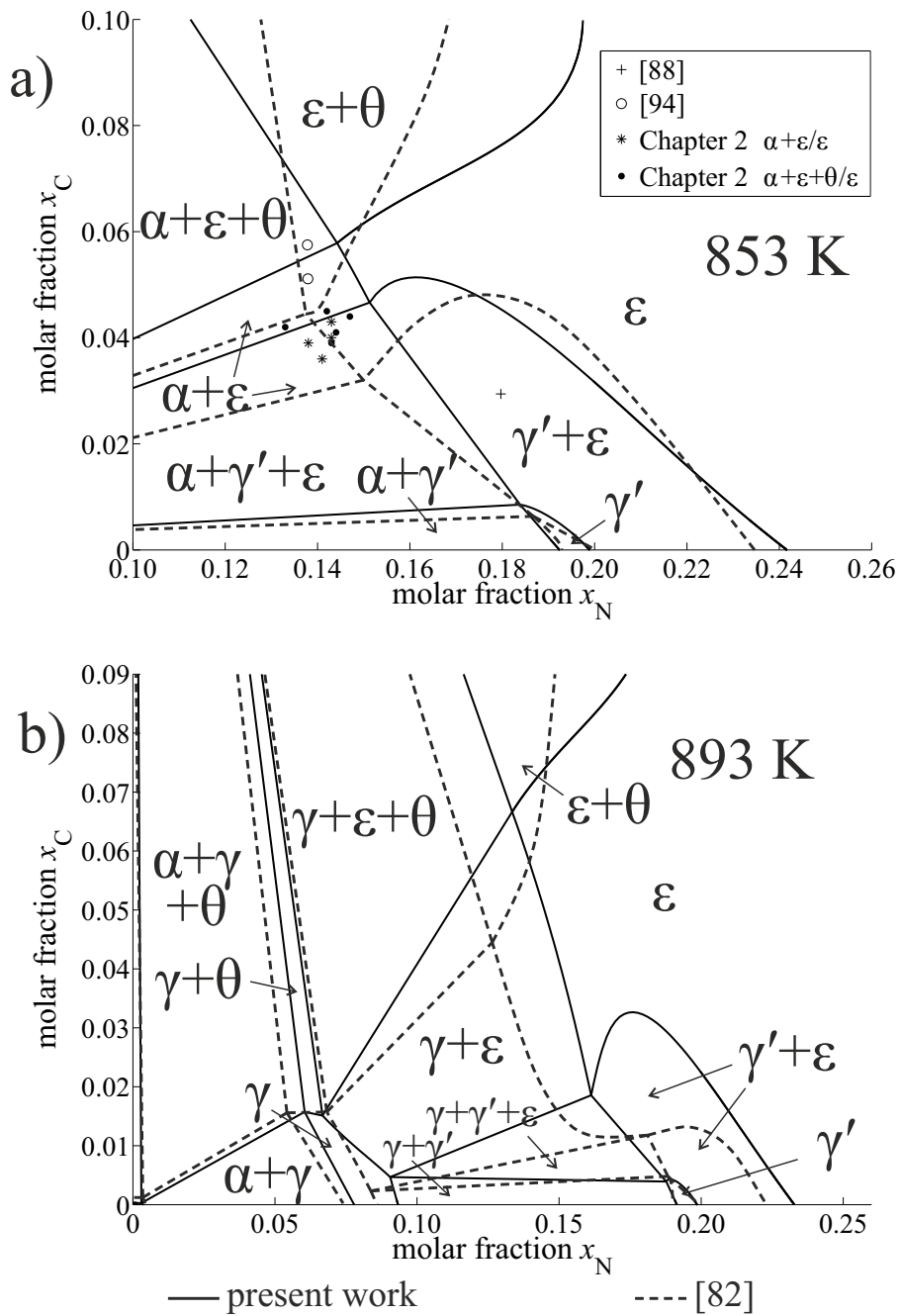


Figure 6.5: Isothermal sections of the Fe–N–C phase diagram calculated using the thermodynamic description from the present work (solid lines) compared with phase boundaries proposed in Reference 82 (dashed lines). a) At 853 K (580 °C), also including separate data from References 88 and 94 and from Chapter 2. b) At 893 K (620 °C).

meaning of the value of ${}^{\circ}G_{\text{Fe:Va}}^{\gamma'} - 4{}^{\circ}G_{\text{Fe}}^{\alpha}$ can be understood as the Gibbs energy of N-vacancy formation according to the formal reaction $(1-x) \text{Fe}_4\text{N} + 4x \alpha\text{-Fe} \rightleftharpoons \text{Fe}_4\text{N}_{1-x}$, as similarly described in References 16 and Chapter 5. As mentioned in Section 6.4, the parameter ${}^{\circ}G_{\text{Fe:C}}^{\gamma'}$ was adjusted in a way that the solubility of C in γ' agrees well with the experimental equilibrium values. Therefore, a physical interpretation is even more difficult. Ab-initio calculations performed in Reference 235 indicated a positive enthalpy of formation of $\gamma'\text{-Fe}_4\text{C}$ as it is the case in the present work.

Experimentally obtained data for the relationship of the activity of N and the N content of γ' [20], for the binary Fe–N system, were discussed in detail in Reference 22. In that work modelling was performed using three different approaches and the results were compared with the thermodynamic description from Reference 41. The “Langmuir-type approach” in Reference 22 is identical to the model applied in the present work. The other two models (“Wagner-Schottky (WS) approach” and “Gorsky-Bragg-Williams (GBW) approach”) allow for (dis)order of N. In Figure 1 in Reference 22, a function characterizing the deviation of the thermodynamic data from the expected values according to a Langmuir-type model (yielding a constant value for this function), is plotted showing the good fit of the WS and GBW models to the experimental data from Reference 20. Thus, it was concluded [22] that a model allowing for disorder is needed in order to give a meaningful description of the thermodynamics of the γ' phase, with the “WS approach” and the “GBW approach” giving equally meaningful descriptions.

Using the expressions for the Gibbs energy of γ' in Reference 236 it can be shown that also the WS and GBW models, allowing for disorder of N, can be expressed in the compound energy formalism [51] using a sublattice model indicated by the formula unit $\text{Fe}_4(\text{N},\text{Va})(\text{N},\text{Va})_3$, i.e., as compared to the sublattice model applied in the present work with the formula unit $\text{Fe}_4(\text{N},\text{Va})$, with a second interstitial sublattice, and ideal (WS) or regular (GBW) interactions. Following the conclusion from Reference 22, it was then tried to use a model equivalent to the “WS approach” from Reference 22 in the binary Fe–N system. The optimization of the model parameters, however, gave unreasonable results with e.g. γ' replacing the γ phase or no disorder in γ' at all. This is caused by a lack of any direct experimental data quantifying disorder in γ' . Other approaches to the thermodynamics of the γ' phase adopt the cluster variation method [200–202,237], but the experimental data do not allow to prefer one or the other model:

If realistic errors for the N-content determination in Reference 20 are assumed (approximately 5 %), the resulting deviations from the experimental results of the model used in the present work can be ascribed to this experimental uncertainty. Therefore, and also because the solubility of C in γ' is considered, it was decided to adopt the two-sublattice model in the

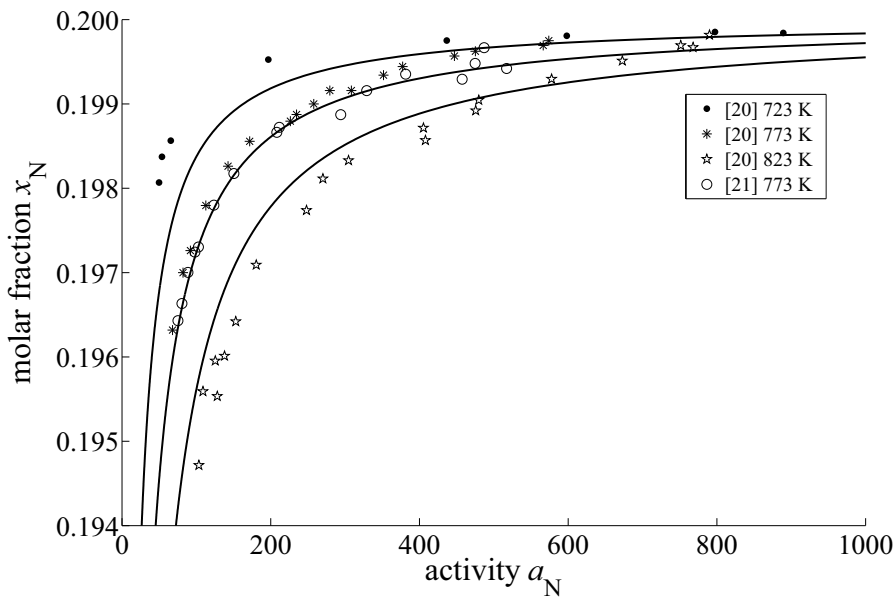


Figure 6.6: Comparison of the predicted relationship of N activity and N content for binary γ' (solid lines) and the experimental data from References 20 and 21

present work, giving a reasonable agreement of the predicted activity curves and the data from References 20 and 21 (see Figure 6.6).

6.5.4 The thermodynamics of the ϵ phase

The values of the Gibbs energy of the end-members of ϵ , ${}^{\circ}G_{\text{Fe:C}}^{\epsilon}$ and ${}^{\circ}G_{\text{Fe:N}}^{\epsilon}$ have been taken from previous descriptions [41, 227]. The enthalpies of formation following from these Gibbs-energy functions are compatible with recent ab-initio data from Reference 238, predicting negative values close to the one following from the applied Gibbs-energy function for various ordering states of nitrides with the formula Fe_2N . The values for the corresponding carbides with the formula Fe_2C from Reference 238 are positive as it is the case for the Gibbs-energy function applied in the present work, whereas they are considerably smaller.

The relationship of the activity of N and the N content in ϵ for the binary Fe–N system as obtained from the present thermodynamic description is shown in Figure 6.7. The prediction agrees well with the (rather inaccurate) experimental data (errors in the range of 5 at.% to 10 at.%) from Reference 225, as follows from Figure 6.7. Considering the more accurate data from Reference 36, shown in Figure 6.7 as well, good agreement occurs in the region of low N content and low N activity; at higher N activities lower N contents are predicted than experimentally observed. It was not possible to reproduce these data better without losing the good

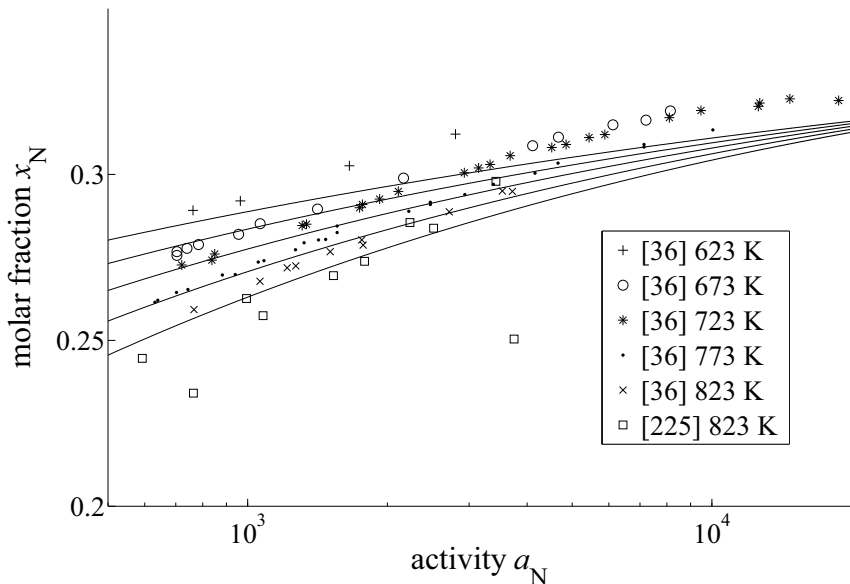


Figure 6.7: Comparison of the relationship of N activity and N content in binary ϵ resulting from the thermodynamic description from the present work (lines), with T increasing from 623 K to 823 K (350 °C to 550 °C) in steps of 50 K from top to bottom, and experimental data from References 36 and 225.

agreement with the two- and three-phase equilibrium data in which ϵ participates. In the present work, the thermodynamics of the ϵ phase have been described focusing on correct description of the available solid-solid equilibrium data. The description of the activity of N in ϵ on the basis of the gas-solid equilibrium data from References 36 and 225 could be better described by using models more explicitly considering the state of order in ϵ than that in the present case.

Several approaches have been presented in the literature to describe the thermodynamic behaviour of ϵ in the range of high N content, i.e. close to the maximum N content of $x_{\text{N}} = 1/3$. Descriptions on the basis of a long-range order, GBW model of ϵ have been presented in References 64, 65 and 66, similar to the approach mentioned above for γ' [22], and descriptions on the basis of the cluster variation method have been presented in References 200 and 203. Finally, ordering in ϵ and also the equilibrium with orthorhombic $\zeta\text{-Fe}_2\text{N}$ (not considered in the present work), which can formally be described as ordered ϵ , have been investigated recently by first-principles calculations [204]. Recognizing the large homogeneity ranges of N and C in ϵ and the necessary extension of the binary model into the ternary Fe–N–C system, it is reasonable to apply a sub-regular solution model for ϵ indicated by the formula unit $\text{Fe}(\text{C},\text{N},\text{Va})_{1/2}$, and therefore handle all non-ideal (e.g. ordering) effects by introducing interaction parameters instead of applying a physically more meaningful, but disproportionately complex long-range

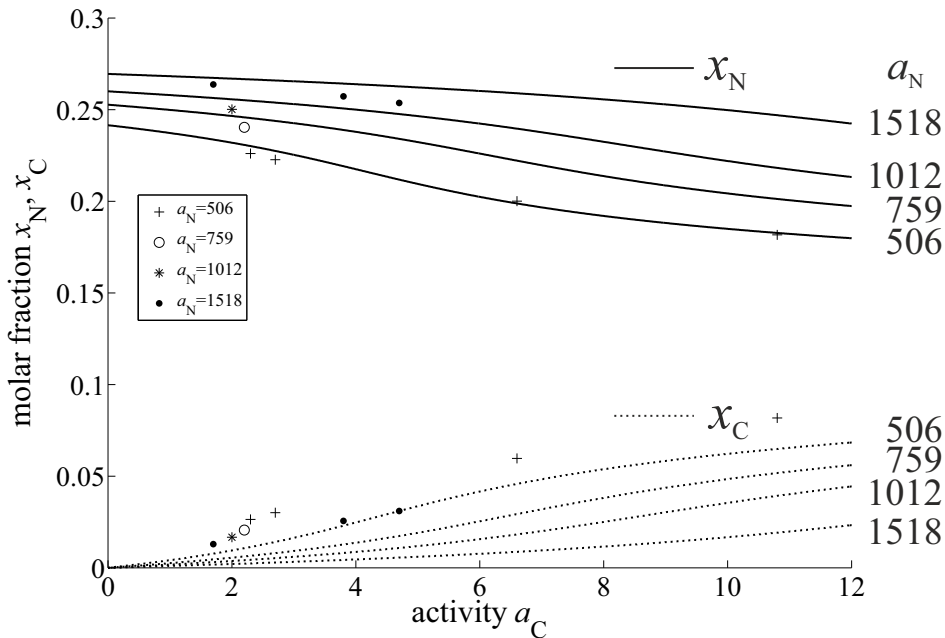


Figure 6.8: The relationships of N and C activities and N content (solid lines) and C content (dotted lines) of ϵ at 843 K (570 °C) as predicted by the thermodynamic description from the present work and as determined experimentally in Reference 95 (individual data points).

order model. This approach has been adopted in the present work, thereby enabling successful description of the equilibria in both the binary Fe–N system and especially the ternary Fe–N–C system.

In the present work, the function for ${}^{\circ}G_{\text{Fe:N}}^{\epsilon}$ has been taken from Reference 41. Comparison of the Gibbs energy of $\epsilon\text{-Fe}_2\text{N}$ as predicted by this function and by the thermodynamic description for ϵ from Reference 43, i.e. setting $y_{\text{N}}^{\epsilon} = 1/2$ for the 1:1 model applied there, shows that the corresponding Gibbs-energy values are virtually identical over a large temperature range.

The relationships of the N and C activities and the N and C contents of ϵ at 843 K (570 °C) have been plotted in Figure 6.8 together with the experimental data from Reference 95. The agreement is very good for N. Compared to the experimental data, the predicted C contents are too low for high N activities; for low N activities, the predicted values are closer to the experimentally determined ones. Similar experimental investigations have been performed in Reference 239, but are not included here recognizing the application of technical steels, i.e. a high impurity content, for the specimens used in Reference 239.

A general trend visible in Figure 6.8 is the obvious mutual influence of N and C: an increase in the C activity leads to a decrease of the N content and vice versa. This can be discussed as follows:

Simultaneous interstitial diffusion of N and C in ϵ is governed by the thermodynamic factor

$$\vartheta_{ij} = \frac{y_i}{RT} \frac{\partial \mu_i}{\partial y_j} \quad (6.6)$$

with the chemical potential of component i (=N,C), μ_i , being the proportional constant between the intrinsic diffusion coefficients and the corresponding self-diffusion coefficients [72,81] (see also Chapter 2. It has been found that at both 823 K and 853 K (550 °C and 580 °C) the off-diagonal components of ϑ_{ij} are positive (see Reference 81 and Chapter 2). This information has been used as a constraint during the optimization: the thermodynamic description from the present work results in positive values of the off-diagonal components of the thermodynamic factor over a large composition range of ϵ . Only at low N and C contents, not covered by the experimentally observable homogeneity ranges of ϵ , negative values of those off-diagonal components of ϑ_{ij} occur.

The present thermodynamic description predicts that a small miscibility gap occurs in ϵ below approximately 855 K (582 °C) close to the line connecting Fe₂N and Fe₂C. No experimental data exist to (in)validate this result.

6.6 Conclusions

1. New thermodynamic descriptions for the Fe–N system and the Fe–N–C system have been developed by focusing on the equilibria involving the γ' and ϵ phases.
2. A simple ideal-solution model for the γ' phase has been used to successfully describe its homogeneity range; the past models either use considerably more model parameters to yield a similar description of the experimental data or unrealistically model γ' as a stoichiometric phase.
3. In the binary Fe–N system, the new thermodynamic description reproduces the experimental data better than previously published thermodynamic descriptions, especially the $\gamma'+\epsilon$ equilibrium. The agreement with the experimental data for both the N content of ϵ and the activity of N at the phase boundary γ'/ϵ has been improved significantly.
4. The thermodynamic descriptions available in literature cannot reproduce recently obtained experimental data. Therefore, a thermodynamic description of the ternary Fe–N–C system correctly describing especially the recently experimentally observed temperatures of the invariant reactions has been developed. The new thermodynamic description for the ternary Fe–N–C system also well reproduces the recently obtained experimental phase

boundaries in the system as well as the (positive) off-diagonal components of the thermodynamic factor (pertaining to diffusion in ϵ ; as determined from experiments).

Chapter 7

Summary

The systems Fe–N, Fe–C and Fe–N–C are highly relevant for technically applied nitriding and nitrocarburising of iron and steels [1, 2]. On the basis of recent studies [16, 29, 74–82], those systems were further investigated in the present work. Therefore, nitriding and nitrocarburising experiments were performed, using pure Fe, Fe–N and Fe–C alloys as substrates. Experimental studies have been performed and presented in Chapters 2, 3 and 4. On the basis of these experiments and data from the literature, new thermodynamic descriptions have been obtained in Chapters 5 (Fe–C) and 6 (Fe–N and Fe–N–C).

7.1 Experimental

7.1.1 Specimen preparation

In total, three different alloys have been used that were prepared in a similar way. For the pure Fe specimens and the Fe–N specimens, pure Fe (Alfa Aesar, 99.98 wt.%) was cast into ingots of the dimensions 80 mm × 30 mm × 10 mm. For the Fe–C specimens, Fe and C were cast into an ingot of the same dimensions with a nominal composition corresponding to the eutectoid composition in the Fe–C phase diagram [3]. The ingots were cold-rolled to a thickness of about 1 mm and cut into rectangular specimens of 20 mm × 12 mm. The specimens were ground and polished to a final thickness of 0.5 mm to 1.0 mm, depending on the designated use.

The pure Fe and Fe–N specimens were recrystallised. The Fe–N specimens were treated at 853 K over night in an atmosphere containing 10.6 vol.% NH₃ and 89.4 vol.% H₂, resulting in pure α -Fe[N] with a N content of 0.36 at.% to 0.38 at.%. The Fe–C specimens were encapsulated in fused silica tubes containing Ar and treated in a crucible furnace at approximately 1273 K (γ range) for 1 h and cooled on a metallic surface. This heat treatment resulted in a fine pearlitic microstructure.

Before the nitriding or nitrocarburising treatments, the specimens were polished again with 1 µm diamond suspension.

7.1.2 Nitriding and nitrocarburising treatments, secondary annealing

Nitriding and nitrocarburising treatments were performed in a fused silica tube furnace at temperatures of 823 K to 873 K (controlled within ± 1 K), with treatment times of 1 h to 16 h. The furnace is equipped with gas supplies for NH₃, H₂, CO, CO₂, CH₄ (not used in this work), H₂O and N₂. Therefore, defined activities of N and C can be controlled, which, in an ideal case, also define the resulting phase and composition at the surface of the specimen [1, 23, 24]. The treatment is terminated by quenching the specimen in water, lifting it into the cold zone of the furnace or setting the heating power to zero, resulting in different cooling rates.

Secondary annealing of some of the nitrided or nitrocarburised and encapsulated specimens was performed at 673 K to 773 K for 5 min to 16 h.

7.1.3 Specimen characterisation

For qualitative phase analysis, all specimens were investigated by XRD in a Philips X’Pert MPD diffractometer using Co-K_α radiation. Cross-sections were manufactured by embedding a piece of each specimen in resin and grinding and polishing. For light-microscopical analysis, the specimens were etched in 1 % Nital containing some HCl [90, 123]. Some specimens were further stained using Groesbeck solution [124]. Correspondingly resulting micrographs were used for layer-thickness measurements using the software Olympus Stream. EPMA analysis was performed on a Cameca SX 100 using the un-etched, polished cross-section, quantifying Fe, N and C. For EBSD analysis, an additional oxide polishing step using Struers OPS was applied. EBSD analysis was performed on a LEO 438VP SEM. The resulting EBSD maps were evaluated using the software EDAX OIM Analysis 7 [140].

7.2 Results and discussion

7.2.1 N and C interstitial diffusion and thermodynamic interactions in ε-iron carbonitride

In a recent study, simultaneous diffusion of N and C in ϵ/γ' double layers at 823 K was investigated [81]. In Chapter 2, diffusion of N and C in pure ϵ layers and θ/ϵ double layers at

853 K was investigated, expanding the basic method of Reference 81 to distinctly different microstructures. By the combination of light-microscopical analysis of layer-growth kinetics and concentration-depth profiles obtained by EPMA, the full diffusivity matrix in ϵ in the considered N and C concentration range was determined. Other than in Reference 81, the resulting concentration-depth profiles had a strong curvature, preventing the use of a linear function for fitting. Instead, an error function with a phenomenological parameter was used.

A new graphical evaluation method did not only yield values for the components of the diffusivity matrix, but also provided direct information about their errors and, thereby, the quality of the obtained data. The diffusivity matrix has been determined as

$$D(853\text{ K}) = \begin{pmatrix} D_{NN} & D_{NC} \\ D_{CN} & D_{CC} \end{pmatrix} = \begin{pmatrix} 50 & 4.9 \\ 4.9 & 5.5 \end{pmatrix} \times 10^{-15} \text{ m}^2 \text{ s}^{-1}. \quad (7.1)$$

The values are consistent with both binary [105, 108, 112, 113, 115] and ternary [81] diffusion data from the literature.

From the ratios of the components of the diffusivity matrix, ratios of the thermodynamic factors, a purely thermodynamic quantity can be obtained. In agreement with the data from Reference 81, those ratios were shown to be positive, which cannot be reproduced using the thermodynamic description of the ϵ phase from Reference 41, but agrees with the thermodynamic description from Reference 43. The positive values of the off-diagonal components of the diffusivity matrix imply a strong influence of the N (C) concentration-depth profile on the C (N) flux.

Further investigations showed that, in principle, the values of the diffusivity matrix as determined in Chapter 2 can also be applied to other microstructures, e.g. $\epsilon/\gamma/\epsilon$ triple layer resulting from nitriding of Fe–C alloys.

7.2.2 Microstructural development and crystallographic properties of decomposing Fe–N–C compound layers

In the last years, several studies on Fe–N–C compound layers have been performed, see References 29, 75, 81 and 82 and Chapter 2. Thereby, the specimens were always quenched in order to terminate the nitriding/nitrocarburising treatment. In the case of technical nitriding and nitrocarburising, these fast cooling rates cannot be achieved. Therefore, the development of θ/ϵ and ϵ layers forming at 853 K and $\theta/\epsilon/\gamma$ and ϵ/γ layers forming at 873 K upon slow cooling has been investigated in Chapter 3.

The γ phase formed only at the higher treatment temperature of 873 K. It was found to decompose into a $\alpha+\gamma'+\theta$ microstructure resembling a combination of typical lamellar pearlite [136] and coarsened granular braunite [137], which could in principle occur via a metastable eutectoid reaction according to $\gamma \rightleftharpoons \alpha + \gamma' + \theta$.

Upon slow cooling, ϵ decomposed into a plate-like microstructure. EBSD investigations revealed that the plates consist of γ' and ϵ with an orientation relationship according to

$$\{0001\}_{\text{hcp}} \parallel \{111\}_{\gamma'}, \langle \bar{2}110 \rangle_{\text{hcp}} \parallel \langle 1\bar{1}0 \rangle_{\gamma'}, \quad (7.2)$$

which has already been found between γ' and ϵ in the literature [142–144]. Furthermore, some coarse γ' grains were found occurring in the former ϵ (sub)layer.

In order to investigate the decomposition of ϵ in detail and simulate the slow cooling process in a more controlled manner, secondary annealing experiments at 673 K and 773 K were performed on quenched specimens. Thereby, the plate-like structure was observed even at very short annealing times. This instability of ϵ can be explained by thermodynamics: the ϵ single-phase field extends to rather small N and C contents at higher temperatures. Upon slow cooling or annealing, the composition of ϵ thus formed close to the substrate lies in a two or three phase field. At longer annealing times, coarse γ' were observed, eventually forming a closed γ' sublayer growing back in the direction of the surface of the specimen.

7.2.3 The $\alpha+\epsilon$ two-phase equilibrium in the Fe–N–C system – experimental investigations and thermodynamic calculations

In contrast to early experimental works [83, 84, 129], the occurrence of an equilibrium of α and ϵ in a narrow temperature range is recognised in all recent thermodynamic descriptions of the system [39, 41, 43, 45–47]. However, these thermodynamic descriptions predict (i) two different sequences of invariant reactions leading from the $\gamma'+\theta$ equilibrium to the $\alpha+\epsilon$ equilibrium upon increasing temperature and (ii) distinctly different temperatures of those reactions.

In a former work, the range in which those reactions occur could already been narrowed down to 833 K to 843 K [75]. In Chapter 4, the $\alpha+\epsilon$ equilibrium was studied again in detail. Thermodynamic calculations using the thermodynamic descriptions from the literature revealed that two different variants for the (sequence of) invariant temperatures leading from the $\alpha+\epsilon$ equilibrium at higher temperatures to the $\gamma'+\theta$ equilibrium at lower temperatures are realised: type I represents the transition via the single invariant reaction $\alpha+\epsilon \rightleftharpoons \gamma'+\theta$, while type II involves the ternary eutectoid reaction $\epsilon \rightleftharpoons \alpha + \gamma' + \theta$ followed by the pseudo-binary eutectoid reaction $\epsilon \rightleftharpoons \gamma' + \theta$. Experimental investigations were designed in particular to determine both the temperature(s)

and the type of the (sequence of) invariant reactions. Therefore, experiments at small temperature steps between 823 K and 863 K were performed. Due to the difficult establishment of equilibrium close to the invariant temperature, it was impossible to obtain microstructures directly proofing the occurrence of one of the both types of (sequence of) invariant reactions. The temperature range in which these reactions occur, however, could be narrowed down to 840 K to 844 K.

7.2.4 A thermodynamic model for non-stoichiometric cementite; the Fe–C phase diagram

Indications for a non-stoichiometry of cementite have been found frequently in the past [5–15]. However, the data were either not accurate enough or the experimental conditions did not allow establishment of equilibrium, preventing the inclusion of a homogeneity range of cementite in former thermodynamic models of the Fe–C system [31–34].

Recently, the C-vacancy content of cementite in equilibrium with α or γ has been quantified in a large temperature range [16]. Therefore, it was possible to apply these data in order to obtain a new thermodynamic description of the cementite phase in Chapter 5, correctly describing its homogeneity range in equilibrium with those phases. The new thermodynamic description preserves the well-established invariant equilibria in the Fe–C system and was shown to be compatible with various literature data.

7.2.5 Thermodynamics of the Fe–N and Fe–N–C systems; the Fe–N and Fe–N–C phase diagrams revisited

Various thermodynamic descriptions of the Fe–N [31, 35–43] and Fe–N–C [39, 41, 43–47] systems exist in the literature. Experimental investigations from the last years, see References 29, 75, 79 and 82 and Chapters 2–4, however, show disagreement of the ternary descriptions from the past. Also for the Fe–N system, new data is available [30, 82].

Therefore, new thermodynamic descriptions of both the Fe–N system and the Fe–N–C system have been provided in Chapter 6. As thermodynamic description of the Fe–C subsystem, the model obtained in Chapter 5 was used. Compared to the thermodynamic descriptions from the past, the new thermodynamic description of the Fe–N system improves especially the agreement for the γ'/ϵ equilibrium. Using the newly obtained data on the invariant temperatures in the Fe–N–C system from Reference 82 and Chapter 4 and the phase boundaries determined experimentally in Reference 82 as a basis, the optimisation of the thermodynamic description of the ternary Fe–N–C system has been performed. The new thermodynamic description described

both the older literature data and the recently obtained experimental information correctly. Furthermore, the correct sign of the off-diagonal components of the thermodynamic factors as determined experimentally in Reference 81 and Chapter 2 is reproduced.

Kapitel 8

Zusammenfassung

Die Systeme Fe–N, Fe–C und Fe–N–C sind sehr bedeutsam für das technisch angewandte Nitrieren und Nitrocarburieren von Eisen und Stählen [1,2]. Auf Basis von Studien aus den letzten Jahren [16, 29, 74–82] wurden diese Systeme in der vorliegenden Arbeit weiter untersucht. Dazu wurden Nitrier- und Nitrocarburierexperimente an reinem Fe, Fe–N- und Fe–C-Legierungen durchgeführt. Die experimentellen Studien sind in den Kapiteln 2, 3 und 4 dargestellt. Die auf Basis dieser Experimente und zusätzlicher Literaturdaten erlangten neuen thermodynamischen Beschreibungen dieser Systeme sind in den Kapiteln 5 (Fe–C) und 6 (Fe–N und Fe–N–C) dargestellt.

8.1 Experimentalteil

8.1.1 Probenherstellung

Für die Untersuchungen in der vorliegenden Arbeit wurden drei unterschiedliche Legierungen verwendet, die auf ähnliche Weise hergestellt wurden. Für die Reineisenproben und die Proben aus der Fe–N-Legierung wurde reines Eisen (Alfa Aesar, 99.98 wt.%) in prismatische Barren abgegossen (80 mm × 30 mm × 10 mm). Für die Proben aus der Fe–C-Legierung wurde Fe und C mit einer Soll-Zusammensetzung, die der eutektoiden Zusammensetzung im Fe–C-Phasendiagramm entspricht [3], in Barren der gleichen Dimensionen abgegossen. Durch Kaltwalzen wurden Bleche mit einer Dicke von etwa 1 mm hergestellt und aus diesen rechteckige Proben (20 mm × 12 mm) herausgetrennt. Die Proben wurden je nach Verwendungszweck auf eine Dicke von 0.5 mm bis 1 mm geschliffen und anschließend poliert.

Die Reineisenproben und Fe–N-Proben wurden rekristallisiert. Die Fe–N-Proben wurden in einer Atmosphäre, die aus 10.6 vol.% NH₃ und 89.4 vol.% H₂ zusammengesetzt war, bei 853 K über Nacht nitriert. Dabei wurde reines α-Fe[N] mit einem N-Gehalt von 0.36 at.% bis 0.38 at.% erhalten. Die Fe–C-Proben wurden unter Ar-Atmosphäre in Quarzglas eingeschmolzen und für

1 h bei etwa 1273 K in einem Tiegelofen austenitisiert. Anschließend wurden sie bei Raumtemperatur auf einer metallischen Oberfläche abgekühlt, wodurch ein feines perlitisches Gefüge erhalten wurde.

Vor den Nitrier- und Nitrocarburierbehandlungen wurden die Proben erneut mit Diamantsuspension (1 µm Körnung) poliert.

8.1.2 Nitrier- und Nitrocarburierbehandlungen, Auslagerungsversuche

Die Nitrier- und Nitrocarburierversuche wurden in einem Quarzglas-Röhrenofen bei Temperaturen von 823 K bis 873 K (auf 1 K genau geregelt) mit Behandlungszeiten von 1 h bis 16 h durchgeführt. Der verwendete Ofen kann Atmosphären mit definierter Zusammensetzung aus NH₃, H₂, CO, CO₂, CH₄ (in dieser Arbeit nicht verwendet), H₂O und N₂ bereitstellen, um die Aktivitäten von N und C in der Gasphase zu steuern. Im Idealfall stellt sich dabei ein Gleichgewicht an der Oberfläche der Probe ein, das bestimmt, welche Phase mit welcher Zusammensetzung an der Oberfläche der Probe auftritt [1, 23, 24]. Der Versuch kann durch Abschrecken in Wasser, Heben der Probe in die kalte Zone des Ofens oder Reduktion der Heizleistung auf null beendet werden. Dabei werden verschiedene Abkühlraten erreicht.

Auslagerungsversuche wurden mit nitrierten oder nitrocarburierten Proben, die in Quarzglas eingeschmolzen wurden, bei Temperaturen von 673 K bis 773 K und Behandlungszeiten zwischen 5 min und 16 h durchgeführt.

8.1.3 Untersuchungsmethoden

Alle Proben wurden einer qualitativen Phasenanalyse durch Röntgenbeugung unterzogen, bei der ein Philips X’Pert MPD-Diffraktometer mit Co-K_α-Strahlung verwendet wurde. Querschliffe der Proben wurden hergestellt, indem ein Stück der Probe in Kunststoff eingebettet wurde und anschließend geschliffen und poliert wurde. Für lichtmikroskopische Untersuchungen wurden die Proben mit 1 % Nital, das etwas HCl enthält, geätzt [90, 123]. Manche Proben wurden außerdem mit Groesbeck-Lösung behandelt [124]. Die entstehenden Bilder wurden für Schichtdickenmessungen mit der Software Olympus Stream verwendet. Für die Mikrosondenmessungen an ungeätzten, polierten Querschliffen wurde eine Cameca SX 100 Mikrosonde verwendet, um gleichzeitig den Gehalt an Fe, N und C zu bestimmen. Für die EBSD-Messungen wurden die Proben zusätzlich mit Struers OPS oxidpoliert. Die Messungen wurden an einem LEO 438VP-Rasterelektronenmikroskop durchgeführt. Die entstehenden Daten wurden mit der Software EDAX OIM Analysis 7 ausgewertet [140].

8.2 Ergebnisse und Diskussion

8.2.1 Interstitielle Diffusion von N und C und thermodynamische Wechselwirkungen in ϵ -Eisencarbonitrid

Eine Arbeit aus den letzten Jahren beschäftigte sich mit der gleichzeitigen Diffusion von N und C in ϵ/γ' -Doppelschichten bei 823 K [81]. Daraufhin wurde in Kapitel 2 die Diffusion von N und C in reinen ϵ -Schichten und θ/ϵ -Doppelschichten bei 853 K untersucht und dabei das grundlegende Verfahren aus der vorherigen Arbeit [81] auf grundlegend andere Mikrostrukturen erweitert. Durch die Verbindung von lichtmikroskopischen Untersuchungen der Schichtwachstumskinetik und mit der Mikrosonde gemessenen Konzentrations-Tiefen-Profilen konnten alle Komponenten der Diffusionskoeffizientenmatrix in ϵ im betrachteten Zusammensetzungsbereich bestimmt werden. Im Gegensatz zu früheren Untersuchungen [81] wurde eine starke Krümmung der Konzentrations-Tiefen-Profile beobachtet, was die Annäherung als lineare Funktion verhinderte. Stattdessen wurde eine Fehlerfunktion mit einem phänomenologischen Parameter verwendet.

Eine neuartige graphische Auswertungsmethode lieferte nicht nur die Werte der einzelnen Komponenten der Diffusionskoeffizientenmatrix, sondern auch Informationen über die jeweiligen Fehlergrenzen der Komponenten und damit die Qualität der erhaltenen Daten. Die bestimmte Diffusionskoeffizientenmatrix lautet

$$D(853\text{ K}) = \begin{pmatrix} D_{NN} & D_{NC} \\ D_{CN} & D_{CC} \end{pmatrix} = \begin{pmatrix} 50 & 4.9 \\ 4.9 & 5.5 \end{pmatrix} \times 10^{-15} \text{ m}^2 \text{ s}^{-1}. \quad (8.1)$$

Die Werte der Komponenten lassen sich mit Literaturwerten für binäre [105, 108, 112, 113, 115] und ternäre [81] Diffusion in Einklang bringen.

Aus den Verhältnissen der Komponenten der Diffusionskoeffizientenmatrix lassen sich die Verhältnisse der thermodynamischen Faktoren, einer rein thermodynamischen Größe bestimmen. Die bestimmten Verhältnisse sind wie in einer früheren Arbeit [81] positiv. Dieses Verhalten lässt sich nur mit der thermodynamischen Beschreibung der ϵ -Phase von Kunze [43], nicht aber mit derjenigen von Du [41] erklären. Die positiven Werte der Kreuz-Komponenten der Diffusionskoeffizientenmatrix deuten auf einen großen Einfluss des Konzentrations-Tiefen-Profiles von N (C) auf den Diffusionsfluss von C (N) hin.

Weitergehende Untersuchungen zeigten, dass sich die Werte der Diffusionskoeffizientenmatrix im Prinzip auch auf andere Mikrostrukturen anwenden lassen, z.B. $\epsilon/\gamma'/\epsilon$ -Dreifachschichten, die beim Nitrieren von Fe–C-Legierungen auftreten.

8.2.2 Entwicklung der Mikrostruktur und kristallographische Eigenschaften von sich zersetzen Fe–N–C–Verbindungsschichten

In den letzten Jahren wurden viele Untersuchungen an Fe–N–C–Verbindungsschichten durchgeführt [29, 75, 81, 82], siehe auch Kapitel 2. Dabei wurden die Proben abgeschreckt, um die Nitrier-/Nitrocarburierbehandlungen zu beenden. Beim technischen Nitrieren und Nitrocarburieren können so hohe Kühlraten nicht erreicht werden. Daher wurde in Kapitel 3 die Entwicklung von θ/ϵ - und ϵ -Schichten, die sich bei 853 K bilden, und $\theta/\epsilon/\gamma$ - und ϵ/γ -Schichten, die sich bei 893 K bilden, beim langsamen Abkühlen untersucht.

Die γ -Phase wurde nur bei der höheren Behandlungstemperatur von 873 K gebildet. Sie zerstellt sich beim Abkühlen in eine Mikrostruktur, die wie eine Kombination von lamellarem Perlit [136] und vergröbertem körnigem Braunit [137] wirkt. Diese Zersetzung lässt sich formal durch eine metastabile eutektoidre Reaktion $\gamma \rightleftharpoons \alpha + \gamma' + \theta$ erklären.

Beim langsamen Abkühlen zerstetzt sich ϵ in eine plättchenenartige Mikrostruktur. EBSD-Untersuchungen zeigten, dass diese Platten aus γ' und ϵ bestehen, die zueinander in einer Orientierungsbeziehung nach

$$\{0001\}_{\text{hcp}} \parallel \{111\}_{\gamma'}, \langle \bar{2}110 \rangle_{\text{hcp}} \parallel \langle 1\bar{1}0 \rangle_{\gamma'} \quad (8.2)$$

stehen, die bereits in der Literatur nachgewiesen wurde [142–144]. Außerdem bildeten sich gröbere γ' -Körper in der ehemaligen ϵ -(Sub-)Schicht.

Um die Zersetzung von ϵ im Detail zu untersuchen und den Abkühlprozess auf kontrollierte Art zu simulieren, wurden Auslagerungsversuche bei 673 K und 773 K an abgeschreckten Proben durchgeführt. Dabei wurde die plättchenartige Mikrostruktur bereits bei sehr kurzen Auslagerungszeiten beobachtet. Die Instabilität von ϵ kann durch die Thermodynamik erklärt werden: Das ϵ -Einphasengebiet dehnt sich bei höheren Temperaturen bis hin zu relativ geringen N- und C-Gehalten aus. Bei niedrigeren Temperaturen, die beim langsamen Abkühlen oder Auslagern auftreten, liegt die Zusammensetzung, mit der ϵ nahe des Substrates gebildet wurde, in einem Zwei- oder Dreiphasengebiet. Nach längeren Auslagerungszeiten wurden grobe γ' -Körper beobachtet, die schließlich eine geschlossene γ' -Schicht bilden, die sich rückwärts in Richtung der Oberfläche ausbreitet.

8.2.3 Das $\alpha+\epsilon$ -Zweiphasengleichgewicht im Fe–N–C-System – experimentelle Untersuchungen und thermodynamische Berechnungen

Im Unterschied zu frühen experimentellen Arbeiten [83, 84, 129] wurde das Auftreten eines Gleichgewichts zwischen α und ϵ in allen neueren thermodynamischen Beschreibungen des Systems Fe–N–C anerkannt [39, 41, 43, 45–47]. Allerdings weichen diese thermodynamischen Beschreibungen stark voneinander ab, indem sie (i) zwei unterschiedliche (Abfolgen der) invariant(en) Reaktion(en) und (ii) deutlich verschiedene Temperaturen vorhersagen, bei denen diese invarianten Reaktionen auftreten, durch die bei steigender Temperatur das $\gamma'+\theta$ -Gleichgewicht durch das $\alpha+\epsilon$ -Gleichgewicht ersetzt wird.

Eine frühere experimentelle Arbeit konnte bereits den Temperaturbereich, in dem diese Reaktionen auftreten, auf 833 K bis 843 K eingrenzen [75]. In Kapitel 4 wurde das Gleichgewicht zwischen α und ϵ erneut im Detail untersucht. Thermodynamische Berechnungen mit den thermodynamischen Beschreibungen aus der Literatur zeigten, dass zwei verschiedene Varianten für die (Abfolge der) invariant(en) Reaktion(en), die bei steigender Temperatur das $\gamma'+\theta$ -Gleichgewicht in das $\alpha+\epsilon$ -Gleichgewicht überführen, auftreten: Typ I steht für den Übergang in einer einzelnen Reaktion $\alpha+\epsilon \rightleftharpoons \gamma'+\theta$, während bei Typ II die ternäre eutektoide Reaktion $\epsilon \rightleftharpoons \alpha+\gamma'+\theta$ und die pseudo-binäre eutektoide Reaktion $\epsilon \rightleftharpoons \gamma'+\theta$ auftreten. Experimentelle Untersuchungen mit kleinen Temperaturschritten zwischen 823 K und 863 K wurden gezielt dazu entworfen, um die Temperatur(en) und den Typ der (Abfolge der) invariant(en) Reaktion(en) zu bestimmen. Da sich allerdings die Gleichgewichte nahe der invarianten Temperatur(en) nur sehr langsam einstellen, war es nicht möglich, Mikrostrukturen zu erhalten, die eindeutig nachweisen, welche (Abfolge der) invariant(en) Reaktion(en) auftritt. Der Temperaturbereich, in dem diese Reaktion(en) auftritt/auftreten konnte auf 840 K bis 844 K eingegrenzt werden.

8.2.4 Ein thermodynamisches Modell für nicht-stöchiometrischen Zementit; das Fe–C-Phasendiagramm

Hinweise auf die Nicht-Stöchiometrie von Zementit wurden in der Vergangenheit bereits häufig gefunden [5–15]. Dennoch verhinderten entweder die Qualität der Daten oder die experimentellen Bedingungen, die das Einstellen eines Gleichgewichts nicht erlaubten, dass ein Homogenitätsbereich für Zementit mit in die früheren thermodynamischen Beschreibungen des Systems Fe–C [31–34] einbezogen wurde.

In einer kürzlich veröffentlichten Arbeit wurde der C-Leerstellenanteil von Zementit im Gleichgewicht mit α oder γ über einen großen Temperaturbereich quantifiziert. Dadurch war es

möglich, diese Daten anzuwenden, um in Kapitel 5 eine neue thermodynamische Beschreibung von Zementit zu erhalten, die seinen Homogenitätsbereich im Gleichgewicht mit diesen Phasen korrekt beschreibt. Die neue thermodynamische Beschreibung reproduziert die gängigen Daten für die invarianten Gleichgewichte im System Fe–C und ist kompatibel mit thermodynamischen Daten aus der Literatur.

8.2.5 Thermodynamik der Systeme Fe–N und Fe–N–C; die Fe–N- und Fe–N–C-Phasendiagramme

In der Literatur existieren bereits viele thermodynamische Beschreibungen für das Fe–N- [31, 35–43] und das Fe–N–C-System [39, 41, 43–47]. Die Übereinstimmung der Vorhersagen dieser Modelle mit experimentelle Untersuchungen aus den letzten Jahren [29, 75, 79, 82] (siehe auch Kapitel 2–4) ist allerdings nicht ausreichend. Für das binäre Fe–N-System sind ebenfalls neuere Daten verfügbar [30, 82].

Auf Basis der neuen Daten wurden daher in Kapitel 6 neue thermodynamische Beschreibungen des Systeme Fe–N und Fe–N–C erstellt. Für das System Fe–C wurde das Modell aus Kapitel 5 verwendet. Die neue thermodynamische Beschreibung des Systems Fe–N verbessert vor allem die Übereinstimmung mit den experimentellen Daten für das Gleichgewicht γ'/ϵ . Die neue thermodynamische Beschreibung des ternären Fe–N–C-Systems reproduziert sowohl ältere als auch neue experimentelle Daten korrekt. Außerdem wird das korrekte Vorzeichen der thermodynamischen Faktoren, die in einer früheren Arbeit [81] und in Kapitel 2 bestimmt wurden, vorhergesagt.

Bibliography

- [1] E.J. Mittemeijer and M.A.J. Somers (eds.). *Thermochemical Surface Engineering of Steels*. Woodhead Publishing, Cambridge (2015).
- [2] D. Liedtke, U. Baudis, J. Boßlet, U. Huchel, H. Klümper-Westkamp, W. Lerche, and H.-J. Spies. *Wärmebehandlung von Eisenwerkstoffen – Nitrieren und Nitrocarburieren*. expert verlag, Renningen, Germany (2006).
- [3] H. Okamoto. *J. Phase Equilib.* 13 (1992) 543–565. doi:10.1007/BF02665767.
- [4] H.A. Wriedt, N.A. Gokcen, and R.H. Nafziger. *J. Phase Equilib.* 8 (1987) 355–377. doi:10.1007/BF02869273.
- [5] N.J. Petch. *J. Iron Steel Inst.* 149 (1944) 143–150.
- [6] A.A. Zhukov, V.A. Shalashov, V.K. Tomas, and B.Y. Ul'yanova. *Met. Sci. Heat Treat.* 12 (1970) 16–18. doi:10.1007/BF00651707.
- [7] A.A. Zhukov, L.E. Shterenber, V.A. Shalashov, V.K. Thomas, and N.A. Berezivskaya. *Acta Metall.* 21 (1973) 195–197. doi:10.1016/0001-6160(73)90003-5.
- [8] A.A. Zhukov and R.L. Snezhnoi. *Acta Metall.* 21 (1973) 199–201. doi:10.1016/0001-6160(73)90004-7.
- [9] A.A. Zhukov and R.L. Snezhnoi. *Acta Metall.* 23 (1975) 1103–1110. doi:10.1016/0001-6160(75)90114-5.
- [10] A.A. Zhukov. *Russ. Metall.* (1976) 147–150.
- [11] T. Okamoto and H. Matsumoto. *Metal Science* 9 (1975) 8–12. doi:10.1179/030634575790445170.
- [12] F.X. Kayser and Y. Sumitomo. *J. Phase Equilib.* 18 (1997) 458–464. doi:10.1007/BF02647702.
- [13] L. Battezzati, M. Baricco, and S. Curiotto. *Acta Mater.* 53 (2005)(6) 1849–1856. doi:10.1016/j.actamat.2004.12.035.
- [14] V.I. Voronin, I.F. Berger, Y.N. Gornostyrev, V.N. Urtsev, A.R. Kuznetsov, and A.V. Shmakov. *JETP Lett.* 91 (2010) 143–146. doi:10.1134/s0021364010030094.
- [15] D. Walker, R. Dasgupta, J. Li, and A. Buono. *Contrib. Mineral. Petrol.* 166 (2013) 935–957. doi:10.1007/s00410-013-0900-7.

- [16] A. Leineweber, S.L. Shang, and Z.K. Liu. *Acta Mater.* 86 (2015) 374–384. doi:10.1016/j.actamat.2014.11.046.
- [17] A. Kagawa and T. Okamoto. *Trans. Japan Inst. Met.* 22 (1981) 137–143. doi:10.2320/matertrans1960.22.137.
- [18] H.S. Kitaguchi, S. Lozano-Perez, and M.P. Moody. *Ultramicroscopy* 147 (2014) 51–60. doi:10.1016/j.ultramic.2014.06.004.
- [19] D.H. Jack and K.H. Jack. *Mater. Sci. Eng.* 11 (1973) 1–27. doi:10.1016/0025-5416(73)90055-4.
- [20] H.J. Grabke. *Ber. Bunsen-Ges. Phys. Chem.* 73 (1969) 596–601. doi:10.1002/bbpc.19690730617.
- [21] H.A. Wriedt. *Trans. TMS-AIME* 245 (1969) 43–46.
- [22] B.J. Kooi, M.A.J. Somers, and E.J. Mittemeijer. *Metall. Mater. Trans. A* 27A (1996) 1055–1061. doi:10.1007/BF02649774.
- [23] E.J. Mittemeijer and J.T. Slycke. *Surf. Eng.* 12 (1996) 152–162. doi:10.1179/sur.1996.12.2.152.
- [24] A. Leineweber, T. Gressmann, and E.J. Mittemeijer. *Surf. Coat. Technol.* 206 (2012) 2780–2791. doi:10.1016/j.surfcoat.2011.11.035.
- [25] E.J. Mittemeijer. *ASM Handbook, Volume 4A, Steel Heat Treating Fundamentals and Processes*, chapter Fundamentals of Nitriding and Nitrocarburizing. ASM International (2013) 619–646.
- [26] M.W. Chase Jr. *NIST-JANAF Thermochemical Tables, Fourth Edition*. J. Phys. Chem. Ref. Data, Monograph 9 (1998).
- [27] R. Hoffmann, E.J. Mittemeijer, and M.A.J. Somers. *Härt.-Tech. Mitt.* 51 (1996) 126–169.
- [28] E. Lehrer. *Z. Elektrochem.* 36 (1930) 383–392. doi:10.1002/bbpc.19300360606.
- [29] T. Woehrle, A. Leineweber, and E.J. Mittemeijer. *Metall. Mater. Trans. A* 43A (2012) 2401–2413. doi:10.1007/s11661-012-1100-1.
- [30] J. Stein, R.E. Schacherl, M.S. Jung, S. Meka, B. Rheingans, and E.J. Mittemeijer. *Int. J. Mater. Res. (formerly Z. Metallkd.)* 104 (2013) 1053–1065. doi:10.3139/146.110968.
- [31] J. Ågren. *Metall. Trans. A* 10A (1979) 1847–1852. doi:10.1007/BF02811728.
- [32] P. Gustafson. *Scand. J. Metall.* 14 (1985) 259–267.
- [33] B. Hallstedt, D. Djurovic, J. von Appen, R. Dronkowski, A. Dick, F. Körmann, T. Hickel, and J. Neugebauer. *CALPHAD* 34 (2010) 129–133. doi:10.1016/j.calphad.2010.01.004.

- [34] R. Naraghi, M. Selleby, and J. Ågren. *CALPHAD* 46 (2014) 148–158. doi:10.1016/j.calphad.2014.03.004.
- [35] M. Hillert and M. Jarl. *Metall. Trans. A* 6A (1975) 553–559. doi:10.1007/BF02658414.
- [36] L. Maldzinski, Z. Przylecki, and J. Kunze. *Steel Res.* 57 (1986) 645–649.
- [37] J. Kunze. *Steel Res.* 57 (1986) 361–367.
- [38] K. Frisk. *CALPHAD* 11 (1987) 127–134. doi:10.1016/0364-5916(87)90004-6.
- [39] J. Kunze. *Nitrogen and Carbon in Iron and Steel. Thermodynamics*. Akademie-Verlag, Berlin (1990).
- [40] K. Frisk. *CALPHAD* 15 (1991) 79–106. doi:10.1016/0364-5916(91)90028-I.
- [41] H. Du. *J. Phase Equilib.* 14 (1993) 682–693. doi:10.1007/BF02667880.
- [42] A. F. Guillermet and H. Du. *Z. Metallkd.* 85 (1994) 154–163.
- [43] J. Kunze. *Härt.-Tech. Mitt.* 51 (1996) 348–355.
- [44] S. Hertzman. *Metall. Trans. A* 18 (1987) 1753–1766. doi:10.1007/bf02646207.
- [45] J. Slycke, L. Sproge, and J. Ågren. *Scand. J. Metall.* 17 (1988) 122–126.
- [46] H. Du and M. Hillert. *Z. Metallkd.* 82 (1991) 310–316.
- [47] P. Franke and H.J. Seifert (eds.). *Landolt-Börnstein - Group IV Physical Chemistry, Volume 19C1 - Thermodynamic Properties of Inorganic Materials compiled by SGTE. Ternary Steel Systems: Phase Diagrams and Phase Transition Data*. Springer (2012). doi:10.1007/978-3-540-88142-1_67.
- [48] P. J. Spencer. *CALPHAD* 32 (2008) 1–8. doi:10.1016/j.calphad.2007.10.001.
- [49] A.T. Dinsdale. *CALPHAD* 15 (1991) 317–425. doi:10.1016/0364-5916(91)90030-N.
- [50] H. Lukas, S.G. Fries, and B. Sundman. *Computational Thermodynamics – The Calphad Method*. Cambridge University Press (2007).
- [51] M. Hillert. *J. Alloys Compd.* 320 (2001) 161–176. doi:10.1016/S0925-8388(00)01481-X.
- [52] M. Hillert and L.-I. Staffansson. *Acta Chem. Scand.* 24 (1970) 3618–3626. doi:10.3891/acta.chem.scand.24-3618.
- [53] H. Kopp. *Philos. Trans. R. Soc. Lond.* 155 (1865) 71–202. doi:10.1098/rstl.1865.0003.
- [54] M. Hillert. *Phase Equilibria, Phase Diagrams and Phase Transformations*. Cambridge University Press (2007). doi:10.1017/cbo9780511812781.

- [55] G. Inden. In W. Pitsch (ed.), *Project meeting CALPHAD V*. III.4–1–13.
- [56] M. Hillert and M. Jarl. *CALPHAD* 2 (1978) 227–238. doi:10.1016/0364-5916(78)90011-1.
- [57] O. Redlich and A.T. Kister. *Ind. Eng. Chem.* 40 (1948) 345–348. doi:10.1021/ie50458a036.
- [58] M. Hillert. *CALPHAD* 4 (1980) 1–12. doi:10.1016/0364-5916(80)90016-4.
- [59] C. Wagner and W. Schottky. *Z. Phys. Chem. B* 11 (1930) 163–210.
- [60] W. Gorsky. *Z. Phys.* 50 (1928)(1-2) 64–81. doi:10.1007/bf01328593.
- [61] W.L. Bragg and E.J. Williams. *Proc. R. Soc. London, Ser. A* 145 (1934) 699–730. doi:10.1098/rspa.1934.0132.
- [62] W.L. Bragg and E.J. Williams. *Proc. R. Soc. London, Ser. A* 151 (1935) 540–566. doi:10.1098/rspa.1935.0165.
- [63] E.J. Williams. *Proc. R. Soc. London, Ser. A* 152 (1935)(875) 231–252. doi:10.1098/rspa.1935.0188.
- [64] B.J. Kooi, M.A.J. Somers, and E.J. Mittemeijer. *Metall. Mater. Trans. A* 25A (1994) 2797–2814. doi:10.1007/BF02649230.
- [65] M.A.J. Somers, B.J. Kooi, L. Maldzinski, E.J. Mittemeijer, A.A. van der Horst, A.M. van der Kraan, and N.M. van der Pers. *Acta Mater.* 45 (1997) 2013–2025. doi:10.1016/S1359-6454(96)00307-2.
- [66] M.I. Pekelharing, A. Böttger, M.A.J. Somers, M.P. Steenvoorden, A.M. van der Kraan, and E.J. Mittemeijer. *Mater. Sci. Forum* 318–320 (1999) 115–120. doi:10.4028/www.scientific.net/MSF.318-320.115.
- [67] S.-L. Chen, S. Daniel, F. Zhang, Y.A. Chang, X.-Y. Yan, F.-Y. Xie, R. Schmid-Fetzer, and W.A. Oates. *CALPHAD* 26 (2002)(2) 175–188. doi:10.1016/s0364-5916(02)00034-2.
- [68] R.H. Davies, A.T. Dinsdale, J.A. Gisby, J.A.J. Robinson, and S.M. Martin. *CALPHAD* 26 (2002) 229–271. doi:10.1016/s0364-5916(02)00036-6.
- [69] C.W. Bale, P. Chartrand, S.A. Degterov, G. Eriksson, K. Hack, R. Ben Mahfoud, J. Melançon, A.D. Pelton, and S. Petersen. *CALPHAD* 26 (2002) 189–228. doi:10.1016/s0364-5916(02)00035-4.
- [70] J.-O. Andersson, T. Helander, L. Höglund, P. Shi, and B. Sundman. *CALPHAD* 26 (2002) 273–312. doi:10.1016/S0364-5916(02)00037-8.
- [71] B. Sundman, U.R. Kattner, M. Palumbo, and S.G. Fries. *Integr. Mater. Manuf. Innov.* 4 (2015)(1) 1:1–15. doi:10.1186/s40192-014-0029-1.

- [72] J.S. Kirkaldy and D.J. Young. *Diffusion in the condensed state*. The Institute of Metals, London (1987).
- [73] M.E. Glicksman. *Diffusion in solids : field theory, solid-state principles, and applications*. Wiley, New York (2000).
- [74] T. Gressmann, M. Nikolussi, A. Leineweber, and E.J. Mittemeijer. *Scr. Mater.* 55 (2006) 723–726. doi:10.1016/j.scriptamat.2006.06.022.
- [75] M. Nikolussi, A. Leineweber, E. Bischoff, and E.J. Mittemeijer. *Int. J. Mater. Res. (formerly Z. Metallkd.)* 98 (2007) 1086–1092. doi:10.3139/146.101576.
- [76] M. Nikolussi, A. Leineweber, and E.J. Mittemeijer. *Acta Mater.* 56 (2008) 5837–5844. doi:10.1016/j.actamat.2008.08.001.
- [77] M. Nikolussi, A. Leineweber, and E.J. Mittemeijer. *J. Mater. Sci.* 44 (2009) 770–777. doi:10.1007/s10853-008-3160-6.
- [78] M. Nikolussi, A. Leineweber, and E.J. Mittemeijer. *Philos. Mag.* 90 (2010) 1105–1122. doi:10.1080/14786430903292365.
- [79] T. Wöhrle, A. Leineweber, and E.J. Mittemeijer. *J. Heat Treatm. Mat.* 65 (2010) 243–248. doi:10.3139/105.110069.
- [80] T. Woehrle, A. Leineweber, and E.J. Mittemeijer. *Metall. Mater. Trans. A* 43A (2012) 610–618. doi:10.1007/s11661-011-0870-1.
- [81] T. Woehrle, A. Leineweber, and E.J. Mittemeijer. *Metall. Mater. Trans. A* 44A (2013) 2548–2562. doi:10.1007/s11661-013-1640-z.
- [82] T. Woehrle, H. Cinaroglu, A. Leineweber, and E.J. Mittemeijer. *Int. J. Mater. Res. (formerly Z. Metallkd.)* 107 (2016) 192–202. doi:10.3139/146.111341.
- [83] E. Scheil, W. Mayr, and J. Müller. *Arch. Eisenhüttenwes.* 33 (1962) 385–392.
- [84] F.K. Naumann and G. Langenscheid. *Arch. Eisenhüttenwes.* 36 (1965) 677–682.
- [85] D. Gerardin, H. Michel, J.P. Morniroli, and M. Gantois. *Mem. Sci. Rev. Metall.* 74 (1977) 457–467.
- [86] J. Matauscheck and H. Trenkler. *Härt.-Tech. Mitt.* 32 (1977) 177–181.
- [87] E.J. Mittemeijer, W.T.M. Straver, P.F. Colijn, P.J. van der Schaaf, and J.A. van der Hoeven. *Scr. Metall.* 14 (1980) 1189–1192. doi:10.1016/0036-9748(80)90254-9.
- [88] A. Wells and T. Bell. *Heat Treat. Met.* 10 (1983) 39–44.
- [89] H.C.F. Rozendaal, F. Colijn, and E.J. Mittemeijer. *Surf. Eng.* 1 (1985) 30–42. doi:10.1179/sur.1985.1.1.30.

- [90] A. Wells. *J. Mater. Sci.* 20 (1985) 2439–2445. doi:10.1007/BF00556072.
- [91] A. Wells. *Thin Solid Films* 128 (1985) L33–L36. doi:10.1016/0040-6090(85)90347-5.
- [92] M.A.J. Somers and E.J. Mittemeijer. *Surf. Eng.* 3 (1987) 123–137. doi:10.1179/sur.1987.3.2.123.
- [93] X. Zuyao and L. Lin. *Mater. Sci. Technol.* 3 (1987) 325–328. doi:10.1179/mst.1987.3.5.325.
- [94] M.A.J. Somers, P.F. Colijn, W.G. Sloof, and E.J. Mittemeijer. *Z. Metallkd.* 81 (1990) 33–43.
- [95] S. Pietzsch, S. Böhmer, and H.-J. Spies. In *Proceedings of the Second International Conference on Carburizing and Nitriding with Atmospheres*. 295–300.
- [96] H. Du, M.A.J. Somers, and J. Ågren. *Metall. Mater. Trans. A* 31A (2000) 195–211. doi:10.1007/s11661-000-0065-7.
- [97] J. Chipman. *Metall. Trans.* 3 (1972) 55–64. doi:10.1007/BF02680585.
- [98] H. Ohtani, M. Hasebe, and T. Nishizawa. *Trans. ISIJ* 24 (1984) 857–864. doi:10.2355/isijinternational1966.24.857.
- [99] R. Kohlhaas, P. Duenner, and N. Schmitz-Pranghe. *Z. Angew. Phys.* 23 (1967) 245–249.
- [100] M.A.J. Somers, N.M. van der Pers, D. Schalkoord, and E.J. Mittemeijer. *Metall. Trans. A* 20A (1989) 1533–1539. doi:10.1007/BF02665509.
- [101] T. Liapina, A. Leineweber, E.J. Mittemeijer, and W. Kockelmann. *Acta Mater.* 52 (2004) 173–180. doi:10.1016/j.actamat.2003.09.003.
- [102] M. Nikolussi, S.L. Shang, T. Gressmann, A. Leineweber, E.J. Mittemeijer, Y. Wang, and Z.-K. Liu. *Scr. Mater.* 59 (2008) 814–817. doi:10.1016/j.scriptamat.2008.06.015.
- [103] P. Grieveson and E.T. Turkdogan. *Trans. TMS-AIME* 230 (1964) 407–414.
- [104] P. Grieveson and E.T. Turkdogan. *Trans. TMS-AIME* 230 (1964) 1604–1609.
- [105] B. Prenosil. *Konove Mater.* 3 (1965) 69–87.
- [106] A.E. Lord and D.N. Beshers. *Acta Metall.* 14 (1966) 1659–1672. doi:10.1016/0001-6160(66)90018-6.
- [107] J.R.G. Da Silva and R.B. McLellan. *Mater. Sci. Eng.* 26 (1976) 83–87. doi:10.1016/0025-5416(76)90229-9.
- [108] Y. M. Lakhtin and Y. D. Kogan. *Nitriding of Steel*. Mashinostroenie, Moscow (1976).
- [109] J. Colwell, G.W. Powell, and J.L. Ratliff. *J. Mater. Sci.* 12 (1977) 543–548. doi:10.1007/BF00540279.

- [110] H.C.F. Rozendaal, E.J. Mittemeijer, P.F. Colijn, and P.J. van der Schaaf. *Metall. Trans. A* 14A (1983) 395–399. doi:10.1007/BF02644217.
- [111] P.B. Friehling, F.W. Poulsen, and M.A.J. Somers. *Z. Metallkd.* 92 (2001) 589–595.
- [112] H. Du. Ph.D. thesis, Royal Institute of Technology, Stockholm, Sweden (1994).
- [113] L. Torchane. Ph.D. thesis, INPL Nancy, France (1994).
- [114] M.A.J. Somers and E.J. Mittemeijer. *Metall. Mater. Trans. A* 26A (1995) 57–74. doi:10.1007/BF02669794.
- [115] L. Torchane, P. Bilger, J. Dulcy, and M. Gantois. *Metall. Mater. Trans. A* 27A (1996) 1823–1835. doi:10.1007/BF02651932.
- [116] T. Belmonte, M. Gouné, and H. Michel. *Mater. Sci. Eng. A* 302 (2001) 246–257. doi:10.1016/S0921-5093(00)01830-X.
- [117] A. Fraguera, J.A. Gómez, F. Castillo, and J. Oseguera. *Mathematics and Computers in Simulation* 79 (2009) 1878–1894. doi:10.1016/j.matcom.2007.02.013.
- [118] H. Du and J. Ågren. *Metall. Mater. Trans. A* 27A (1996) 1073–1080. doi:10.1007/BF02649776.
- [119] J.-O. Andersson and J. Ågren. *J. Appl. Phys.* 72 (1992) 1350–1355. doi:10.1063/1.351745.
- [120] F.J.J. van Loo. *Prog. Solid St. Chem.* 20 (1990) 47–99. doi:10.1016/0079-6786(90)90007-3.
- [121] M. Kizilyalli, J. Corish, and R. Metselaar. *Pure Appl. Chem.* 71 (1999) 1307–1325. doi:10.1351/pac199971071307.
- [122] A.A. Kodentsov, G.F. Bastin, and F.J.J. van Loo. *J. Alloys Compd.* 320 (2001) 207–217. doi:10.1016/S0925-8388(00)01487-0.
- [123] P.F. Colijn, E.J. Mittemeijer, and H.C.F. Rozendaal. *Z. Metallkd.* 74 (1983) 620–627.
- [124] G. Petzow. *Metallographic Etching: Techniques for Metallography, Ceramography, Plastography*. ASM International (1999).
- [125] J.S. Duerr and R.E. Ogilvie. *Anal. Chem.* 44 (1972) 2361–2367. doi:10.1021/ac60322a012.
- [126] J.L. Pouchou and F. Pichoir. *Rech. Aerosp.* (1984) 167–192.
- [127] X. Gu, G. M. Michal, F. Ernst, H. Kahn, and A. H. Heuer. *Metall. Mater. Trans. A* 45A (2014) 4268–4279. doi:10.1007/s11661-014-2377-z.
- [128] R.M. Asimov. *Trans. AIME* 230 (1964) 611–613.

- [129] K.H. Jack. *Proc. R. Soc. London, Ser. A* 185 (1948) 41–55. doi:10.1098/rspa.1948.0101.
- [130] A. Leineweber, T. Liapina, T. Gressmann, M. Nikolussi, and E.J. Mittemeijer. *Adv. Sci. Tech.* 46 (2006) 32–41. doi:10.4028/www.scientific.net/AST.46.32.
- [131] L. Cheng and E.J. Mittemeijer. *Metall. Trans. A* 21A (1990) 13–26. doi:10.1007/BF02656420.
- [132] L. Cheng, A. Böttger, and E.J. Mittemeijer. *Metall. Trans. A* 23A (1992) 1129–1145. doi:10.1007/BF02665045.
- [133] E.J. Mittemeijer. *Fundamentals of Materials Science*. Springer, Heidelberg (2011). ISBN 978-3-642-10499-2. doi:10.1007/978-3-642-10500-5.
- [134] S. Malinov, A.J. Böttger, E.J. Mittemeijer, M.I. Pekelharing, and M.A.J. Somers. *Metall. Mater. Trans. A* 32A (2001) 59–73. doi:10.1007/s11661-001-0102-1.
- [135] M.A.J. Somers and E.J. Mittemeijer. *Metall. Trans. A* 21A (1990) 901–912. doi:10.1007/bf02656574.
- [136] M. Hillert. In V.F. Zackay and H.L. Aaronson (eds.), *Decomposition of austenite by diffusional processes*. 197–247.
- [137] S.C. Xiong, A. Redjaïmia, and M. Gouné. *J. Mater. Sci.* 44 (2009) 632–638. doi:10.1007/s10853-008-3054-7.
- [138] E.J. Mittemeijer and U.S. Welzel (eds.). *Modern Diffraction Methods*. Wiley-VCH (2013).
- [139] A.A. Coelho. Topas. Bruker AXS GmbH, Karlsruhe (2003).
- [140] EDAX OIM Analysis, Version 7.0.1 (2013).
- [141] B. Schwarz, H. Göhring, S. R. Meka, R. E. Schacherl, and E. J. Mittemeijer. *Metall. Mater. Trans. A* 45A (2014) 6173–6186. doi:10.1007/s11661-014-2581-x.
- [142] D. Gerardin, J.P. Morniroli, H. Michel, and M. Gantois. *J. Mater. Sci.* 16 (1981) 159–169. doi:10.1007/BF00552070.
- [143] W. Schröter, R. Russev, K. Ibendorf, and E. Vatev. *Wiss. Z. d. Techn. Hochsch. Karl-Marx-Stadt* 24 (1982) 786–794.
- [144] X. Xu, L. Wang, Z. Yu, and Z. Hei. *Metall. Mater. Trans. A* 27A (1996) 1347–1352. doi:10.1007/BF02649871.
- [145] W.L. Chen, C.L. Wu, Z.R. Liu, S. Ni, Y. Hong, Y. Zhang, and J.H. Chen. *Acta Mater.* 61 (2013) 3963–3972. doi:10.1016/j.actamat.2013.02.058.
- [146] J.R. Davis (ed.). *ASM Handbook Volume 3 – Alloy phase diagrams*. ASM International (1992).

- [147] V. Raghavan. *Phase Diagrams of Ternary Iron Alloys* (1987) 153–165.
- [148] E. Vatev, R.R. Varna, W. Schröter, and K. Ibendorf. *Neue Hütte* 28 (1983) 389–393.
- [149] C. Ruset, A. Bloyce, and T. Bell. *Heat Treat. Met.* 22 (1995) 95–100.
- [150] T. Bell, Y. Sun, and A. Suhadi. *Vacuum* 59 (2000) 14–23. doi:10.1016/S0042-207X(00)00250-5.
- [151] H.S. Cho and T. Bell. *Met. Mater. Int.* 8 (2002) 93–98. doi:10.1007/BF03027034.
- [152] T. Liapina, A. Leineweber, and E.J. Mittemeijer. *Scr. Mater.* 48 (2003) 1643–1648. doi:10.1016/S1359-6462(03)00136-2.
- [153] T. Liapina, A. Leineweber, and E.J. Mittemeijer. *Metall. Mater. Trans. A* 37A (2006) 319–330. doi:10.1007/s11661-006-0003-4.
- [154] V. Raghavan. *Trans. Indian Inst. Met.* 37 (1984) 293–301.
- [155] V. Raghavan. *J. Phase Equilib.* 14 (1993) 620–621. doi:10.1007/BF02669146.
- [156] E. Scheil. *Arch. Eisenhüttenwes.* 9 (1936) 571–573.
- [157] H.L. Lukas, E.-T. Henig, and G. Petzow. *Z. Metallkd.* 77 (1986) 360–367.
- [158] B. Predel, M. Hoch, and M. Pool. *Phase Diagrams and Heterogeneous Equilibria*. Springer Berlin Heidelberg (2004). doi:10.1007/978-3-662-09276-7.
- [159] A. Prince. *Alloy Phase Equilibria*. Elsevier Publishing Company, Amsterdam (1966).
- [160] B. Sundman and J. Ågren. *J. Phys. Chem. Solids* 42 (1981) 297–301. doi:10.1016/0022-3697(81)90144-X.
- [161] B. Uhrenius and H. Harvig. *Met. Sci.* 9 (1975) 67–82. doi:10.1179/030634575790444379.
- [162] M. Jarl. *Scand. J. Metall.* 7 (1978) 93–101.
- [163] M. Hillert. *Phase equilibria, phase diagrams, and phase transformations: their thermodynamic basis*. Cambridge University Press, Cambridge (1998).
- [164] H. Oettel and H. Schumann (eds.). *Metallografie*. Wiley-VCH, Weinheim, Germany (2011).
- [165] W.A. Oates and T.B. Flanagan. *J. Mater. Sci.* 16 (1981) 3235–3243. doi:10.1007/BF00586283.
- [166] I. Ansara and B. Sundman. *CALPHAD* 24 (2000) 181–182. doi:10.1016/S0364-5916(00)00022-5.
- [167] S. Umino. *Sci. Repts. Tohoku Imp. Univ.* 23 (1935) 665–793.

- [168] L.S. Darken and R.W. Gurry. *Trans. AIME* 191 (1951) 1015–1018.
- [169] R. Hultgren, P.T. Desai, D.T. Hawkins, M. Gleiser, and K.K. Kelley. *Selected values of the thermodynamic properties of binary alloys*. Am. Soc. Met., Metals Park, Ohio (1973) 477–488.
- [170] G. Naeser. *Mitt. Kais.-Wilh.-Inst. Eisenforschg.* 16 (1934) 207–210.
- [171] M. Umemoto, Z.G. Liu, K. Masuyama, and K. Tsuchiya. *Scr. Mater.* 45 (2001) 391–397. doi:10.1016/S1359-6462(01)01016-8.
- [172] S.V. Meschel and O.J. Kleppa. *J. Alloys Compd.* 257 (1997) 227–233. doi:10.1016/S0925-8388(97)00023-6.
- [173] W. Stuckens and A. Michel. *Comptes Rendus Hebdomadaires des Séances de l'Academie des Sciences* 253 (1961) 2358–2360.
- [174] L.J. Dijkstra. *Trans. AIME* 185 (1949) 252–260.
- [175] J.K. Stanley. *Trans. AIME* 185 (1949) 752–761.
- [176] C.A. Wert. *Trans. AIME* 188 (1950) 1242–1244.
- [177] G. Borelius and S. Berglund. *Arkiv för Fysik* 4 (1951) 173–182.
- [178] E. Lindstrand. *Acta Metall.* 3 (1955) 431–435. doi:10.1016/0001-6160(55)90130-9.
- [179] E.F. Petrova, M.I. Lapshina, and L.A. Shvarsman. *Soviet Phys. Doklady* 3 (1958) 872–876.
- [180] R.P. Smith. *Trans. TMS-AIME* 224 (1962) 105–111.
- [181] J.C. Swartz. *Trans. TMS-AIME* 245 (1969) 1083–1092.
- [182] M. Hasebe, H. Ohtani, and T. Nishizawa. *Metall. Trans. A* 16A (1985) 913–921. doi:10.1007/bf02814843.
- [183] J.-L. Bonnentien and J. Bigot. *Mater. Trans., JIM* 41 (2000) 78–81. doi:10.2320/matertrans1989.41.78.
- [184] R.B. McLellan and P. Chraska. *Mater. Sci. Eng.* 7 (1971) 305–317. doi:10.1016/0025-5416(71)90014-0.
- [185] G. Lagerberg and Å. Josefsson. *Acta Metall.* 3 (1955) 236–244. doi:10.1016/0001-6160(55)90058-4.
- [186] J. Merlin, P. Merle, S. Garnier, M. Bouzekri, and M. Soler. *Metall. Mater. Trans. A* 35A (2004) 1655–1661. doi:10.1007/s11661-004-0074-z.
- [187] T. Heumann and J. Große-Wördemann. *Arch. Eisenhüttenwes.* 30 (1959) 35–39.

- [188] R.P. Smith. *Trans. AIME* 215 (1959) 954–957.
- [189] M.G. Benz and J.F. Elliott. *Trans. TMS-AIME* 221 (1961) 323–331.
- [190] E. Scheil, T. Schmidt, and J. Wünning. *Arch. Eisenhüttenwes.* 32 (1961) 251–260.
- [191] H. Seltz, H.J. McDonald, and C. Wells. *Trans. AIME* 140 (1940) 263–278.
- [192] A. Dick, F. Körmann, T. Hickel, and J. Neugebauer. *Phys. Rev. B* 84 (2011) 125101–1–9. doi:10.1103/PhysRevB.84.125101.
- [193] L.J.E. Hofer and E.M. Cohn. *J. Am. Chem. Soc.* 81 (1959) 1576–1582. doi:10.1021/ja01516a016.
- [194] I.N. Shabanova and V.A. Trapeznikov. *JETP Lett.* 18 (1973) 339–341.
- [195] J. Häglund, G. Grimvall, and T. Jarlborg. *Phys. Rev. B* 44 (1991) 2914–2919. doi:10.1103/physrevb.44.2914.
- [196] S. Khmelevskyi, A.V. Ruban, and P. Mohn. *J. Phys.: Condens. Matter* 17 (2005) 7345–7352. doi:10.1088/0953-8984/17/46/018.
- [197] E. Schürmann and R. Schmid. *Arch. Eisenhüttenwes.* 50 (1979) 185–188.
- [198] L.S.I. Liyanage, S.-G. Kim, J. Houze, S. Kim, M.A. Tschopp, M.I. Baskes, and M.F. Horstemeyer. *Phys. Rev. B* 89 (2014) 094102–1–11. doi:10.1103/physrevb.89.094102.
- [199] A.A. Zhukov and R.L. Snezhnoi. *Russ. Metall.* (1976) 145–152.
- [200] M.I. Pekelharing, A.J. Böttger, and E.J. Mittemeijer. *Philos. Mag.* 83 (2003) 1775–1796. doi:10.1080/1478643031000097115.
- [201] S. Shang and A.J. Böttger. *Acta Mater.* 53 (2005) 255–264. doi:10.1016/j.actamat.2004.09.009.
- [202] A.J. Böttger, D.E. Nanu, and A. Marashdeh. *Comput. Mater. Sci.* 95 (2014) 8–12. doi:10.1016/j.commatsci.2014.07.004.
- [203] S. Shang and A.J. Böttger. *Acta Mater.* 51 (2003) 3597–3606. doi:10.1016/s1359-6454(03)00177-0.
- [204] M.B. Bakkelund. *Thermodynamics of the hexagonal close-packed iron-nitrogen system from first-principles*. Ph.D. thesis, Technical University of Denmark (2015).
- [205] D. Gerardin, H. Michel, and M. Gantois. *Scr. Metall.* 11 (1977) 557–561. doi:10.1016/0036-9748(77)90108-9.
- [206] E. Lehrer. *Z. Techn. Phys.* 10 (1929) 177–185.
- [207] O. Eisenhut and E. Kaupp. *Z. Elektrochem.* 36 (1930) 392–404. doi:10.1002/bbpc.19300360607.

- [208] P.H. Emmett, S.B. Hendricks, and S. Brunauer. *J. Am. Chem. Soc.* 52 (1930) 1456–1464. doi:10.1021/ja01367a024.
- [209] E. Lehrer. *Z. Elektrochem.* 36 (1930) 460–473. doi:10.1002/bbpc.19300360711.
- [210] S. Brunauer, M.E. Jefferson, P.H. Emmett, and S.B. Hendricks. *J. Am. Chem. Soc.* 53 (1931) 1778–1786. doi:10.1021/ja01356a020.
- [211] C. Guillaud and H. Creveaux. *Compt. Rend. Acad. Sci. Paris* 222 (1946) 1170–1172.
- [212] L.B. Paranjpe, M. Cohen, M.B. Bever, and C.F. Floe. *Trans. AIME* 188 (1950) 261–267.
- [213] A. Burdese. *Metall. Ital.* 47 (1955) 357–361.
- [214] N.S. Corney and E.T. Turkdogan. *J. Iron Steel Inst.* 180 (1955) 344–348.
- [215] J.D. Fast and M.B. Verrijp. *J. Iron Steel Inst.* 180 (1955) 337–343.
- [216] W. Pitsch and E. Houdremont. *Arch. Eisenhüttenwes.* 27 (1956) 281–284.
- [217] A. Burdese. *Ann. Chim. (Rome, Italy)* 49 (1959) 1873–1884.
- [218] M. Nacken and J. Rahmann. *Arch. Eisenhüttenwes.* 33 (1962) 131–140.
- [219] H.A. Wriedt (1964). Unpublished results listed in H.A. Wriedt, N.A. Gokcen, and R.H. Nafziger, *J. Phase Equilib.* 8 (1987) 355–377.
- [220] D. Atkinson and C. Bodsworth. *J. Iron Steel Inst.* 208 (1970) 587–593.
- [221] K. Abiko and Y. Imai. *Trans. Japan Inst. Met* 18 (1977) 113–124.
- [222] H.H. Podgurski and F.N. Davis. *Acta Metall.* 29 (1981) 1–9. doi:10.1016/0001-6160(81)90081-x.
- [223] Data shown in J. Kunze, Nitrogen and Carbon in Iron and Steel. Thermodynamics. Akademie-Verlag, Berlin, 1990, cited as Z. Przylecki, L. Maldzinski, private communication.
- [224] M.A.J. Somers and E.J. Mittemeijer. *Metall. Trans. A* 21A (1990) 189–204. doi:10.1007/BF02656436.
- [225] W.D. Jentzsch and S. Böhmer. *Krist. Techn.* 12 (1977) 1275–1283. doi:10.1002/crat.19770121209.
- [226] H. Schenck, M.G. Frohberg, and F. Reinders. *Stahl Eisen* 83 (1963) 93–99.
- [227] J.-O. Andersson. *CALPHAD* 12 (1988) 9–23. doi:10.1016/0364-5916(88)90025-9.
- [228] B.J. Kooi, M.A.J. Somers, and E.J. Mittemeijer. *Metall. Mater. Trans. A* 27A (1996) 1063–1071. doi:10.1007/BF02649775.

- [229] D.K. Inia, M.H. Pröpper, W.M. Arnoldbik, A.M. Vredenberg, and D.O. Boerma. *Appl. Phys. Lett.* 70 (1997) 1245–1247. doi:10.1063/1.118542.
- [230] E.H. Du Marchie van Voorthuysen, B. Feddes, N.G. Chechenin, D.K. Inia, A.M. Vredenberg, and D.O. Boerma. *phys. stat. sol. (a)* 177 (2000) 127–133.
- [231] E.H. Du Marchie van Voorthuysen, D.O. Boerma, and N.C. Chechenin. *Metall. Mater. Trans. A* 33A (2002) 2593–2598. doi:10.1007/s11661-002-0380-2.
- [232] A. Leineweber, J. Aufrecht, and E. J. Mittemeijer. *Int. J. Mater. Res. (formerly Z. Metallk.)* 97 (2006) 753–759. doi:10.3139/146.101298.
- [233] Y. Imai, M. Sohma, and T. Suemasu. *J. Alloys Compd.* 611 (2014) 440–445. doi:10.1016/j.jallcom.2014.04.171.
- [234] J.-S. Chen, C. Yu, and H. Lu. *J. Alloys Compd.* 625 (2015) 224–230. doi:10.1016/j.jallcom.2014.11.130.
- [235] C.M. Fang, M.A. van Huis, B.J. Thijssse, and H.W. Zandbergen. *Phys. Rev. B* 85 (2012) 054116–1–7. doi:10.1103/physrevb.85.054116.
- [236] B.J. Kooi. *Iron-Nitrogen Phases: thermodynamics, long-range order and oxidation behaviour*. Ph.D. thesis, TU Delft (1995).
- [237] M.I. Pekelharing, A.J. Böttger, M.A.J. Somers, and E.J. Mittemeijer. *Metall. Mater. Trans. A* 30A (1999) 1945–1953. doi:10.1007/s11661-999-0005-0.
- [238] C.M. Fang, M.A. van Huis, J. Jansen, and H.W. Zandbergen. *Phys. Rev. B* 84 (2011) 094102–1–10. doi:10.1103/PhysRevB.84.094102.
- [239] S. Hoja, H. Klümper-Westkamp, F. Hoffmann, and H.-W. Zoch. *J. Heat Treatm. Mat.* 65 (2010) 22–29. doi:10.3139/105.110045.

List of publications

1. H. Göhring, A. Leineweber, E.J. Mittemeijer
N and C interstitial diffusion and thermodynamic interactions in ϵ -iron carbonitride, Metall. Mater. Trans. A, 46A (2015) 3612–3626, doi:10.1007/s11661-015-2982-5
Chapter 2 of this thesis. Used with friendly permission of Springer.
2. H. Göhring, S. Kante, A. Leineweber, E.J. Mittemeijer
Microstructure development and crystallographic properties of decomposing Fe–N–C compound layers, Int. J. Mater. Res. (formerly Z. Metallkd.) 107 (2016) 203–216, doi:10.3139/146.111330
Chapter 3 of this thesis. Used with friendly permission of Carl Hanser Verlag.
3. H. Göhring, A. Leineweber, E.J. Mittemeijer
The $\alpha+\epsilon$ two-phase equilibrium in the Fe–N–C system – experimental investigations and thermodynamic calculations, Metall. Mater. Trans. A 47A (2016) 4411–4424, doi:10.1007/s11661-016-3605-5
Chapter 4 of this thesis. Original published under Creative Commons Attribution 4.0 International License (<http://creativecommons.org/licenses/by/4.0/>). Changes were made to cross-references and layout. References to supplementary material were removed.
4. H. Göhring, A. Leineweber, E.J. Mittemeijer
A thermodynamic model for non-stoichiometric cementite; the Fe–C phase diagram, CALPHAD 52 (2016) 38–46, doi:10.1016/j.calphad.2015.10.014
Chapter 5 of this thesis. Used with friendly permission of Elsevier.
5. H. Göhring, O. Fabrichnaya, A. Leineweber, E.J. Mittemeijer
Thermodynamics of the Fe–N and Fe–N–C systems; the Fe–N and Fe–N–C phase diagrams revisited, Metall. Mater. Trans. A 47A (2016) 6173–6186, doi:10.1007/s11661-016-3731-0
Chapter 6 of this thesis. Original published under Creative Commons Attribution 4.0 International License (<http://creativecommons.org/licenses/by/4.0/>). Changes were made to cross-references and layout. References to supplementary material were removed.
6. B. Schwarz, H. Göhring, S.R. Meka, R.E. Schacherl, E.J. Mittemeijer
Pore formation upon nitriding iron and iron-based alloys: the role of alloying elements and grain boundaries, Metall. Mater. Trans. A, 45A (2014) 6173–6186, doi: 10.1007/s11661-014-2581-x
7. A. Leineweber, S. Kante, N. Schäfer, H. Göhring, E.J. Mittemeijer
Orientation relationships in iron carbonitride compound layers and their relation with

diffusional transformations, Proc. Int. Conf. Solid-Solid Phase Transform. Inorg. Mater. 2015, 155–162.

8. T. Steiner, S.R. Meka, H. Göhring, E.J. Mittemeijer
Alloying element nitride stability in nitrided iron-based alloys; denitriding of nitrided Fe–V alloys, Mater. Sci. Technol. 2016, doi:10.1080/02670836.2016.1155254

Curriculum vitae

Persönliche Angaben

Name	Holger Josef Göhring
Geburtsdatum	23.10.1985
Geburtsort	Waiblingen

Universitäre Bildung

2012–2016	Promotion am Max-Planck-Institut für intelligente Systeme (ehemals Max-Planck-Institut für Metallforschung), Stuttgart und Institut für Materialwissenschaft der Universität Stuttgart, Thema der Dissertation: Interaction of carbon and nitrogen in iron, Hauptberichter: Prof. Dr. Ir. E.J. Mittemeijer
2006–2012	Studium der Werkstoffwissenschaft an der Universität Stuttgart. Abschluss: Diplom-Ingenieur

Zivildienst

2005–2006	Deutsches Rotes Kreuz, Kreisverband Rems-Murr
-----------	---

Schulbildung

1998–2005	Staufer-Gymnasium Waiblingen. Abschluss: Abitur
1992–1998	Karolinger-Grund- und Hauptschule Waiblingen

Danksagung

Die vorliegende Arbeit wurde am Max-Planck-Institut für intelligente Systeme (ehemals Max-Planck-Institut für Metallforschung) in Stuttgart und am Institut für Materialwissenschaft der Universität Stuttgart angefertigt. An dieser Stelle möchte ich mich bei allen bedanken, die einen Beitrag zu dieser Arbeit geleistet haben.

An erster Stelle möchte ich meinem Doktorvater Prof. Dr. Ir. Eric Jan Mittemeijer für die Aufnahme in seiner Abteilung, die Überlassung dieses interessanten Themas und sein Vertrauen in meine Arbeit danken. Dabei möchte ich besonders sein großes Engagement während der Betreuung der Arbeit und sein großes Interesse an meiner Arbeit während unzähliger wissenschaftlicher Diskussionen mit ihm hervorheben. Seine Anregungen hatten großen Einfluss auf die Arbeit, ließen mir aber trotzdem die Freiheit, meine eigenen wissenschaftlichen Ideen zu verwirklichen.

Ich danke Prof. Dr. Joachim Bill für die freundliche Übernahme des Mitberichts und Prof. Dr. Thomas Schleid für die Bereitschaft, den Prüfungsvorsitz zu übernehmen.

Prof. Dr. Andreas Leineweber war bis zu seinem Ruf an die TU Bergakademie Freiberg mein täglicher Betreuer. Ihm gebührt ein besonderer Dank für sein Engagement, viele fruchtbare Diskussionen und Ideen, die die Arbeit voranbrachten und seine stetige Hilfsbereitschaft. Ganz besonders möchte ich ihm dafür danken, dass er auch nach seinem Weggang vom MPI keine Mühen gescheut hat, meine Arbeit weiterhin zu unterstützen und dafür immer Zeit gefunden hat, ob für telefonische Diskussionen oder zum Gegenlesen der Manuskripte.

Besondere Erwähnung verdient auch Dr. Olga Fabrichnaya (TU Bergakademie Freiberg), die mich in die Grundlagen der thermodynamischen Modellierung einführte und mir bei der Arbeit an den Kapiteln 5 und 6 mit Rat und Tat zur Seite stand. Stefan Kante (M. Sc.) danke ich für seine Mitarbeit am Kapitel 3.

Außerdem möchte ich mich bei allen Mitarbeitern des Instituts und besonders der Abteilung Mittemeijer bedanken, die mir mit ihrer Hilfsbereitschaft zur Seite standen. Ich habe die freundliche und kollegiale Atmosphäre sehr genossen. Besonders erwähnen möchte ich Siglinde Haug (StEM, MPI für Festkörperforschung) für die Unterstützung bei den Mikrosondenmessungen, Dr. Ewald Bischoff für die Durchführung der EBSD-Messungen, Dr. Gábor Csiszár, Dr. Matej Fonović, Dr. Zoltan Hegedus, Dr. Benjamin Schwarz und Dipl.-Ing. Tobias Steiner für viele wissenschaftliche und nicht-wissenschaftliche Diskussionen und Ute Schestag und Winfried Engelhardt für technische Unterstützung jeglicher Art.

Zu guter Letzt möchte ich die Menschen erwähnen, die mir persönlich am wichtigsten sind und die mir während der letzten Jahre immerzu Halt gegeben haben: meine Familie, meine Freunde und ganz besonders meine Freundin Pascaline. Ich danke euch von Herzen.

Erklärung über die Eigenständigkeit der Dissertation

Ich versichere, dass ich die vorliegende Arbeit mit dem Titel

Interaction of carbon and nitrogen in iron

selbständig verfasst und keine anderen als die angegebenen Quellen und Hilfsmittel benutzt habe; aus fremden Quellen entnommene Passagen und Gedanken sind als solche kenntlich gemacht.

Holger Göhring

Stuttgart, den 15. März 2016
